Contributions to computational geotechnics

Non-isothermal flow in low-permeable porous media

Dissertation
zur Erlangung des Grades eines Doktors der Naturwissenschaften

der Geowissenschaftlichen Fakultät
der Eberhard-Karls-Universität Tübingen

vorgelegt von
Joëlle De Jonge
aus Ixelles (Belgien)

2005

Tag der mündlichen Prüfung: 24. Juni 2005

Dekan: Prof. Klaus G. Nickel, Ph.D.

1. Berichterstatter: Prof. Dr. Olaf Kolditz

2. Berichterstatter: Dr. Stefan Finsterle, USA

Zusammenfassung

Um thermische (T), hydraulische (H) und mechanische (M) Prozesse, ihre Kopplungen und ihren Einfluß auf das Systemverhalten besser zu verstehen, werden T-H-M Modelle entwickelt. Diese Modelle lassen Modellierungen im Nahbereich des Systems zu. Die Simulierung von nicht-isothermen, thermo-hydraulischen (TH) Prozessen ist für Anwendungen wie Geothermie, Wärmeunterstützte Grundwassersanierung, und Atommüllentsorgung wichtig. Diese Doktorarbeit richtet sich spezifisch an den Anwendungen für Atommüllentsorgung aus, vor Allem an den thermischen und hydraulischen Prozessen in diesem Bereich.

Thermische Prozesse kommen durch die Wärmestrahlung des Abfalls zustande und zeichnen sich durch den Wärmetransport vom Kanister zum Bentonitpuffer aus. Andere wichtige thermische Prozesse sind Verdampfung und Kondensierung, die mit dem Phasenwechsel zwischen wässeriger- und gas Phase assoziiert sind. Wichtige hydraulische Prozesse sind das Eindringen von Wasser von dem Gastgestein in den Puffer und dann in den Kanister, sowie quellen und schrumpfen des Bentonitpuffers. Bentonit quillt durch das Eindringen von Wasser und trocknet durch den Wärmetransport des Abfalls.

Das Ziel der Arbeit ist die mathematische Formulierung der Prozesse und ihre Integrierung in den objekt-orientierten finite-elemente Code GeoSys/RockFlow.

Puffer, Gastgestein und Fluide (in der wässerigen und gas Phase) formen gemeinsam ein mehrphasiges-mehrkomponenten System (poröses Medium). Das TH Modell benötigt drei Bilanzgleichungen, eine für die Wasserkomponente, eine für die Luftkomponente und eine für Energie. Die drei Primärvariablen sind Gasdruck, Wassersättigung und Temperatur.

Um die Bilanzgleichungen zu lösen, werden Gleichungen, die das System beschreiben, benötigt. Dies sind Materialparameter, wie zum Beispiel Kapillardruck - Sättigungsbeziehungen oder Dichtegleichungen. Für die beschriebenen Prozesse sind diese Materialparameter und Zustandsgleichungen meist nicht-linear und meist Funktionen der Temperatur, der Sättigung und des Drucks. Nicht nur das Material, sondern auch der thermodynamische Zustand des Systems muß beschrieben werden. Dies wird mit Zustandsgleichungen erreicht, zum Beispiel Funktionen zur Berechnung des Wasserdrucks, oder der Massenfraktionen. Materialparameter und Zustandsgleichungen werden in die Bilanzgleichungen substituiert, es resultieren die drei Modellgleichungen in Differentialform. Diese Gleichungen werden nach Umformungen von GeoSys/RockFlow gelöst.

Die Implementierung läßt Phasenwechsel zwischen den Fluidphasen (wasser und gas) explizit zu. Das Modell ermöglicht Simulationen von sehr undurchlässigem Tonmaterial mit hohen Kapillardrücken. Beispiele der Modellvalidierung werden gezeigt, wo Ton durch hohe Temperaturen entsättigt wird.

Summary

To better understand the coupling of thermal (T), hydraulic (H) and mechanical (M) processes (T-H-M processes) and their influence on the system behaviour, models allowing T-H-M coupling are developed. These models allow simulations in the near-field of the system. The modeling of non-isothermal thermo-hydraulic (TH) processes is important for applications such as geothermal energy generation, heat supported environmental remediation, and nuclear waste disposal. The work presented herein focuses on deep geological disposal of nuclear waste, and more specifically on the thermal and hydraulic processes in this application.

Thermal processes result directly from the heat radiation of the waste and include heat transport from the core to the bentonite buffer. Other processes of importance are vaporization and condensation associated with phase changes between the liquid and gaseous phases. Hydraulic processes of importance include water intrusion from the host rock to the buffer and eventually to the core, as well as swelling and shrinking processes in the bentonite. Bentonite swells as a result of water intrusion from the host rock and dries as a result of the heat transport from the core.

The objective of the work is to formulate the processes mathematically and to integrate them into the object-oriented simulator GeoSys/RockFlow.

Buffer, host rock, and fluids in the gas and liquid phase form a multiphase-multicomponental system (porous medium). The TH model consists of a set of three balance equations. One balance equation for the water component, one balance equation for the air component and one energy balance equation. The three primary, or independent variables are gas pressure, water saturation, and temperature.

To solve these balance equations, equations describing the material modelled are necessary. Material properties include for example capillary pressure-saturation relationships, density equations, or viscosity calculations. For those processes, material parameters and state variables are highly non-linear and mostly functions of temperature, saturation, and pressure. Other than describing the material, the thermodynamic state of the system has to be described. This is achieved with equations of state, as for example functions for the calculation of liquid pressure or mass fractions. When the material properties and the state functions are inserted into the balance equations, governing equations in the differential form are obtained. After numerical transformations, these equations are then solved by GeoSys/RockFlow.

The implementation allows phase changes between the fluid phases (gas and liquid) to occur explicitly. The model allows the simulation of processes in very low permeability clays with high capillary pressures. Examples for code validation are shown, where low permeability clay is desaturated.

Acknowledgement

I thank Prof. Olaf Kolditz for giving me the opportunity to work on this interesting topic, for his input and excellent guidance and supervision during these three years. I thank him too for contributing to an exceptional (musical) work atmosphere, as well as his encouragement and understanding.

I thank the Federal Agency of Geosciences and Natural Resources (BGR) for their support of this research project and making the funds available for this work. In particular I thank Dr. Wallner and Dr. Shao, as well as Dr. Liedtke. I would also like to thank Thomas Nowak and Herbert Kunz for constructive discussions and great help.

I would like to extend warm thanks to Stefan Finsterle and Rainer Helmig for their good guidance and enthousiastic discussions and willingness to help at different stages of my work.

I would like to acknowledge the constant support of the DECOVALEX project members. Their scientific input and support was invaluable. In particular I would like to thank Lanru Jing, Alain Millard, Son Ngyuen, Sebastia Olivella, and Amel Rejeb.

Without my work group and other ZAG members this whole research would have been exceptionally difficult. I thank them for being so supportive scientifically and on personal matters, and for creating a fun and light work atmosphere.

My heartfelt thanks go to my friends, in particular Jannine Bothner, Chris Fisher, Tobias Clauß and Katrin Hieke. They have known how to encourage me, listened to my complaints and turned hard times good.

Last but not least I would like to thank my parents, who although far away, were there when I needed them and believed in me.

List of Symbols

a ..... Component air $[-]$
c ..... Specific heat capacity $[\frac{\mathrm{J}}{\mathrm{kg \cdot K}}]$
$\mathbf{C}$ ..... Mass matrix, subscript: variable $[\mathrm{kg}]$
D ..... Diffusion coefficient $[\frac{\mathrm{m}^2}{\mathrm{s}}]$
$\mathbf{g}$ ..... Gravity vector $[\frac{\mathrm{m}}{\mathrm{s}^2}]$
g ..... Gas Phase, superscript $[-]$
h ..... Enthalpy $[\frac{\mathrm{J}}{\mathrm{kg}}]$
h ..... Heat, subscript $[-]$
$\mathbf{J}$ ..... Flux $[\frac{\mathrm{kg}}{\mathrm{m \cdot s}}]$
k ..... Component (subscript) $[-]$
k ..... Permeability $[\mathrm{m}^2]$
$\mathbf{k}$ ..... Permeability tensor $[\mathrm{m}^2]$
k_{rel} .... Relative permeability $[-]$
$\mathbf{K}$ ..... Conductivity matrix $[\frac{\mathrm{W}}{\mathrm{m \cdot K}}]$
K_H .... Henry coefficient $[\frac{1}{\mathrm{Pa}}]$
l ..... Liquid phase, superscript $[-]$
M ..... Molar mass $[\frac{\mathrm{kg}}{\mathrm{mol}}]$
m ..... Mass $[\mathrm{kg}]$
n ..... Porosity $[-]$
p ..... Pressure $[\mathrm{Pa}]$
$\mathbf{p}$ ..... Pressure vector $[\mathrm{Pa}]$
p_{c} ..... Capillary pressure $[\mathrm{Pa}]$
$\mathbf{p}_{\mathsf{c}}$ ..... Capillary pressure vector $[\mathrm{Pa}]$
Q ..... Source term $[\frac{\mathrm{m}^3}{\mathrm{s}}]$
R ..... Gas constant $[\frac{\mathrm{J}}{\mathrm{mol \cdot K}}]$
RHS .. Right hand side terms $[-]$
S ..... Saturation $[-]$
$\mathbf{S}$ ..... Saturation vector $[-]$
S_{eff} .... Effective saturation $[-]$
S_{max} ... Maximum saturation $[-]$
S_r ..... Residual saturation $[-]$
s ..... Solid phase, superscript $[-]$
Sat ..... Saturated, subscript $[-]$
T ..... Temperature $[\mathrm{K}]$
$\mathbf{T}$ ..... Temperature vector $[\mathrm{K}]$
t ..... Time $[\mathrm{s}]$
u ..... Internal energy $[\frac{\mathrm{J}}{\mathrm{kg}}]$
V ..... Volume $[\mathrm{m}^3]$
$\mathbf{v}$ ..... Velocity vector $[\frac{\mathrm{m}}{\mathrm{s}}]$
X ..... Mass fraction $[-]$
$\mathbf{X}$ ..... Mass fraction vector $[-]$
w ..... Water component, subscript $[-]$

β_p ..... Fluid compressibility coefficient $[\frac{1}{\mathrm{Pa}}]$
β_T ..... Thermal expansion coefficient $[\frac{1}{\mathrm{K}}]$
γ ..... Fluid phase (superscript) $[-]$
λ ..... Thermal conductivity $[\frac{\mathrm{J}}{\mathrm{K \cdot m \cdot s}}]$
μ ..... Fluid viscosity $[\mathrm{Pa \cdot s}]$
ρ ..... Density $[\frac{\mathrm{kg}}{\mathrm{m}^3}]$
θ ..... Time collocation factor $[-]$
ψ ..... Thermodynamic variable $[-]$
0 ..... Initial or reference value, subscript $[-]$

1 Introduction

1.1 Work Description and Motivation

The work presented herein is the development of a numerical tool to simulate thermal (T) and hydraulic (H) processes and their combined effects in low-permeable porous media. The thermal and hydraulic processes are described mathematically through material properties and state equations. The process interactions are especially complex in low-permeable porous media such as bentonite, as swelling and suction play an important role. The state equations are incorporated into general thermodynamic balance equations for mass and energy, in order to form a set of equations. The material properties and the set of governing equations are implemented into the finite element simulator GeoSys/RockFlow in the programming languages C/C++. The treatment of numerical formulations becomes different for low-permeable porous media, as the right hand side terms of the algebraic equations gain importance due to the significant role of suction in these materials.

The aim of the implementation is applications in nuclear waste storage. In this field of application clays and other low permeable materials are gaining importance as a barrier material to protect against groundwater contamination. It is therefore essential to study these materials in a large number of thermodynamic situations. Numerical simulations can enable this. The model is calibrated with the help of laboratory tests and can then be used for predictions to help with material engineering and performance assessment considerations.

1.2 The Rockflow Program

GeoSys/Rockflow is currently in the third generation of its development. Development started in 1985 at the University of Hannover. At the time, GeoSys/Rockflow was only known as Rockflow, and written as separate modules in Fortran. Each developer produced a stand-alone module. By 1996 the following modules were present (Kolditz [1999], p. 115-118): Groundwater flow (Wollrath [1990]), tracer transport (Kröhn [1991]), multiphase flow (Helmig [1993]), coupling of boundary and finite elements (Shao [1994]), density-dependent flow (Ratke et al. [1996]).

After that, came the second phase of the code's development, which was driven by applications in the field of environmental geology and geothermics (Lege et al. [1996], Kolditz [1997]), including projects like the geothermal hot dry rock research project at Soultz-sous-Forêts in France and Rosemanowes in the UK (Kolditz and Clauser [1998]).

From 1996, the third phase of code development was characterized by radical changes: The program was rewritten in ANSI-C to enable the use of dynamic data structures and object-oriented programming. Another significant change in the structure of the program was, that whereas developers still wrote their own model, an effort was made to couple these models, as demanded by applications. Coupling models meant the introduction of version management and a more unified data structure. The coupling of the models allows Rockflow to start playing a role in the simulation of coupled processes: Models for reactive transport (Habbar [2001]), adaptive methods and groundwater flow (Kaiser [2001]), multiphase flow (Thorenz [2001b]), gas transport and heat transport (Kolditz [1996]) emerge. Acompanying process modeling, adaptive mesh methods are developed (Barlag [1997], Schulze-Ruhfus).

In parallel to development of numerical methods, part of the research was invested in structural modeling methods. Methods for geometric descriptions of porous and fractured media evolve (Rother [2001], Kasper). These mesh generation and meshing methods are essential to the adaptive mesh process modeling methods. Sylvia Moenickes worked specifically on mesh generation for fractured porous media (Moenickes [2004]). In this field, a good cooperation exists with Prof. Takeo Taniguchi from Okayama University, Japan.

The coupling of fluid flow and mechanical processes is of particular interest in soil mechanics. In 2000, first approaches in the development of RockFlow were made in order to handle the consolidation problem (Kolditz et al. [2000]). Swelling of bentonite material began to be an important field of research (Kohlmeier et al. [2002], Kohlmeier et al. [2002]).

The ongoing code developments at the University of Hannover focus on coupled thermal, hydraulic and mechanical processes. Starting from linear material models and integrating existing and well validated flow and transport modules, the treatment of complex simulations in combination with a user-friendly control system are the aim of the current research work (Kohlmeier et al. [2003a]).

Since 2001, Rockflow is also developed at the University of Tübingen, in the Center for Applied Geoscience (ZAG). The group, headed by Olaf Kolditz grew rapidly to encompass various fields of research. The current developments of the group can be split into three categories: Conceptual model development, numerical model development and software development. In the first category, work has been undertaken for geotechnical applications (Kolditz and De Jonge [2004], Wang and Kolditz [2003], Xie et al. [2003a]), regional groundwater modeling (Beinhorn and Kolditz [2003]), groundwater remediation (Bauer and Kolditz [2003], Bauer et al. [2004], Kolditz et al. [2003]), and geothermal reservoir modeling (McDermott and Kolditz [2003]). In terms of numerical model development, the finite element library was extended, the code was re-organized to benefit from further object-orientation and to allow an easier switching between process couplings. This will be elaborated in the code section of this paper. In terms of software development, activities can be summarized as follows: reorganization of RockFlow into GeoSys: GEOLib, MSHLib, FEMLib, creation and encapsulation of process-oriented objects (PCS), code parallelization (in cooperation with the HPC Center Stuttgart), development of GUI (Multi-View, 3-D graphics).

1.3 Methods of Implementation into GeoSys/RockFlow

There are three main possible methods for the implementation of multiphase-multicomponental formulations into the GeoSys/RockFlow. The first method is the explicit calculation of accumulation terms. The second method, the explicit density calculation and the third method is a fully implicit scheme with respect to the field quantities. This work presents the process for implementing the first method.

1.4 Previous Work in Nuclear Waste Storage Modeling

Studies of thermo-hydraulic-mechanical (THM) processes in partially saturated, thermo-elastic porous media, without phase change effects were presented by Geraminegad and Saxena [1986]. Alonso et al. [1987] discussed the theoretical background of THM modeling including all important effects. Olivella et al. [1994], Gawin et al. [1995] and Gens et al. [1998] introduced

the compositional approach for THM modeling of multiphase-multicomponental systems. In their book, Lewis and Schrefler [1998] gave an excellent overview on coupled processes and their modeling in the field of deformation and consolidation theory of porous media. Kanno et al. [1999] developed and applied a THM model to study the temperature dependency of hydraulic conductivity in saturated porous media and water diffusivity in unsaturated porous media. An excellent overview on existing THM codes is given by Rutqvist et al. [2001]. A major part of this work is based on the implementation of multiphase processes without phase change into GeoSys/RockFlow (Thorenz [2001b]).

There are some very good models available for specific applications. In the field of geotechnical engineering, that we are considering here, the important findings from literature are the following. The porous media theory is widely used, and whereas many models do not simulate phase change and use the Richard's approximation, a few include phase change and are moving towards multiphase-multicomponental formulations. However non-isothermal behavior in swelling materials has not been researched extensively enough.

1.5 Report Organisation

The report follows the train of thought one would have for the implementation of this work. First, the physical processes considered are described verbally (section 2). These processes then have to be treated mathematically. The starting point is the development of the governing equations (section 3), including the choice of primary variables, expression of balance equations, material properties and equations of state. The numerical handling of these equations is the subject of section 4. Finally, benchmarking examples are given in section 5.

2 THM Processes

We need THM models to faithfully represent non-isothermal flow and deformation processes. Figure 1 gives an overview of the different processes that take place in the near-field of underground disposal sites for heat-generating wastes. Usually, the depth of deep geological storage of highly active nuclear waste is planned between 500m and 1000m below sea level. Solid materials usually involved are the waste itself; the waste canister, usually made of copper; a buffer material, usually bentonite or a bentonite-sand mixture; a backfill material, usually sand; and the host medium, either granite, clay, or salt. Fluids involved are air and water. Hydraulic processes are marked in blue, thermal processes in red and mechanical processes in brown. The core at the centre heats the near-field and causes non-isothermal conditions. The bentonite buffer is an engineered barrier system that acts as an interface between the waste and the host rock. Buffer, host rock, and fluids in the gas and liquid phase form a multiphase-multicomponental system, or porous medium.

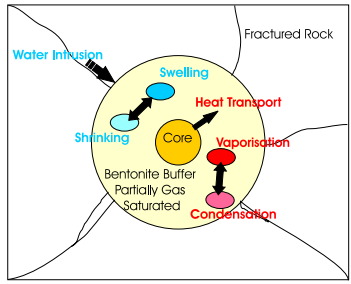

Figure 1: THM Processes

A complete THM model consists of a set of balance equations that take account of the phase changes. Often, only the liquid fluid phase is included in the model, which only allows an approximation of phase transitions.

One of the difficulties in establishing THM models is that many of the processes illustrated in Figure 1 are non-linear and sometimes very difficult to express mathematically, for example the relationship between capillary pressure and saturation.

2.1 Thermal processes

Thermal processes are a direct result of the heat radiation of the nuclear waste. Typically, high-level nuclear waste will be stored and cooled until the waste, encased in a copper canister will not exceed $100°C$. The surrounding buffer material and the host rock will normally have temperatures not exceeding room temperatures, or at the most $40°C$. Heat radiation into the host medium will decrease over hundreds of years.

The temperature gradient between waste and host rock creates a thermal gradient and influences hydraulic material properties such as fluid density or viscosity, and solid material properties by inducing heat stresses on the materials. Affected material properties and their mode of implementation in GeoSys/RockFlow are shown in Table 1.

Other than directly influencing material properties, the temperature difference between the waste and the host environment has an influence on the thermodynamic state of the system. Temperature influences capillary pressure-saturation relationships by approximately 20% (Engelhardt et al. [2003]). Temperature also directly influences the saturation of the surrounding materials, as the high temperatures induce phase transitions from liquid to gaseous phase, and condensation from gaseous to liquid phase in the cooler regions. This is also reflected in the mass fractions.

Table 1: Material properties directly related to temperature in GeoSys/RockFlow

Property	Dependencies	User Input
Heat conductivity	$n,\ S$	$\lambda_{sat},\ \lambda^g,\ \lambda^l$
Heat capacity	constant	c
Density	$p,\ T$	$T_0,\ \beta_T,\ p_0,\ \beta_p$
	T	$T_0,\ \beta_T$
Viscosity	$p,\ T$	-
Capillary pressure	$S,\ T$	$p_c - S$ relationship, T_0 set to $25°C$
Mass fractions	p, T	-

2.2 Hydraulic processes

The main hydraulic process involved is water intrusion from the water-saturated host rock into the buffer and backfill materials. The infiltrated water will eventually reach the core. Water intrusion is one of the main reasons for choosing bentonite or a bentonite-sand mixture as a buffer material. Bentonite swells as its water saturation increases. This helps with sealing off the waste and canister, and so assists in preventing chemical leakage. Xie et al. [2003b] gives a detailed description of bentonite swelling mechanisms.

The main material properties concerned by hydraulic processes are fluid density and viscosity, soil intrinsic and relative permeabilities, capillary pressure, saturation and mass fractions. Their mode of implementation are summarized in Table 2.

Hydraulic processes also change the state of the system in that water intrusion, for example, is directly related to water saturation of the porous medium, which in turn is related to relative permeabilities and capillary pressure. In the systems considered in nuclear waste storage applications, capillary pressure is a major quantity, as it is very high, up to $10^{10}Pa$ at low liquid saturations of the buffer material. This means that water is literally sucked into the buffer material.

Table 2: Material properties directly related to hydraulic processes in GeoSys/RockFlow

Property	Dependencies	User Input
Saturation	$p_{\mathsf{c}}(T)$	depending on chosen function
Capillary pressure	$S,\ T$	$p_{\mathsf{c}} - S$ relationship, T_0 set to $25°C$
Equil. Vapour pressure	T	-
Equil. Air pressure	ρ	-
Diffusion coefficient	constant	constant for each fluid phase
Intrinsic permeability	constant	constant
Relative permeability	S	$k_{\mathsf{rel}} - S$ relationship
Density	$p,\ T$	$T_0, \beta_T, p_0, \beta_p$
	p	$p_0,\ \beta_p$
Viscosity	$p,\ T$	depending on chosen model
Mass fractions	$p,\ T$	-
Swelling model	$n,\ k_{\mathsf{rel}},\ S$	depending on chosen model

3 Governing Equations

This chapter shows the development of the governing equations used in GeoSys/RockFlow for the modeling of non-isothermal flow in porous media. The equations are built in three stages; the thermodynamic balance equations form the base, into which equations of state and material properties are substituted. The resulting equations in differential form constitute the necessary set of equations to define the material and thermodynamic state of the material to be modeled. This process is illustrated in Figure 2.

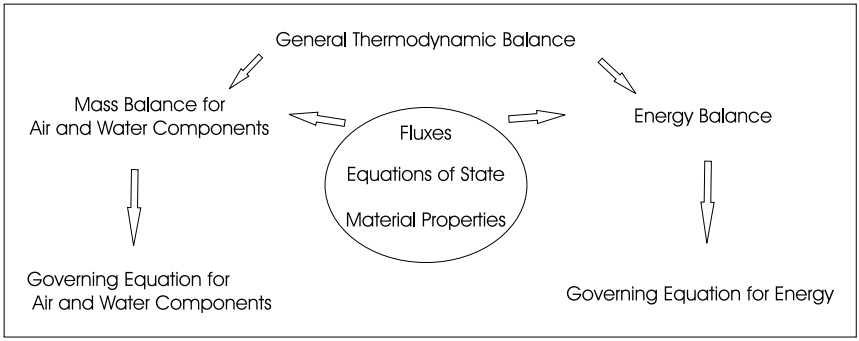

Figure 2: Flow chart for the development of governing equations

All formulations are based on the general thermodynamic balance equation.

$$\frac{d\psi}{dt} = \frac{\partial\psi}{\partial t} + \mathbf{v}\nabla\psi = -\psi\nabla\cdot\mathbf{v} + Q^{\psi} \tag{1}$$

Variable	**Symbol**
Primary Variables	
Gas Pressure (for the air component)	p^g
Liquid Saturation (for the water component)	S^l
Temperature (for the energy component)	T
Secondary Variables	
Vapour Pressure	$p^g_{w,sat}$
Capillary Pressure	p_{C}
Enthalpy	h^g_w
Mass Fractions	X^γ_k
Internal Energy	u^γ

Table 3: Primary and secondary variables

The implementation method is based on a componental approach for the development of the mass balance equations. This means that governing equations are developed for the water component and for the air component. This is preferred to an approach, where governing equations are developed for the liquid phase and the gas phase, as for example in [Thorenz, 2001a]. A governing equation for the energy equation is developed separately. A primary variable is chosen to be associated with each governing equation, i.e. liquid phase saturation is associated with the water component and gas phase pressure is associated with the air component. Temperature is associated with the energy equation (Table 3).

3.1 Balance Equations

3.1.1 Mass Balance equation

Equation (2) shows the mass balance equation for the water and air components. It is derived from the general thermodynamic balance equation.

$$\frac{\partial}{\partial t}(nS^l\rho_k^l + nS^g\rho_k^g) + \nabla\cdot(\mathbf{J}_k^{ls} + \mathbf{J}_k^{gs}) + \nabla\cdot(\mathbf{J}_k^g + \mathbf{J}_k^l) = Q_k \tag{2}$$

$n\,[-]$ is porosity, $S\,[-]$ is saturation, $\rho\,[\frac{kg}{m^3}]$ is density, $\mathbf{J}\,[\frac{kg}{m\cdot s}]$ is flux, and $Q\,[\frac{m^3}{s}]$ is a source-sink term. The superscripts l, g, and s denote the liquid phase, gas phase, and solid phase. The subscript k denotes the component, which is air (a) or water (w) in this case. The first term is the mass storage term. The second term on the left hand side are advective mass fluxes. The last represents diffusive fluxes. The right hand side term is a sink or source term for mass entering or leaving the system.

In the expression for the advective fluxes, the relative velocity of the liquid phase or gaseous phase relative to the solid phase in the water species is used. Because of this, terms containing the solid phase displacement velocity in the water species have to be added to the balance. However, since this method does not include solid phase displacement, the solid velocity terms cancel out of the equation.

The spatial deformation of porosity, saturation and liquid density in the water species is much smaller than the temporal variation. Hence the spatial variation of these variables can be neglected. The flux of the liquid phase in the water component can also be neglected. However, in the air component the liquid diffusive flux cannot be neglected.

3.1.2 Energy Balance Equation

The balance equation for equilibrium temperature in the porous medium is given by Equation (3) [Emmert, 1997].

$$\begin{aligned} &\frac{\partial}{\partial t}\left((1-n)\rho^s u^s + nS^g\rho^g u^g + nS^l\rho^l u^l\right) \\ +\ &(\nabla\cdot\mathbf{J}_h^s + \nabla\cdot\mathbf{J}_h^g + \nabla\cdot\mathbf{J}_h^l) = Q_h \end{aligned} \tag{3}$$

$u\ [\frac{J}{kg}]$ is the internal energy and $\mathbf{J}_h\ [\frac{J}{m \cdot s}]$ is heat flux, composed of advective, diffusive, and conductive flux. The first term is the heat storage. The second term is heat flux. The right hand side term is a sink or source term representing heat provided to, or taken away from, the system.

3.2 Fluxes

For the water and air component, two types of fluxes have to be considered: advective fluxes and diffusive fluxes. Additionally, conductive fluxes are considered in the energy balance equation.

3.2.1 Advective Fluxes

Advective fluxes are movements of the liquid phase or gas phase relative to the solid phase. We use an extension of the Darcy equation to express advective flux in terms of the primary variables and capillary pressure.

$$\begin{aligned} \mathbf{J}_k^{ls} &= nS^l\rho_k^l(\mathbf{v}^l - \mathbf{v}^s) \\ &= -\rho_k^l \frac{k_{\mathsf{rel}}^l \mathbf{k}}{\mu^l}(\nabla p^l - \rho^l \mathbf{g}) = -\rho_k^l \frac{k_{\mathsf{rel}}^l \mathbf{k}}{\mu^l}(\nabla p^g - \nabla p_{\mathsf{c}} - \rho^l \mathbf{g}) \end{aligned} \tag{4}$$

$$\begin{aligned} \mathbf{J}_k^{gs} &= nS^g\rho_k^g(\mathbf{v}^g - \mathbf{v}^s) \\ &= -\rho_k^g \frac{k_{\mathsf{rel}}^g \mathbf{k}}{\mu^g}(\nabla p^g - \rho^g \mathbf{g}) \end{aligned} \tag{5}$$

$$\begin{aligned} \mathbf{J}_h^{\gamma s} &= \mathbf{J}_h^g + \mathbf{J}_h^l \\ &= nS^l\rho^l(\mathbf{v}^l - \mathbf{v}^s) + nS^g\rho^g(\mathbf{v}^g - \mathbf{v}^s) \end{aligned} \tag{6}$$

3.2.2 Diffusive Fluxes

The diffusive flux within the gaseous phase can also be expressed in terms of primary variables, using the diffusion coefficient and mass fraction. The equations below show the diffusive fluxes.

$$\mathbf{J}_k^g = nS^g\rho_k^g(\mathbf{v}_k^g - \mathbf{v}^g) = -nS^g\rho_k^g D^g \nabla X_k^g \tag{7}$$

$$\mathbf{J}_k^l = nS^l\rho_k^l(\mathbf{v}_k^l - \mathbf{v}^l) \tag{8}$$

$$\mathbf{J}_u^g = -\nabla \cdot (D\rho^g h_a^g \nabla X_a^g) - \nabla \cdot (D\rho^g h_w^g \nabla X_w^g) \tag{9}$$

3.2.3 Conductive Fluxes

Equation (10) shows the conductive heat flux.

$$\mathbf{J}_t = -\nabla \cdot (\lambda \nabla T) \tag{10}$$

3.3 Equations of State

Equations of state define the thermodynamic state of the system that is described by the balance equations. State variables are expressed mathematically and replaced into the balance equations.

3.3.1 Saturated vapour pressure – $p^g_{w,sat}(T)$

Calculations of vapor pressure in GeoSys/RockFlow are based on the following assumption:

$$p^g_w \equiv p^g_{w,sat}(T) \tag{11}$$

Saturated vapour pressure is dependent on temperature, as described by the Clausius-Clapeyron equation (12). Vapour pressure is illustrated in Figure 3.

$$p^g_{w,sat}(T) = p_0 \exp\left[(\frac{1}{T_0} - \frac{1}{T})\frac{h^g_w M_w}{R}\right] \tag{12}$$

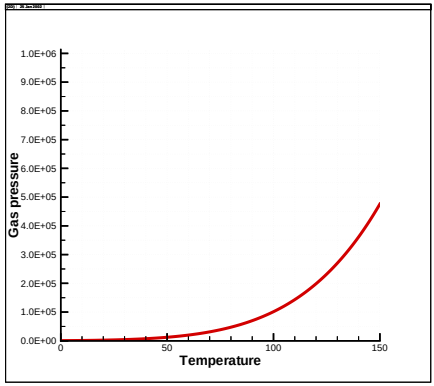

Figure 3: Vapour pressure, $p^g_{w,sat}$

3.3.2 Gas pressure of the air component – $p^g_a(p^g, T)$

The gas pressure in the air component depends on temperature and the pressure of the gas phase.

$$p^g_a(p^g, T) = p^g - p^g_{w,sat}(T) \tag{13}$$

3.3.3 Mass Fractions – $X_k^\gamma(p^g, T)$

Mass fraction is the fraction by mass of a component in a phase, compared to the other components in the same phase. The addition of the mass fractions for a given phase is equal to unity. Mass fractions for both components, depending on gas pressure and equilibrium temperature, are illustrated in Figure 4. The vapor pressure curve is added in bold red.

$$\begin{aligned} X_w^g(p^g,T) &= \frac{m_k^\gamma}{\sum_k m^\gamma} \\ X_w^g(p^g,T) &= 1 - X_a^g \\ X_a^g &= \frac{[p^g - p_{w,sat}^g(T)]M_a}{RT\rho^g} \\ X_w^l(p^g,T) &= 1 - X_a^l \\ X_a^l &= \frac{M_a}{M_a - M_w(1 - [K_H(T)p_a^g]^{-1})} \end{aligned} \tag{14}$$

Where,

$$X_w^g(p^g, T, \rho^g(p^g, T)) \equiv X_w^g(p^g, T) \tag{15}$$

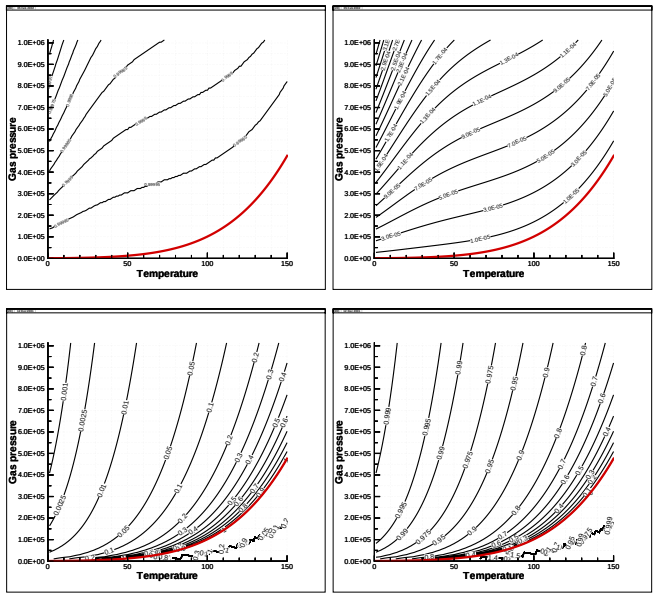

Figure 4: Mass Fractions; top left:X_w^l, top right:X_w^g bottom left:X_a^l, bottom right:X_a^g

3.3.4 Enthalpy – h

Enthalpy is defined by $h = u + pV$. The phase enthalpies can be defined by means of the specific heat capacities at constant pressure. The liquid phase is assumed to be incompressible.

$$
\begin{aligned}
h^g &= c_p^g T + \frac{p^g}{\rho^g} && (16)\\
h^l &= c_p^l T && (17)\\
h^\gamma &= X_a^\gamma h_a^\gamma + X_w^\gamma h_w^\gamma && (18)
\end{aligned}
$$

Enthalpy of the gas phase in water–h_w^g Enthalpy can be defined as the heat content of a fluid. In this case we consider the vaporization enthalpy of the liquid phase. Enthalpy as a function of temperature is tabulated in steam tables of the American Society of Mechanical Engineers (ASME) of 1967 and illustrated in Figure 5 . A program calculating the values based on these steam tables was developed as a freeware program by Michael Lynn McGuire of WinSim, Inc. (http://www.winsim.com/steam/steam.html). GeoSys/RockFlow uses this software as a means of steam table value lookup. Resulting values for enthalpy have been verified against steam table values.

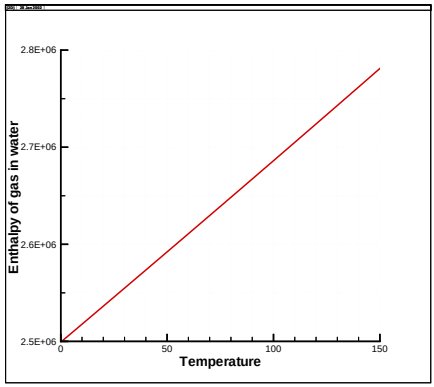

Figure 5: Enthalpy of the gas phase in water, h_w^g

Comparing the software's equations and the equation for vapor pressure, we have,

$$
\begin{aligned}
\frac{y}{\rho_1} &= -h_w^g \frac{M_w}{RT_0}\\
\frac{1}{\rho_2} &= h_w^g \frac{M_w}{R(T_0 - T)} && (19)
\end{aligned}
$$

where all terms are dimensionless and T_0 is a reference temperature.

3.3.5 Internal energy – u

Internal energy is defined as the energy associated with the random, disordered motion of molecules. The internal energy is calculated for each phase. The liquid phase is assumed to be incompressible.

$$\begin{aligned} u^g &= c_v^g T + \frac{p^g}{\rho^g} \\ u^l &= c_v^l T \end{aligned} \tag{20}$$

3.4 Material Properties

3.4.1 Density

Phase densities – $\rho^\gamma(T)$ Total fluid density is composed of the addition of partial density terms.

$$\rho^\gamma = \rho_a^\gamma + \rho_w^\gamma \tag{21}$$

This is illustrated for the gas phase in Appendix 1, where vapor density (ρ_w^g), gas phase density (ρ_a^g) in the air component and gas density (ρ^g) are plotted as a function of pressure and temperature. Figure 6 shows the gas density.

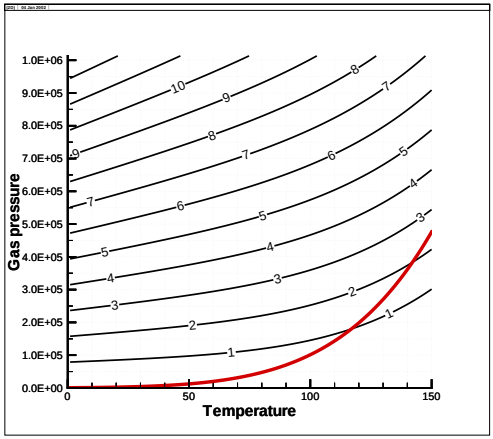

Figure 6: Gas phase density, ρ^g

$$\begin{aligned} \rho^\gamma(T) &= \rho_0^\gamma(1 + \beta_T^\gamma(T - T_0)) \\ \rho^\gamma(p^g, T) &= \rho_0^\gamma(1 + \beta_T^\gamma(T - T_0) + \beta_p^\gamma(p - p_0)) \end{aligned} \tag{22}$$

Partial Densities Partial densities, such as water vapor density are calculated from the appropriate phase density and mass fraction.

3.4.2 Fluid viscosity – μ

The viscosity of fluids depends on pressure and temperature. The viscosity of liquids depends highly on temperature, whereas for most cases the variation of viscosity with pressure can be neglected for liquids. Water presents an exception as in that its viscosity decreases with pressure at constant temperature. Changes in temperature have opposite effects on liquids than on gases: with decreasing temperature the viscosity of a liquid rises, while the viscosity of a low density gas decreases. In our case, concentration of the liquid in the medium also plays a role.

Most often in the applications of this work, viscosity was approximated by a constant value. For gas phase viscosity the following function was also used (Reid et al. [1988]).

$$\mu^g(p,T) = \mu_0 \left(1 + \frac{A p_r^{3/2}}{B p_r + (1 + C p_r^D)^{-1}}\right) \tag{23}$$

with the following parameters:

$$\begin{array}{ll} p_r = p/p_{\mathsf{crit}} & T_r = T/T_{\mathsf{crit}} \\ A = \dfrac{\alpha_1}{T_r}\exp(\alpha_2 T_r^a) & B = A(\beta_1 T_r - \beta_2) \\ C = \dfrac{\gamma_1}{T_r}\exp(\gamma_2 T_r^c) & D = \dfrac{\delta_1}{T_r}\exp(\delta_2 T_r^d) \end{array} \tag{24}$$

$$p_{\mathsf{crit}} = 33.9 \times 10^4\, Pa \quad T_{\mathsf{crit}} = 126.2\, K$$

$$\begin{array}{lll} \alpha_1 = 1.9824 \times 10^{-3} & \alpha_2 = 5.2683 & a = -0.5767 \\ \beta_1 = 1.65552 & \beta_2 = 1.2760 & \\ \gamma_1 = 0.1319 & \gamma_2 = 3.7035 & c = -79.8678 \\ \delta_1 = 2.9496 & \delta_2 = 2.9190 & d = -16.6169 \end{array}$$

3.4.3 Capillary pressure – p_{c}

The capillary pressure can be defined as the tendency of a porous medium to suck in the wetting fluid phase or to repel the non-wetting phase. Capillary pressure results from the pressure discontinuity at the interface between two immiscible fluids. Capillary pressure depends on the geometry of the void space, on the nature of solids and liquids and on the degree of saturation. In porous media the geometry of the void space is idealized. Thus, the dependence reduces to saturation for any given porous media. Care has to be taken, as capillary pressure is not the same for drainage and re-wetting. The function connecting capillary pressure and saturation has to be determined by laboratory experiments for every new porous medium. As an approximation a linear relationship can be used. There are, however, analytical functions that can be used, such as the van Genuchten (1980) model. α, n, m are function parameters.

$$S_{\mathsf{eff}} = \frac{S^l - S_r^l}{1 - S_r^l} = (1 + (\alpha\, p_{\mathsf{c}})^n)^m \qquad , \qquad p_{\mathsf{c}} > 0 \tag{25}$$

$$p_{\mathsf{c}} = \begin{cases} 0 & S^l > S^l_{\mathsf{max}} \\ \frac{\rho^l g}{\alpha}(S^{-1/m}_{\mathsf{eff}} - 1)^{1/n} & S^l_r < S^l < S^l_{\mathsf{max}} \\ p_{\mathsf{c\ max}} & S^l < S^l_r \end{cases} \tag{26}$$

Brooks and Corey (1964) developed the following model.

$$S_{\mathsf{eff}} = \frac{S^l - S^l_r}{1 - S^l_r} = \left(\frac{p_b}{p_{\mathsf{c}}}\right)^{\lambda} \qquad , \qquad p_{\mathsf{c}} \geq p_b \tag{27}$$

$$p_{\mathsf{c}} = \begin{cases} 0 & S^l > S^l_{\mathsf{max}} \\ p_b \left(\frac{1}{S_{\mathsf{eff}}}\right)^{1/\lambda} & S^l_r < S^l < S^l_{\mathsf{max}} \\ p_{\mathsf{c\ max}} & S^l < S^l_r \end{cases} \tag{28}$$

p_b is the so-called bubbling pressure, the minimum pressure at which the gaseous phase exists, λ is the pore size distribution index.

Another model example is that of Havercamp et al. (1977), where the formulas are given in terms of pressure head $h = p^l/g\rho^l$ and moisture content $\theta = nS^l$.

$$\theta = \frac{\alpha(\theta_s - \theta_r)}{\alpha + |h|^{\beta}} + \theta_r \tag{29}$$

$$h = \left(-\frac{\alpha}{\theta}(\theta - \theta_s + \theta_r)\right)^{1/\beta} \tag{30}$$

θ	volumetric water (moisture) content		$[cm^3/cm^3]$
θ_r	residual volumetric water content	0.075	$[cm^3/cm^3]$
θ_s	saturated volumetric water content	0.287	$[cm^3/cm^3]$
$h(\theta)$	soil water pressure head relative to the atmosphere		$[cm]$
α		1.611×10^6	$[Pa^{-1}]$
β		3.96	

Table 4: Model parameters for the Havercamp et al. model

Also included in the program is the temperature dependence of capillary pressure. The following function is implemented (Olivella and Gens [2000]), where $p_{\mathsf{c}(T)}$ is the correction factor to capillary pressure due to system temperature differing from $298K$.

$$
\begin{aligned}
c &= \frac{100 - T}{647.3} \\
c_0 &= \frac{100 - T_0}{647.3} \\
\sigma_T &= (1. - 0.625 \cdot c) \cdot 0.2358 \cdot c^{1.256}) \\
\sigma_{T0} &= (1. - 0.625 \cdot c_0) \cdot 0.2358 \cdot c^{1.256}) \\
p_{\mathsf{c}(T)} &= \frac{\sigma_T}{\sigma_{T0}} \\
p_{\mathsf{c}} &= p_{\mathsf{c}(S)} \cdot p_{\mathsf{c}(T)}
\end{aligned} \tag{31}
$$

3.4.4 Permeability – k

Permeability is a user defined constant in the input file and that is different for each solid material.

3.4.5 Relative Permeability–k_{rel}

For porous media containing more than one fluid, the concept of relative permeability is introduced. The relative permeability is used to calculate the effective permeability $(k_{\mathsf{rel}}^{\gamma} S^{\gamma})\mathbf{k}$, which is described in the extended Darcy law. The relationship depends strongly on the saturations. Different relationships are possible: constant values, user-defined functions, linear functions, potential functions, or functions found in literature, such as the van Genuchten Model (1980),

$$
k_{\mathsf{rel}}(h) = \frac{1 - (\alpha h)^{n-2} \left[1 + (\alpha h)^n\right]^{-m}}{\left[1 + (\alpha h)^n\right]^{2m}} \tag{32}
$$

or the relationship developed by Haverkamp et al.(1977)

$$
k_{\mathsf{rel}}(h) = K_s \frac{A}{A + |h|^{\beta}} \tag{33}
$$

$$
h = \left(-\frac{\alpha}{\theta}(\theta - \theta_s + \theta_r) \right)^{1/\beta} \tag{34}
$$

or the Brooks and Corey model (1966)

$$
S_{\mathsf{eff}} = \frac{S^l - S_r^l}{S_{\mathsf{max}}^l - S_r^l} \tag{35}
$$

$$
k_{\mathsf{rel}}^l = S_{\mathsf{eff}}^4 \tag{36}
$$

3.4.6 Specific heat capacity – c

The specific heat is the amount of heat per unit mass required to raise the temperature by one degree Celsius. This does not apply if a phase change is encountered, because the heat added or removed during a phase change does not change the temperature. Specific heat capacity can be expressed at constant volume or at constant pressure.

$$c_V = \frac{\partial u}{\partial T} \tag{37}$$

$$c_p = \frac{\partial h}{\partial T} \tag{38}$$

3.4.7 Thermal conductivity – λ

During thermal conduction, heat is exchanged between molecules due to their collision. For a fluid or solid continuum, thermal conduction can be described by Fourier's Law at the macroscopic level as the proportional relationship between the flux of thermal energy by conduction and temperature, with the thermal conductivity λ as a proportionality coefficient.

The thermal conductivity is specific to the fluid, through which the flux takes place. In gases and liquids, λ depends on temperature and pressure. However the pressure dependency is far smaller than the temperature dependency. At low gas density, the thermal conductivity of gases increases with temperature. However the thermal conductivity of most liquids decreases with temperature. Polar liquids may have a maximum in the temperature dependency of thermal conductivity.

The thermal conductivity considered here is the overall thermal conductivity of the porous medium. Overall thermal conductivity is a function of porosity and saturation. It is given by the geometric mean approximation

$$\lambda = (1-n)\lambda^s + nS^l\lambda^l + nS^g\lambda^g \tag{39}$$

3.4.8 Diffusion coefficient – D

In the model a constant value is currently used for the diffusion coefficient, which can be specified by the user for each fluid phase as an approximation to tortuosity and saturation dependent formulations.

3.5 Governing Equations

3.5.1 Governing equation for the air and water components

To obtain the governing equation, fluxes, state functions, and material functions are substituted into the mass balance equation (2).

$$
\begin{aligned}
& nX_k^g \left(S^g \frac{\partial \rho^g}{\partial p^g} + S^l \frac{\partial \rho^l}{\partial p^l} \right) \frac{\partial p^g}{\partial t} \\
- \quad & \nabla \cdot \left(\rho^g X_k^g \frac{k_{\mathsf{rel}}^g \mathbf{k}}{\mu^g} \nabla p^g \right) - \nabla \cdot \left(\rho^l X_k^l \frac{k_{\mathsf{rel}}^l \mathbf{k}}{\mu^l} \nabla p^g \right) \\
+ \quad & n(-\rho^g X_k^g + \rho^l X_k^l) \frac{\partial S^l}{\partial t} \\
+ \quad & \underbrace{(S^g \rho^g + S^l \rho^l) \mathbf{m}^T \mathbf{L} \frac{\partial \mathbf{u}^s}{\partial t}}_{\text{MH coupling term}} \\
= \quad & Q_k \\
+ \quad & (n S^l X_k^l \frac{\partial \rho^l}{\partial p^l}) \frac{\partial p_{\mathsf{c}}}{\partial t} - \nabla \cdot \left(\rho^l X_k^l \frac{k_{\mathsf{rel}}^l \mathbf{k}}{\mu^l} \nabla p_{\mathsf{c}} \right) \\
- \quad & \nabla \cdot \left(\rho^g X_k^g \frac{k_{\mathsf{rel}}^g \mathbf{k}}{\mu^g} \rho^g \mathbf{g} \right) + \nabla \cdot \left(\rho^l X_k^l \frac{k_{\mathsf{rel}}^l \mathbf{k}}{\mu^l} \rho^l \mathbf{g} \right) \\
+ \quad & \underbrace{\nabla \cdot (n S^g \rho^g D_k^g \nabla X_k^g)}_{\text{TH coupling term}}
\end{aligned}
\tag{40}
$$

β_p is the fluid compressibility, p is liquid phase pressure, t is time, $\mathbf{k}$ is permeability tensor, μ is liquid viscosity, $\mathbf{g}$ is gravity vector, $\mathbf{u}^s$ is solid phase displacement, $\mathbf{m}^T$ and $\mathbf{L}$ are matrix operators. $\mathbf{L}$ is an operator that gives the relationship between displacement and strain, X is mass fraction, p_{c} is capillary pressure, k_{rel} is relative permeability, and D is componental diffusion coefficient.

The mechanical - hydraulic (MH) and thermal - hydraulic (TH) coupling terms of deformation and heat transport to the flow processes are highlighted. The MH coupling term is only shown here as a reminder that GeoSys/RockFlow is capable of this coupling. Mechanical processes are, however, not within the scope of this work. Coupling is also due to dependencies of material and state functions such as density, viscosity, capillary pressure, vapor pressure, mass fractions on the primary variables: gas pressure, liquid saturation, temperature, and solid displacement.

3.5.2 Governing equation for the energy component

The governing equation for the energy component is obtained by inserting the equation of the fluxes into the balance equation and by using the equations of state. The implementation of the governing equation for the energy component allows the activation and deactivation of latent heat terms through keywords in the input file, according to the requirements of the problem to be solved.

$$
\begin{aligned}
& \left((1-n) \rho^s c^s + n S^g \rho^g c^g + n S^l \rho^l c^l + n S^l \beta_T \Delta h \right) \frac{\partial T}{\partial t} \\
+ \quad & \left(\rho^g c^g \frac{k_{\mathsf{rel}}^g \mathbf{k}}{\mu^g} (\nabla p^g - \rho^g \mathbf{g}) \right.
\end{aligned}
$$

$$
\begin{aligned}
& +\rho^l c^l \frac{k^l_{\mathsf{rel}}\mathbf{k}}{\mu^l}(\nabla p^l - \rho^l \mathbf{g})\Big)\nabla T \\
- \quad & \nabla \cdot \Big(\Big((1-n)\lambda^s + nS^g\lambda^g + nS^l\lambda^l\Big)\nabla T\Big) \\
= \quad & \rho Q_T \underbrace{-n\Delta h\frac{\partial S^l}{\partial t} - nS^l\beta\Delta h\frac{\partial p^l}{\partial t} - \nabla \mathbf{v}^l \Delta h}_{Enthalpy\ source\ term}
\end{aligned}
\tag{41}
$$

$c\,[\frac{J}{kg\cdot K}]$ is heat capacity, $\lambda\,[\frac{J}{K\cdot m\cdot s}]$ is thermal conductivity, and $h\,[\frac{J}{kg}]$ is enthalpy.

We now have three governing equations in differential form, one for each primary variable. Together with the equations of state and with the material properties, they form a complete set of equations.

4 Numerical Formulation

In this section, the physical concepts derived mathematically in the previous section are formulated numerically. The three governing equations (water component, air component, energy conservation) are the starting point.

4.1 Weak Formulation

The governing equations cannot be solved numerically as they stand. They have to be approximated. The approximation method used is the method of weighted residuals. The weighting functions associated with this process have been defined by the Bubnov-Galerkin method, which sets the weighting function equal to the interpolation function. For any given element, the interpolation function is equal to the shape function N. The resulting equation is called the weak formulation. Once the Bubnov-Galerkin method is applied, a time collocation, i.e. the time within the time step, at which the variables are calculated, is defined. The resulting equation is called weak formulation with time collocation. Figure 7 illustrates this process.

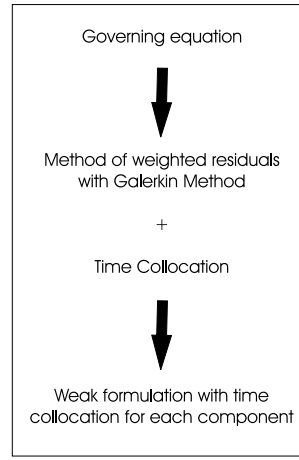

Figure 7: Numerical Approximation Procedure

4.2 Algebraic Equations

The algebraic equations are derived from the weak formulation with time discretization. Each term is written in matrix form. The matrices are the element matrices. This is the formulation needed for the implementation of the equations into the code. The element matrices are implemented individually for each element type, calculated and then combined according to the algebraic equations. The algebraic equations for the non-isothermal multicomponent model are detailed in Kolditz and De Jonge [2004].

4.3 Element Matrices

The terms in the weak integral with time discretization can be expressed as matrices when considered for a particular finite element. 1-D, 2-D triangular and quadratic, as well as 3-D hexahedral element matrices were implemented for the calculation of non-isothermal processes as part of this work. Element matrices contain an integral that has to be approximated numerically. The approximation is done with the help of shape functions, which depend on the dimension and the shape of the mesh elements. Details can be found in De Jonge et al. [2004].

4.4 System Matrix and Right Hand Side Vector

The system matrix assembles the element matrices. The form of the system matrix and right hand side (RHS) vector depends on the chosen coupling scheme. Equation 42 shows a completely partitioned coupling scheme. Equation 43 shows a coupling scheme, where the primary variables for the air and water components, i.e. gas pressure and liquid saturation are coupled and temperature is calculated separately.

$$\begin{aligned}
[\theta(\mathbf{K}_w^{ls} + \mathbf{K}_w^{gs})][\hat{\mathbf{p}}^g] &= RHS_P \\
\left[\frac{1}{\Delta t}\left(\mathbf{C}_w^g - \mathbf{C}_w^l\right) - \mathbf{K}_w^{ls}\frac{\partial p_\mathsf{c}}{\partial S}\right][\hat{\mathbf{S}}^l] &= RHS_S \\
\left(\frac{1}{\Delta t}\mathbf{C}_t^s - \theta\mathbf{K}_t^s\right)[\hat{\mathbf{T}}]_{\tau+1}^{n+1} &= RHS_T
\end{aligned} \tag{42}$$

$$\begin{aligned}
\begin{bmatrix} \theta(\mathbf{K}_a^{gs} + \mathbf{K}_a^{ls}) & \frac{1}{\Delta t}\left(\mathbf{C}_a^g - \mathbf{C}_a^l\right) - \mathbf{K}_a^{ls}\frac{\partial p_\mathsf{c}}{\partial S} \\ \theta(\mathbf{K}_w^{gs} + \mathbf{K}_w^{ls}) & \frac{1}{\Delta t}\left(\mathbf{C}_w^g - \mathbf{C}_w^l\right) - \mathbf{K}_w^{ls}\frac{\partial p_\mathsf{c}}{\partial S} \end{bmatrix} \begin{bmatrix} \hat{\mathbf{p}}^g \\ \hat{\mathbf{S}}^l \end{bmatrix} &= RHS \\
\left(\frac{1}{\Delta t}\mathbf{C}_t^s - \theta\mathbf{K}_t^s\right)[\hat{\mathbf{T}}]_{\tau+1}^{n+1} &= RHS_T
\end{aligned} \tag{43}$$

5 Benchmarking

In this section, two benchmark examples are presented.

5.1 Benchmarks th_partitioned, th_monolithic

This example is to qualitatively test the effect of the large capillary pressures up to 10^{10} Pa occurring in extremely low-permeable bentonite materials. Also, we compare the different coupling schemes for solving the set of coupled equations. For this purpose we start with a simple 1-D case. A one meter long bentonite column is heated on the left hand side, triggering bentonite desaturation. Initial and boundary conditions are illustrated in Figure 8. Results for the partitioned coupling scheme are illustrated in figure 9 and for the monolithic coupling scheme in figure 10. A more detailed description of this example, as well as a discussion of results is given in Kolditz and De Jonge [2004].

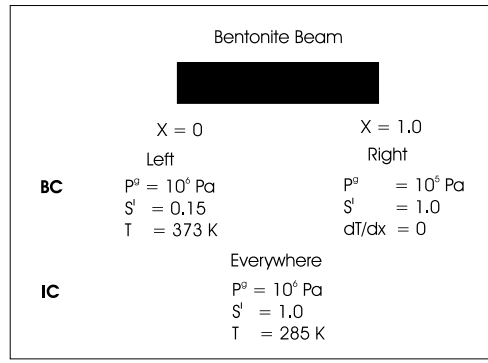

Figure 8: Example initial and boundary conditions

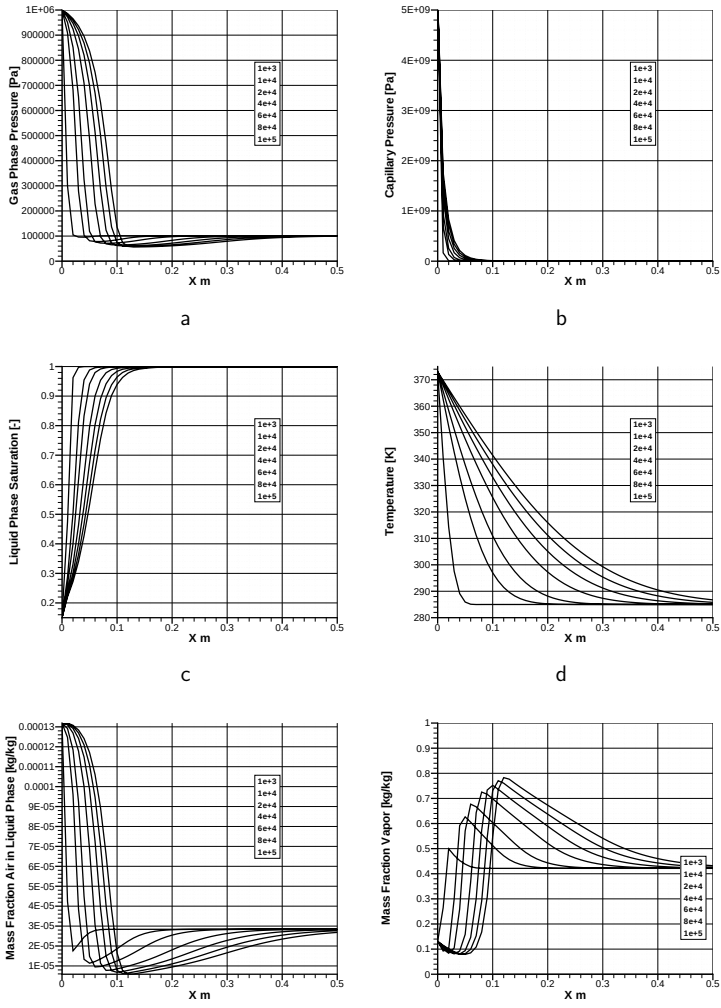

Figure 9: Computation results for Example 1 using the TH^2/M model (partitioned coupling scheme)

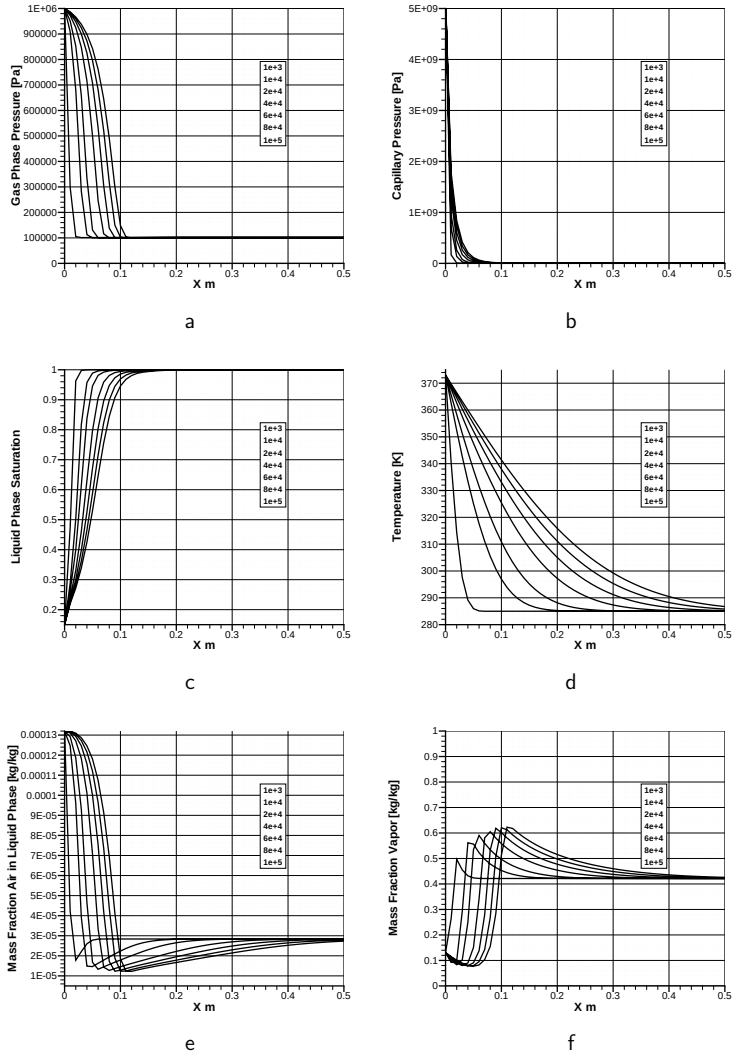

Figure 10: Computation results using the TH^2/M model (monolithic coupling scheme)

The second aim of this benchmark was to compare results obtained with different elements. Figure 11 shows the results when using a mesh made up of 3-D hexahedral finite elements. Figure 12 shows a comparison between results obtained by using 1-D linear, 2-D quadrilateral, and 3-D hexahedral finite elements for the calculation of this benchmark.

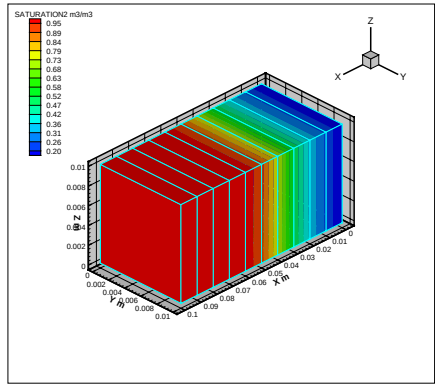

Figure 11: Benchmark th_partitioned with $3-D$ hexahedral elements

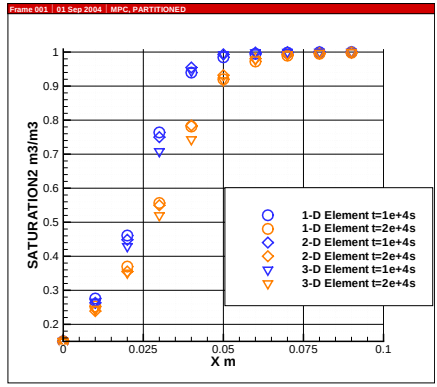

Figure 12: Benchmark th_partitioned comparison of different element types

5.2 Benchmarks desat

These test cases are based on an example proposed by Olivella and Gens [2000]. This example portrays the desaturation of a bentonite sample due to heating in a closed system. The set-up is as illustrated in Fig. 13. A detailed description of the benchmarks is given in Kolditz and De Jonge [2004].

Because the capillary pressures in bentonite are very high (up to $10^4 MPa$, a large suction pressure is initiated, that strongly favors saturation of the sample from the open side (at the right). Vapor movement, and hence desaturation due to sample heating can only be modelled if vapor flow is encouraged. This is due to the vapour diffusion term of the balance equation for fluid masses (air and water components). Olivella and Gens [2000] introduced a dual relative permeability model, i.e. different relative permeabilities for gases and liquids, so that vapor movement is favored at low liquid phase saturations (S^l), when capillary pressure is highest. This dual permeability model is based on experimental evidence for bentonite.

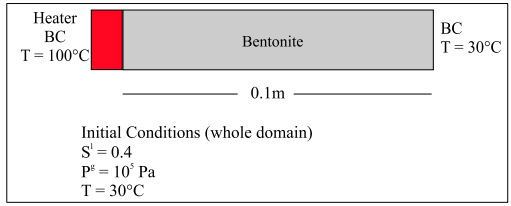

Figure 13: Definition of the test case

The results thus show successful modeling of a desaturation process in bentonite due to evaporation, by using the TH^2/M model. We obtained very similar results as the experimental results shown in Olivella and Gens [2000], as illustrated in Figure 14b. Additionally, we used this benchmark to check different element types for TH^2/M processes. We obtain identical results for different element types (bar, triangular, quadrilateral elements) which serves as a verification test for element implementations.

When latent heat terms are activated in the energy equation, examples extending beyond $100°C$ can be simulated. To show this, the desat benchmark was run with a temperature boundary condition of $130°C$ instead of $100°C$. The results are illustrated in figure 15, including a comparison to experimental results.

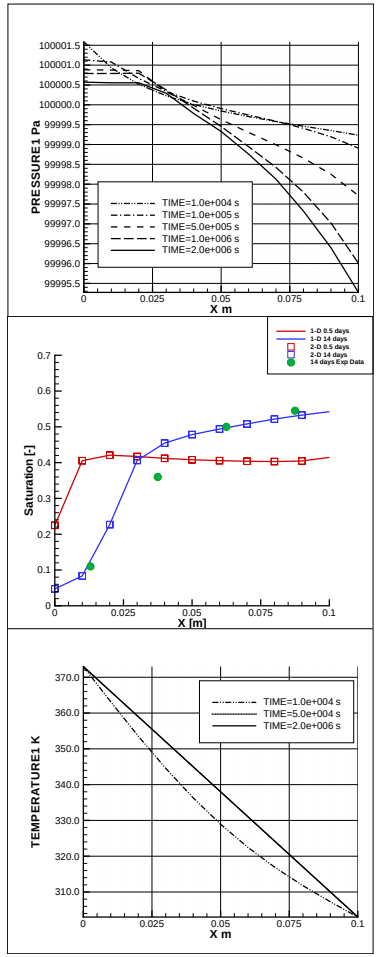

Figure 14: Profiles along the buffer material: gas pressure, liquid saturation, temperature (from top to bottom) for time points between 10^4 seconds and 14 days

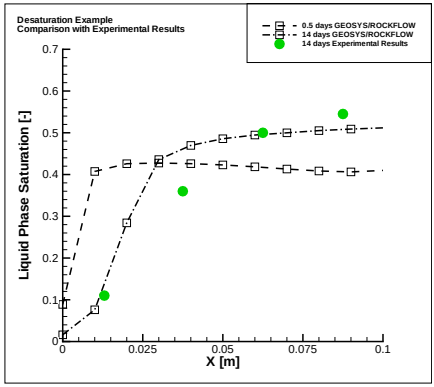

Figure 15: Liquid phase saturation profiles along the buffer material for temperature boundary condition of $130°C$, and inclusion of latent heat terms. Comparison to experimental data.

References

E. E. Alonso, A. Gens, and D. W. Hight. Special problem soils: general report. In *Proc. 9th European Conf. on Soil Mechanics and Foundation Engineering*, volume 3, Rotterdam, 1987. Balkema.

C. Barlag. *Adaptive Methoden zur Modellierung von Stofftransport im Kluftgestein*. Bericht nr. 52, Universität Hannover, 1997.

S. Bauer and O. Kolditz. Virtueller aquifer: Ermittlung von na-abbaukonstanten im feld - bestimmung der parameterunsicherheit. *Proceedings 5. Symposium Natural Attenuation, Frankfurt, Germany*, 2003.

S. Bauer, M. Xie, and O. Kolditz. Prozess-orientierung und objektorientierte programmentwicklung für mehrkomponenten-transportmodelle im grundwasser. *Mitteilungen des DGFZ, Dresden, Germany*, 2004. to be published.

M. Beinhorn and O. Kolditz. Density dependent flow in unconfined aquifers - application to the jordan valley. Rockflow-report 2003-13, Center of Applied Geosciences, University of Tübingen, April 2003.

J. De Jonge, W. Wang, and O. Kolditz. Non-isothermal flow processes in porous media, part II : Finite element method - shape functions and element matrices. Rockflow-Report 2004-1, Center for Applied Geosciences, University of Tübingen, 2004.

M. Emmert. *Numerische Modellierung nichtisothermer Gas-Wasser Systeme in porösen Medien*. PhD thesis, Insitut für Wasserbau, Universität Stuttgart, 1997.

I. Engelhardt, S. Finsterle, and C. Hofstee. Experimental and numerical investigation of flow phenomena in non-isothermal, variably saturated bentonite/crushed rock mixtures. *Vadose Zone Journal*, 2, 2003. available at http://www.vadosezonejournal.org.

D. Gawin, P. Baggio, and B. A. Schrefler. Coupled heat, water and gas flow in deformable porous media. *Int. J. Num. Meth. Fluids*, 20:969–987, 1995.

A. Gens, A. J. Garcia-Molina, S. Olivella, E. E. Alonso, and F. Huertas. Analysis of a full scale in-situ test simulating repository conditions. *Int. J. Anal. Num. Meth. Geomech.*, 22: 515–548, 1998.

M. Geraminegad and S. K. Saxena. A coupled thermoelastic model for saturated-unsaturated porous media. *Géotechnique*, 36:539–550, 1986.

A. Habbar. *Direkte und inverse geochemische Mehrkomponentenmodelle*. PhD thesis, Universität Hannover, 2001.

R. Helmig. *Theorie und Numerik der Mehrphasenströmungen in geklüftet-porösen Medien*. Bericht Nr. 34/1993, Universität Hannover, 1993.

R. Kaiser. *Gitteradaption für gekoppelte Prozesse in klüftig-porösen Medien*. PhD thesis, Universität Hannover, 2001.

T. Kanno, T. Fujita, H. Ishikawa, K. Hara, and M. Nakano. Coupled thermo-hydro-mechanical modelling of bentonite buffer material. *Int. J. Numer. Anal. Meth. Geomech.*, 23:1281–1307, 1999.

M. Kohlmeier, R. Kaiser, O. Kolditz, and W. Zielke. Finite element simulation of consolidation and bentonite swelling in the framework of unsaturated porous media. *Developments in Water Science*, 47:57–64, 2002.

O. Kolditz. Stoff- und Wärmetransport im Kluftgestein. Habilitationsschrift, Bericht Nr. 47/1996, Institut für Strömungsmechanik und Elektronisches Rechnen im Bauwesen, Universität Hannover, 1996.

O. Kolditz. *Strömung, Stoff- und Wärmetransport im Kluftgestein*. Borntraeger-Verlag, Berlin-Stuttgart, 1997.

O. Kolditz and C. Clauser. Numerical simulation of flow and heat transfer in fractured crystalline rocks: Application to the hot dry rock site at Rosemanowes (UK). *Geothermics*, 28: 1–26, 1998.

O. Kolditz and J. De Jonge. Non-isothermal two-phase flow in porous media. *Computational Mechanics*, 2004.

O. Kolditz, M. Kohlmeier, and C. Thorenz. Numerical methods for fluid flow in deformable porous media. In *Proc. Conference on "Teilgesättigte Böden"*, Bauhaus-Universität Weimar, 2000.

O. Kolditz, W. Wang, J.de Jonge, M. Xie, and S. Bauer. A process-oriented approach to compute thm problems in porous media - part 1: Theoretical and informatics background. *Proceedings of the ISSMGE International Conference 2003*, Sept 2003.

O. Kolditz, Editor. Festschrift zum 60. Geburtstag von Professor Werner Zielke. Bericht 59/1999, Institut für Strömungsmechanik und Elektron. Rechnen im Bauwesen der Universität Hannover, 1999.

Kolditz et al. Annual report 2003. ROCKFLOW-Preprint 2003-49, Center of Applied Geosciences, University of Tübingen, Tübingen, 2003.

K.-P. Kröhn. *Simulation von Transportvorgängen im klüftigen Gestein mit der Methode der Finiten-Elemente*. Bericht Nr. 29/1991, Universität Hannover, 1991.

T. Lege, O. Kolditz, and W. Zielke. *Strömungs- und Transportmodelle — Methodenhandbuch zur Erkundung des Untergrunds von Deponien und Altlasten, Band 2*. Springer-Verlag, 1996.

R. W. Lewis and B. A. Schrefler. *The finite element method in the static and dynamic deformation and consolidation of porous media*. Wiley, 1998.

C. McDermott and O. Kolditz. Coupled hydraulic-geomechanical effective stress model with application to the ktb site: Determination of discrete fracture network parameters from a pump test. ROCKFLOW-Preprint [2003-24], Center of Applied Geosciences, University of Tübingen, 2003.

S. Moenickes. Grid generation for simulation of flow and transport processes in fractured-porous media. Dissertation, Fachbereich Bauingenieur- und Vermessunswesen der Universität Hannover, January 2004.

S. Olivella, J. Carrera, A. Gens, and E. E. Alonso. Nonisothermal multiphase flow of brine and gas through saline media. *Transport in Porous Media*, 15:271–293, 1994.

S. Olivella and A. Gens. Vapour transport in low permeability unsaturated soil with capillary effects. *Transport in Porous Media*, 40:219–241, 2000.

R. Ratke, O. Kolditz, and W. Zielke. Rockflow-DM2- 3-D Dichteströmungsmodell. Technischer bericht, Institut für Strömungsmechanik und Elektronisches Rechnen im Bauwesen, Universität Hannover, 1996.

R. C. Reid, J. M. Prausnitz, and B. E. Poling. *The properties of liquids and gases*. McGraw-Hill, Singapore, 1988.

T. Rother. *Geometric modelling of fractured-porous geosystems*. PhD thesis, Universität Hannover, 2001.

J. Rutqvist, L. Börgesson, M. Chijimatsu, A. Kobayashi, L. Jing, T. S. Nguyen, J. Noorishad, and C.-F. Tsang. Thermodynamics of partially saturated geologic media: governing equations and formulation of four finite element models. *International Journal of Rock Mechanics & Mining Sciences*, 38:105–127, 2001.

H. Shao. *Simulation von Strömungs- und Transportvorgängen in geklüftet porösen Medien mit gekoppelten Finite-Elemente- und Rand-Element-Methoden*. Bericht Nr. 37/1994, Universität Hannover, 1994.

C. Thorenz. *Model Adaptive Simulation of Multiphase and Density Deiven Flow in Fractured and Porous Media*. PhD thesis, Institut für Strömunsmechanik und Elektron. Rechnen im Bauwesen der Universität Hannover, 2001a.

C. Thorenz. *Model adaptive simulation of multiphase and density driven flow in fractured and porous media*. PhD thesis, Universität Hannover, 2001b.

W. Wang and O. Kolditz. Numerical analysis of elasto-plastic consolidation in porous media. ROCKFLOW-Preprint [2003-1], Center of Applied Geosciences, University of Tübingen, 2003.

J. Wollrath. *Ein Strömungs- und Transportmodell für klüftiges Gestein und Untersuchungen zu homogenen Ersatzsystemen*. Bericht Nr.28/1990, Universität Hannover, 1990.

M. Xie, O. Kolditz, S. Tripathy, and T. Schanz. Numerical moedlling of swelling processes in compacted bentonite. Rockflow-report 2002-4, Centre of Applied Geosciences, University of Tübingen, Soil Mechanics Laboratory Bauhaus-University Weimar, 2003a.

M. Xie, W. Wang, J. De Jonge, and O. Kolditz. Numerical modeling of swelling processes in highly compacted bentonites. In Stephanson, editor, *GeoProc 2003*, pages 1001–1009. accepted paper, 2003b.

List of Publications

O. Kolditz and J. De Jonge (2004): Non-isothermal two-phase flow in porous media. *Computational Mechanics*, Vol. 33, No. 5, April 2004.

J. De Jonge and O. Kolditz (2002): Non-isothermal flow processes in porous media, part I : Governing equations and finite element implementation. Center of Applied Geosciences, University of Tübingen, RockFlow-Report 2002-1. 2002.

J. De Jonge, W. Wang, and O. Kolditz (2004): Non-isothermal flow processes in porous media, part II : Finite element method - shape functions and element matrices. RockFlow-Report 2004-1, Center of Applied Geosciences, University of Tübingen, 2004.

J. De Jonge, M. Xie and O. Kolditz (2003): Numerical implementation of thermally and hydraulically coupled processes in non-isothermal porous media. GeoProc 2003 Proceedings, Stockholm 13-15.10.2003. To be published as a book chapter in "Coupled Thermo-Hydro-Mechanical Processes in Geo-Systems, edited by O. Stephansson, J. Hudson, L. Jing."

J. De Jonge, I. Engelhardt, O. Kolditz (2003): Benchmarking non-isothermal multi-phase numerical simulations. ROCKFLOW-Preprint [2003-12], Center of Applied Geosciences, University of Tübingen.

M. Xie, W. Wang, J. De Jonge and O. Kolditz (2004): Numerical modelling of swelling pressure in unsaturated expansive elasto-plastic porous media. Center of Applied Geoscience Geohydrology/Hydroinformatics University of Tübingen, Germany. (Submitted to Transport in Porous Media, July 2004)

O. Kolditz, W. Wang, J. De Jonge, M. Xie, and S. Bauer (2003): A process-oriented approach to compute THM problems in porous media - Part 1: Theoretical and informatics background. Center of Applied Geosciences, University of Tübingen. (Invited lecture) Proceedings of the ISSMGE International Conference 2003, Sept. 18-19, Weimar, Germany

O. Kolditz, W. Wang, J. De Jonge, M. Xie, and S. Bauer (2003): A process-oriented approach to compute THM problems in porous media - Part 2: Numerical Applications. Center of Applied Geosciences, University of Tübingen. (Invited lecture) Proceedings of the ISSMGE International Conference 2003, Sept. 18-19, Weimar, Germany

J. De Jonge, O. Kolditz, W.Wang, M. Xie, H. Shao, T. Nowak, H. Kunz, M. Kohlmeier, and G. Ziefle (2004): Development of numerical tools for modeling THM coupling processes in nuclear waste storage applications - RockFlow/Geosys and its Pre- and Postprocessors. (In preparation for Int. J. Rock Mech. Min. Sci.)

Non-isothermal two-phase flow in porous media

Journal publication:

Computational Mechanics, Volume 33, No. 5

April 2004

Computational Mechanics (2004) © Springer-Verlag 2004
DOI 10.1007/s00466-003-0537-0

Non-isothermal two-phase flow in low-permeable porous media

O. Kolditz, J. De Jonge

Abstract In this paper, we consider non-isothermal two-phase flow of two components (air and water) in gaseous and liquid phases in extremely low-permeable porous media through the use of the finite element method (FEM). Interphase mass transfer of the components between any of the phases is evaluated by assuming local thermodynamic equilibrium between the phases. Heat transfer occurs by conduction and multiphase advection. General equations of state for phase changes (Clausius–Clapeyron and Henry law) as well as multiphase properties for the low-permeable bentonites are implemented in the code. Additionally we consider the impact of swelling/shrinking processes on porosity and permeability changes. The numerical model is implemented in the context of the simulator RockFlow/RockMech (RF/RM), which is based on object-oriented programming techniques. The finite element formulations are written in terms of dimensionless quantities. This has proved to be advantageous for preconditioning composite system matrices of coupled multi-field problems. Three application examples are presented. The first one examines differences between the Richards' approximation and the multicomponent/multiphase approach, and between two numerical coupling schemes. The second example serves as partial verification against experimental results and to demonstrate coherence between different element types. The last example shows simultaneous desaturation and resaturation in one system.

Keywords Non-isothermal multiphase flow, Porous media, Object-oriented programming, Geotechnics

List of Symbols

A	System matrix [–]
A	Advection matrix [–]
a	Component air [–]
b	Right hand side vector [–]
c	Heat capacity [J/Kg·K]
C	Mass matrix, subscript: variable [kg]
Cp	Compressibility number [–]
D	Diffusion coefficient [m^2/s]
Di	Diffusivity number [–]
e	Void ratio [–]
g	Gravity vector [m/s^2]
g	Gas Phase, superscript [-]
h	Enthalpy [J/kg]
h	Heat, subscript [–]
J	Flux [kg/m·s]
$\mathbf{J}_A$	Advective flux [kg/m·s]
$\mathbf{J}_D$	Diffusive flux [kg/m·s]
$\mathbf{J}_h$	Heat flux [J/m·s]
$\mathbf{J}_{A_h}$	Advective heat flux [J/m·s]
$\mathbf{J}_{D_h}$	Diffusive heat flux [J/m·s]
k	Component (subscript)[–]
k	Permeability [m^2]
k	Permeability tensor [m^2]
k_{rel}	Relative permeability [–]
k^{ε}_{rel}	Rel. perm. due to swelling[–]
K	Conductivity matrix [W/m·K]
K_H	Henry coefficient [1/Pa]
l	Liquid phase, superscript [–]
M	Molar mass [kg/mol]
m	Mass [kg]
N	Interpolation function [–]
n	Porosity [–]
n	Time step number [–]
Ne	Neumann number [–]
p	Pressure [Pa]
p	Pressure vector [Pa]
p_c	Capillary pressure [Pa]
$p_{c\,max}$	Maximum capillary pressure [Pa]
$\mathbf{p}_c$	Capillary pressure vector [Pa]
p_{crit}	Critical pressure [Pa]
$p^g_{w,sat}$	Vapour pressure [Pa]f
Q	Source term [m^3/s]
R	Gas constant [J/mol·K]
RHS	Right hand side terms [–]
S	Saturation [–]
S	Saturation vector [–]
S_{eff}	Effective saturation [–]
S_{max}	Maximum saturation [–]
S_r	Residual Saturation [–]
St	Storativity number [1/Pa]
s	Solid phase, superscript [–]
T	Temperature [K]

Received: 6 June 2003/Accepted: 25 November 2003
Published online: 16 January 2004

O. Kolditz (✉), J. De Jonge
Center for Applied Geoscience, Geohydrology/HydroInformatics
University of Tübingen Sigwartstrasse 10,
72076 Tübingen, Germany
e-mail: Kolditz@uni-tuebingeu.de

The work presented in this paper was partially funded by the Federal Institute of Geosciences and Natural Resources (BGR). We thank Dr. Wallner and Dr. Shao from the BGR for their support of this research. Furthermore, we wish to acknowledge the Deutsche Forschungsgemeinschaft (DFG) for their interest and support of this work.

T	Temperature vector [K]
t	Time [s]
u	Solution vector [–]
u	Internal energy [J/kg]
v	Velocity vector [m/s]
x	Mole fraction [–]
X	Mass fraction [–]
X	Mass fraction vector [–]
w	Water component, subscript [–]
β_P	Fluid compressibility coefficient [1/Pa]
β_T	Thermal expansion coefficient [1/K]
γ	Fluid phase (superscript)[–]
λ	Thermal conductivity [J/K·m·s]
μ	Fluid viscosity [Pa·s]
ρ	Density kg/m^3 Density
Θ	Time collocation factor [–]
Ω	Domain [–]
0	Initial or reference value, subscript [–]

1 Introduction

Clays and bentonites receive increasing attention as technical buffer materials in geological barriers that isolate waste. Therefore, detailed knowledge of the behavior of these materials under a large variety of thermodynamical conditions is of special interest. In order to obtain a good knowledge of the processes involved, we develop numerical models of the physical processes and their coupling. The process interactions are especially complex in low-permeable porous media, such as bentonite, as swelling and suction play an important role. Equally, the treatment of numerical formulations becomes different, as the right hand side terms of the algebraic equations gain importance. The objective of this paper is to present a new model for the general FE simulator RockFlow/RockMech (RF/RM) as an analysis tool for these processes.

Figure 1 gives an overview on THM processes. Coupling processes have been studied in detail in the past, but analysis and evaluation of these systems at larger scales is still a challenge to research. An excellent review on coupled processes has been presented by Tsang, 1991. A number of numerical methods have been developed for the purpose of modeling non-isothermal flow in multiphase systems. A very essential aspect in those hydraulic, thermal and mechanical operations is the understanding of induced coupled processes. First models to evaluate those coupled processes were built up by [1, 19, 33–35,45–47, 51]. More recently, a model was developed by Korsawe et al., 2000. That model is based on the concept of rational mechanics and is using the Raviart–Thomas mixed finite element method, as well as a an implicit Euler time discretization. The model is only developed for the special case of a rigid soil skeleton.

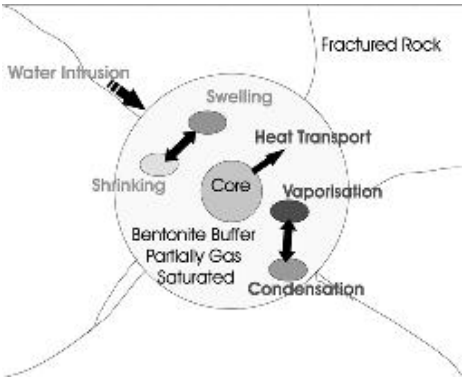

Fig. 1. TH^2/M processes in bentonite buffer systems, [10]

Modeling of non-isothermal flow in porous media is of interest in several practical areas, such as groundwater remediation techniques, use of geothermal energy, or geotechnical technologies for waste isolation. Modeling is, in particular, useful to evaluate the impact of coupling phenomena on overall system performance.

In the field of groundwater remediation techniques, thermally enhanced procedures, such as steam injection, are recognized techniques to treat subsurface contamination by non-aqueous phase liquids (NAPLs). Numerical models for simulation of the related non-isothermal processes were developed by [9, 11, 13–15, 20]. These codes have found wide application in simulating NAPL remediation for systems with relatively large permeability.

Natural thermo-hydraulic processes in the surrounding area of geothermal reservoirs have been studied by a large number of authors (e.g. [41, 42]). An excellent review of modeling thermo-hydraulic processes in geothermal systems is presented by [40]. [5] investigated the effect of injection of colder water into a fracture near a geothermal reservoir, and the advance of the thermal front along the fracture was simulated with a numerical model. The role of fracture networks in geothermal reservoirs is discussed and demonstrated in site studies by [22]. Long-term fluid and heat extraction from geothermal systems result in significant deformation processes [29, 27] presented a THM model for geothermal systems, where capillarity effects are neglected.

In geomechanical models the stress state and the resulting deformation process is of special interest. As a consequence the solid phase has to be treated explicitly. The interaction of fluid (phase) flow and solid (phase) deformation in the framework of the porous medium approach can be modeled based on the consolidation theory [4, 49]. Modeling of geotechnical barriers for heat emitting waste often requires a coupled thermo-hydro-mechanical (THM) analysis. First studies of THM processes in that field were presented by [8]. However, only one fluid phase was considered. In that case, multiphase effects and phase change processes can not be addressed. [6] and [48] investigated swelling and shrinking phenomena in bentonites. They developed a material model for porosity and permeability changes with undergoing moisture transport. Studies of THM processes in partially saturated, thermo-elastic porous media without phase change effects were presented by [18]. [2] discussed the theoretical background of THM modeling including all important effects. [36], [16] and [17] introduced the

compositional approach for THM modeling of multiphase-multicomponental systems. In their book, [28] gave an excellent overview on coupled processes and their modeling in the field of deformation and consolidation theory of porous media. [21] developed and applied a THM model to study the temperature dependency of hydraulic conductivity in saturated porous media and water diffusivity in unsaturated porous media. An excellent overview on existing THM codes is given by [44]. Most of the cited models in this paragraph have found wide application in simulating geotechnical systems. In most cases the systems analyzed were restricted to relatively large permeabilities.

As this literature review shows, there are some very good models available for specific applications. In the field of geotechnical engineering that we are considering here, the important findings from literature are the following. The porous media theory is widely used, and whereas many models do not consider phase change and use the Richard's approximation, a few are considering phase change and moving towards multiphase-multicomponental formulations. However non-isothermal behavior in swelling materials has not been researched extensively. There is also a big gap in research on numerical stability analysis of codes modeling such systems.

The RF/RM code is an existing finite element code, which has its background in fracture hydraulics. As the field of application was getting wider, the need to be able to simulate situations in low-permeable porous media became apparent. The authors believe that combining codes is not an option in this situation, because of the complex coupling. It therefore became necessary to make use of the object-oriented features of RF/RM and implement a new model.

In this paper the details of the mathematical and numerical multiphase-multicomponental formulation for porous media, as well as the code implementation are described. Test examples are shown to illustrate the code.

The numerical model TH^2/M has been developed for the purpose of modeling non-isothermal multiphase flow in porous media. The capital letters TH^2/M denote a fully coupled thermo-hydraulic model with a weak mechanical coupling and 2 is the number of fluid phases. Mechanical effects of clay swelling/shrinking are incorporated via the phenomenological model by [6] and [48]. Previously, work on isothermal multiphase flow had been done by [50]. For non-isothermal multiphase flow however, a new process kernel had to be implemented. TH^2/M is a part of the multi-purpose finite element simulator RF/RM, which is based on an object-oriented software architecture (www.rockflow.net, [25]).

2 Physico-chemical processes

Non-isothermal multiphase flow in porous media involves several complex interacting phenomena. We consider the porous medium a three component system, with the components air, water, and soil. Each of these components can be present in three phases (gas, liquid, and solid phase). Although air and soil consist of several components, they are treated as a single pseudo component with average properties. The chemical composition may be different in each phase.

Hydraulic processes result from pressure and gravitational and frictional forces described by the extension of Darcy's law for multiphase flow and illustrated in Fig. 1. We have to deal with concurrent flow of compressible (gas phase) and incompressible fluids (liquid phase). The mobility of the fluid phases is characterized by their relative permeabilities. Relative permeability is in turn related to capillary pressure via saturation, as shown in the van Genuchten equations [52]. In particular in materials with very small grain fractions such as bentonite, extremely large capillary pressures up to 10^{10} =Pa can exist.

Transport of the components (air, water, and soil) occurs by advection and diffusion in the fluid phases. Mechanisms of interphase mass transfer for the water component include evaporation into the gas phase and corresponding condensation of the water vapor from the gas phase. Mechanisms of interphase mass transfer for the air component include dissolution in the liquid phase and corresponding release based on the equilibrium partitioning between the gas and liquid phases. It is assumed that all phases are in local chemical and thermal equilibrium. We have to deal with following phase change processes (i.e. mass transfer between phases): evaporation of liquid water species to the gas phase, solution of gaseous air species in the liquid phase.

The system is characterized by strong heat transfer in a three-phase system (gas, liquid, solid phases), in which the mass transfer of components between the phases (i.e. evaporation, condensation) is significant. Heat transfer occurs due to multiphase advection and conduction. Effects of phase transitions between the gas and liquid phases are taken into account by considering latent heat.

Clay-like materials and bentonites swell/shrink with the presence/absence of water. The swelling effect results from additional embedding of water molecules into the solid matrix. As a consequence of this process, porosity and permeability change. Swelling/shrinking is a strong hydro-mechanical coupling phenomenon.

There is a strong dependence of fluid material properties on temperature and pressure, such as for density, viscosity, and thermal conductivity. The overall material properties of the porous medium itself depend in a large extent on the liquid saturation distribution and its evolution. Those complexities of non-linear processes limit the general application of analytical solution techniques.

The above processes are constrained by the following assumptions:

- All components of the gas phase obey the ideal gas law.
- Partial pressure of water in the gas phase is equal to the saturated vapor pressure of water at the local temperature.
- Regarding vapor flow, two assumptions are made. Firstly, the Knudsen number is proportional to (length of mean free path)/(characteristic dimension) and is used in momentum and mass transfer in general and very low pressure gas flow calculations in particular. It can be seen from the work of [37], that as permeability

decreases, Knudsen diffusivity becomes very small. This is why Knudsen diffusivity has been neglected in the TH^2/M model so far, but it will be implemented in the future, for accuracy. Secondly, the Klinkenberg, or gas slip effect arises when the dimensions of the moving molecule and that of the path are close to equal. The molecules at the interface are usually assumed stationary. Under gas slip conditions though, they are moved and create additional vapor flux. According to [3], the Klinkenberg effect is relevant for gas flow at low pressures. Since our applications are mainly taking place in the subsurface, gas pressures are not very low. Typically, gas pressures in laboratory experiments in this field are kept above atmospheric pressure.

- Chemical and thermal local equilibrium is assumed.
- We work with idealized void spaces in the solid matrix.
- Componental diffusion is only taken into account in the gas phase.
- The model enables the user to work with the Richards approximation, if chosen.

3 Model equations

The theoretical framework is composed of four parts: balance equations (Sect. 3.1), fluxes (3.2), and equations of state (3.3), which are used to derive the governing equations (3.4). The primary variables of the model are gas pressure p^g, liquid saturation S^l, and temperature T, as shown in Table 1.

3.1 Balance equations

In a non-isothermal system containing two components, two mass balance equations and a heat balance equation are required to fully describe the system. A multiphase/multicomponent approach is used to derive the balance equations for mass conservation of each component (Eq. 1). Subscripts refer to the components air ($k = a$) and water ($k = w$), whereas superscripts indicate gaseous ($\gamma = g$) and liquid phases ($\gamma = l$).

$$\frac{\partial}{\partial t}(nS^g\rho_k^g + nS^l\rho_k^l) + \nabla \cdot \mathbf{J}_k^g + \nabla \cdot \mathbf{J}_k^l = Q_k \tag{1}$$

where n is porosity, S^γ is fluid phase saturation, ρ_k^γ is component mass per unit volume of the fluid phase. The total flux of component k in phase γ: $\mathbf{J}_k^\gamma = \mathbf{J}_{\mathrm{A}k}^\gamma + \mathbf{J}_{\mathrm{D}k}^\gamma$ consists of an advective $\mathbf{J}_\mathrm{A}$ and a diffusive part $\mathbf{J}_\mathrm{D}$. Q_k is the componental source term, i.e. generation of component k per unit volume.

The heat balance equation for the porous medium consisting of three phases (solid, gas, liquid) is given by

$$\frac{\partial}{\partial t}\left((1-n)\rho^s u^s + nS^g\rho^g u^g + nS^l\rho^l u^l\right) + (\nabla \cdot \mathbf{J}_h^s + \nabla \cdot \mathbf{J}_h^g + \nabla \cdot \mathbf{J}_h^l) = Q_h \tag{2}$$

Table 1. Primary and secondary variables

Primary variable	Symbol
Gas pressure (for the air component)	p^g
Liquid saturation (for the water component)	S^l
Temperature (for the energy component)	T

where u^γ is phase internal energy, ρ^γ is phase density. The total heat flux in phase γ: $\mathbf{J}_h^\gamma = \mathbf{J}_{\mathrm{Ah}}^\gamma + \mathbf{J}_{\mathrm{Dh}}^\gamma$ includes both an advective $\mathbf{J}_{Ah}^\gamma$ and a diffusive part $\mathbf{J}_{Dh}^\gamma$. Q_h is the heat source term, i.e. heat generation rate per unit volume. The phase change terms cancel out with the addition of the individual phases. We work under the assumption of local thermodynamic equilibrium, meaning that all phase temperatures are equal.

3.2 Flux terms

In general, two types of fluxes have to be considered: advective fluxes and diffusive fluxes of fluid mass or energy.

Advective componental fluxes $\mathbf{J}_{\mathrm{AK}}^\gamma$ are movements of components k with the fluid phase γ relative to the solid phase. We use an extension of the Darcy equation to express advective fluxes in terms of the primary variables. If convenient, capillary pressure can be used instead of a corresponding fluid phase pressure: $p_\mathrm{c} = p^g - p^l$.

$$\mathbf{J}_{Ak}^\gamma = nS^\gamma\rho_k^\gamma(\mathbf{v}^\gamma - \mathbf{v}^s) = nS^\gamma\rho^\gamma X_k^\gamma(\mathbf{v}^\gamma - \mathbf{v}^s) = -\rho^\gamma X_k^\gamma\frac{k_{rel}^\gamma\mathbf{k}}{\mu^\gamma}(\nabla p^\gamma - \rho^\gamma\mathbf{g}) \tag{3}$$

where k_{rel}^γ is the fluid phase relative permeability, $\mathbf{k}$ is the reference permeability tensor, μ^γ is the fluid phase dynamic viscosity, and $\mathbf{g}$ is the gravitational acceleration vector. X_k^γ is the mass fraction, which is discussed in detail in Sect. 3.3.

Advective internal energy flux in a fluid phase γ is defined as

$$\mathbf{J}_{Ah}^\gamma = u^\gamma\mathbf{J}_{A}^\gamma = u^\gamma nS^\gamma\rho^\gamma(\mathbf{v}^\gamma - \mathbf{v}^s) = -u^\gamma\rho^\gamma\frac{k_{\mathrm{rel}}^\gamma\mathbf{k}}{\mu^\gamma}(\nabla p^\gamma - \rho^\gamma\mathbf{g}) \tag{4}$$

Diffusive mass flux of components within the fluid phase is given by Fick's law and is driven by mass fractions.

$$\mathbf{J}_{Dk}^\gamma = nS^\gamma\rho_k^\gamma(\mathbf{v}_k^g - \mathbf{v}^g) = -nS^\gamma\rho^\gamma D_k^\gamma\nabla X_k^\gamma \tag{5}$$

where D_k^γ is the diffusion coefficient of component k in phase γ. Note, that due to balance requirements $\mathbf{J}_{Da}^\gamma + \mathbf{J}_{Dw}^\gamma = 0$. This relationship ensures that the total diffusive mass flux in a fluid phase summed over all components is zero with respect to the average mass velocity [11].

Total diffusive heat flux in the porous medium is given by Fourier's law for heat conduction

$$\mathbf{J}_{Dh} = -\lambda\nabla T \tag{6}$$

where λ is the thermal conductivity of the porous medium

$$\lambda = (1-n)\lambda^s + nS^g\lambda^g + nS^l\lambda^l \tag{7}$$

3.3 Equations of state

The set of balance equations needed to solve for the primary variables is not complete without the equations of state. Furthermore, equations of state link the balance equations for water, air and energy with each other and

describe the physical state of the system that is modelled. In non-isothermal flows, major non-linearities in the model equations arise from large variations of secondary variables and parameters. Therefore, an accurate computation of secondary variables and material functions is of considerable importance. A complete list of the secondary variables along with their dependence on the primary variables is given in Table 2. The following sections show how those properties are calculated.

Componental mass density – $\rho_k^\gamma(\boldsymbol{p}^\gamma, \boldsymbol{T})$

In the framework of the multi-componental approach, the phase density is composed by the sum of the corresponding partial componental mass densities ρ_k^γ,

$$\rho^\gamma = \rho_a^\gamma + \rho_w^\gamma = X_a^\gamma \rho^\gamma + X_w^\gamma \rho^\gamma \tag{8}$$

where X_k^γ is the mass fraction of the component k in phase γ. Mass fractions are defined as

$$X_k^\gamma = \frac{m_k^\gamma}{m^\gamma} = \frac{\rho_k^\gamma}{\rho^\gamma} \tag{9}$$

where m is the mass of component k in phase γ.

Therefore, mass conservation of components during phase changes is represented by the constraining condition $X_a^\gamma + X_w^\gamma = 1$

To derive relationships for componental densities, we have to employ the assumption of local thermodynamic equilibrium. The equilibrium restrictions for the vapor pressure (p_w^g) is given by the Clausius–Clapeyron equation (Eq. 10). The partial pressure of water in the gas phase is assumed to be equal to the saturated vapor pressure of water at the local temperature

$$p_w^g \equiv p_{w,sat}^g(T) = p_0 \exp\left[\left(\frac{1}{T_0} - \frac{1}{T}\right)\frac{h_w^g M_w}{R}\right] \tag{10}$$

The equilibrium restrictions for mass of dissolved air in liquid phase (ρ_a^l) is described by Henry's law (11) in terms of mole fractions,

$$x_a^g = K_H p_a^g \tag{11}$$

where K_H is the Henry coefficient, which is defined for a binary water-air system as

$$K_H = \left(0.8942 + 1.47\exp^{-0.04394T}\right) \times 10^{-10} \quad \text{in} \quad \text{Pa}^{-1} \tag{12}$$

Mole fractions are defined as

$$x_k^\gamma = \frac{n_k^\gamma}{n^\gamma} = \frac{p_k^\gamma}{p^\gamma} \tag{13}$$

where n is the number of moles of component k in phase γ. Water vapor is assumed to be an ideal gas. According to the Clausius–Clapeyron equation (10), the partial mass density of water species in the gas phase (vapor mass) is

$$\begin{aligned}\rho_w^g &= \frac{M_w}{RT} p_w^g = X_w^g \rho^g \\ &= \frac{M_w}{RT} p_0 \exp\left[\left(\frac{1}{T_0} - \frac{1}{T}\right)\frac{h_w^g M_w}{R}\right]\end{aligned} \tag{14}$$

where M_w is the molecular weight of water, R is the universal gas constant, T is equilibrium temperature in Kelvin. The value of vapor pressure is calculated from steam table equations given by the International Formulation Committee [31] and [32].

After some transformations, the partial mass density of the air species in the liquid phase (mass of dissolved air) can be determined from Henry's law (Eq. 11), as shown in Eq. (16).

$$\begin{aligned}\rho_a^l &= X_a^l \rho^l \\ &= \frac{M_a}{M_a - M_w(1 - [K^H(T) p_a^g]^{-1})} \rho^l\end{aligned} \tag{15}$$

Vapour diffusivity–D_w^g

Molecular diffusion of water species in air is governed by Fick's law. The user can choose between a constant vapour diffusivity function and a function given by [38].

$$D_w^g = 5.9 \times 10^{-12} \frac{T^{2.3}}{p^g} \quad in \quad [m^2 s^{-1}] \tag{16}$$

In the equation, T is in C and p in MPa.

Table 2. Summary of secondary variables

Secondary Variables	Needed in balance equation					
	Water		Air		Energy	
	Liq	gas	liq	gas	liq	gas
Saturated water pressure		$p_{w,sat}^g$				
Capillary pressure	p_c					
Enthalpy		h_w^g			h^l	h^g
Mass fractions	X_w^l	X_w^g	X_a^l	X_a^g		
Pressure		p_w^g		p_a^g		
Internal energy					u^l	u^g
Fluid density	ρ_w^l	ρ_w^g	ρ_a^l	ρ_a^g		
Fluid viscosity	μ^l	μ^g	μ^l	μ^g		
Specific heat capacity					c	
Thermal conductivity					λ	
Diffusion coefficient					D	
Therm compress	β_T^l					
Permeability		k	k			
Relative permeability	k_{re}		k_{rel}			

Fluid phase density – $\rho^{\gamma}(\boldsymbol{p}^{\gamma}, \boldsymbol{T})$
The liquid phase density is approximated by the following linear function,

$$\rho^{l}(p^{l}, T) = \rho_0^{l}(1 + \beta_p^{l}(p^{l} - p_0^{l}) + \beta_T^{l}(T - T_0)) \tag{17}$$

where β_p is the compressibility coefficient and β_T is the thermal expansion coefficient.

Temporal changes of the liquid density can now be expressed in terms of primary variables

$$\frac{\partial \rho^{l}}{\partial t} = \rho_0^{l}\beta_p^{l}\frac{\partial p^{l}}{\partial t} + \rho_0^{l}\beta_T^{l}\frac{\partial T}{\partial t} \tag{18}$$

Gas phase density is calculated as the sum of the componental mass densities (Eq. 8), which follow the ideal gas law.

$$\rho^{g}(p^{g}, T) = \frac{M_a}{RT}p^{g} + \frac{(M_w - M_a)}{RT}p^{g}_{w,\mathrm{sat}}(T) \tag{19}$$

Temporal changes of the gas phase density can now be expressed in terms of primary variables

$$\frac{\partial \rho^{g}}{\partial t} = \frac{M_a}{RT}\frac{\partial p^{g}}{\partial t} + \frac{(M_w - M_a)}{RT}\frac{\partial p^{g}_{w,\mathrm{sat}}}{\partial T}\frac{\partial T}{\partial t} \tag{20}$$

Fluid phase viscosity – $\mu^{\gamma}(\boldsymbol{p}^{\gamma}, \boldsymbol{T})$
The gas phase viscosity for non-isothermal flow is calculated as a function of pressure and temperature [43]

$$\mu^{g}(p, T) = \mu_0(T)\left(1 + \frac{Ap_r^{3/2}}{Bp_r + (1 + Cp_r^{D})^{-1}}\right) \tag{21}$$

where A, B, C, and D are coefficients, and $p_r = p/p_{\mathrm{crit}}$. Water vapor viscosity can be computed from steam table values. Alternatively, the user can choose a constant viscosity function.

Specific enthalpy – h^{γ}
Specific enthalpy of liquid phase h^{l} is assumed to be independent of compositional effects and is computed as a function of pressure and temperature only. The partial water enthalpy h_w^{l} is calculated from steam table functions [31] and [32]. Specific enthalpy of the gas phase is a function of composition and is calculated as mass fraction weighted sum of the componental enthalpies.

$$h^{g} = X_a^{g}h_a^{g} + X_w^{g}h_w^{g} \tag{22}$$

Again, water vapor specific enthalpy h_w^{g} can be evaluated from steam table functions [31] and [32]. The specific air enthalpy in gas phase is

$$h_a^{g} = c_a T + \frac{p_a^{g}}{\rho_a^{g}} \tag{23}$$

where c_a is the heat capacity of air.

Capillary pressure – $\boldsymbol{p_c}(\boldsymbol{S}^{l}, \boldsymbol{T})$
The capillary pressure can be defined as the tendency of a porous medium to suck in the wetting fluid phase or to repel the non-wetting phase. Capillary pressure results from the pressure discontinuity at the interface between two immiscible fluids. Capillary pressure depends on the geometry of the void space, on the nature of solids and liquids and on the degree of saturation. In porous media the geometry of the void space is idealized. Thus, the dependence reduces to saturation for any given porous media. Care has to be taken, as capillary pressure is not the same for drainage and re-wetting. The function connecting capillary pressure and saturation has to be determined by laboratory experiments for every new porous medium. Frequently, an analytical functions is used, such as the [52] model

$$p_{\mathrm{c}}(S^{l}) = \begin{cases} 0 & \mathrm{S^{l} > S^{l}_{max}} \\ \frac{\rho^{l}g}{\alpha}(S_{\mathrm{eff}}^{-1/m} - 1)^{1/n} & \mathrm{S^{l}_{r} < S^{l} < S^{l}_{max}} \\ p_{\mathrm{c\,max}} & \mathrm{S^{l} < S^{l}_{r}} \end{cases} \tag{24}$$

with the effective saturation

$$S_{\mathrm{eff}} = \frac{S^{l} - S_r^{l}}{1 - S_r^{l}} = (1 + (\alpha p_{\,c})^{n})^{m}, \quad p_{\,c} > 0 \tag{25}$$

where α, m, and n are the van Genuchten parameters and S_r^{l} is the liquid residual saturation. Additionally, capillary pressure is a function of temperature. The function is given by [39].

$$\sigma(T) = (1 - 0.625a)(0.2358a^{1.256})$$
$$a = \frac{374.15 - T}{647.3} \tag{26}$$

where T is in °C, and $T < 360°$ C.

Relative permeability – $\boldsymbol{k}^{l}_{\mathrm{rel}}(\boldsymbol{S}^{l})$ and $\boldsymbol{k}^{g}_{\mathrm{rel}}(\boldsymbol{S}^{l})$
For porous media containing more than one fluid, the concept of relative permeability is introduced. The relative permeability is used to calculate the effective permeability $(k^{\gamma}_{rel}S^{\gamma})\mathbf{k}$, which is described in the extended Darcy law. The relationship strongly depends on the saturations. Different relationships are possible: constant values, user-defined functions, linear functions, potential functions, or functions found in literature, such as the van Genuchten model [52],

$$k^{l}_{\mathrm{rel}}(S^{l}) = S_{\mathrm{eff}}^{1/2}\left(1 - (1 - S_{\mathrm{eff}}^{1/m})^{m}\right)^{2} \tag{27}$$

$$k^{g}_{\mathrm{rel}}(S^{l}) = 1 - k^{l}_{\mathrm{rel}} \tag{28}$$

where m is the van Genuchten parameter.

Capillary pressure and relative permeabilities are among the most important parameters affecting multiphase flow.

Swelling/Shrinking effects
Material models for bentonites have successively been developed e.g. by [7] corresponding to a large range of pressures, void ratios, temperatures and materials itself. In particular, they investigated the elastic and plastic behavior of swelling clays in detail. In RF/RM, the user can choose to include swelling and shrinking effects with the elastic volumetric model for MX-80 bentonite by [7].

Swelling pressure reflects the effect of pore fluid compression due to the volume increase of the grain

material. [48] and [6] showed that swelling pressure largely depends on dry porosity, i.e. the packing of the material. They found the relationship between swelling pressure and saturation to be almost linear $p^l = CS^l$.

As a consequence of moisture swelling, the effective porosity as well as permeability are changing. Both parameters are decreasing with increasing water saturation. [48] and [6] found the following relationships for void ratio

$$e(p(S^l)) = e_0 \left(\frac{p(S^l)}{p_0} \right)^{\beta} \tag{29}$$

where

$$\beta = \frac{\Delta \ln e}{\Delta \ln\, p(S^l)} < 0$$

where β is a fitting parameter.

As void ratio is defined as: $e = n/(1-n)$, we can write the following equation for temporal porosity changes.

$$\frac{\partial n}{\partial t} = \frac{\partial n}{\partial p^\gamma} \frac{\partial p^\gamma}{\partial t} = \frac{e_0 \beta}{p_0} \left(\frac{p^\gamma}{p_0} \right)^{\beta - 1} \frac{\partial p^\gamma}{\partial t}$$
$$= \frac{e_0 \beta}{S_0} \left(\frac{S^\gamma}{S_0} \right)^{\beta - 1} \frac{\partial S^\gamma}{\partial t} \tag{30}$$

The dependency of saturated permeability on swelling pressure is given by [48] and [6] as follows,

$$k^\varepsilon_{rel}(p(S^l)) = k^\varepsilon_{rel0} \left(\frac{e(p(S^l))}{e_0} \right)^{\eta},$$

$$\text{where} \quad \eta = \frac{\Delta(\ln k^\varepsilon_{\mathrm{rel}})}{\Delta(\ln\, e)} \quad , \quad 0.5 < e < 2 \tag{31}$$

where $k^\varepsilon_{\mathrm{rel}}$ is the relative permeability due to swelling processes, and η is a fitting parameter. A new approach to model swelling processes in porous media based on hydro-chemical coupled analysis is presented by [53].

3.4 Model equations

The system of model equations to determine the chosen field variables: fluid gas pressure p^g, fluid liquid saturation S^l and equilibrium temperature T is based on the balance equations for fluid mass and heat (Sect. 3.1) in combination with the flux terms (Sect. 3.2) and the equations of state (Sect. 3.3).

Fluid component equation

Based on the fluid mass balance (1) the following model equation can be derived.

$$\left(nS^g X^g_k \frac{\partial \rho^g}{\partial p^g} \right) \frac{\partial p^g}{\partial t} - \nabla \cdot \left(\rho^g X^g_k \frac{k^g_{\mathrm{rel}} \mathbf{k}}{\mu^g} \nabla p^g \right)$$
$$+ n \rho^g X^g_k \frac{\partial S^g}{\partial t} + (nS^l X^l_k \frac{\partial \rho^l}{\partial p^l}) \frac{\partial p^l}{\partial t} - \nabla \cdot \left(\rho^l X^l_k \frac{k^l_{\mathrm{rel}} \mathbf{k}}{\mu^l} \nabla p^l \right)$$
$$+ n \rho^l X^l_k \frac{\partial S^l}{\partial t}$$
$$= Q_k$$
$$- \nabla \cdot \left(\rho^g X^g_k \frac{k^g_{\mathrm{rel}} \mathbf{k}}{\mu^g} \rho^g \mathbf{g} \right) + \nabla \cdot \left(\rho^l X^l_k \frac{k^l_{\mathrm{rel}} \mathbf{k}}{\mu^l} \rho^l \mathbf{g} \right)$$
$$+ \nabla \cdot (nS^g \rho^g D^g_k \nabla X^g_k) \tag{32}$$

In order to introduce the selected primary variables: gas pressure and liquid saturation, we use the relationships (33) to substitute liquid pressure and gas saturation:

$$p^l = p^g - p_c$$
$$S^g = 1 - S^l \tag{33}$$
$$X^l_k = 1 - X^g_k$$

Then we obtain the fluid component equation in terms of primary variables.

$$nX^g_k \left(S^g \frac{\partial \rho^g}{\partial p^g} + S^l \frac{\partial \rho^l}{\partial p^l} \right) \frac{\partial p^g}{\partial t} - \nabla \cdot \left(\rho^g X^g_k \frac{k^g_{\mathrm{rel}} \mathbf{k}}{\mu^g} \nabla p^g \right)$$
$$- \nabla \cdot \left(\rho^l X^l_k \frac{k^l_{\mathrm{rel}} \mathbf{k}}{\mu^l} \nabla p^g \right) + n(-\rho^g X^g_k + \rho^l X^l_k) \frac{\partial S^l}{\partial t}$$
$$= Q_k$$
$$+ (nS^l X^l_k \frac{\partial \rho^l}{\partial p^l}) \frac{\partial p_c}{\partial t} - \nabla \cdot \left(\rho^l X^l_k \frac{k^l_{\mathrm{rel}} \mathbf{k}}{\mu^l} \nabla p_c \right)$$
$$- \nabla \cdot \left(\rho^g X^g_k \frac{k^g_{\mathrm{rel}} \mathbf{k}}{\mu^g} \rho^g \mathbf{g} \right) + \nabla \cdot \left(\rho^l X^l_k \frac{k^l_{\mathrm{rel}} \mathbf{k}}{\mu^l} \rho^l \mathbf{g} \right)$$
$$+ \nabla \cdot (nS^g \rho^g D^g_k \nabla X^g_k) \tag{34}$$

Richards approximation

As an option, the model can be simplified by the Richards approximation, which assumes a constant gas pressure. As a result, there is only one independent unknown in the fluid mass balance equation, which we choose to be liquid pressure (p^l). Then we have only one independent unknown function: liquid pressure (p^l) or phase saturation (S^γ). Using the following relationship

$$\frac{\partial S^l}{\partial t} = \frac{\partial S^l}{\partial p^l} \frac{\partial p^l}{\partial t} = - \frac{\partial S^l}{\partial p_c} \frac{\partial p^l}{\partial t} \tag{35}$$

the fluid component equation (32) can be written for liquid pressure (p^l) as the unknown function.

$$nX^l_k \underbrace{\left(S^l \frac{\partial \rho^l}{\partial p^l} - \rho^l \overbrace{\frac{\partial S^l}{\partial p_c}}^{m} \right)}_{n} \frac{\partial p^l}{\partial t} - \nabla \cdot \left(\rho^l X^l_k \frac{k^l_{\mathrm{rel}} \mathbf{k}}{\mu^l} \nabla p^l \right) = Q_k$$
$$+ \nabla \cdot \left(\rho^l X^l_k \frac{k^l_{\mathrm{rel}} \mathbf{k}}{\mu^l} \rho^l \mathbf{g} \right) + \nabla \cdot (nS^g \rho^g D^g_k \nabla X^g_k) \tag{36}$$

Equation (36) is explicitly non-linear due to the term m. Additionally, non-linearities arise from material proper-

ties, i.e. from the dependence of phase saturations on liquid pressure according to the capillary pressure function (Eq. 24) as well as from the dependence of relative permeability on phase saturation (Eq. 27) in term n. Either the equation for air or for water species can be used to determine the liquid pressure. Equation (36) can be termed Richards equation for non-isothermal flow.

Thermal energy equation

Based on the heat balance equation (2) for the porous medium consisting of three phases, we obtain the following thermal energy equation.

$$\begin{aligned}
&\left((1-n)\rho^s c^s + nS^g\rho^g c^g + nS^l\rho^l c^l\right)\frac{\partial T}{\partial t}\\
&+\left(\rho^g c^g \frac{k^g_{\mathrm{rel}}\mathbf{k}}{\mu^g}(\nabla p^g - \rho^g\mathbf{g})\right.\\
&\quad\left.+\rho^{lc}\frac{k^l_{\mathrm{rel}}\mathbf{k}}{\mu^l}(\nabla p^l - \rho^l\mathbf{g})\right)\nabla T\\
&\quad-\nabla\cdot\left(\left((1-n)\lambda^s + nS^g\lambda^g + nS^l\lambda^l\right)\nabla T\right)\\
&\quad-\nabla\cdot\left(nS^g\rho^g D^g_a h^g \nabla X^g_a\right)\\
&\quad-\nabla\cdot\left(nS^g\rho^g D^g_w h^g \nabla X^g_w\right)\\
&\quad=\rho Q_T
\end{aligned}\tag{37}$$

4 Numerical scheme

RF/RM uses the finite element method (FEM). Details of the FEM, as applied in the code can be found in Appendix I.

4.1 Algebraic Equations

Time discretization using first-order finite difference schemes and time collocation for spatial terms yield the following system of algebraic equations for the fluid component equation (32) and the heat energy equation (37). The symbol definitions of the finite element matrices are given in the list of symbols.

Fluid component equations ($k = a, w$), where $\theta \in [0,1]$

$$\begin{aligned}
&\left[\frac{1}{\Delta t}(\mathbf{C}_{P_k}{}^g + \mathbf{C}_{P_k}{}^l) + \theta(\mathbf{K}_{P_k}{}^g + \mathbf{K}_{P_k}{}^l)\right][\hat{\mathbf{p}}^g]^{n+1}\\
&\quad+\left[\frac{1}{\Delta t}(\mathbf{C}_{S_k}{}^l - \mathbf{C}_{S_k}{}^g)\right][\hat{\mathbf{S}}^l]^{n+1}\\
&=\left[\frac{1}{\Delta t}(\mathbf{C}_{P_k}{}^g + \mathbf{C}_{P_k}{}^l) - (1-\theta)(\mathbf{K}_{P_k}{}^g + \mathbf{K}_{P_k}{}^l)\right][\hat{\mathbf{p}}^g]^n\\
&\quad+\left[\frac{1}{\Delta t}(\mathbf{C}_{S_k}{}^l - \mathbf{C}_{S_k}{}^g)\right][\hat{\mathbf{S}}^l]^n + \left[\frac{1}{\Delta t}\mathbf{C}_{P_k}{}^l\right]([\hat{\mathbf{p}}_c]^{n+1} - [\hat{\mathbf{p}}_c]^n)\\
&\quad+\left[\mathbf{K}^{ls}_k\right](\theta[\hat{\mathbf{p}}_c]^{n+1} + (1-\theta)[\hat{\mathbf{p}}_c]^n)\\
&\quad-\left[\mathbf{K}^g_k\right](\theta[\hat{\mathbf{X}}^g_k]^{n+1} + (1-\theta)[\hat{\mathbf{X}}^g_k]^n) + (\mathbf{K}^{gs}_k + \mathbf{K}^{ls}_k)\mathbf{g}
\end{aligned}\tag{38}$$

Heat energy equation

$$\begin{aligned}
&\left[\frac{1}{\Delta t}\mathbf{C}_T + \theta\mathbf{A}_T + \theta\mathbf{K}_T\right][\hat{\mathbf{T}}]^{n+1}\\
&\quad=\theta[Q_T]^{n+1}_\tau + (1-\theta)[Q_T]^n\\
&\quad+\left[\frac{1}{\Delta t}\mathbf{C}_T - (1-\theta)\mathbf{A}_T - (1-\theta)\mathbf{K}_T\right][\hat{\mathbf{T}}]^n
\end{aligned}\tag{39}$$

The equations above can be written more compactly as

$$\begin{aligned}
&\left[\frac{1}{\Delta t}\mathbf{C}_{Pa} + \mathbf{K}_{Pa}\right][\hat{\mathbf{p}}^g]^{n+1} + \left[\frac{1}{\Delta t}\mathbf{C}_{Sa}\right][\hat{\mathbf{S}}^l]^{n+1} = \mathrm{RHS}_a\\
&\left[\frac{1}{\Delta t}\mathbf{C}_{Pw} + \mathbf{K}_{Pw}\right][\hat{\mathbf{p}}^g]^{n+1} + \left[\frac{1}{\Delta t}\mathbf{C}_{Sw}\right][\hat{\mathbf{S}}^l]^{n+1} = \mathrm{RHS}_w\\
&\left[\frac{1}{\Delta t}\mathbf{C}_T + \mathbf{K}_T + \mathbf{A}_T\right][\hat{\mathbf{T}}]^{n+1} = \mathrm{RHS}_T
\end{aligned}\tag{40}$$

We introduce the following characteristic numbers to achieve a dimensionless form of the algebraic equations.

$$\begin{aligned}
&\text{Compressibility number } Cp^\gamma_g = \frac{S^\gamma X^\gamma_k \frac{\partial\rho^\gamma}{\partial p^\gamma}}{S^g_0 X^g_k \frac{\partial\rho^g}{\partial p^g}}\\
&\text{von Neu- mann number } Ne^\gamma_g = \frac{\rho^\gamma X^\gamma_k \frac{k^\gamma_{\mathrm{rel}}\mathbf{k}}{\mu^\gamma} S^g_0 X^g_k \frac{\partial\rho^g}{\partial p^g}}{(\Delta x)^2}\frac{\Delta t}{(\Delta x)^2}\\
&\text{Storativity number } St^\gamma_g = \frac{\rho^\gamma X^\gamma_k}{S^g_0 X^g_k \frac{\partial\rho^g}{\partial p^g}}\\
&\text{Diffusivity number } Di^\gamma_g = \frac{nS^\gamma\rho^\gamma D^\gamma_k}{S^g_0 X^g_k \frac{\partial\rho^g}{\partial p^g}}\frac{\Delta t}{(\Delta x)^2}
\end{aligned}\tag{41}$$

Now the fluid component equations (38) can be rewritten as

$$\begin{aligned}
&\left[\left(\frac{S^g}{S^g_0} + Cp^l_g\right) + \theta(Ne^g_g + Ne^l_g)\right][\hat{\mathbf{p}}^g]^{n+1}\\
&\quad+\left[\left(-St^g_g + St^l_g\right)\right][\hat{\mathbf{S}}^l]^{n+1}\\
&=\left[\left(\frac{S^g}{S^g_0} + Cp^l_g\right) - (1-\theta)(Ne^g_g + Ne^l_g)\right][\hat{\mathbf{p}}^g]^n\\
&\quad+\left[\left(-St^g_g + St^l_g\right)\right][\hat{\mathbf{S}}^l]^n + \left[Cp^l_g\right]([\hat{\mathbf{p}}_c]^{n+1} - [\hat{\mathbf{p}}_c]^n)\\
&\quad+\left[Ne^l_g\right](\theta[\hat{\mathbf{p}}_c]^{n+1} + (1-\theta)[\hat{\mathbf{p}}_c]^n)\\
&\quad-\left[Di^g_g\right](\theta[\hat{\mathbf{X}}^g_a]^{n+1} + (1-\theta)[\hat{\mathbf{X}}^g_a]^n) + (Ne^g_g + Ne^l_g)\mathbf{g}
\end{aligned}\tag{42}$$

4.2 Coupling schemes

There are different techniques to solve the coupled equation system (38) and (39): partitioned and monolithic

schemes, as well as combinations of both. The partitioned scheme means subsequent solution of individual equations embedded in an iteration scheme for the coupling,

$$\begin{aligned}
\left[\frac{1}{\Delta t}\mathbf{C}_{Pa}+\mathbf{K}_{Pa}\right][\hat{\mathbf{p}}^g] &= \mathrm{RHS}_a-\left[\frac{1}{\Delta t}\mathbf{C}_{Sa}\right][\hat{\mathbf{S}}^l]\\
\left[\frac{1}{\Delta t}\mathbf{C}_{Sa}\right][\hat{\mathbf{S}}^l] &= \mathrm{RHS}_w-\left[\frac{1}{\Delta t}\mathbf{C}_{Pa}+\mathbf{K}_{Pa}\right][\hat{\mathbf{p}}^g]\\
\left[\frac{1}{\Delta t}\mathbf{C}_{T}+\mathbf{K}_{T}+\mathbf{A}_{T}\right][\hat{\mathbf{T}}] &= \mathrm{RHS}_T
\end{aligned} \tag{43}$$

where

$$\mathbf{C}_{Pa}=\sum^{\gamma}\mathbf{C}_{P}^{\gamma}_{k}$$

The monolithic scheme means solution of all equations in a single step.

$$\begin{bmatrix}
\frac{1}{\Delta t}\mathbf{C}_{Pa}+\mathbf{K}_{Pa} & \frac{1}{\Delta t}\mathbf{C}_{Sa} & \\
\frac{1}{\Delta t}\mathbf{C}_{Pw}+\mathbf{K}_{Pw} & \frac{1}{\Delta t}\mathbf{C}_{Sw} & \\
 & & \frac{1}{\Delta t}\mathbf{C}_{T}+\mathbf{K}_{T}+\mathbf{A}_{T}
\end{bmatrix}
\bullet
\begin{bmatrix}\hat{\mathbf{p}}^g\\ \hat{\mathbf{S}}^l\\ \hat{\mathbf{T}}\end{bmatrix}
=
\begin{bmatrix}\mathrm{RHS}_a\\ \mathrm{RHS}_w\\ \mathrm{RHS}_T\end{bmatrix} \tag{44}$$

Due to the weak coupling between the flow and heat transport process, we use the following coupling scheme.

$$\begin{aligned}
&\begin{bmatrix}
\frac{1}{\Delta t}\mathbf{C}_{Pa}+\mathbf{K}_{Pa} & \frac{1}{\Delta t}\mathbf{C}_{Sa}\\
\frac{1}{\Delta t}\mathbf{C}_{Pw}+\mathbf{K}_{Pw} & \frac{1}{\Delta t}\mathbf{C}_{Sw}
\end{bmatrix}
\begin{bmatrix}\hat{\mathbf{p}}^g\\ \hat{\mathbf{S}}^l\end{bmatrix}
=
\begin{bmatrix}\mathrm{RHS}_a\\ \mathrm{RHS}_w\end{bmatrix}\\
&\left[\tfrac{1}{\Delta t}\mathbf{C}_{T}+\mathbf{K}_{T}+\mathbf{A}_{T}\right][\mathbf{T}]=[\mathrm{RHS}_T]
\end{aligned} \tag{45}$$

The multiphase flow problem is handled with a monolithic scheme, whereas the heat transport problem is treated separately. This reflects the strong coupling of the multiphase flow and a weaker coupling between flow and heat transport. The non-linearities in the above equations are resolved using a Picard fixpoint iteration scheme (e.g. [23]).

Appendix II shows the algebraic equations for the partitioned and monolithic coupling schemes.

4.3 Code implementation

Object-oriented (OO) methods become more and more important in scientific computing in order to develop software in teams, and to be able to extend the code continuously for new applications [30].

RF/RM is based on object-oriented principles programmed in C-objective and C++. The code consists of a collection of independent units (objects) with specific purposes in order to solve initial-boundary-value multi-field problems (Table 3).

As a result of the numerical approximation method, a set of a algebraic equations can be derived.

$$\mathbf{A}_i(t,\mathbf{x},\mathbf{u}_i,\mathbf{u}_j)\mathbf{u}_i=\mathbf{b}_i(t,\mathbf{x},\mathbf{u}_i,\mathbf{u}_j) \tag{46}$$

where i,j denote different processes, with $\mathbf{A}_i$ system matrix of process i, t time, $\mathbf{x}$ coordinates, $\mathbf{u}_i$ solution vector (primary variable) of process i, $\mathbf{b}_i$ right-hand-side (RHS) vector of process i. Dependence of process i on process j means coupling, and dependence of system matrix on solution itself means non-linearity.

The idea is that required data and algorithms to solve algebraic equation systems can be generalized: (1) initialize equation system and solution vector (IC), (2) calculate element matrices, (3) assemble equation system, (4) incorporate boundary conditions and source terms, (5) solve equation system, (5) calculate secondary variables, (6) store results for next iteration / step. In addition to object-orientation, we introduce an process-orientated concept [24]. Processes (PCS objects) can handle the complete solution procedure of PDEs. The most important methods are given below:

```
1 - void CRFProcess::PCSCreateProcesses(void)
2 - void CRFProcess::PCSConfigProcess(int
      pcs_type)
3 - void CRFProcess::PCSExecuteProcess(EQUA-
      TION_SYSTEM *pcs_eqs)
```

The first step (1) is creating the data structures of PCS, which is basically the equation system (EQS) and pointer to basic objects (3). Depending on the type of process (e.g. flow, mass or heat transport, deformation) the PCS object is configured (2). In this step virtual PCS functions are overwritten, i.e. a specific function to calculate element matrices for two-phase/two-componental flow is selected. The processes created are inserted into a list, which is the

Table 3. RF/RM objects

Acronym	Subject	Examples
GEO	geometric objects	points, polylines, surfaces, volumes
ELE	elements	different finite element types
IC	initial conditions	$u_i(t=0,x)$
BC	boundary conditions	$u_i(t,x=b)$
ST	source terms	$\nabla u_i(t,x=b)$
MAT	materials	fluid, solid, porous medium properties
NUM	numerics	parameter of numerical method
TIM	time	parameter of time discretization
KER	kernel	finite element matrices
EQS	equation system	system matrix, solution vector, RHS vector

last step of the pre-processing part. In the processing part, PCS instances are executed (3) with the general steps described above but with specified properties and methods. In the case of coupled multi-field problems (such as non-isothermal two-phase flow) we have to consider the process interactions.

Object-orientation allows the combination of flow, transport, and deformation modules, based on the same data structures. This allows a wide field of application.

5
Examples

Three examples are presented here. The first example shows a desaturation process in a simple 1-D case. The aim of this example is to compare the three models presented in this paper. The second example serves to compare RF/RM to experimental results, and to compare calculations using 1-D and 2-D elements. The third example includes desaturation and resaturation in a 2-D setup.

5.1
Example 1–low permeability desaturation process

5.1.1
Problem description

This example is to qualitatively test the effect of the large capillary pressures up to 10^{10} Pa occurring in extremely low-permeable bentonite materials (Fig. 3). Also, we compare the different coupling schemes for solving the set of coupled equations (Sect. 2). For this purpose we start with a simple 1-D case. A one meter long bentonite column is heated on the left hand side. Element discretization length is $\Delta x = 0.01$ m. The initial conditions of the system are: atmospheric gas pressure, full liquid saturation and a temperature of 12 °C. The heater has a constant temperature of 100 °C. Flow boundary conditions on the left side are gas pressure of 10^6 Pa and 15% liquid saturation. On the right side we have atmospheric pressure, full liquid saturation and no diffusive heat flux. As a consequence, a typical desaturation process of bentonite is triggered. The complete set of initial and boundary conditions is given in Fig. 2. The material properties for this example are summarized in Table 4. Figure 3 shows the capillary pressure–saturation relationship.

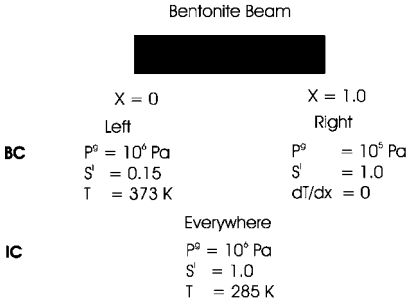

Fig. 2. Example initial and boundary conditions

5.1.2
Results and discussion

The series of Figs. 4, 5, 6 shows calculated profiles along the bentonite beam at several time stages, $t = 10^3$ to 10^5 s for the Richards model, the partitioned, and monolithic schemes of the multiphase-multicomponental (TH^2/M) model. All the depicted results in this series are calculated using the Börgesson swelling model. The benchmark results with all three models show how the saturation front moves from left to right, and how temperature moves towards a linear distribution. Flow dynamics results are illustrated by Figs. 4a, b, c; 5a, b, c; 6a, b, c. In these figures pressure and saturation curves illustrate the desaturation process, i.e the advance of the gas phase front from the left to the right side. As usual for multiphase systems, there is the typical sharp saturation front in the beginning, which becomes smoother with time. Figures. 4d, 5d, and 6d show temperature evolution along the bentonite column. The temperature distribution is nearly the same for all models. This is due to heat diffusion being the dominating transport mechanism. Heat advection and dispersion are very small in a low-permeable medium. Figs. 4e, f; 5e, f; and 6e, f illustrate component (air, water) transport. Componental mass fractions depend on both, temperature and gas pressure distributions. Vapour mass in the gas phase X_w^g and dissolved air mass in the liquid phase X_a^l are secondary variables, which are calculated according to Eqs. (15) and (11), respectively.

Between the partitioned and monolithic scheme there are not many differences, as may be expected. There is a slight undershooting of the gas pressure in the partitioned scheme, which is be due to the partitioned coupling scheme. This shows that the partitioned scheme is not as accurate as the monolithic scheme. The undershooting has repercussions on the values of the mass fractions. For both coupling schemes, it can be seen that the mass fractions are influenced by gas pressure where it is above atmospheric and then temperature dominates the mass fraction term.

This is also where the main difference with the Richard's approximation resides. Since the gas pressure is kept at atmospheric pressure in that case, only temperature effects are seen in the mass fractions. Hence, phase transitions are not taken into account. At a temperature of 100 °C and pressure of 101325 Pa the gas phase is fully saturated with water vapour $X_w^l = 1$. However, at gas pressures of 10^6 Pa, as often used in laboratory experiments, the water vapour mass fraction at a temperature of 100 °C is equal to $X_w^l = 0.065$. This emphasizes the necessity to take the gas phase dynamics into account. The different advances of the gas pressure and temperature fronts result in peaks of vapour mass fraction at the gas pressure front.

There are differences in the evolution of capillary pressure with time for the Richards model and the TH^2/M

Table 4. Material properties

Symbol	Meaning	Value/Ref	Unit
Fluid properties			
ρ^g	Gas density	Eq (19)	kg/m^3
β_p^g	Gas compress. coeff.	6.67×10^{-6}	Pa^{-1}
ρ^l	Liquid density	Eq (17)	kg/m^3
β_p^l	Liq. compress. coeff.	4.70×10^{-7}	Pa^{-1}
μ^g	Gas viscosity	1.8×10^{-5}	Pa\s
μ^l	Liquid viscosity	1.2×10^{-3}	Pa\s
c^g	Gas heat capacity	1.01×10^3	
c^l	Liquid heat capacity	4.2×10^3	
λ^g	Gas heat conductivity	0.026	W/(m\K)
λ^l	Liquid heat conductivity	0.6	W/(m\K)
Medium properties			
ρ	Density	1830	kg/m^3
n	Porosity	0.407	
c	Heat capacity	1.6×10^3	
λ	Heat conductivity	0.718	W/(m\K)
k	Permeability	8.23×10^{-20}	m^2
p_c	Capillary pressure	Eq (24) Fig. 3	Pa
k_{rel}	Relative permeability	Eq (27, 28)	

models. The differences of the advance of saturation and capillary pressure fronts indicate additional mechanisms for fluid redistribution. Firstly, the additional fluid transport is a result of componental diffusion effects. Secondly, there are evaporation effects due to the advance of the thermal front. Both of these effects are not taken into account by the Richard's approximation.

In this case it can be observed that the Richard's approximation gives very similar results for saturation and temperature. Should one be interested in phase changes and mass fractions, the Richards's approximation would give an incomplete illustration. The applicability of the Richard's approximation remains thus one of scope and aim of the calculation.

Figure 7 shows a comparison between the Richard's approximation run with and without the Börgesson swelling model. With the swelling model, the saturation curve gets a second point of inflection and the desaturation process is much more rapid. This phenomenon is due to the pore space reduction in the swollen bentonite, which causes a swelling pressure that squeezes the water out.

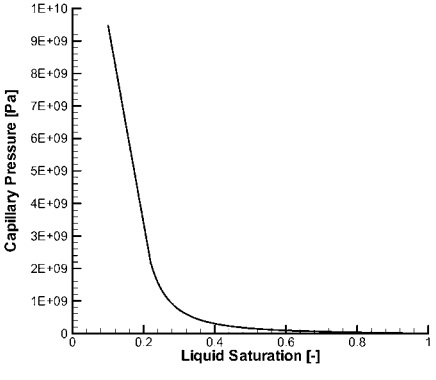

Fig. 3. Capillary pressure as function of liquid saturation $p_c(S^l)$

5.2 Example 2–desaturation by evaporation

5.2.1 Problem description

This test case is based on an example proposed by [37]. This example portrays the desaturation of a bentonite sample due to heating in a closed system. The set-up is as illustrated in Fig. 8.

The corresponding material parameters are as summarized in Table 5.

Because the capillary pressures in bentonite are very high (up to 10^4 MPa, as shown in Fig. 9), a large suction pressure is initiated, that strongly favors saturation of the sample from the open side (at the right). Vapor movement, and hence desaturation due to sample heating can only be modelled if vapor flow is encouraged. This is due to the vapour diffusion term of the balance equation for fluid masses (air and water components).

[37] were introducing a dual relative permeability model, i.e. different relative permeabilities for gases and liquids, so that vapor movement is favored at low liquid phase saturations (S^l), when capillary pressure is highest. This dual permeability model is based on experimental evidence for bentonite. The reason behind it is, that in the dry bentonite accessible pore spaces are larger resulting in higher permeability. When bentonite is wet however, it swells and pore spaces are reduced accordingly. Figure 9 (right) shows an example of such a dual relative permeability model for bentonite used in this study.

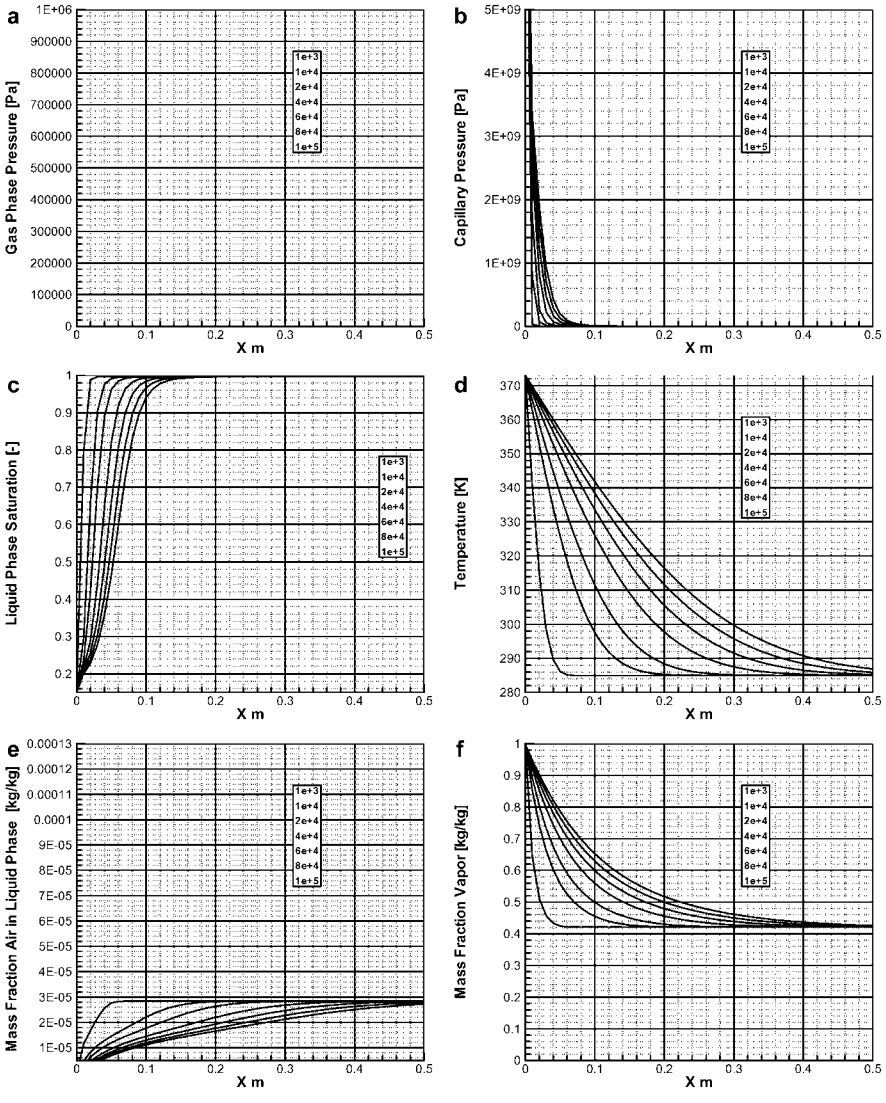

Fig. 4. Computation results for example 1 using the Richard's model

5.2.2 Results and discussion

Because there are no saturation and pressure boundary conditions in the example, these parameters are free to fall and rise. This can be observed in the results shown in Fig. 10b. From the initial liquid phase saturation of 0.4, the value drops progressively next to the heater, as expected. On the right boundary, where temperature is maintained at 30 °C, the effects of capillary pressure can be seen through the higher value of liquid phase saturation. Gas phase pressure shows a small response to the saturation distribution. Where liquid saturation drops,

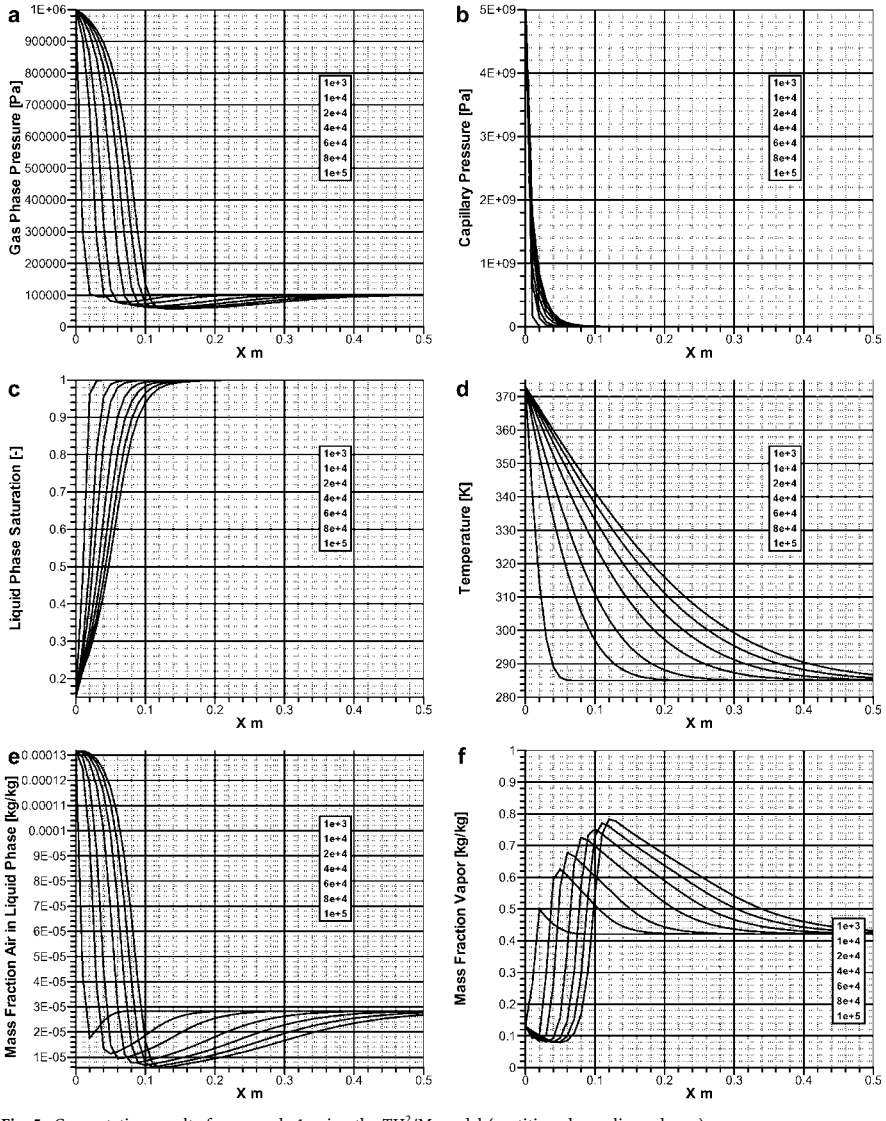

Fig. 5. Computation results for example 1 using the TH^2/M model (partitioned coupling scheme)

and by reciprocity gas saturation increases, gas pressure also increases. At the right boundary, the decrease in gas pressure corresponds to the increase in liquid saturation (Fig. 10a). One can see that the stationary temperature is reached in less than 0.5 days (Fig. 10c). Vapor mass fraction responds to the temperature distribution immediately.

The results thus show successful modeling of a desaturation process in bentonite due to evaporation, by using the TH^2/M model. We obtained very similar results

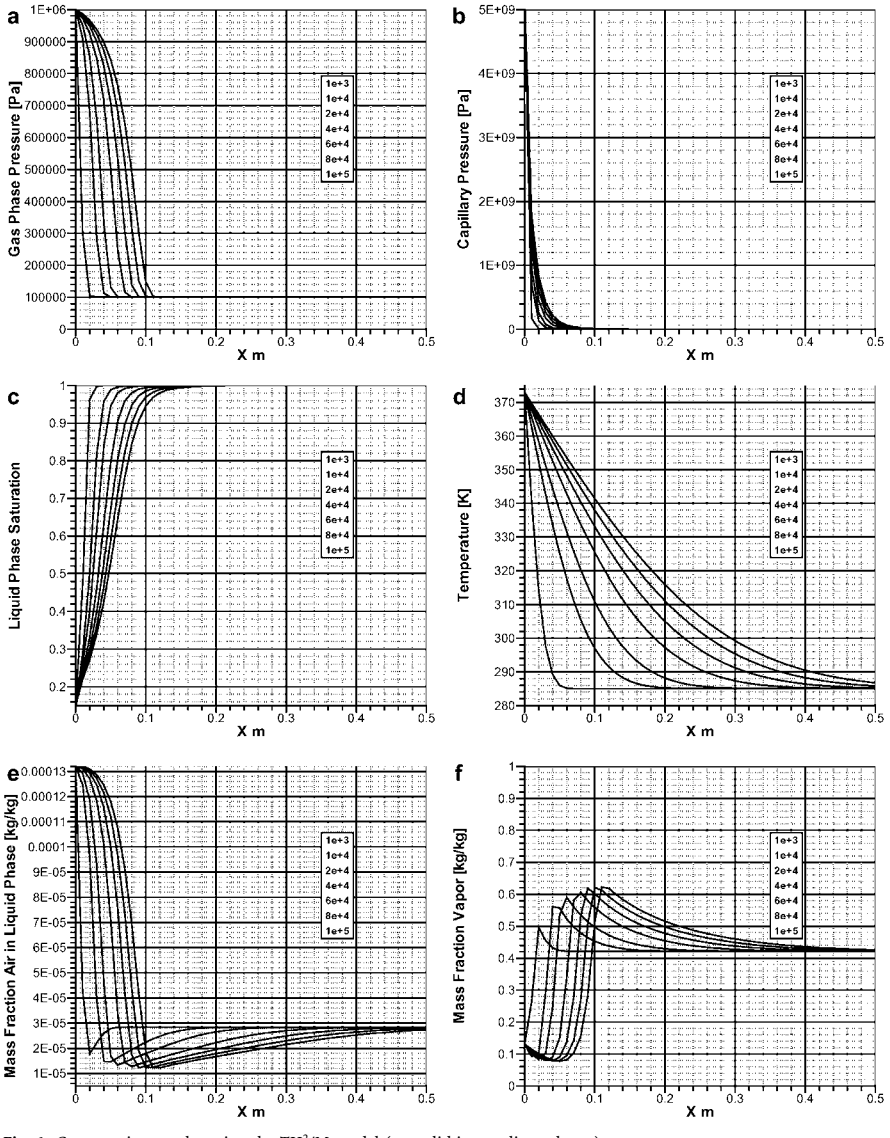

Fig. 6. Computation results using the TH^2/M model (monolithic coupling scheme)

as the experimental results shown in [37], as illustrated in Figs. 10b. Additionally, we used this benchmark to check different element types for TH^2/M processes. We obtain identical results for different element types (bar, triangular, quadrilateral elements) which serves as a verification test for element implementations.

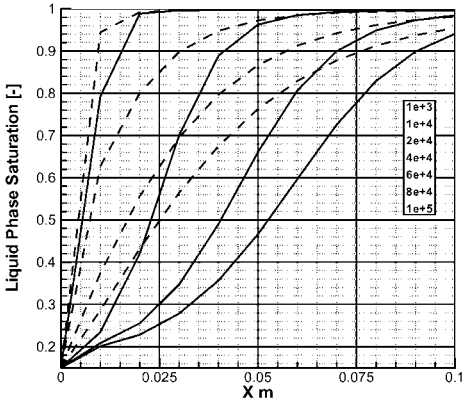

Fig. 7. Comparison of liquid phase saturation with (line) and without (dashed line) the Börgesson swelling model

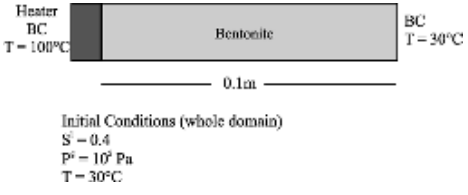

Fig. 8. Definition of the test case

5.3
Example 3–Desaturation/re-saturation of bentonite sample

5.3.1
Problem description

This 2-D example shows desaturation and resaturation processes in the near-field of heat emitting containments. The example shows that qualitatively the code is able to reproduce these processes. In an x-z plane, a heating element is modelled at the left hand side. At the lower border a fracture is modelled by placing a fully liquid phase saturated boundary condition. This setup is illustrated in Figure 11. Material parameters are same as in Example 2 (Table 5).

5.3.2
Results and Discussion

Figure 12 shows the temporal evolution of liquid saturation, as well as temperature and gas pressure patterns. There are two interesting regions. Firstly, near the heater there is desaturation due to evaporation and vapor diffusion. Secondly, the fracture supplies liquid water into the system which is transported to the heater due to capillary forces. The desaturation near the heater results in increased suction. After 5×10^5 the heater area is almost flooded by liquid water delivered from the fracture.

Table 5. Material properties

Parameter	Unit	Value
Porosity	[m^3/m^3]	0.44
Permeability	[m^2]	5×10^{-19}
Relative permeability	[–]	Figure 9
Capillary pressure	[–]	Figure 9
Bentonite density	[kg/m^3]	1650
Bentonite heat capacity	[J/kgK]	1605
Bentonite heat conductivity	[J/Kms]	0.5

Due to this increased suction, water supplied by the fracture is forced upward towards the less liquid saturated region. As the water recharge is good, the area saturates progressively. In regions of OP1 and OP2, it can be seen from Fig. 12a, that saturation rises constantly from the initial low liquid saturation. This region is not affected by the heater and thus does not show any desaturation. At observation points OP3, OP6, OP7 and OP8 this is not the case. Here desaturation precedes resaturation. The amount of desaturation is in direct proportion with distance to the heater and inversely distance from the fracture. Temperature shown in Fig. 12e propagates in a wave-like manner around the heating element and is not influenced by the fracture. Gas pressure on the other hand is only minimally influenced by the heater, but strongly influenced by the fracture. The minimal influence of the heater can be observed by the slope against horizontal of the gas pressure front.

6
Summary and conclusions

We presented a finite element model for non-isothermal two-phase flow in porous media. This model accounts for flow of liquid-gas systems including phase changes (evaporation/condensation and gas solution/dissolution) as well as for swelling processes. The algebraic equations of the multi-field problem resulting from the method of weighted residuals can be solved in a sequential way (partitioned algorithm) and in one step (monolithic algorithm). We introduced a dimensionless formulation in order to improve the conditioning of the system matrix. This numerical formulation also substantially improved the convergence behavior.

The first example showed the comparison between the coupling schemes mentioned above and the Richard's approximation. The example results demonstrated that

- The monolithic coupling scheme is more correct and precise for calculation of gas phase pressure.
- Results for the multiphase/multicomponental formulation and the Richard's approximation give similar results, except for the calculation of mass fractions.
- The adequacy of the Richard's approximation is for this example, one of scope.
- Incorporating swelling effects makes a significant difference in the saturation profile.

The second example allowed verification against experimental results and comparison between numerical

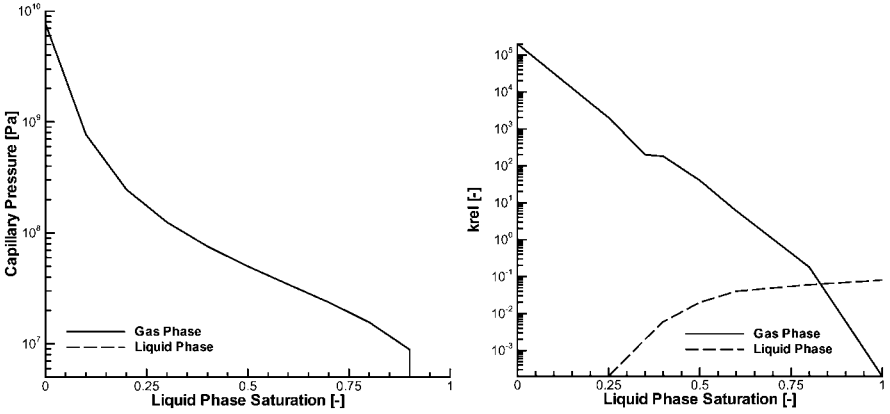

Fig. 9. Capillary pressure–saturation relationship (left), Dual relative permeability–saturation relationships (right)

elements in one and two dimensions. The final example, was a two-dimensional one and showed qualitative results for the mutual influence of desaturation and saturation processes.

While there is still scope for code improvement, we believe that these examples show that the existing code is able to faithfully reproduce situations encountered in low-permeable porous media under non-isothermal conditions, where the scope is to model the thermal and hydraulic processes.

Appendix I: FE formulations

We use the method of weighted residuals to derive the weak forms of the differential field equations for gas fluid pressure, liquid saturation and temperature. The unknown functions are approximated by trial solutions $(\hat{p}^g, \hat{S}^l, \hat{T})$ based on nodal values $(\hat{p}_i^g, \hat{S}_i^l, \hat{T}_i)$ and interpolation functions (N_i).

$$\hat{p}^g = \sum_i N_i \hat{p}_i^g \quad , \quad \hat{S}^l = \sum_i N_i \hat{S}_i^l \quad ,$$
$$\hat{T} = \sum_i N_i \hat{T}_i \tag{47}$$

In order to reduce the order of spatial derivatives we use the Gauss-Ostrogradskian integral theorem. Time derivatives are approximated by finite differences. Based on the model equations (34), (36), (37) we yield the following weak forms for the determination of the primary variables.

Fluid component equation

Primary variables are $\hat{\mathbf{p}}^g$ and $\hat{\mathbf{S}}^l$, where e.g $(\hat{\mathbf{p}}^g)^T = [\hat{p}_1^g \hat{p}_2^g \dots \hat{p}_i^g]$ is node vector of gas pressures.

$$\left[\int_\Omega \mathbf{N}^T \left(n S_k^g X_k^g \frac{\partial \rho^g}{\partial p^g} + n S^l X_k^l \frac{\partial \rho^l}{\partial p^l} \right) \mathbf{N} \mathrm{d}\Omega \right] \left[\frac{\mathrm{d}\hat{\mathbf{p}}^g}{\mathrm{d}t}\right]$$
$$+ \left[\int_\Omega \nabla \mathbf{N}^T \left(\rho^g X_k^g \frac{k_{\mathrm{rel}}^g \mathbf{k}}{\mu^g} + \rho^l X_k^l \frac{k_{\mathrm{rel}}^l \mathbf{k}}{\mu^l} \right) \nabla \mathbf{N} \mathrm{d}\Omega \right] [\hat{\mathbf{p}}^g]$$
$$- \left[\int_\Omega \mathbf{N}^T \left(n \rho^g X_k^g - n \rho^l X_k^l \right) \mathbf{N} \mathrm{d}\Omega \right] \left[\frac{\mathrm{d}\hat{\mathbf{S}}^l}{\mathrm{d}t}\right]$$
$$= \int_\Omega \mathbf{N}^T Q_k \mathrm{d}\Omega + \left[\int_\Omega \mathbf{N}^T \left(n S^l X_k^l \frac{\partial \rho^l}{\partial p^l} \right) \mathbf{N} \mathrm{d}\Omega \right] \left[\frac{\mathrm{d}\hat{\mathbf{p}}_c}{\mathrm{d}t}\right]$$
$$+ \left[\int_\Omega \nabla \mathbf{N}^T \left(\rho^l X_k^l \frac{k_{\mathrm{rel}}^l \mathbf{k}}{\mu^l} \right) \nabla \mathbf{N} \mathrm{d}\Omega \right] [\hat{\mathbf{p}}_c]$$
$$- \left[\int_\Omega \nabla \mathbf{N}^T (n S^g \rho^g X_k^g D_k^g) \nabla \mathbf{N} \mathrm{d}\Omega \right] [\hat{\mathbf{X}}_k^g]$$
$$- \int_\Omega \nabla \mathbf{N}^T \left(\rho^g X_k^g \frac{k_{\mathrm{rel}}^g \mathbf{k}}{\mu^g} \rho^g \mathbf{g} + \rho^l X_k^l \frac{k_{\mathrm{rel}}^l \mathbf{k}}{\mu^l} \rho^l \mathbf{g} \right) \mathrm{d}\Omega \tag{48}$$

Heat energy equation

Primary variable is $\hat{\mathbf{T}}$

$$\left[\int_\Omega \mathbf{N}^T \left((1-n) \rho^s c^s + n \rho^g c^g + n \rho^l c^l \right) \mathbf{N} \mathrm{d}\Omega \right] \left[\frac{\mathrm{d}\hat{\mathbf{T}}}{\mathrm{d}t}\right]$$
$$+ \left[\int_\Omega \mathbf{N}^T \left(n \rho^g \mathbf{J}^{gs} + n \rho^l \mathbf{J}^{ls} \right) \nabla \mathbf{N}^T \mathrm{d}\Omega \right] [\hat{\mathbf{T}}]$$
$$+ \left[\int_\Omega \nabla \mathbf{N}^T \left((1-n) \lambda^s + n \lambda^g + n \lambda^l \right) \nabla \mathbf{N} \mathrm{d}\Omega \right] [\hat{\mathbf{T}}]$$
$$= \int_\Omega \mathbf{N}^T Q_t \mathrm{d}\Omega \tag{49}$$

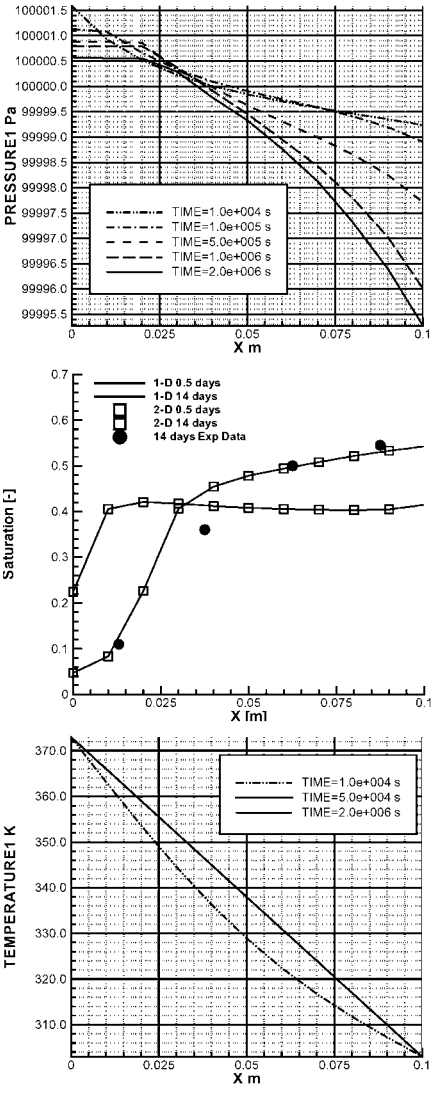

Fig. 10. Profiles along the buffer material: gas pressure, liquid saturation, temperature (from top to bottom) for time points between 10^4 s and 14 days

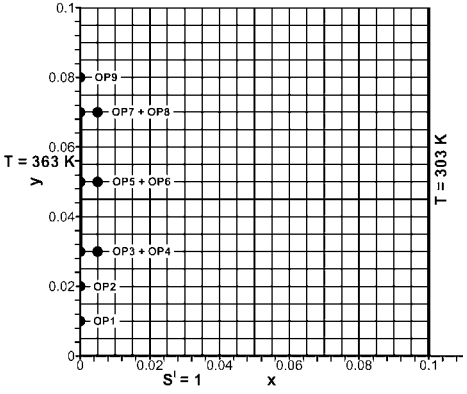

Fig. 11. Geometry and boundary conditions of example 3

$$\left[\left(\frac{S^g}{S_0^g}+Cp_g^l\right)+\theta(Ne_g^g+Ne_g^l)\right][\hat{\mathbf{p}}^g]^{n+1}$$
$$=\left[\left(\frac{S^g}{S_0^g}+Cp_g^l\right)-(1-\theta)(Ne_g^g+Ne_g^l)\right][\hat{\mathbf{p}}^g]^n$$
$$-\left[\left(-St_g^g+St_g^l\right)\right]([\hat{\mathbf{S}}^l]^{n+1}-[\hat{\mathbf{S}}^l]^n)$$
$$+\left[Cp_g^l\right]([\hat{\mathbf{p}}_c]^{n+1}-[\hat{\mathbf{p}}_c]^n)+\left[Ne_g^l\right](\theta[\hat{\mathbf{p}}_c]^{n+1}$$
$$+(1-\theta)[\hat{\mathbf{p}}_c]^n)-\left[Di_g^g\right](\theta[\hat{\mathbf{X}}_a^g]^{n+1}+(1-\theta)[\hat{\mathbf{X}}_a^g]^n)$$
$$+(Ne_g^g+Ne_g^l)\mathbf{g} \qquad (50)$$

Water component equation ($k=a$) for determination of S^l

$$\left[\left(-St_g^g+St_g^l\right)\right][\hat{\mathbf{S}}^l]^{n+1}=\left[\left(-St_g^g+St_g^l\right)\right][\hat{\mathbf{S}}^l]^n$$
$$-\left[\left(Cp_g^g+Cp_g^l\right)\right]([\hat{\mathbf{p}}^g]^{n+1}-[\hat{\mathbf{p}}^g]^n)$$
$$-\left[\left(Ne_g^g+Ne_g^l\right)\right](\theta[\hat{\mathbf{p}}^g]^{n+1}-(1-\theta)[\hat{\mathbf{p}}^g]^n)$$
$$+\left[Cp_g^l\right]([\hat{P}_c]^{n+1}-[\hat{P}_c]^n)+[Ne_l^l](\theta[\hat{P}_c]^{n+1}+(1-\theta)[\hat{P}_c]^n)$$
$$-\left[Di_g^g\right](\theta[\hat{\mathbf{X}}_a^g]^{n+1}+(1-\theta)[\hat{\mathbf{X}}_a^g]^n)+(Ne_l^g+Ne_l^l)\mathbf{g} \quad (51)$$

Appendix II: coupling Schemes

Partitioned TH²/M Scheme
Air component equation ($k=a$) for determination of p^g

Monolithic TH²/M Scheme
Air component equation ($k=a$)

$$\left[\left(\frac{S^g}{S_0^g}+Cp_g^l\right)+\theta(Ne_g^g+Ne_g^l)\right][\hat{\mathbf{p}}^g]^{n+1}$$
$$+\left[\left(-St_g^g+St_g^l\right)\right][\hat{\mathbf{S}}^l]^{n+1}$$
$$=\left[\left(\frac{S^g}{S_0^g}+Cp_g^l\right)-(1-\theta)(Ne_g^g+Ne_g^l)\right][\hat{\mathbf{p}}^g]^n$$
$$+\left[\left(-St_g^g+St_g^l\right)\right][\hat{\mathbf{S}}^l]^n$$

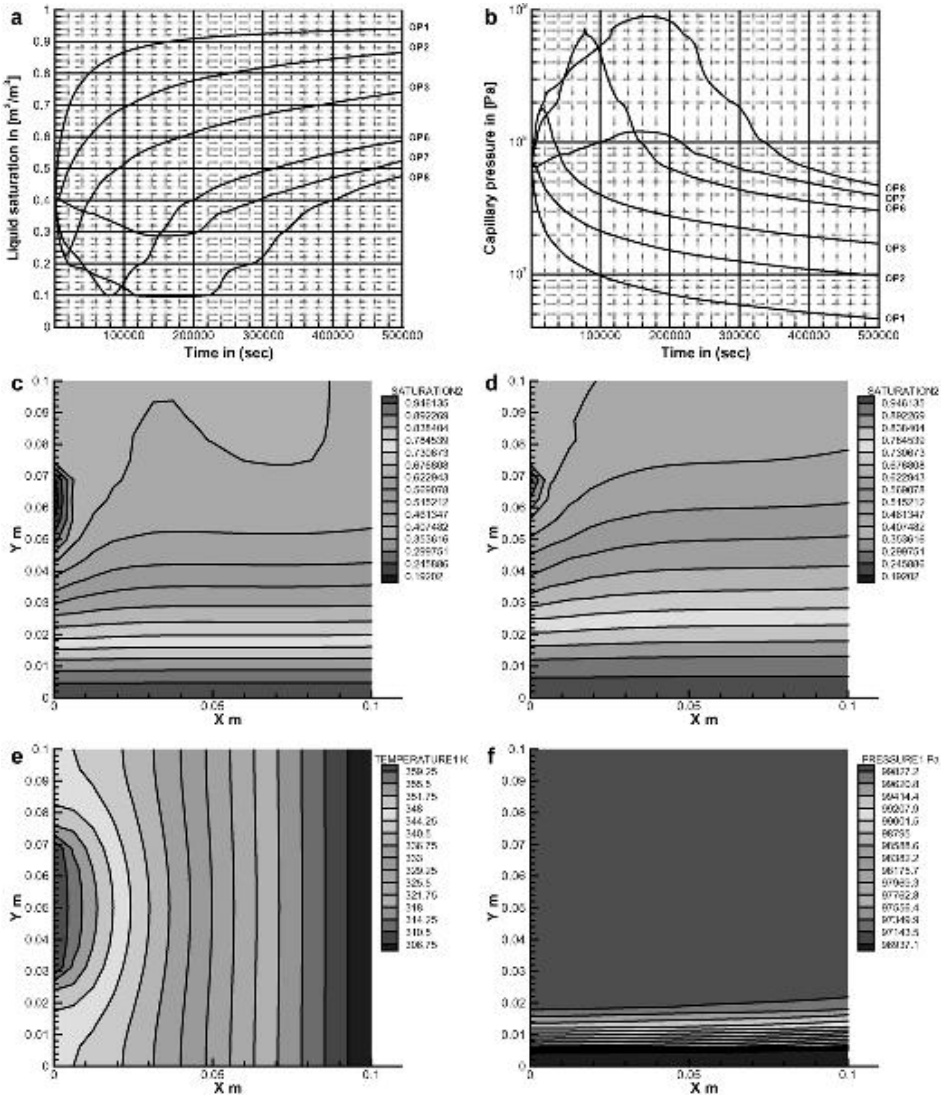

Fig. 12. TH²/M processes in bentonite: **a**, **b** Profiles over time of liquid phase saturation and capillary pressure, **c**, **d** liquid saturation at $10^5, 5 \times 10^5$ s, **e**, **f**, temperature and gas pressure at 5×10^5 s

$$+ \left[Cp_g^l\right]([\hat{\mathbf{p}}_c]^{n+1} - [\hat{\mathbf{p}}_c]^n) + \left[Ne_g^l\right](\theta[\hat{\mathbf{p}}_c]^{n+1} + (1-\theta)[\hat{\mathbf{p}}_c]^n) - \left[Di_g^g\right](\theta[\hat{\mathbf{X}}_a^g]^{n+1} + (1-\theta)[\hat{\mathbf{X}}_a^g]^n) + (Ne_g^g + Ne_g^l)\mathbf{g} \tag{52}$$

Water component equation ($k = a$)

$$\begin{aligned}
&\left[\left(\frac{S^g}{S_0^g}+Cp_g^l\right)+\theta(Ne_g^g+Ne_g^l)\right][\hat{\mathbf{p}}^g]^{n+1}\\
&\quad+\left[(-St_g^g+St_g^l)\right][\hat{\mathbf{S}}^l]^{n+1}\\
&=\left[\left(\frac{S^g}{S_0^g}+Cp_g^l\right)-(1-\theta)(Ne_g^g+Ne_g^l)\right][\hat{\mathbf{p}}^g]^n\\
&\quad+\left[(-St_g^g+St_g^l)\right][\hat{\mathbf{S}}^l]^n\\
&\quad+\left[Cp_g^l\right]([\hat{\mathbf{p}}_c]^{n+1}-[\hat{\mathbf{p}}_c]^n)+\left[Ne_g^l\right](\theta[\hat{\mathbf{p}}_c]^{n+1}+(1-\theta)[\hat{\mathbf{p}}_c]^n)\\
&\quad-\left[Di_g^g\right](\theta[\hat{\mathbf{X}}_a^g]^{n+1}+(1-\theta)[\hat{\mathbf{X}}_a^g]^n)\\
&\quad+(Ne_g^g+Ne_g^l)\mathbf{g}
\end{aligned}\tag{53}$$

References

1. **Abe H, Sekine H, Shibuya Y** (1983) Thermoelastic analysis of a cracklike reservoir in a hot dry rock during extraction of geothermal energy. J. Energy Resour. Techn. 105: 503–508
2. **Alonso EE, Gens A, Hight DW** (1987) Special problem soils: general report. In Proc. 9th European Conf. on soil mechanics and foundation engineering, vol 3 Rotterdam, Balkema
3. **Bear J** (1972) Dynamics of fluids in porous media. Elsevier, New York
4. **Biot MA** (1941) General theory of three-dimensional consolidation. J. Appl. Phys. 12: 155–164
5. **Bodvarsson GS, Tsang CF** (1982) Injection and thermal breakthrough in fractured geothermal reservoirs. J. Geophys. Res. 87(B2): 1031–1048
6. **Börgesson L** (1985) Water flow and swelling pressure in non-saturated bentonite-based clay barriers. Eng. Geology 314: 229–237
7. **Börgesson L, Johannesson LE, Sanden T, Herneling H** (1995) Modelling of the physical behavior of water sturated clay barriers–laboratory tests, material models and finite elemt application. Technical Report 95, SKB. 20
8. **Borsetto M, Cricci D, Hueckel T, Peano A** (1984) On numerical models for the analysis of nuclear waste disposal in geologic clay formations. In: Lewis RW (ed) Numerical Methods for Transient and Coupled Problems, Swansea, Pineridge Press
9. **Class H, Helmig R, Bastian P** (2002) Numerical simulation fo nonisothermal multiphase multicomponent processes in porous media – 1. an efficient solution technique. Adv. Water Resour. 25: 533–550
10. **De Jonge J, Kolditz O** (2002) Non-isothermal flow processes in porous media, part I : governing equations and finite element implementation. Rockflow-Report 2002-1, Centre of Applied Geosciences, University of Tübingen
11. **Falta RW, Pruess K, Javandel I, Witherspoon PA** (1992a) Numerical modeling of steam injection for the removal of nonaqueous phase liquids from the subsurface – 2. code validation and application. Water Resour. Res. 28(2): 451–465
12. **Falta RW, Pruess K, Javandel I, Witherspoon PA** (1992b) Numerical modeling of steam injection for the removal of nonaqueous phase liquids from the subsurface – 1. numerical formulation. Water Resour. Res. 28(2): 433–449
13. **Forsyth PA** (1991) A control volume finite element approach to NAPL groundwater contamination. Siam J. Sci. Stat. Comput. 12(5): 1029–1057
14. **Forsyth PA** (1993) Three dimensional modeling of steam flush for DNAPL site remediation. Technical report CS-93-56, Department of Comupter Science, University of Waterloo
15. **Forsyth PA, Shao BY** (1991) Numerical simulation of gas venting for napl site remediation. Adv. Water Resour. 14: 354–367
16. **Gawin D, Baggio P, Schrefler BA** (1995) Coupled heat, water and gas flow in deformable porous media. Int. J. Numer. Meth. Fluids 20: 969–987
17. **Gens A, Garcia-Molina AJ, Olivella S, Alonso EE, Huertas F** (1998). Analysis of a full scale in-situ test simulating repository conditions. Int. J. Anal. Numer. Meth. Geomech. 22: 515–548
18. **Geraminegad M, Saxena SK** (1986) A coupled thermoelastic model for saturated-unsaturated porous media. Géotechnique 36: 539–550
19. **Guvanasen V, Huyakorn PS** (1986) Finite element simulation of fluid and energy transport in deformable fractured porous media. In: Proc. VI Int. Conference on Finite Elements in Water Resources
20. **Helmig R** (1997) Multiphase flow and transport processes in the subsurface. Springer, Berlin
21. **Kanno T, Fujita T, Ishikawa H, Hara K, Nakano M** (1999) Coupled thermo-hydro-mechanical modelling of bentonite buffer material. Int. J. Numer. Anal. Meth. Geomech. 23: 1281–1307
22. **Kolditz O** (2001) Non-linear flow in fractured rock. Int. J. Numer. Meth. Heat Fluid Flow 11(6): 547–575
23. **Kolditz O** (2002) Computational methods in environmental fluid mechanics. Springer Publisher
24. **Kolditz O, Bauer S** (2003) A process-oriented approach to compute multi-field problems in porous media. Accepted by J. Hydroinformatics.
25. **Kolditz O, Bauer S, Beinhorn M, de Jonge J, Kalbacher T, McDermott C, Wang W, Xie M, Kaiser R, Kohlmeier M** (2003) Rockflow – theory and users manual, release 3.9. Technical report, Groundwater modeling group, Center for Applied Geosciences, University of Tübingen, Institute of Fluid Mechanics, University of Hannover
26. **Korsawe J, Perau E, Potthoff S, Starke G** (2000) Numerical approximation of water-air two-phase flow by the mixed finite element method. To appear in Computers and Geotechnics, Revised version of May 2003
27. **Lewis RW, Roberts PJ, Schrefler BA** (1989) Finite element modelling of two-phase heat and fluid flow in deforming porous media. Transport Porous Media 4: 319–334
28. **Lewis RW, Schrefler BA** (1998) The finite element method in the static and dynamic deformation and consolidation of porous media. Wiley
29. **Lippmann MJ, Narasimham TN, Witherspoon PA** (1976) Numerical simulation of reservoir compaction in liquid-dominated geothermal systems. In Proc. 2nd Int. Symposium Land Subsidence, pp. 179–189. IAHS
30. **Masters I, Cross JT, Lewis RW**(1997) A review of object oriented programming techniques in finite element methods. In Intnernational Conference for Numerical Methods in Thermal Problems, pp. 1001–1009. Pineridge Press
31. **McClintock RB, Silvestri GJ** (1968) Formulations and iterative procedures for the calculation of properties of steam. The American Society of Mechanical Engineers
32. **McClintock RB, Silvestri GJ** (1970) Some improved steam property calculation procedures. J. Eng. Power
33. **Noorishad J, Ayaollahi MS, Witherspoon P** (1982) A finite-element method for coupled stress and fluid flow analysis in fractured rock masses. Int. J. Rock Mech. Min. Sci. 19: 185–193
34. **Noorishad J, Tsang CF** (1987) Simulation of coupled thermal-hydraulic-mechanical interactions in fluid injection into fractured rocks. In: Tsang, CF (ed.), Coupled processes associated with nuclear waste repositories. San Diego, CA
35. **Noorishad J, Tsang CF, Witherspoon PA** (1984) Coupled thermal-hydraulic-mechanical phenomena in saturated

fractured porous rocks: numerical apporach. J. Geophys. Res. 89(B12): 10365–10373
36. **Olivella S, Carrera J, Gens A, Alonso EE** (1994) Non-isothermal multiphase flow of brine and gas through saline media. Transport Porous Media 15: 271–293
37. **Olivella S, Gens A** (2000) Vapour transport in low permeability unsaturated soil with capillary effects. Transport Porous Media 40: 219–241
38. **Pollock DW** (1986) Simulation of fluid flow and energy transport processes associated with high–level riadioactive waste disposal in unsaturated alluvium. Water Resour. Res. 22(5): 765–775
39. **Pruess K** (1987) Tough user's guide. Report LBNL-20700, Lawrence Berkeley National Laboratory, Berkeley, CA
40. **Pruess K** (1990) Modeling of geothermal reservoirs: Fundamental processes, computer simulations and field applications. Geothermics 19(1): 3–15
41. **Pruess K, Narasimhan T** (1982) On fluid reserves and the production of superheated steam from fractured, vapor-dominated geothermal reservoirs. J. Geophys. Res. 87(B11): 9329–9339
42. **Pruess K, Narasimhan T** (1985) A practical method for modeling fluid and heat flow in fractured porous media. Society Petroleum Eng. J. 25(1): 14–26
43. **Reid RC, Prausnitz JM, Poling BE**(1988) The properties of liquids and gases. McGraw-Hill, Singapore
44. **Rutqvist J, Börgesson L, Chijimatsu M, Kobayashi A, Jing L, Nguyen TS, Noorishad J, Tsang C-F** (2001) Thermodynamics of partially saturated geologic media: governing equations and formulation of four finite element models. Int. J. Rock Mech. Mining Sci. 38: 105–127
45. **Sekine H, Mura T** (1980) Characterization of a penny-shaped reservoir in a hot dry rock. J. Geophys. Res. 85(B7): 3811–3816
46. **Shibuya Y, Sekine T, Takahashi Y** (1985a). Heat extraction through a geothermal reservoir on an oblique fault plane. Int J. Numer. Anal. Meth. Geomech. 11: 143–153
47. **Shibuya Y, Sekine T, Takahashi Y, Abe H** (1985b) Multiple artificial geothermal cracks in a hot dry rock mass for extraction of heat. J. Energy Resour. Technol. 107: 274–279
48. **Studer J, Ammann W, Meier P, Müller C, Glauser E** (1984) Verfüllen und Versiegeln von Stollen, Schächten und Bohrlöchern. Technischer Bericht 84-33, Nagra, Baden, Schweiz
49. **Terzaghi K** (1925) Erdbaumechanik auf bodenphysikalischer Grundlage. Deuticke, Wien
50. **Thorenz C, Kosakowski G, Kolditz O, Berkowitz B** (2001). An experimental and numerical investigation of saltwater movement in partially saturated systems. Water Resour. Res. 38(6). 10.1029/2001WR000364
51. **Tsang CF** (1991) Coupled hydromechanical-thermo-mechanical processes in rock fractures. Rev. Geophys. 29(4): 537–551
52. **Van Genuchten MT** (1980) A closed-form equation for predicting the hydraulic conductivity of unsaturated soils. Soil Sci. Soc. Am. J. 44: 892–898
53. **Xie M, Wang W, De Jonge J, Kolditz O** (2003) Numerical modeling of swelling processes in highly compacted bentonites. In: Stephanso (ed.) GeoProc 2003, pp 1001–1009. accepted paper

Non-isothermal flow processes in porous media, Part I:

Governing equations and finite element implementation

Technical report, Nr. 2002-1

Center of Applied Geosciences

University of Tübingen

Centre of Applied Geosciences
University of Tübingen

Non-Isothermal Flow Processes in Porous Media

Part I: Governing Equations and Finite Element Implementation

Joëlle De Jonge & Olaf Kolditz

ROCKFLOW – Preprint
[2002-1]

Tübingen
April 2002
Version 2002.4.25

Contents

List of Figures

List of Tables

Introduction

This report describes a particular method for the implementation of mulicomponent-multiphase model formulations into a fully coupled thermo-hydraulic (TH/M) model for non-isothermal flow processes. The model presented here is meant to be joined with a hydrological-mechanical (HM/T) model developed at the University of Hannover to form a complete thermo-hydraulic-mechanical model (THM).

THM Processes

We need THM models to faithfully represent non-isothermal flow and deformation processes. Figure 1 gives an overview of the different processes that take place in the near-field of underground disposal sites for heat-generating wastes. Hydraulic processes are marked in blue, thermal processes in red and mechanical processes in brown. The core at the centre heats the near-field and causes non-isothermal conditions. The bentonite buffer is an engineered barrier system that acts as an interface between the waste and the host rock.

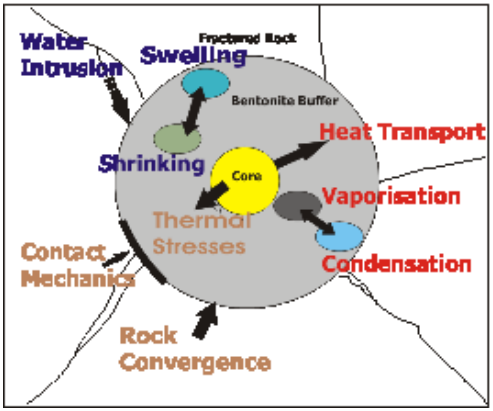

Figure 1: THM Processes

Buffer, host rock, and fluids in the gas and liquid phase form a multiphase-multicomponental system, or porous medium. The processes should be treated for the whole system in its entirety.

A complete THM model consists of a set of balance equations that take account of the phase changes. Often, only the liquid fluid phase is included in the model,

which only allows an approximation of phase transitions.

One of the difficulties in establishing THM models is that many of the processes illustrated in Figure 1 are non-linear and sometimes very difficult to express mathematically, as for example the relationship between capillary pressure and saturation.

The Rockflow Program

Rockflow is an object oriented modelling program. A program description is outside the scope of this report. A good description of the program can be found in [Kolditz, 2002].

The multiphase flow modelling capabilities implemented in the program are mainly based on the work done by Carsten Thorenz [Thorenz, 2001], who developed the corresponding Rockflow kernels. However, to account for non-isothermal processes including phase changes of fluid components we have to make use of the componental approach [Forsyth, 1988]. This is a substantial extension, therefore, we decided to set up a new Rockflow kernel for a multiphase-multicomponental formulation: RF-MPC.

Methods of Implementation of Non-Isothermal Flow Processes in Porous Media into Rockflow

There are three main methods for the implementation of multiphase-multicomponental formulations into the Rockflow code. The first method is the explicit calculation of accumulation terms. The second method, the explicit density calculation and the third method is a fully implicit scheme with respect to the field quantities. This report only describes the process for implementing the first method. The implementation of the other two methods will be the subjects of later reports.

Report Organisation

The organization of this report follows the implementation steps: In Chapter 1, we derive the governing equations from conservation principles. In Chapter 2, we show how the finite element method is applied to the governing equations. We present the implementation of state variables and material functions into Rockflow in Chapter 3 presents the material and component functions and their implementation in RockFlow. The implementation of the element and system matrices will be the subject of subsequent reports.

Acknowlegement

This project is funded by the Federal Agency of Geosciences and Natural Resources (BGR) under grant 2-1003822. We thank Dr. Wallner and Dr. Shao for their support of this research project.

1 Governing Equations

All formulations are based on the general balance equation.

$$\frac{d\psi}{dt} = \frac{\partial \psi}{\partial t} + \mathbf{v}^E \nabla \psi = -\psi \nabla \cdot \mathbf{v}^E + q^\psi \quad (1)$$

Method 1 expresses the equations in terms of gas pressure, gas saturation (Table 1).

The method is based on a componental approach. This means that governing equations are developed for the water component and for the air component. This is preferred to an approach, where governing equations are developed for the liquid phase and the gas phase, as for example in [Thorenz, 2001]. A governing equation for the energy equation is developed separately. A primary variable is associated with each governing equation, i.e. gas saturation (1-liquid saturation) is associated with the water component and gas pressure is associated with the air component. Temperature is associated with the energy equation.

The balance equation and the governing equation are shown in this section for both components, water and air and for the energy equation.

Variable	**Symbol**
Primary Variables	
Gas Pressure (for the air component)	p^g
Gas Saturation (for the water component)	S^g
Temperature (for the energy component)	T
Secondary Variables	
Vapour Pressure	$p^g_{w,sat}$
Capillary Pressure	p_c
Enthalpy	h^g_w
Mass Fractions	X^γ_k
Internal Energy	u^γ

Table 1: Primary and secondary variables

1.1 Balance Equations

1.1.1 Mass Balance equation

Equation (2) shows the mass balance equation for the water and air components. In the expression for the advective fluxes, the relative velocity of the liquid phase or gaseous phase relative to the solid phase in the water species is used. Because of this, terms containing the solid phase displacement velocity in the water species have to be added to the balance. However, since this method does not include displacement, the solid velocity terms cancel out of the equation.

The spatial deformation of porosity, saturation and liquid density in the water species is much smaller than the temporal variation. Hence the spatial variation of these variables can be neglected in all methods. The flux of the liquid phase in the water component can be neglected. In the air component the liquid diffusive flux cannot be neglected.

$$\frac{\partial}{\partial t}(nS^l\rho_k^l + nS^g\rho_k^g) + \nabla \cdot (\mathbf{J}_k^{ls} + \mathbf{J}_k^{gs}) + \nabla \cdot (\mathbf{J}_k^g + \mathbf{J}_k^l) = Q_k \tag{2}$$

1.1.2 Energy Balance Equation

The balance equation for equilibrium temperature in the porous medium is given by Equation (3) [Emmert, 1997]. The first term is the heat storage. The second term is the advective heat flux. This term is the heat flux of the liquid and gaseous phase relative to the solid phase. The third term is the diffusive heat flux term. Diffusive heat flux is only relevant for the gas phase, but in both components, air and water. This term only gets into the equation because there are multiple components. The fourth term is the conductive heat flux. On the RHS the sink term is listed, using the Darcy velocity.

The phase change terms cancel out with the addition of the individual phases. We work under the assumption of local thermodynamic equilibrium, meaning that all phase temperatures are equal.

$$\frac{\partial u\rho}{\partial t} + (\nabla \cdot \mathbf{J}_u^{gs} + \nabla \cdot \mathbf{J}_u^{ls} + \nabla \cdot \mathbf{J}_u^g + \nabla \cdot \mathbf{J}_t) = \mathbf{q}_e \tag{3}$$

1.2 Fluxes

For the water and air component, two types of fluxes have to be considered: advective fluxes and diffusive fluxes.

1.2.1 Advective Fluxes

Advective fluxes are movements of the liquid phase or gas phase relative to the solid phase. We use an extension of the Darcy equation to express advective flux in terms of the primary variables. Capillary pressure is of interest too, as it can be measured.

$$\begin{aligned}
\mathbf{J}_k^{ls} &= nS^l\rho_k^l(\mathbf{v}^l - \mathbf{v}^s) \\
&= -\rho_k^l \frac{k_{\mathsf{rel}}^l \mathbf{k}}{\mu^l}(\nabla p^l - \rho^l \mathbf{g}) = -\rho_k^l \frac{k_{\mathsf{rel}}^l \mathbf{k}}{\mu^l}(\nabla p^g - \nabla p_{\mathsf{c}} - \rho^l \mathbf{g})
\end{aligned} \tag{4}$$

$$\begin{aligned}
\mathbf{J}_k^{gs} &= nS^g\rho_k^g(\mathbf{v}^g - \mathbf{v}^s) \\
&= -\rho_k^g \frac{k_{\mathsf{rel}}^g \mathbf{k}}{\mu^g}(\nabla p^g - \rho^g \mathbf{g})
\end{aligned} \tag{5}$$

$$\begin{aligned}
\mathbf{J}_u^{\gamma s} &= nS^l\rho^l(\mathbf{v}^l - \mathbf{v}^s) + nS^g\rho^g(\mathbf{v}^g - \mathbf{v}^s) \\
&= -\rho^l h^l \frac{k_{\mathsf{rel}}^l \mathbf{k}}{\mu^l}(\nabla p^l - \rho^l \mathbf{g}) - \rho^g h^g \frac{k_{\mathsf{rel}}^g \mathbf{k}}{\mu^g}(\nabla p^g - \rho^g \mathbf{g}) \\
&= -\rho^l h^l \frac{k_{\mathsf{rel}}^l \mathbf{k}}{\mu^l}(\nabla p^g - p_{\mathsf{c}}^{(S)}) - \rho^g h^g \frac{k_{\mathsf{rel}}^g \mathbf{k}}{\mu^g}(\nabla p^g - \rho^g \mathbf{g})
\end{aligned} \tag{6}$$

1.2.2 Diffusive Fluxes

The diffusive flux within the gaseous phase can also be expressed in terms of primary variables, using the diffusion coefficient and mass fraction. The equations below show the diffusive fluxes.

$$\mathbf{J}_k^g = nS^g\rho_k^g(\mathbf{v}_k^g - \mathbf{v}^g) = -nS^g\rho_k^g D^g \nabla X_k^g \tag{7}$$

$$\mathbf{J}_k^l = nS^l\rho_k^l(\mathbf{v}_k^l - \mathbf{v}^l) \tag{8}$$

$$\mathbf{J}_u^g = -\nabla \cdot (D\rho^g h_a^g \nabla X_a^g) - \nabla \cdot (D\rho^g h_w^g \nabla X_w^g) \tag{9}$$

1.2.3 Conductive Fluxes

Equation (10) shows the conductive heat flux.

$$\mathbf{J}_t = -\nabla \cdot (\lambda \nabla T) \tag{10}$$

1.3 Equations of State

The set of equations needed to solve for the primary variables is not complete without the equations of state. Furthermore, equations of state link the balance equations for water, air and energy with each other and describe the physical state of the system that is modelled.

Saturated vapour pressure–$p^g_{w,sat}(T)$

We define the following equilibrium condition:

$$p^g_w \equiv p^g_{w,sat}(T) \tag{11}$$

Saturated vapour pressure is dependent on temperature, as described by the Clausius-Clapeyron equation (12). Vapour pressure is illustrated in Figure 2.

$$p^g_{w,sat}(T) = p_0 \exp\left[(\frac{1}{T_0} - \frac{1}{T})\frac{h^g_w M_w}{R}\right] \tag{12}$$

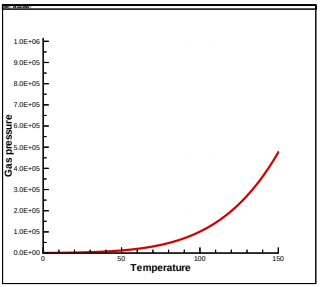

Figure 2: Vapour pressure, $p^g_{w,sat}$

Gas pressure of the air component– $p^g_a(p^g, T)$

The gas pressure in the air component depends on temperature and the pressure of the gas phase.

$$p^g_a(p^g, T) = p^g - p^g_{w,sat}(T) \tag{13}$$

Mass Fractions–$X_k^\gamma(p^g, T)$

Mass fraction is the fraction by mass of the phase of a component, compared to the other components in the same phase. The addition of the mass fractions for a given phase is equal to unity. Mass fractions for both components are illustrated in Figure 3.

$$\begin{aligned} X_w^g(p^g, T) &= 1 - X_a^g \\ X_a^g &= \frac{[p^g - p_{w,sat}^g(T)]M_a}{R(T + 273.15)\rho^g} \\ X_w^l(p^g, T) &= 1 - X_a^l \\ X_a^l &= \frac{M_a}{M_a - M_w(1 - [K^H(T)p_a^g]^{-1})} \end{aligned} \tag{14}$$

Enthalpy–h

Enthalpy is defined by $h = u + pV$. The phase enthalpies can be defined with help of the specific heat capacities at constant pressure. The liquid phase is assumed to be incompressible.

$$h^g = c_p^g T + \frac{p^g}{\rho^g} \tag{15}$$

$$h^l = c_p^l T \tag{16}$$

$$h^\gamma = X_a^\gamma h_a^\gamma + X_w^\gamma h_w^\gamma \tag{17}$$

Enthalpy of the gas phase in water–h_w^g

Enthalpy can be defined as the heat content of a fluid. In this case we consider the vapourisation enthalpy of the liquid phase. Enthalpy as a function of temperature is tabulated in steam tables of the American Society of Mechanical Engineers (ASME) of 1967 and illustrated in Figure 4 . A software calculating the values based on these steam tables was developed as a freeware by Michael Lynn McGuire of WinSim, Inc. (http://www.winsim.com/steam/steam.html)

Comparing the software's equations and the equation for vapour pressure, we have,

$$\begin{aligned} \frac{y}{\rho_1} &= -h_w^g \frac{M_w}{RT_0} \\ \frac{1}{\rho_2} &= h_w^g \frac{M_w}{R(T_0 - T)} \end{aligned} \tag{18}$$

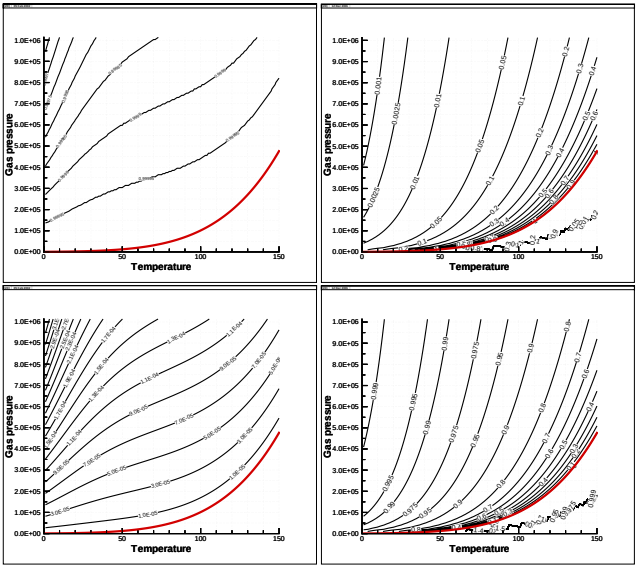

Figure 3: Mass Fractions; top left:X_w^l, top right:X_w^g bottom left:X_a^l, bottom right:X_a^g

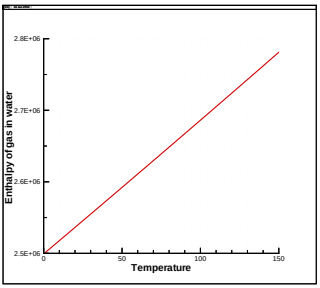

Figure 4: Enthalpy of the gas phase in water, h_w^g

where all terms are dimensionless and T_0 is a reference temperature.

u – Internal energy

Internal energy is defined as the energy associated with the random, disordered motion of molecules. The internal energy is calculated for each phase. The liquid phase is assumed to be incompressible.

$$\begin{aligned} u^g &= c_v^g T + \frac{p^g}{\rho^g} \\ u^l &= c_v^l T \end{aligned} \tag{19}$$

1.4 Material Properties

The material properties describe the components that are to be modelled. They can be divided into thermal, hydraulic and mechanical properties.

Phase densities–$\rho^{\gamma}(T)$

Total fluid density is composed of the addition of partial density terms.

$$\rho^{\gamma} = \rho_a^{\gamma} + \rho_w^{\gamma} \tag{20}$$

This is illustrated for the gas phase in Appendix 1, where vapour density (ρ_w^g), gas phase density (ρ_a^g) in the air component and gas density (ρ^g) are plotted as a function of pressure and temperature. Figure 5 shows the gas density.

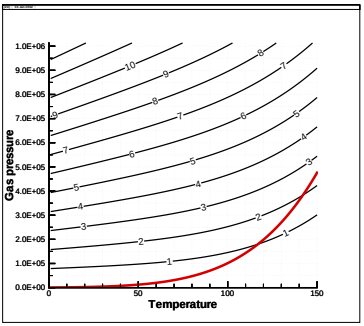

Figure 5: Gas phase density, ρ^g

$$\begin{aligned}
\rho^l(T) &= \rho_0^l(1+\beta_T^l(T-T_0)) \\
\rho^g(p^g,T) &= \rho_a^g + \rho_w^g \\
&= \frac{M_a^g}{RT}p_a^g + \frac{M_w^g}{RT}p_w^g \\
&= \frac{M_a}{RT}(p^g - p_{w,sat}^g) + \frac{M_w}{RT}p_{w,sat}^g \\
&= \frac{M_a}{RT}p^g + \frac{(M_w - M_a)}{RT}p_{w,sat}^g
\end{aligned} \tag{21}$$

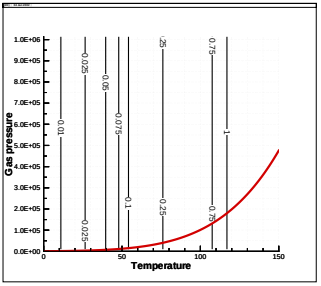

Figure 6: Water vapour density

Water vapour density–$\rho_w^g(p^l, T)$

Water vapour density is the mass of water per unit volume of gas phase. Figure 1.4 illustrates the water vapour density function, and and also shows the vapour pressure curve.

Water vapour density can be defined in terms of mass fractions or with help of the ideal gas law, Kelvin's equation or the psychromatic law as shown below.

$$\rho_w^g = X_w^g \rho^g = \frac{M_w}{TR} p_w^g \qquad \text{Ideal gas law}$$

$$\rho_w^g = \frac{M_w}{TR} p_{w,sat}^g(T)\, f(p_c, T) \qquad \text{Kelvin's equation}$$

$$\rho_w^g = \frac{M_w}{TR} \exp\left[(\frac{1}{T_0} - \frac{1}{T})\frac{h_w^g M_w}{R}\right] \exp\left[\frac{-p_c(S^g) M_w}{R(273.15K + T)\rho^l}\right] \qquad \text{Psychromatic law}$$

$$\frac{\partial \rho_w^g}{\partial t} = \frac{M_w}{TR}\frac{\partial \rho_w^g}{\partial p_c}\frac{\partial p_c}{\partial S^g}\frac{\partial S^g}{\partial t} + \frac{M_w}{TR}(\frac{\partial p_w^g}{\partial T} - \frac{p_w^g}{T})\frac{\partial T}{\partial t} \tag{22}$$

Water liquid density–ρ_w^l

Water liquid phase density is the mass of water per unit liquid phase volume.

$$\rho_w^l = X_w^l \rho^l \tag{23}$$

Gaseous air density–$\rho_a^g(p^g, T)$

The gaseous air density is the mass of air per unit volume of gas phase. It is a function of gas pressure and temperature.

$$\begin{aligned}
\rho_a^g &= X_a^g \rho^g \\
\rho_a^g &= \frac{M_a}{TR} p_a^g && \text{Ideal gas law} \\
\rho_a^g &= \frac{M_a}{TR} (p^g - p_w^g) && \text{Dalton's law} \\
\frac{\partial \rho_a^g}{\partial t} &= \frac{M_a}{TR} (\frac{\partial \rho^g}{\partial t} - \frac{\partial \rho_w^l}{\partial t})
\end{aligned} \tag{24}$$

Dissolved air density–$\rho_a^l(p^g, T)$

Dissolved air density is the mass of air per unit volume of the liquid phase.

$$\rho_a^l = X_a^l \rho^l = \frac{M_a}{M_a - M_w(1 - \frac{1}{K_H p_a^g})} \rho^l(p^l, T) \qquad \text{Henry's law} \tag{25}$$

μ – Fluid viscosity

Viscosity is defined as shearing stress per unit area divided by a velocity gradient and it has the dimension of $N\,s/m^2$ or $Pa\,s$. All gases and most fluids follow Newton's law of viscosity, as shown below.

$$\tau_{yx} = -\mu \frac{\partial v}{\partial y} \tag{26}$$

The viscosity of fluids depends on pressure and temperature. The viscosity of liquids depends highly on temperature, whereas for most cases the variation of viscosity with pressure can be neglected for liquids. Water presents an exception as in that its viscosity decreases with pressure at constant temperature. Changes in temperature have opposite effects on liquids than on gases: with decreasing temperature the viscosity of a liquid rises, while the viscosity of a low density gas decreases.In our case, concentration of the liquid in the medium also plays a role.

$$\begin{aligned}
\mu^\alpha(C, T) &= \frac{\mu}{f1 + f2} \\
f1 &= f(C) \\
f2 &= f(T)
\end{aligned} \tag{27}$$

- Non-isothermal flow of water (de Marsily 1986) (Fig. 7)

$$\mu^w(T) = 2.285 \times 10^{-5} + 1.01 \times 10^{-3} \log T \tag{28}$$

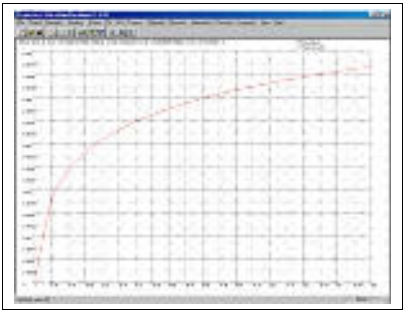

Figure 7: Water viscosity as a function of temperature

- Non-isothermal flow of gas (Reid et al. 1988) (Fig. 8)

$$\mu^g(p,T) = \mu_0 \left(1 + \frac{A p_r^{3/2}}{B p_r + (1 + C p_r^D)^{-1}}\right) \tag{29}$$

with the following parameters:

$$\begin{array}{ll} p_r = p/p_{\text{crit}} & T_r = T/T_{\text{crit}} \\ A = \dfrac{\alpha_1}{T_r} \exp(\alpha_2 T_r^a) & B = A(\beta_1 T_r - \beta_2) \\ C = \dfrac{\gamma_1}{T_r} \exp(\gamma_2 T_r^c) & D = \dfrac{\delta_1}{T_r} \exp(\delta_2 T_r^d) \end{array} \tag{30}$$

$$\begin{array}{lll} p_{\text{crit}} = 33.9 \times 10^4\, Pa & T_{\text{crit}} = 126.2\, K & \\ \alpha_1 = 1.9824 \times 10^{-3} & \alpha_2 = 5.2683 & a = -0.5767 \\ \beta_1 = 1.65552 & \beta_2 = 1.2760 & \\ \gamma_1 = 0.1319 & \gamma_2 = 3.7035 & c = -79.8678 \\ \delta_1 = 2.9496 & \delta_2 = 2.9190 & d = -16.6169 \end{array}$$

- Non-isothermal flow of brines (Lever and Jackson 1985)

$$\mu^w(T,C) = \mu_0 \frac{1 + 1.85\omega - 4.1\omega^2 + 44.5\omega^3}{1 + 0.7063\zeta - 0.04832\zeta^2} \tag{31}$$

with:

$$\omega = \frac{C}{\rho} \quad , \quad \zeta = \frac{T - 150°C}{100°C} \tag{32}$$

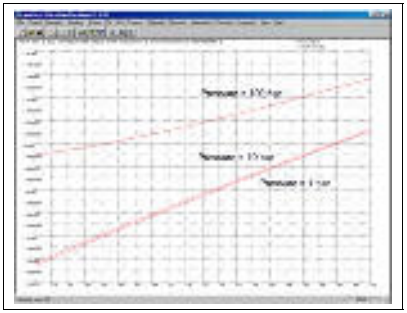

Figure 8: Gas viscosity as a function of temperature and pressure

Capillary pressure–p_c

The capillary pressure can be defined as the tendency of a porous medium to suck in the wetting fluid phase or to repel the non-wetting phase. Capillary pressure results from the pressure discontinuity at the interface between two immiscible fluids. Capillary pressure depends on the geometry of the void space, on the nature of solids and liquids and on the degree of saturation. In porous media the geometry of the void space is idealized. Thus, the dependence reduces to saturation for any given porous media. Care has to be taken, as capillary pressure is not the same for drainage and re-wetting. The function connecting capillary pressure and saturation has to be determined by laboratory experiments for every new porous medium. As an approximation a linear relationship can be used. There are, however, analytical functions that can be used, such as the van Genuchten (1980) model

$$S_{\text{eff}} = \frac{S^w - S_r^w}{1 - S_r^w} = (1 + (\alpha\, p_c)^n)^m \qquad , \qquad p_c > 0 \tag{33}$$

$$p_c = \begin{cases} 0 & S^w > S^w_{\text{max}} \\ \frac{\rho^w g}{\alpha}(S_{\text{eff}}^{-1/m} - 1)^{1/n} & S_r^w < S^w < S^w_{\text{max}} \\ p_{c\ \text{max}} & S^w < S_r^w \end{cases} \tag{34}$$

Brooks and Corey (1964) developed the following model.

$$S_{\text{eff}} = \frac{S^w - S_r^w}{1 - S_r^w} = \left(\frac{p_b}{p_c}\right)^{\lambda} \qquad , \qquad p_c \geq p_b \tag{35}$$

$$p_{\mathsf{c}} = \begin{cases} 0 & S^w > S^w_{\mathsf{max}} \\ p_b \left(\frac{1}{S_{\mathsf{eff}}}\right)^{1/\lambda} & S^w_r < S^w < S^w_{\mathsf{max}} \\ p_{\mathsf{c\ max}} & S^w < S^w_r \end{cases} \tag{36}$$

p_b is the so-called bubbling pressure, the minimum pressure at which the gaseous phase exists, λ is the pore size distribution index.

Another model example is that of Havercamp et al. (1977), where the formulas are given in terms of pressure head $h = p^w/g\rho^w$ and moisture content $\theta = nS^w$.

$$\theta = \frac{\alpha(\theta_s - \theta_r)}{\alpha + |h|^\beta} + \theta_r \tag{37}$$

$$h = \left(-\frac{\alpha}{\theta}(\theta - \theta_s + \theta_r)\right)^{1/\beta} \tag{38}$$

θ	volumetric water (moisture) content		$[cm^3/cm^3]$
θ_r	residual volumetric water content	0.075	$[cm^3/cm^3]$
θ_s	saturated volumetric water content	0.287	$[cm^3/cm^3]$
$h(\theta)$	soil water pressure head relative to the atmosphere		$[cm]$
α		1.611×10^6	$[Pa^{-1}]$
β		3.96	

Table 2: Model parameters for the Havercamp et al. model

Permeability–k

Permeability is a constant that is used defined in the input file and that is different for each solid material.

Relative Permeability–k_{rel}

For porous media containing more than one fluid, the concept of relative permeability is introduced. The relative permeability is used to calculate the effective permeability $(k^\gamma_{\mathsf{rel}} S^\gamma)\mathbf{k}$, which is described in the extended Darcy law. The relationship depends strongly on the saturations. Different relationships are possible: constant values, user-defined functions, linear functions, potential functions, or functions found in literature, such as the van Genuchten Model (1980),

$$k_{\mathsf{rel}}(h) = \frac{1 - (\alpha h)^{n-2}\left[1 + (\alpha h)^n\right]^{-m}}{\left[1 + (\alpha h)^n\right]^{2m}} \tag{39}$$

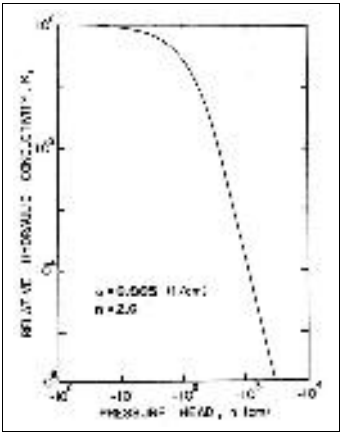

Figure 9: Relative permeability functions (Source: van Genuchten Model (1980))

or the relationship developed by Haverkamp et al.(1977)

$$k_{\text{rel}}(h) = K_s \frac{A}{A + |h|^{\beta}} \tag{40}$$

$$h = \left(-\frac{\alpha}{\theta}(\theta - \theta_s + \theta_r)\right)^{1/\beta} \tag{41}$$

or the Brooks and Corey model (1966)

$$S_{\text{eff}} = \frac{S^w - S_r^w}{S_{\text{max}}^w - S_r^w} \tag{42}$$

$$k_{\text{rel}}^w = S_{\text{eff}}^4 \tag{43}$$

Material constants

$$
\begin{aligned}
M_w &= 18.016 \frac{kg}{kmol} \\
M_a &= 28.96 \frac{kg}{kmol} \\
R &= 8.31451 \frac{kJ}{kmol K} \\
\beta_T^l &= \frac{1}{\rho_0^l} \frac{\partial \rho}{\partial T}
\end{aligned} \tag{44}
$$

c – Specific heat capacity

The specific heat is the amount of heat per unit mass required to raise the temperature by one degree Celsius. This does not apply if a phase change is encountered, because the heat added or removed during a phase change does not change the temperature. Specific heat capacity can be expressed at constant volume or at constant pressure.

$$c_V = \frac{\partial u}{\partial T} \tag{45}$$

$$c_p = \frac{\partial h}{\partial T} \tag{46}$$

λ – Thermal conductivity

During thermal conduction, heat is exchanged between molecules, due to the kinetic energy resulting because of their collision. For a fluid or solid continuum, thermal conduction can be described by Fourier's Law at the macroscopic level as the proportional relationship between the flux of thermal energy by conduction and temperature, with the thermal conductivity λ as a proportionality coefficient.

The thermal conductivity is specific to the fluid, through which the flux takes place. In gases and liquids, λ depends on temperature and pressure. However the pressure dependency is far smaller than the temperature dependency. At low gas density, the thermal conductivity of gases increases with temperature. However the thermal conductivity of most liquids decreases with temperature. Polar liquids may have a maximum in the temperature dependency of thermal conductivity.

The thermal conductivity considered here is the overall thermal conductivity of the porous medium. Overall thermal conductivity is a function of porosity and saturation. It is given by the geometric mean approximation

$$\lambda = (1-n)\lambda^s + nS^l\lambda^l + nS^g\lambda^g \tag{47}$$

There are different models of expressing thermal conductivity. In DECOVALEX II, the dependency of thermal conductivity from saturation was expressed by

$$\lambda(S) = 0.5 + 1.2S \tag{48}$$

D – Diffusion coefficient

The diffusion coefficient can be expressed by the following function.

$$D = \tau n S^g D_m \tag{49}$$

In the model, however, a constant value is currently used for the diffusion coefficient.

1.5 Governing Equations

1.5.1 Governing equation for the air and water components

To obtain the governing equation, fluxes, state functions, and material functions are substituted into the mass balance equation (2).

$$
\begin{aligned}
- \quad & \nabla \cdot \left(\rho^g X_k^g \frac{k_{\mathsf{rel}}^g \mathbf{k}}{\mu^g} \nabla p^g \right) - \nabla \cdot \left(\rho^l X_k^l \frac{k_{\mathsf{rel}}^l \mathbf{k}}{\mu^l} \nabla p^g \right) \\
= \quad & Q_k \\
- \quad & \frac{\partial}{\partial t} (n S^l \rho^l X_k^l + n S^g \rho^g X_k^g) \\
+ \quad & \nabla \cdot (n S^g \rho^g D^g \nabla X_k^g) \\
- \quad & \nabla \cdot \left(\rho^l X_k^l \frac{k_{\mathsf{rel}}^l \mathbf{k}}{\mu^l} \nabla p_{\mathsf{c}} \right) \\
- \quad & \nabla \cdot \left(\rho^l X_k^l \frac{k_{\mathsf{rel}}^l \mathbf{k}}{\mu^l} \rho^l \mathbf{g} \right) - \nabla \cdot \left(\rho^g X_k^g \frac{k_{\mathsf{rel}}^g \mathbf{k}}{\mu^g} \rho^g \mathbf{g} \right)
\end{aligned}
\tag{50}
$$

1.5.2 Governing equation for the energy component

The governing equation for the energy component is obtained by inserting the equation of the fluxes into the balance equation an by using the equations of state

Primary variables: $p^g, S^g / X_w^g, T$

$$
\begin{aligned}
& (1-n) \rho^s c^s \frac{\partial T}{\partial t} + n \frac{\partial \rho^g S^g u^g}{\partial t} + n \frac{\partial \rho^l S^l u^l}{\partial t} \\
- \quad & \nabla \cdot (\rho^l h^l \frac{k_{\mathsf{rel}}^l \mathbf{k}}{\mu^l} (\nabla p^g - \nabla p_{\mathsf{c}} - \rho^l \mathbf{g})) - \nabla \cdot (\rho^g h^g \frac{k_{\mathsf{rel}}^g \mathbf{k}}{\mu^g} (\nabla p^g - \rho^g \mathbf{g})) \\
- \quad & \nabla \cdot (\lambda \nabla T) \\
- \quad & \nabla \cdot (D \rho^g h_a^g \nabla X_a^g) - \nabla \cdot (D \rho^g h_w^g \nabla X_w^g) \\
= \quad & \rho Q_T
\end{aligned}
\tag{51}
$$

We now have three governing equations in differential form, one for each primary variable. Together with the equations of state and with the material properties, they form a complete set of equations.

2 Numerical Formulation

In this section, the physical concepts derived in the previous section are formulated numerically. The three governing equations (water component, air component, energy conservation) are the starting point.

The governing equations cannot be solved numerically as they stand. They have to be approximated. The approximation method used is the method of weighted residuals. The weighting functions associated with this process have been defined by the Bubnov-Galerkin method, which sets the weighting function equal to the interpolation function. For any given element, the interpolation function is equal to the shape function N. The resulting equation is called the weak formulation. Once the Bubnov-Galerkin method is applied a time collocation, i.e. the time within the time step, at which the variables are calculated. The resulting equation is called weak formulation with time collocation. Figure 10 illustrates this process.

Figure 10: Numerical Approximation Procedure

2.1 Weak Formulation

2.1.1 Air and water components

Based on equation (51) we have:

$$+ \quad \left[\int_\Omega \nabla \mathbf{N}^T \left(\rho^l X_k^l \frac{k_{\mathsf{rel}}^l \mathbf{k}}{\mu^l}\right) \nabla \mathbf{N}\, d\Omega + \int_\Omega \nabla \mathbf{N}^T \left(\rho^g X_k^g \frac{k_{\mathsf{rel}}^g \mathbf{k}}{\mu^g}\right) \nabla \mathbf{N}\, d\Omega\right] [\hat{\mathbf{p}}^g]$$
$$= \quad \int_\Omega \mathbf{N}^T Q_k\, d\Omega$$

$$
\begin{aligned}
&+ \quad \left[\int_\Omega \nabla \mathbf{N}^T \left(\rho^l X_k^l \frac{k_{\mathsf{rel}}^l \mathbf{k}}{\mu^l} \frac{dp_\mathsf{c}}{dS}\right) \nabla \mathbf{N}\, d\Omega\right] [\hat{\mathbf{S}}^g] \\
&- \quad \frac{d}{dt}\int_\Omega \mathbf{N}^T ([n\hat{\mathbf{S}}^l \rho^l \hat{\mathbf{X}}_k^l] d\Omega \\
&- \quad \frac{d}{dt}\int_\Omega \mathbf{N}^T ([n\hat{\mathbf{S}}^g \rho^g \hat{\mathbf{X}}_k^g] d\Omega \\
&+ \quad \left[\int_\Omega \nabla \mathbf{N}^T (nS^g \rho^g D^g) \nabla \mathbf{N}\, d\Omega\right] [\hat{\mathbf{X}}_k^g] \\
&- \quad \int_\Omega \nabla \mathbf{N}^T \left(\rho^l X_k^l \frac{k_{\mathsf{rel}}^l \mathbf{k}}{\mu^l} \rho^l \mathbf{g}\right) d\Omega - \int_\Omega \nabla \mathbf{N}^T \left(\rho^g X_k^g \frac{k_{\mathsf{rel}}^g \mathbf{k}}{\mu^g} \rho^g \mathbf{g}\right) d\Omega \qquad (52)
\end{aligned}
$$

Weak formulation and time discretization

The next step is to include the time discretization. Here a time θ collocation factor is included.

$$
\begin{aligned}
&+ \quad \left[\int_\Omega \nabla \mathbf{N}^T \left(\rho^l X_k^l \frac{k_{\mathsf{rel}}^l \mathbf{k}}{\mu^l}\right) \nabla \mathbf{N}\, d\Omega + \int_\Omega \nabla \mathbf{N}^T \left(\rho^g X_k^g \frac{k_{\mathsf{rel}}^g \mathbf{k}}{\mu^g}\right) \nabla \mathbf{N}\, d\Omega\right] \theta [\hat{\mathbf{p}}^g]_{\tau+1}^{n+1} \\
&= \quad \int_\Omega \mathbf{N}^T Q_k\, d\Omega \\
&- \quad \left[\int_\Omega \nabla \mathbf{N}^T \left(\rho^l X_k^l \frac{k_{\mathsf{rel}}^l \mathbf{k}}{\mu^l}\right) \nabla \mathbf{N}\, d\Omega + \int_\Omega \nabla \mathbf{N}^T \left(\rho^g X_k^g \frac{k_{\mathsf{rel}}^g \mathbf{k}}{\mu^g}\right) \nabla \mathbf{N}\, d\Omega\right] (1-\theta) [\hat{\mathbf{p}}^g]^n \\
&+ \quad \left[\int_\Omega \nabla \mathbf{N}^T \left(\frac{\partial p_\mathsf{c}}{\partial S} \rho^l X_k^l \frac{k_{\mathsf{rel}}^l \mathbf{k}}{\mu^l}\right) \nabla \mathbf{N}\, d\Omega\right] \theta [\hat{\mathbf{S}}^g]_\tau^{n+1} \\
&+ \quad \left[\int_\Omega \nabla \mathbf{N}^T \left(\frac{\partial p_\mathsf{c}}{\partial S} \rho^l X_k^l \frac{k_{\mathsf{rel}}^l \mathbf{k}}{\mu^l}\right) \nabla \mathbf{N}\, d\Omega\right] (1-\theta) [\hat{\mathbf{S}}^g]_\tau^n \\
&- \quad \frac{1}{\Delta t}\theta \int_\Omega \mathbf{N}^T [n\rho^l \hat{\mathbf{X}}_k^l \mathbf{N} \hat{\mathbf{S}}^l]_\tau^{n+1}\, d\Omega - \frac{1}{\Delta t}(1-\theta) \int_\Omega \mathbf{N}^T [n\rho^l \hat{\mathbf{X}}_k^l \mathbf{N} \hat{\mathbf{S}}^l]_\tau^n\, d\Omega \\
&- \quad \frac{1}{\Delta t}\theta \int_\Omega \mathbf{N}^T [n\rho^g \hat{\mathbf{X}}_k^g \mathbf{N} \hat{\mathbf{S}}^g]_\tau^{n+1}\, d\Omega - \frac{1}{\Delta t}(1-\theta) \int_\Omega \mathbf{N}^T [n\rho^g \hat{\mathbf{X}}_k^g \mathbf{N} \hat{\mathbf{S}}^g]_\tau^n\, d\Omega \\
&- \quad \left[\int_\Omega \nabla \mathbf{N}^T (nS^g \rho^g D^g) \nabla \mathbf{N}\, d\Omega\right] \theta [\hat{\mathbf{X}}_k^g]_\tau^{n+1} - \left[\int_\Omega \nabla \mathbf{N}^T (nS^g \rho^g D^g) \nabla \mathbf{N}\, d\Omega\right] (1-\theta) [\hat{\mathbf{X}}_k^g]_\tau^n \\
&+ \quad \int_\Omega \nabla \mathbf{N}^T \left(\rho^l X_k^l \frac{k_{\mathsf{rel}}^l \mathbf{k}}{\mu^l} \rho^l \mathbf{g}\right) \theta\, d\Omega + \int_\Omega \nabla \mathbf{N}^T \left(\rho^l X_k^l \frac{k_{\mathsf{rel}}^l \mathbf{k}}{\mu^l} \rho^l \mathbf{g}\right) (1-\theta)\, d\Omega \\
&+ \quad \int_\Omega \nabla \mathbf{N}^T \left(\rho^g X_k^g \frac{k_{\mathsf{rel}}^g \mathbf{k}}{\mu^g} \rho^g \mathbf{g}\right) \theta\, d\Omega + \int_\Omega \nabla \mathbf{N}^T \left(\rho^g X_k^g \frac{k_{\mathsf{rel}}^g \mathbf{k}}{\mu^g} \rho^g \mathbf{g}\right) (1-\theta)\, d\Omega \qquad (53)
\end{aligned}
$$

2.1.2 Energy Component

As for the water and air components, the governing equation for the energy equation has to be discretized. The weak formulation is presented directly with time discretization.

$$
\begin{aligned}
& \frac{1}{\Delta t}\left[\int_\Omega \mathbf{N}^T\left((1-n)\rho^s c^s\right)\mathbf{N}\,d\Omega\right][\hat{\mathbf{T}}]_{\tau+1}^{n+1} \\
- & \left[\int_\Omega \nabla\mathbf{N}^T\left(\boldsymbol{\kappa}\right)\nabla\mathbf{N}\,d\Omega\right]\theta[\hat{\mathbf{T}}]_{\tau+1}^{n+1} \\
= & \int_\Omega \mathbf{N}^T\rho Q_T\,d\Omega \\
+ & \frac{1}{\Delta t}\left[\int_\Omega \mathbf{N}^T\left((1-n)\rho^s c^s\right)\mathbf{N}\,d\Omega\right][\hat{\mathbf{T}}]^n \\
+ & \left[\int_\Omega \nabla\mathbf{N}^T\left(\boldsymbol{\kappa}\right)\nabla\mathbf{N}\,d\Omega\right](1-\theta)[\hat{\mathbf{T}}]^n \\
- & \frac{1}{\Delta t}\left[\int_\Omega \mathbf{N}^T\left(n\rho^g u^g\right)\mathbf{N}\,d\Omega\right][\hat{\mathbf{S}}^g]_\tau^{n+1} + \frac{1}{\Delta t}\left[\int_\Omega \mathbf{N}^T\left(n\rho^g u^g\right)\mathbf{N}\,d\Omega\right][\hat{\mathbf{S}}^g]^n \\
- & \frac{1}{\Delta t}\left[\int_\Omega \mathbf{N}^T\left(n\rho^l u^l\right)\mathbf{N}\,d\Omega\right][\hat{\mathbf{S}}^l]_\tau^{n+1} + \frac{1}{\Delta t}\left[\int_\Omega \mathbf{N}^T\left(n\rho^l u^l\right)\mathbf{N}\,d\Omega\right][\hat{\mathbf{S}}^l]^n \\
+ & \theta\left[\int_\Omega \nabla\mathbf{N}^T\left(\rho^g h^g\frac{k^g_{\mathsf{rel}}\mathbf{k}}{\mu^g}\right)\nabla\mathbf{N}\,d\Omega\right][\hat{\mathbf{p}}^g]_\tau^{n+1} - (1-\theta)\left[\int_\Omega \nabla\mathbf{N}^T\left(\rho^g h^g\frac{k^g_{\mathsf{rel}}\mathbf{k}}{\mu^g}\right)\nabla\mathbf{N}\,d\Omega\right][\hat{\mathbf{p}}^g]^n \\
+ & \theta\left[\int_\Omega \nabla\mathbf{N}^T\left(\rho^l h^l\frac{k^l_{\mathsf{rel}}\mathbf{k}}{\mu^l}\right)\nabla\mathbf{N}\,d\Omega\right][\hat{\mathbf{p}}^g]_\tau^{n+1} - (1-\theta)\left[\int_\Omega \nabla\mathbf{N}^T\left(\rho^l h^l\frac{k^l_{\mathsf{rel}}\mathbf{k}}{\mu^l}\right)\nabla\mathbf{N}\,d\Omega\right][\hat{\mathbf{p}}^g]^n \\
- & \theta\left[\int_\Omega \nabla\mathbf{N}^T\left(\rho^l h^l\frac{k^l_{\mathsf{rel}}\mathbf{k}}{\mu^l}\right)\nabla\mathbf{N}\,d\Omega\right][\hat{\mathbf{p}}_c^g]_\tau^{n+1} + (1-\theta)\left[\int_\Omega \nabla\mathbf{N}^T\left(\rho^l h^l\frac{k^l_{\mathsf{rel}}\mathbf{k}}{\mu^l}\right)\nabla\mathbf{N}\,d\Omega\right][\hat{\mathbf{p}}_c^g]^n \\
+ & \theta\left[\int_\Omega \nabla\mathbf{N}^T\left(D\rho^g h_a^g\right)\nabla\mathbf{N}\,d\Omega\right][\hat{\mathbf{X}}_a^g]_\tau^{n+1} \\
+ & (1-\theta)\left[\int_\Omega \nabla\mathbf{N}^T\left(D\rho^g h_a^g\right)\nabla\mathbf{N}\,d\Omega\right][\hat{\mathbf{X}}_a^g]^n \\
+ & \theta\left[\int_\Omega \nabla\mathbf{N}^T\left(D\rho^g h_w^g\right)\nabla\mathbf{N}\,d\Omega\right][\hat{\mathbf{X}}_w^g]_\tau^{n+1} \\
+ & (1-\theta)\left[\int_\Omega \nabla\mathbf{N}^T\left(D\rho^g h_w^g\right)\nabla\mathbf{N}\,d\Omega\right][\hat{\mathbf{X}}_w^g]^n \\
- & \theta\int_\Omega \nabla\mathbf{N}^T\left(\rho^g h^g\frac{k^g_{\mathsf{rel}}\mathbf{k}}{\mu^g}\rho^g\mathbf{g}\right)d\Omega + (1-\theta)\int_\Omega \nabla\mathbf{N}^T\left(\rho^g h^g\frac{k^g_{\mathsf{rel}}\mathbf{k}}{\mu^g}\rho^g\mathbf{g}\right)d\Omega \\
- & \theta\int_\Omega \nabla\mathbf{N}^T\left(\rho^l h^l\frac{k^l_{\mathsf{rel}}\mathbf{k}}{\mu^l}\rho^l\mathbf{g}\right)d\Omega + (1-\theta)\int_\Omega \nabla\mathbf{N}^T\left(\rho^l h^l\frac{k^l_{\mathsf{rel}}\mathbf{k}}{\mu^l}\rho^l\mathbf{g}\right)d\Omega \qquad (54)
\end{aligned}
$$

Finite element equation

In practice, the equations are calculated over elemental volumes. The union of these elemental volumes forms the entire domain.

$$\Omega = \bigcup \Omega^e \tag{55}$$

2.2 Algebraic Equations

The algebraic equation is derived from the weak formulation with time discretization. Each term is written in matrix form. The matrices are element matrices. Their properties are described in the next section. This is the formulation needed for the implementation of the equations into the code.

2.2.1 Algebraic equation of the air and water components

$$\begin{aligned}
\theta(\mathbf{K}_k^{ls}+\mathbf{K}_k^{gs})[\hat{\mathbf{p}}^g]_{\tau+1}^{n+1} &= \theta[\mathbf{r}_k]_\tau^{n+1}+(1-\theta)[\mathbf{r}_k]^n \\
&- (1-\theta)(\mathbf{K}_k^{ls}+\mathbf{K}_k^{gs})[\hat{\mathbf{p}}^g]^n \\
&- \frac{1}{\Delta t}\left([\mathbf{C}_k]_\tau^{n+1}-[\mathbf{C}_k]^n\right) \\
&+ \theta\mathbf{K}_k^{ls}\frac{\partial p_c}{\partial S}[\hat{S}^g]_\tau^{n+1}+(1-\theta)\mathbf{K}_k^{ls}\frac{\partial p_c}{\partial S}[\hat{S}^g]^n \\
&+ (\rho^l\mathbf{g}_k^{ls}+\rho^g\mathbf{g}_k^{gs}) \\
&+ (1-\theta)\mathbf{K}_k^g[\hat{\mathbf{X}}_k^g]_\tau^{n+1}+\theta\mathbf{K}_k^g[\hat{\mathbf{X}}_k^g]_\tau^n
\end{aligned} \tag{56}$$

2.2.2 Algebraic equation of the energy component

$$\begin{aligned}
\left(\frac{1}{\Delta t}\mathbf{C}_t^s-\theta\mathbf{K}_t^s\right)[\hat{\mathbf{T}}]_{\tau+1}^{n+1} &= \theta[\mathbf{r}_t]_\tau^{n+1}+(1-\theta)[\mathbf{r}_t]^n \\
&+ \left(\frac{1}{\Delta t}\mathbf{C}_t^s+\theta\mathbf{K}_t^s\right)[\hat{\mathbf{T}}]^n \\
&- \frac{1}{\Delta t}\mathbf{C}_u^g[\hat{\mathbf{S}}^g]_\tau^{n+1}+\frac{1}{\Delta t}\mathbf{C}_u^g[\hat{\mathbf{S}}^g]^n \\
&- \frac{1}{\Delta t}\mathbf{C}_u^l[\hat{\mathbf{S}}^l]_\tau^{n+1}+\frac{1}{\Delta t}\mathbf{C}_u^l[\hat{\mathbf{S}}^l]^n \\
&+ \theta(\mathbf{K}_h^g+\mathbf{K}_h^l)[\hat{\mathbf{p}}^g]_\tau^{n+1}+(1-\theta)(\mathbf{K}_h^g+\mathbf{K}_h^l)[\hat{\mathbf{p}}^g]^n \\
&+ \theta\mathbf{K}_h^l[\hat{\mathbf{p}}_c^g]_\tau^{n+1}+(1-\theta)\mathbf{K}_h^l[\hat{\mathbf{p}}_c^g]^n \\
&+ (\rho^l\mathbf{G}_w^{ls}+\rho^g\mathbf{G}_w^{gs})\mathbf{g} \\
&+ \theta\mathbf{K}_a^g[\hat{\mathbf{X}}_a^g]_\tau^{n+1}+(1-\theta)\mathbf{K}_a^g[\hat{\mathbf{X}}_a^g]_\tau^n \\
&+ \theta\mathbf{K}_w^g[\hat{\mathbf{X}}_w^g]_\tau^{n+1}+(1-\theta)\mathbf{K}_w^g[\hat{\mathbf{X}}_w^g]_\tau^n
\end{aligned} \tag{57}$$

Finite element equation

The union of all elemental volumes forms the domain.

$$\Omega=\bigcup\Omega^e \tag{58}$$

2.3 Element Matrices

Element matrices contain an integral that has to be approximated numerically. The approximation is done with the help of shape functions, which depend on the dimension and the shape of the mesh elements.

In the first part of this section, the element matrices are evaluated for 1-dimensional linear elements. In the second part of this section the same matrix types are evaluated for 2-dimensional triangular elements.

2.3.1 1-D Linear Element Matrices

The shape functions for 1-D elements are as follows in global coordinates.

$$\begin{aligned} N_1^e(r) &= \frac{x_2 - x}{x_2 - x_1} \\ N_2^e(r) &= \frac{x - x_1}{x_2 - x_1} \end{aligned} \tag{59}$$

In local coordinates, the shape functions are expressed by

$$\begin{aligned} N_1^e(r) &= \frac{1 - r}{2} \\ N_2^e(r) &= \frac{r - 1}{2} \end{aligned} \tag{60}$$

Below, the element matrices for the water component are evaluated for 1-D linear elements. The matrices in equations (61) to (64) are used in the algebraic equations of the air and water components. The matrices in equations (65) to (69) are used in the algebraic equation of the energy component.

Conductivity Matrix/ Capillarity Matrix The conductivity matrix and capillarity matrix are equal. They are matrices of K-type integral: $\int \nabla \mathbf{N} f(u_i) \nabla \mathbf{N} d\Omega$.

$$\begin{aligned} \mathbf{K}_k^{\gamma s} &= \int_{\Omega^e} \nabla \mathbf{N}^T \left(\rho^\gamma X_k^\gamma \frac{k_{\mathsf{rel}}^\gamma \mathbf{k}}{\mu^\gamma} \right) \nabla \mathbf{N} \, d\Omega^e \\ &= \int_{V^e} \begin{bmatrix} \nabla \mathbf{N}_1 \\ \nabla \mathbf{N}_2 \end{bmatrix}^T \left(\rho^\gamma X_k^\gamma \frac{k_{\mathsf{rel}}^\gamma \mathbf{k}}{\mu^\gamma} \right) \begin{bmatrix} \nabla \mathbf{N}_1 & \nabla \mathbf{N}_2 \end{bmatrix} dV^e \\ &= A^e \int_{L^e} \begin{bmatrix} \partial \mathbf{N}_1 / \partial x' \\ \partial \mathbf{N}_2 / \partial x' \end{bmatrix}^T \left(\rho^\gamma X_k^\gamma \frac{k_{\mathsf{rel}}^\gamma \mathbf{k}_{x'}}{\mu^\gamma} \right) \begin{bmatrix} \partial \mathbf{N}_1 / \partial x' \\ \partial \mathbf{N}_2 / \partial x' \end{bmatrix}^T dx' \\ &= A^e \int_{-1}^{+1} \begin{bmatrix} \partial \mathbf{N}_1 / \partial r \\ \partial \mathbf{N}_2 / \partial r \end{bmatrix} [J_{1D}^{-1}]^T \left(\rho^\gamma X_k^\gamma \frac{k_{\mathsf{rel}}^\gamma \mathbf{k}_{x'}}{\mu^\gamma} \right) \end{aligned}$$

$$
\begin{aligned}
& \times [J_{1D}^{-1}] \begin{bmatrix} \partial \mathbf{N}_1/\partial x' \\ \partial \mathbf{N}_2/\partial x' \end{bmatrix}^T \det J_{1D}\, dr \\
= & \left(\rho^\gamma X_k^\gamma \frac{k_{\mathsf{rel}}^\gamma \mathbf{k}}{\mu^\gamma} \right)^e \frac{A^e}{L^e} \begin{bmatrix} 1 & 0 \\ 0 & 1 \end{bmatrix}^T
\end{aligned} \tag{61}
$$

Capacitance Matrix The capacitance matrix is a matrix of the type C-type integral: $\int \mathbf{N} f(u_i) \mathbf{N} d\Omega$

$$
\begin{aligned}
\mathbf{C}_k^\gamma &= \int_{\Omega^e} \mathbf{N}^T \left(n \rho^\gamma \hat{X}_k^\gamma \right) \mathbf{N}\, d\Omega^e \\
&= \int_{V^e} \begin{bmatrix} N_1 \\ N_2 \end{bmatrix}^T \left(n \rho^\gamma \hat{X}_k^\gamma \right) \begin{bmatrix} N_1 & N_2 \end{bmatrix} dV^e \\
&= A^e \int_{L^e} \begin{bmatrix} N_1 \\ N_2 \end{bmatrix}^T \left(n \rho^\gamma \hat{X}_k^\gamma \right) \begin{bmatrix} N_1 & N_2 \end{bmatrix} dx' \\
&= A^e \int_{-1}^{+1} \begin{bmatrix} N_1 \\ N_2 \end{bmatrix}^T \left(n \rho^\gamma \hat{X}_k^\gamma \right) \begin{bmatrix} N_1 & N_2 \end{bmatrix} \det J_{1D}\, dr \\
&= \left(n \rho^\gamma \hat{X}_k^\gamma \right)^e \frac{A^e L^e}{6} \begin{bmatrix} 2 & 1 \\ 1 & 2 \end{bmatrix}
\end{aligned} \tag{62}
$$

Component Diffusion Matrix The component diffusion matrix is a matrix of the type K-type integral: $\int \nabla \mathbf{N} f(u_i) \nabla \mathbf{N} d\Omega$

$$
\begin{aligned}
\mathbf{D}_k^\gamma &= \int_{\Omega^e} \nabla \mathbf{N}^T \left(n S^\gamma \rho^\gamma D^\gamma \right) \nabla \mathbf{N}\, d\Omega^e \\
&= \int_{V^e} \begin{bmatrix} \nabla N_1 \\ \nabla N_2 \end{bmatrix}^T \left(n S^\gamma \rho^\gamma D^\gamma \right) \begin{bmatrix} \nabla N_1 \\ \nabla N_2 \end{bmatrix}^T dV^e \\
&= A^e \int_{L^e} \begin{bmatrix} \partial N_1/\partial x' \\ \partial N_2/\partial x' \end{bmatrix}^T \left(n S^\gamma \rho^\gamma D^\gamma \right) \begin{bmatrix} \partial N_1/\partial x' \\ \partial N_2/\partial x' \end{bmatrix}^T dx' \\
&= A^e \int_{-1}^{+1} \begin{bmatrix} \partial N_1/\partial r \\ \partial N_2/\partial r \end{bmatrix}^T [J_{1D}^{-1}]^T \left(n S^\gamma \rho^\gamma D^\gamma \right) \\
&\quad \times [J_{1D}^{-1}] \begin{bmatrix} \partial N_1/\partial x' \\ \partial N_2/\partial x' \end{bmatrix}^T \det J_{1D}\, dx' \\
&= \left(n S^\gamma \rho^\gamma D^\gamma \right) \frac{A^e}{L^e} \begin{bmatrix} +1 & -1 \\ -1 & +1 \end{bmatrix}
\end{aligned} \tag{63}
$$

Gravity Forces Gravity forces are written as a matrix of g-type integral: $\int \nabla \mathbf{N} f(u_i) d\Omega$

$$
\begin{aligned}
\mathbf{g}_k^{\gamma s} &= \int_{\Omega^e} \nabla \mathbf{N}^T \left(\rho^\gamma X_k^\gamma \frac{k_{\mathsf{rel}}^\gamma \mathbf{k}}{\mu^\gamma} \rho^\gamma \mathbf{g} \right) d\Omega^e \\
&= \int_{V^e} \left[\begin{array}{c} \nabla \mathbf{N}_1 \\ \nabla \mathbf{N}_2 \end{array} \right]^T \left(\rho^\gamma X_k^\gamma \frac{k_{\mathsf{rel}}^\gamma \mathbf{k}}{\mu^\gamma} \rho^\gamma \mathbf{g} \right) dV^e \\
&= A^e \int_{L^e} \left[\begin{array}{c} \partial \mathbf{N}_1 / \partial x' \\ \partial \mathbf{N}_2 / \partial x' \end{array} \right]^T \left(\rho^\gamma X_k^\gamma \frac{k_{\mathsf{rel}}^\gamma \mathbf{k}}{\mu^\gamma} \rho^\gamma \mathbf{g} \right) dx' \\
&= A^e \int_{-1}^{+1} \left[\begin{array}{c} \partial \mathbf{N}_1 / \partial r \\ \partial \mathbf{N}_2 / \partial r \end{array} \right]^T [J_{1D}^{-1}]^T \left(\rho^\gamma X_k^\gamma \frac{k_{\mathsf{rel}}^\gamma \mathbf{k}}{\mu^\gamma} \rho^\gamma \mathbf{g} \right) \det J_{1D} \, dx' \\
&= \left(\rho^\gamma X_k^\gamma \frac{k_{\mathsf{rel}}^\gamma \mathbf{k}}{\mu^\gamma} \rho^\gamma \mathbf{g} \right) \frac{A^e}{L^e} \left[\begin{array}{c} -1 \\ +1 \end{array} \right] \qquad (64)
\end{aligned}
$$

Heat Capacitance Matrix for the Solid Phase The heat capacitance matrix is a matrix of the type C-type integral: $\int \mathbf{N} f(u_i) \mathbf{N} d\Omega$

$$
\begin{aligned}
\mathbf{C}_t^s &= \int_{\Omega^e} \mathbf{N}^T \left((1-n) \rho^s c^s \right) \mathbf{N} \, d\Omega^e \\
&= \int_{V^e} \left[\begin{array}{c} N_1 \\ N_2 \end{array} \right]^T \left((1-n) \rho^s c^s \right) \left[\begin{array}{cc} N_1 & N_2 \end{array} \right] dV^e \\
&= A^e \int_{L^e} \left[\begin{array}{c} N_1 \\ N_2 \end{array} \right]^T \left((1-n) \rho^s c^s \right) \left[\begin{array}{cc} N_1 & N_2 \end{array} \right] dx' \\
&= A^e \int_{-1}^{+1} \left[\begin{array}{c} N_1 \\ N_2 \end{array} \right]^T \left((1-n) \rho^s c^s \right) \left[\begin{array}{cc} N_1 & N_2 \end{array} \right] \det J_{1D} \, dr \\
&= \left((1-n) \rho^s c^s \right)^e \frac{A^e L^e}{6} \left[\begin{array}{cc} 2 & 1 \\ 1 & 2 \end{array} \right] \qquad (65)
\end{aligned}
$$

Heat Capacitance Matrix for the Gas or Liquid Phase The heat capacitance matrix is a matrix of the type C-type integral: $\int \mathbf{N} f(u_i) \mathbf{N} d\Omega$

$$
\begin{aligned}
\mathbf{C}_t^g &= \int_{\Omega^e} \mathbf{N}^T \left(n \rho^\gamma u^\gamma \right) \mathbf{N} \, d\Omega^e \\
&= \int_{V^e} \left[\begin{array}{c} N_1 \\ N_2 \end{array} \right]^T \left(n \rho^\gamma u^\gamma \right) \left[\begin{array}{cc} N_1 & N_2 \end{array} \right] dV^e \\
&= A^e \int_{L^e} \left[\begin{array}{c} N_1 \\ N_2 \end{array} \right]^T \left(n \rho^\gamma u^\gamma \right) \left[\begin{array}{cc} N_1 & N_2 \end{array} \right] dx'
\end{aligned}
$$

$$
\begin{aligned}
&= A^e \int_{-1}^{+1} \begin{bmatrix} N_1 \\ N_2 \end{bmatrix}^T (n\rho^\gamma u^\gamma) \begin{bmatrix} N_1 & N_2 \end{bmatrix} \det J_{1D}\, dr \\
&= (n\rho^\gamma u^\gamma)^e \frac{A^e L^e}{6} \begin{bmatrix} 2 & 1 \\ 1 & 2 \end{bmatrix} \qquad (66)
\end{aligned}
$$

Heat Conductivity Matrix The conductivity matrix is a matrix of K-type integral: $\int \nabla \mathbf{N} f(u_i) \nabla \mathbf{N} d\Omega$.

$$
\begin{aligned}
\mathbf{K}_t^\gamma &= \int_{\Omega^e} \nabla \mathbf{N}^T \left(nS^g\lambda^g + nS^l\lambda^l + (1-n)\lambda^s \right) \nabla \mathbf{N}\, d\Omega^e \\
&= \int_{V^e} \begin{bmatrix} \nabla \mathbf{N}_1 \\ \nabla \mathbf{N}_2 \end{bmatrix}^T \left(nS^g\lambda^g + nS^l\lambda^l + (1-n)\lambda^s \right) \begin{bmatrix} \nabla \mathbf{N}_1 \\ \nabla \mathbf{N}_2 \end{bmatrix}^T dV^e \\
&= A^e \int_{L^e} \begin{bmatrix} \partial \mathbf{N}_1/\partial x' \\ \partial \mathbf{N}_2/\partial x' \end{bmatrix}^T \left(nS^g\lambda^g + nS^l\lambda^l + (1-n)\lambda^s \right) \begin{bmatrix} \partial \mathbf{N}_1/\partial x' \\ \partial \mathbf{N}_2/\partial x' \end{bmatrix}^T dx' \\
&= A^e \int_{-1}^{+1} \begin{bmatrix} \partial \mathbf{N}_1/\partial r \\ \partial \mathbf{N}_2/\partial r \end{bmatrix}^T [J_{1D}^{-1}]^T \left(nS^g\lambda^g + nS^l\lambda^l + (1-n)\lambda^s \right) [J_{1D}^{-1}] \\
&\quad \times \begin{bmatrix} \partial \mathbf{N}_1/\partial x' \\ \partial \mathbf{N}_2/\partial x' \end{bmatrix}^T \det J_{1D}\, dr \\
&= \left(nS^g\lambda^g + nS^l\lambda^l + (1-n)\lambda^s \right)^e \frac{A^e}{L^e} \begin{bmatrix} +1 & -1 \\ -1 & +1 \end{bmatrix} \qquad (67)
\end{aligned}
$$

Heat advection matrix for the gas and liquid phase The conductivity matrix is a matrix of K-type integral: $\int \nabla \mathbf{N} f(u_i) \nabla \mathbf{N} d\Omega$.

$$
\begin{aligned}
\mathbf{K}_t^{\gamma s} &= \int_{\Omega^e} \nabla \mathbf{N}^T \left(\rho^\gamma \frac{k_{\mathsf{rel}}^\gamma \mathbf{k}}{\mu^\gamma} h^\gamma \right) \nabla \mathbf{N}\, d\Omega^e \\
&= \int_{V^e} \begin{bmatrix} \nabla \mathbf{N}_1 \\ \nabla \mathbf{N}_2 \end{bmatrix}^T \left(\rho^\gamma \frac{k_{\mathsf{rel}}^\gamma \mathbf{k}}{\mu^\gamma} h^\gamma \right) \begin{bmatrix} \nabla \mathbf{N}_1 & \nabla \mathbf{N}_2 \end{bmatrix} dV^e \\
&= A^e \int_{L^e} \begin{bmatrix} \partial \mathbf{N}_1/\partial x' \\ \partial \mathbf{N}_2/\partial x' \end{bmatrix}^T \left(\rho^\gamma \frac{k_{\mathsf{rel}}^\gamma \mathbf{k}}{\mu^\gamma} h^\gamma \right) \begin{bmatrix} \partial \mathbf{N}_1/\partial x' \\ \partial \mathbf{N}_2/\partial x' \end{bmatrix}^T dx' \\
&= A^e \int_{-1}^{+1} \begin{bmatrix} \partial \mathbf{N}_1/\partial r \\ \partial \mathbf{N}_2/\partial r \end{bmatrix}^T [J_{1D}^{-1}]^T \left(\rho^\gamma \frac{k_{\mathsf{rel}}^\gamma \mathbf{k}}{\mu^\gamma} h^\gamma \right) \\
&\quad \times [J_{1D}^{-1}] \begin{bmatrix} \partial \mathbf{N}_1/\partial x' \\ \partial \mathbf{N}_2/\partial x' \end{bmatrix}^T \det J_{1D}\, dr \\
&= \left(\rho^\gamma \frac{k_{\mathsf{rel}}^\gamma \mathbf{k}}{\mu^\gamma} h^\gamma \right)^e \frac{A^e}{L^e} \begin{bmatrix} +1 & -1 \\ -1 & +1 \end{bmatrix} \qquad (68)
\end{aligned}
$$

Component Diffusion Matrix The component diffusion matrix is a matrix of the type K-type integral: $\int \nabla \mathbf{N} f(u_i) \nabla \mathbf{N} d\Omega$

$$
\begin{aligned}
\mathbf{D}_k^\gamma &= \int_{\Omega^e} \nabla \mathbf{N}^T \left(\rho^\gamma D^\gamma h\gamma\right) \nabla \mathbf{N} \, d\Omega^e \\
&= \int_{V^e} \begin{bmatrix} \nabla N_1 \\ \nabla N_2 \end{bmatrix}^T \left(\rho^\gamma D^\gamma h\gamma\right) \begin{bmatrix} \nabla N_1 \\ \nabla N_2 \end{bmatrix}^T dV^e \\
&= A^e \int_{L^e} \begin{bmatrix} \partial N_1/\partial x' \\ \partial N_2/\partial x' \end{bmatrix}^T \left(\rho^\gamma D^\gamma h\gamma\right) \begin{bmatrix} \partial N_1/\partial x' \\ \partial N_2/\partial x' \end{bmatrix}^T dx' \\
&= A^e \int_{-1}^{+1} \begin{bmatrix} \partial N_1/\partial r \\ \partial N_2/\partial r \end{bmatrix}^T [J_{1D}^{-1}]^T \left(\rho^\gamma D^\gamma h\gamma\right) \\
&\quad \times [J_{1D}^{-1}] \begin{bmatrix} \partial N_1/\partial x' \\ \partial N_2/\partial x' \end{bmatrix}^T \det J_{1D} \, dx' \\
&= \left(\rho^\gamma D^\gamma h\gamma\right) \frac{A^e}{L^e} \begin{bmatrix} +1 & -1 \\ +1 & -1 \end{bmatrix}
\end{aligned} \tag{69}
$$

2.3.2 2-D Triangular Matrices

The shape functions for 2-D triangular elements are as shown in equation (shape triangle). The shape functions N_i are the area coordinates L_i, i.e. we have isoparametric elements.

$$
\begin{Bmatrix} N_1 \\ N_2 \\ N_3 \end{Bmatrix} = \frac{1}{2A} \begin{bmatrix} x_2y_3 - x_3y_2 & y_2 - y_3 & x_3 - x_2 \\ x_3y_1 - x_1y_3 & y_3 - y_1 & x_1 - x_3 \\ x_1y_2 - x_2y_1 & y_1 - y_2 & x_2 - x_1 \end{bmatrix} \begin{Bmatrix} 1 \\ x \\ y \end{Bmatrix} \tag{70}
$$

Now the derivatives of the shape functions can be written down.

$$
\frac{\partial \mathbf{N}}{\partial x} = \begin{Bmatrix} \dfrac{\partial N_1}{\partial x} = \dfrac{y_2 - y_3}{2A} \\ \dfrac{\partial N_2}{\partial x} = \dfrac{y_3 - y_1}{2A} \\ \dfrac{\partial N_3}{\partial x} = \dfrac{y_1 - y_2}{2A} \end{Bmatrix} \qquad \frac{\partial \mathbf{N}}{\partial y} = \begin{Bmatrix} \dfrac{\partial N_1}{\partial y} = \dfrac{x_3 - x_2}{2A} \\ \dfrac{\partial N_2}{\partial y} = \dfrac{x_1 - x_3}{2A} \\ \dfrac{\partial N_3}{\partial y} = \dfrac{x_2 - x_1}{2A} \end{Bmatrix} \tag{71}
$$

When element matrices have to be evaluated we are faced with integration of quantities defined in terms of area coordinates. Equation (72) shows that an exact calculation is possible for triangular elements.

$$
\iint_\Delta L_1^a L_2^b L_3^c dx dy = 2\Delta \frac{a!b!c!}{(a+b+c+2)!} \tag{72}
$$

The matrices below are evaluated for an orthotropic medium. The matrices in equations (73) to (76) are used in the algebraic equations of the air and water

components. The matrices in equations (77) to (81) are used in the algebraic equation of the energy component.

Conductivity Matrix/ Capillarity Matrix The conductivity matrix is a matrix of of K-type integral: $\int \nabla \mathbf{N} f(u_i) \nabla \mathbf{N} d\Omega$.

$$
\begin{aligned}
K_{ij}^e &= \int_{\Omega^e} \frac{\partial N_i}{\partial x_\alpha} \left(\rho^\gamma X_k^\gamma \frac{k_{\mathsf{rel}}^\gamma k_{\alpha\beta}}{\mu^\gamma} \right) \frac{\partial N_j}{\partial x_\beta} \, d\Omega^e \\
&= \int_{\Omega^e} \frac{\partial N_i}{\partial x} \left[\left(\rho^\gamma X_k^\gamma \frac{k_{\mathsf{rel}}^\gamma k_{xx}}{\mu^\gamma} \right) \frac{\partial N_j}{\partial x} + \left(\rho^\gamma X_k^\gamma \frac{k_{\mathsf{rel}}^\gamma k_{xy}}{\mu^\gamma} \right) \frac{\partial N_j}{\partial y} \right] d\Omega^e \\
&\quad + \int_{\Omega^e} \frac{\partial N_i}{\partial y} \left[\left(\rho^\gamma X_k^\gamma \frac{k_{\mathsf{rel}}^\gamma k_{yx}}{\mu^\gamma} \right) \frac{\partial N_j}{\partial x} + \left(\rho^\gamma X_k^\gamma \frac{k_{\mathsf{rel}}^\gamma k_{yy}}{\mu^\gamma} \right) \frac{\partial N_j}{\partial y} \right] d\Omega^e \\
&= \left(\rho^\gamma X_k^\gamma \frac{k_{\mathsf{rel}}^\gamma k_{xx}^e}{\mu^\gamma} \right) \int_{\Omega^e} \frac{\partial N_i}{\partial x} \frac{\partial N_j}{\partial x} \, d\Omega^e + \left(\rho^\gamma X_k^\gamma \frac{k_{\mathsf{rel}}^\gamma k_{yy}^e}{\mu^\gamma} \right) \int_{\Omega^e} \frac{\partial N_i}{\partial y} \frac{\partial N_j}{\partial y} \, d\Omega^e \\
&= \left(\rho^\gamma X_k^\gamma \frac{k_{\mathsf{rel}}^\gamma k_{xx}^e}{\mu^\gamma} \right) \int_{\Omega^e} \frac{y_j - y_k}{2A} \frac{y_k - y_i}{2A} \, d\Omega^e \\
&\quad + \left(\rho^\gamma X_k^\gamma \frac{k_{\mathsf{rel}}^\gamma k_{yy}^e}{\mu^\gamma} \right) \int_{\Omega^e} \frac{x_k - x_j}{2A} \frac{x_i - x_k}{2A} \, d\Omega^e \\
&= \left(\rho^\gamma X_k^\gamma \frac{k_{\mathsf{rel}}^\gamma k_{xx}^e}{4A\mu^\gamma} \right) (y_j - y_k)(y_k - y_i) \\
&\quad + \left(\rho^\gamma X_k^\gamma \frac{k_{\mathsf{rel}}^\gamma k_{yy}^e}{4A\mu^\gamma} \right) (x_k - x_j)(x_i - x_k)
\end{aligned}
$$

$$
\begin{aligned}
\mathbf{K}^e &= \int_{\Omega^e} \nabla \mathbf{N} \left(\rho^\gamma X_k^\gamma \frac{k_{\mathsf{rel}}^\gamma \mathbf{k}}{\mu^\gamma} \right) \nabla \mathbf{N}^T \, d\Omega^e \\
&= \left(\rho^\gamma X_k^\gamma \frac{k_{\mathsf{rel}}^\gamma k_{xx}^e}{4A\mu^\gamma} \right) \\
&\quad \times \begin{bmatrix} (y_2 - y_3)(y_2 - y_3) & (y_2 - y_3)(y_3 - y_1) & (y_2 - y_3)(y_1 - y_2) \\ (y_3 - y_1)(y_2 - y_3) & (y_3 - y_1)(y_3 - y_1) & (y_3 - y_1)(y_1 - y_2) \\ (y_1 - y_2)(y_2 - y_3) & (y_1 - y_2)(y_3 - y_1) & (y_1 - y_2)(y_1 - y_2) \end{bmatrix} \\
&+ \left(\rho^\gamma X_k^\gamma \frac{k_{\mathsf{rel}}^\gamma k_{yy}^e}{4A\mu^\gamma} \right) \\
&\quad \times \begin{bmatrix} (x_3 - x_2)(x_3 - x_2) & (x_3 - x_2)(x_1 - x_3) & (x_3 - x_2)(x_2 - x_1) \\ (x_1 - x_3)(x_3 - x_2) & (x_1 - x_3)(x_1 - x_3) & (x_1 - x_3)(x_2 - x_1) \\ (x_2 - x_1)(x_3 - x_2) & (x_2 - x_1)(x_1 - x_3) & (x_2 - x_1)(x_2 - x_1) \end{bmatrix}
\end{aligned}
\tag{73}
$$

Element capacitance matrix The capacitance matrix is a matrix of the type C-type integral: $\int \mathbf{N} f(u_i) \mathbf{N} d\Omega$

$$
\begin{aligned}
C_{ij}^e &= \int_{\Omega^e} N_i \left(n\rho^\gamma \hat{X}_k^\gamma \right)^e N_j \, d\Omega^e \\
&= \left(n\rho^\gamma \hat{X}_k^\gamma \right)^e A \begin{cases} \frac{1}{6} & i = j \\ \frac{1}{12} & i \neq j \end{cases} \\
\mathbf{C}^e &= \int_{\Omega^e} \mathbf{N} \left(n\rho^\gamma \hat{X}_k^\gamma \right)^e \mathbf{N} \, d\Omega^e \\
&= \left(n\rho^\gamma \hat{X}_k^\gamma \right)^e \int_{\Omega^e} \begin{bmatrix} N_1 N_1 & N_1 N_2 & N_1 N_3 \\ N_2 N_1 & N_2 N_2 & N_2 N_3 \\ N_3 N_1 & N_3 N_2 & N_3 N_3 \end{bmatrix} d\Omega^e \\
&= \left(n\rho^\gamma \hat{X}_k^\gamma \right)^e \frac{A}{12} \begin{bmatrix} 2 & 1 & 1 \\ 1 & 2 & 1 \\ 1 & 1 & 2 \end{bmatrix}
\end{aligned} \tag{74}
$$

Component Diffusion Matrix The component diffusion matrix is a matrix of the type K-type integral: $\int \nabla \mathbf{N} f(u_i) \nabla \mathbf{N} d\Omega$

$$
\begin{aligned}
K_{ij}^e &= \int_{\Omega^e} \frac{\partial N_i}{\partial x_\alpha} \left(nS^\gamma \rho^\gamma D_{\alpha\beta}^\gamma \right) \frac{\partial N_j}{\partial x_\beta} \, d\Omega^e \\
&= \int_{\Omega^e} \frac{\partial N_i}{\partial x} \left[\left(nS^\gamma \rho^\gamma D_{xx}^\gamma \right) \frac{\partial N_j}{\partial x} + \left(nS^\gamma \rho_{xy}^\gamma D^\gamma \right) \frac{\partial N_j}{\partial y} \right] d\Omega^e \\
&\quad + \int_{\Omega^e} \frac{\partial N_i}{\partial y} \left[\left(nS^\gamma \rho^\gamma D_{yx}^\gamma \right) \frac{\partial N_j}{\partial x} + \left(nS^\gamma \rho^\gamma D_{yy}^\gamma \right) \frac{\partial N_j}{\partial y} \right] d\Omega^e \\
&= \left(nS^\gamma \rho^\gamma D_{xx}^{\gamma,e} \right) \int_{\Omega^e} \frac{\partial N_i}{\partial x} \frac{\partial N_j}{\partial x} \, d\Omega^e + \left(nS^\gamma \rho^\gamma D_{yy}^{\gamma,e} \right) \int_{\Omega^e} \frac{\partial N_i}{\partial y} \frac{\partial N_j}{\partial y} \, d\Omega^e \\
&= \left(nS^\gamma \rho^\gamma D_{xx}^{\gamma,e} \right) \int_{\Omega^e} \frac{y_j - y_k}{2A} \frac{y_k - y_i}{2A} \, d\Omega^e \\
&\quad + \left(nS^\gamma \rho^\gamma D_{yy}^{\gamma,e} \right) \int_{\Omega^e} \frac{x_k - x_j}{2A} \frac{x_i - x_k}{2A} \, d\Omega^e \\
&= \frac{\left(nS^\gamma \rho^\gamma D_{xx}^{\gamma,e} \right)}{4A} (y_j - y_k)(y_k - y_i) + \frac{\left(nS^\gamma \rho_{yy}^{\gamma,e} D^\gamma \right)}{4A} (x_k - x_j)(x_i - x_k)
\end{aligned}
$$

$$
\begin{aligned}
\mathbf{K}^e &= \int_{\Omega^e} \nabla\mathbf{N}\ (nS^\gamma\rho^\gamma D^\gamma)\ \nabla\mathbf{N}^T\, d\Omega^e \\
&= \frac{(nS^\gamma\rho^\gamma D^{\gamma,e}_{xx})}{4A}\begin{bmatrix} (y_2-y_3)(y_2-y_3) & (y_2-y_3)(y_3-y_1) & (y_2-y_3)(y_1-y_2) \\ (y_3-y_1)(y_2-y_3) & (y_3-y_1)(y_3-y_1) & (y_3-y_1)(y_1-y_2) \\ (y_1-y_2)(y_2-y_3) & (y_1-y_2)(y_3-y_1) & (y_1-y_2)(y_1-y_2) \end{bmatrix} \\
&+ \frac{(nS^\gamma\rho^\gamma D^{\gamma,e}_{yy})}{4A}\begin{bmatrix} (x_3-x_2)(x_3-x_2) & (x_3-x_2)(x_1-x_3) & (x_3-x_2)(x_2-x_1) \\ (x_1-x_3)(x_3-x_2) & (x_1-x_3)(x_1-x_3) & (x_1-x_3)(x_2-x_1) \\ (x_2-x_1)(x_3-x_2) & (x_2-x_1)(x_1-x_3) & (x_2-x_1)(x_2-x_1) \end{bmatrix}
\end{aligned} \tag{75}
$$

Gravity Forces Gravity forces are written as a matrix of g-type integral: $\int \nabla\mathbf{N} f(u_i) d\Omega$.

$$
\begin{aligned}
\mathbf{k}^e &= \int_{\Omega^e} \nabla\mathbf{N}\left(\rho^\gamma X^\gamma_k \frac{k^\gamma_{\mathsf{rel}}\mathbf{k}}{\mu^\gamma}\rho^\gamma\mathbf{g}\right) d\Omega^e \\
&= \begin{bmatrix} \frac{\partial\mathbf{N}_1}{\partial x} & \frac{\partial\mathbf{N}_1}{\partial z} \\ \frac{\partial\mathbf{N}_2}{\partial x} & \frac{\partial\mathbf{N}_1}{\partial z} \\ \frac{\partial\mathbf{N}_3}{\partial x} & \frac{\partial\mathbf{N}_1}{\partial z} \end{bmatrix}\left(\rho^\gamma X^\gamma_k \frac{k^\gamma_{\mathsf{rel}}}{2\mu^\gamma}\rho^\gamma\right)\begin{bmatrix} k_{xx} & k_{xz} \\ k_{zx} & k_{zz} \end{bmatrix}\begin{bmatrix} 0 \\ g \end{bmatrix} \\
&= \begin{bmatrix} \frac{\partial\mathbf{N}_1}{\partial x} & \frac{\partial\mathbf{N}_1}{\partial z} \\ \frac{\partial\mathbf{N}_2}{\partial x} & \frac{\partial\mathbf{N}_1}{\partial z} \\ \frac{\partial\mathbf{N}_3}{\partial x} & \frac{\partial\mathbf{N}_1}{\partial z} \end{bmatrix}\left(\rho^\gamma X^\gamma_k \frac{k^\gamma_{\mathsf{rel}}}{2\mu^\gamma}\rho^\gamma\right)\begin{bmatrix} 0 \\ gk_{zz} \end{bmatrix} \\
&= gk_{zz}\left(\rho^\gamma X^\gamma_k \frac{k^\gamma_{\mathsf{rel}}}{2\mu^\gamma}\rho^\gamma\right)\begin{bmatrix} \frac{\partial\mathbf{N}_1}{\partial z} \\ \frac{\partial\mathbf{N}_2}{\partial z} \\ \frac{\partial\mathbf{N}_3}{\partial z} \end{bmatrix} \\
&= \frac{1}{2A}gk_{zz}\left(\rho^\gamma X^\gamma_k \frac{k^\gamma_{\mathsf{rel}}}{2\mu^\gamma}\rho^\gamma\right)\begin{bmatrix} x_3-x_2 \\ x_1-x_3 \\ x_2-x_1 \end{bmatrix}
\end{aligned} \tag{76}
$$

Heat Capacitance Matrix for the Solid Phase The capacitance matrix is a matrix of the type C-type integral: $\int \mathbf{N} f(u_i)\mathbf{N} d\Omega$

$$
\begin{aligned}
C^e_{ij} &= \int_{\Omega^e} N_i\left((1-n)\rho^s c^s\right)^e N_j\, d\Omega^e \\
&= \left((1-n)\rho^s c^s\right)^e A\begin{cases} \frac{1}{6} & i=j \\ \frac{1}{12} & i\neq j \end{cases} \\
\mathbf{C}^e &= \int_{\Omega^e} \mathbf{N}\left((1-n)\rho^s c^s\right)^e \mathbf{N}\, d\Omega^e
\end{aligned}
$$

$$
\begin{aligned}
&= ((1-n)\rho^s c^s)^e \int_{\Omega^e} \begin{bmatrix} N_1N_1 & N_1N_2 & N_1N_3 \\ N_2N_1 & N_2N_2 & N_2N_3 \\ N_3N_1 & N_3N_2 & N_3N_3 \end{bmatrix} d\Omega^e \\
&= ((1-n)\rho^s c^s)^e \frac{A}{12} \begin{bmatrix} 2 & 1 & 1 \\ 1 & 2 & 1 \\ 1 & 1 & 2 \end{bmatrix}
\end{aligned} \tag{77}
$$

Heat Capacitance Matrix for the Gas or Liquid Phase The capacitance matrix is a matrix of the type C-type integral: $\int \mathbf{N} f(u_i) \mathbf{N} d\Omega$.

$$
\begin{aligned}
C_{ij}^e &= \int_{\Omega^e} N_i \left(n\rho^\gamma u^\gamma\right)^e N_j \, d\Omega^e = \left(n\rho^\gamma u^\gamma\right)^e A \begin{cases} \frac{1}{6} & i = j \\ \frac{1}{12} & i \neq j \end{cases} \\
\mathbf{C}^e &= \int_{\Omega^e} \mathbf{N} \left(n\rho^\gamma u^\gamma\right)^e \mathbf{N} \, d\Omega^e = \left(n\rho^\gamma u^\gamma\right)^e \int_{\Omega^e} \begin{bmatrix} N_1N_1 & N_1N_2 & N_1N_3 \\ N_2N_1 & N_2N_2 & N_2N_3 \\ N_3N_1 & N_3N_2 & N_3N_3 \end{bmatrix} d\Omega^e \\
&= \left(n\rho^\gamma u^\gamma\right)^e \frac{A}{12} \begin{bmatrix} 2 & 1 & 1 \\ 1 & 2 & 1 \\ 1 & 1 & 2 \end{bmatrix}
\end{aligned} \tag{78}
$$

Heat Conductivity Matrix The heat conductivity matrix is a matrix of the type K-type integral: $\int \nabla \mathbf{N} f(u_i) \nabla \mathbf{N} d\Omega$

$$
\begin{aligned}
\mathbf{K}^e &= \int_{\Omega^e} \nabla \mathbf{N} \left(\rho^\gamma \frac{k_{\mathbf{rel}}^\gamma \mathbf{k}}{\mu^\gamma} h^\gamma \right) \nabla \mathbf{N}^T \, d\Omega^e \\
&= \frac{1}{4A} \left(\rho^\gamma \frac{k_{\mathbf{rel}}^\gamma \mathbf{k}_{xx}}{\mu^\gamma} h^\gamma \right) * \\
&\quad \begin{bmatrix} (y_2-y_3)(y_2-y_3) & (y_2-y_3)(y_3-y_1) & (y_2-y_3)(y_1-y_2) \\ (y_3-y_1)(y_2-y_3) & (y_3-y_1)(y_3-y_1) & (y_3-y_1)(y_1-y_2) \\ (y_1-y_2)(y_2-y_3) & (y_1-y_2)(y_3-y_1) & (y_1-y_2)(y_1-y_2) \end{bmatrix} \\
&+ \frac{1}{4A} \left(\rho^\gamma \frac{k_{\mathbf{rel}}^\gamma \mathbf{k}_{yy}}{\mu^\gamma} h^\gamma \right) * \\
&\quad \begin{bmatrix} (x_3-x_2)(x_3-x_2) & (x_3-x_2)(x_1-x_3) & (x_3-x_2)(x_2-x_1) \\ (x_1-x_3)(x_3-x_2) & (x_1-x_3)(x_1-x_3) & (x_1-x_3)(x_2-x_1) \\ (x_2-x_1)(x_3-x_2) & (x_2-x_1)(x_1-x_3) & (x_2-x_1)(x_2-x_1) \end{bmatrix}
\end{aligned} \tag{79}
$$

Heat advection matrix for the gas and liquid phase The heat conductivity matrix is a matrix of the type K-type integral: $\int \nabla \mathbf{N} f(u_i) \nabla \mathbf{N} d\Omega$

$$
\begin{aligned}
\mathbf{K}^e &= \int_{\Omega^e} \nabla \mathbf{N} \left(nS^g \lambda^g + nS^l \lambda^l + (1-n)\lambda^s \right) \nabla \mathbf{N}^T \, d\Omega^e \\
&= \frac{1}{4A} \left(nS^g \lambda^g_{xx} + nS^l \lambda^l_{xx} + (1-n)\lambda^s_{xx} \right) * \\
&\quad \begin{bmatrix} (y_2-y_3)(y_2-y_3) & (y_2-y_3)(y_3-y_1) & (y_2-y_3)(y_1-y_2) \\ (y_3-y_1)(y_2-y_3) & (y_3-y_1)(y_3-y_1) & (y_3-y_1)(y_1-y_2) \\ (y_1-y_2)(y_2-y_3) & (y_1-y_2)(y_3-y_1) & (y_1-y_2)(y_1-y_2) \end{bmatrix} \\
&+ \frac{1}{4A} \left(nS^g \lambda^g_{yy} + nS^l \lambda^l_{yy} + (1-n)\lambda^s_{yy} \right) * \\
&\quad \begin{bmatrix} (x_3-x_2)(x_3-x_2) & (x_3-x_2)(x_1-x_3) & (x_3-x_2)(x_2-x_1) \\ (x_1-x_3)(x_3-x_2) & (x_1-x_3)(x_1-x_3) & (x_1-x_3)(x_2-x_1) \\ (x_2-x_1)(x_3-x_2) & (x_2-x_1)(x_1-x_3) & (x_2-x_1)(x_2-x_1) \end{bmatrix}
\end{aligned} \tag{80}
$$

Component Diffusion Matrix The component diffusion matrix is a matrix of the type K-type integral: $\int \nabla \mathbf{N} f(u_i) \nabla \mathbf{N} d\Omega$

$$
\begin{aligned}
K^e_{ij} &= \int_{\Omega^e} \frac{\partial N_i}{\partial x_\alpha} \left(\rho^\gamma h \gamma D^\gamma_{\alpha\beta} \right) \frac{\partial N_j}{\partial x_\beta} \, d\Omega^e \\
&= \int_{\Omega^e} \frac{\partial N_i}{\partial x} \left[\left(\rho^\gamma h \gamma D^\gamma_{xx} \right) \frac{\partial N_j}{\partial x} + \left(\rho^\gamma h \gamma D^\gamma_{xy} \right) \frac{\partial N_j}{\partial y} \right] d\Omega^e \\
&\quad + \int_{\Omega^e} \frac{\partial N_i}{\partial y} \left[\left(\rho^\gamma h \gamma D^\gamma_{yx} \right) \frac{\partial N_j}{\partial x} + \left(\rho^\gamma h \gamma D^\gamma_{yy} \right) \frac{\partial N_j}{\partial y} \right] d\Omega^e \\
&= \left(\rho^\gamma h \gamma D^{\gamma,e}_{xx} \right) \int_{\Omega^e} \frac{\partial N_i}{\partial x} \frac{\partial N_j}{\partial x} \, d\Omega^e + \left(\rho^\gamma h \gamma D^{\gamma,e}_{yy} \right) \int_{\Omega^e} \frac{\partial N_i}{\partial y} \frac{\partial N_j}{\partial y} \, d\Omega^e \\
&= \left(\rho^\gamma h \gamma D^{\gamma,e}_{xx} \right) \int_{\Omega^e} \frac{y_j - y_k}{2A} \frac{y_k - y_i}{2A} \, d\Omega^e + \left(\rho^\gamma h \gamma D^{\gamma,e}_{yy} \right) \int_{\Omega^e} \frac{x_k - x_j}{2A} \frac{x_i - x_k}{2A} \, d\Omega^e \\
&= \frac{\left(\rho^\gamma h \gamma D^{\gamma,e}_{xx} \right)}{4A} (y_j - y_k)(y_k - y_i) + \frac{\left(\rho^\gamma h \gamma D^{\gamma,e}_{yy} \right)}{4A} (x_k - x_j)(x_i - x_k)
\end{aligned}
$$

$$
\begin{aligned}
\mathbf{K}^e &= \int_{\Omega^e} \nabla\mathbf{N}\ (\rho^\gamma h \gamma D^\gamma)\ \nabla\mathbf{N}^T\, d\Omega^e \\
&= \frac{(\rho^\gamma h \gamma D^{\gamma,e}_{xx})}{4A}
\begin{bmatrix}
(y_2-y_3)(y_2-y_3) & (y_2-y_3)(y_3-y_1) & (y_2-y_3)(y_1-y_2) \\
(y_3-y_1)(y_2-y_3) & (y_3-y_1)(y_3-y_1) & (y_3-y_1)(y_1-y_2) \\
(y_1-y_2)(y_2-y_3) & (y_1-y_2)(y_3-y_1) & (y_1-y_2)(y_1-y_2)
\end{bmatrix} \\
&+ \frac{(\rho^\gamma h \gamma D^{\gamma,e}_{yy})}{4A}
\begin{bmatrix}
(x_3-x_2)(x_3-x_2) & (x_3-x_2)(x_1-x_3) & (x_3-x_2)(x_2-x_1) \\
(x_1-x_3)(x_3-x_2) & (x_1-x_3)(x_1-x_3) & (x_1-x_3)(x_2-x_1) \\
(x_2-x_1)(x_3-x_2) & (x_2-x_1)(x_1-x_3) & (x_2-x_1)(x_2-x_1)
\end{bmatrix}
\end{aligned}
\tag{81}
$$

2.4 System Matrix and Right Hand Side Vector

The system matrix assembles the element matrices. The form of the system matrix and right hand side (RHS) vector depends on the chosen coupling scheme. Equation 82 shows a completely partitioned coupling scheme. Equation 83 shows a coupling scheme, where the primary variables for the air and water components, i.e. gas pressure and gas saturation are coupled and temperature is calculated separately.

$$
\begin{aligned}
[\theta(\mathbf{K}^{ls}_w + \mathbf{K}^{gs}_w)][\hat{\mathbf{p}}^g] &= RHS_P \\
\left[\frac{1}{\Delta t}\left(\mathbf{C}^g_w - \mathbf{C}^l_w\right) - \mathbf{K}^{ls}_w \frac{\partial p_\mathbf{c}}{\partial S}\right][\hat{\mathbf{S}}^g] &= RHS_S \\
\left(\frac{1}{\Delta t}\mathbf{C}^s_t - \theta\mathbf{K}^s_t\right)[\hat{\mathbf{T}}]^{n+1}_{\tau+1} &= RHS_T
\end{aligned}
\tag{82}
$$

$$
\begin{aligned}
\begin{bmatrix}
\theta(\mathbf{K}^{gs}_a + \mathbf{K}^{ls}_a) & \frac{1}{\Delta t}\left(\mathbf{C}^g_a - \mathbf{C}^l_a\right) - \mathbf{K}^{ls}_a \frac{\partial p_\mathbf{c}}{\partial S} \\
\theta(\mathbf{K}^{gs}_w + \mathbf{K}^{ls}_w) & \frac{1}{\Delta t}\left(\mathbf{C}^g_w - \mathbf{C}^l_w\right) - \mathbf{K}^{ls}_w \frac{\partial p_\mathbf{c}}{\partial S}
\end{bmatrix}
\begin{bmatrix} \hat{\mathbf{p}}^g \\ \hat{\mathbf{S}}^g \end{bmatrix} &= RHS \\
\left(\frac{1}{\Delta t}\mathbf{C}^s_t - \theta\mathbf{K}^s_t\right)[\hat{\mathbf{T}}]^{n+1}_{\tau+1} &= RHS_T
\end{aligned}
\tag{83}
$$

3 Code Implementation

To calculate the matrix, the code needs to gain access to the variables. A summary of all state variables and material properties and their implementation into the Rockflow code is shown in Appendix 1. The following sections show the Rockflow functions for state variables and material functions.

3.1 State Variables

In this section the implementation of the state variables is briefly explained . The aim of this section is to enable the reader to understand where these variables can be found in the program. Program details are not in the scope of this section. Table 3 gives an overview of the state variables.

Variable	Function	Used in	Defined in
X_k^γ	`MPCGetMassFraction()`	MPC	KER_MPC
$p_{w,sat}^g$	`MATCalcVapourPressure`	MPC/ENT	MAT_FP
h_k^γ	`MATGetEnthalpy`	ENT	MAT_FP
h^γ	`MATCalcEnthalpyPhase`	ENT	MAT_FP

Table 3: Overview of data access for state variables

3.1.1 Vapour pressure–$p_{w,sat}^g$

Vapour pressure is calculated according to the Claudius Clapeyron equation, using the vapourisation enthalpy library described in section 1.3.

The functions for vapour pressure are located in the MAT_FP kernel of the program, as shown in Table 4.

Description	Function	RF Object
Calculation of vapour pressure	`MATCalcVapourPressure`	MAT_FP

Table 4: Vapour pressure functions

3.1.2 Mass Fractions–X_k^γ

To obtain mass fraction results, we implement the structure shown in Table 5 into the program.

Description	Function	RF Object
Calculation	`MATCalcMassFraction`	MAT-FP
Data access in kernel for finite element matrix calculation	`MPCGetMassFraction`	MPC
Specification of data access	`MPCGetMassFraction = MODGetMassFractionXX`	MOD

Table 5: Mass fraction functions

3.1.3 Internal energy

The function for internal energy are located in the MAT_FP kernel of the program, as shown in Table 6.

Description	Function	RF Object
Calculation of vapour pressure	`MATGetInternalEnergy`	MAT_FP

Table 6: Vapour pressure functions

3.1.4 Phase enthalpy–h^γ

The function for the calculation of all enthalpies is located in the MAT_FP kernel of the program. Table 7 shows the Rockflow functions for enthalpy calculation. The function for the calculation of partial enthalpies works by formula and uses the library for the vapourisation enthalpy. The phase enthalpies are calculated using the mass fraction functions and the partial enthalpies.

Description	Function	RF Object
Calculation of partial enthalpies	`MATGetEnthalpy`	MAT_FP
Calculation of phase enthalpies	`MATCalcEnthalpyPhase`	MAT_FP

Table 7: Enthalpy functions

3.1.5 Vapourisation Enthalpy–h_w^g

As described in Section 1.3 of this report, vapourisation enthalpy is only dependent on temperature and can therefore be tabulated. Therefore, as already mentioned, a library can be used to calculate the function. The library files are included in the model:

```
#include "steam67.h"
#include "mathlib.h"
```

There is no function for the vapourisation enthalpy, as it is calculated directly in the function for vapour pressure and in the function for enthalpy.

3.2 Material Properties

In this section the implementation of material functions is briefly explained . Table 8 gives an overview of the material properties.

Variable	Function	Used in	Defined in
ρ^γ	`GetFluidDensity()`	MAT_FP	MAT_FP
μ^γ	`GetFluidViscosity()`	MMP/MPC	MAT_FP
A^e	`GetElementExchangeArea()`	ELE	ELE
$\mathbf{k}$	`GetPermeabilityTensor()`	ENT/MMP/MPC	MAT_MP
k^γ_{rel}	`CalcAllRelativePermeabilities()`	MAT_MP	MAT_MP
n	`GetSoilPorosity()`	MAT_MP	MAT_MP
S^γ	`MPCGetNodeSaturation()`	MOD	MOD
D^γ	`MATGetDiffusionCoefficient()`	MAT_TP	MAT_TP

Table 8: Overview of data access for material properties used in element matrices

The access to material functions has been changed to a more direct access. Tables 9 and 10 show the old and new procedure. Before, the functions had variable parameter lists, which is no longer the case. The parameters are extracted with the help of a `MODGetNodeIndexX` function, which is defined in the model object. The advantages of this method are:

- more direct, as one function less to hand over
- saves computation time, as no variable parameter lists have to be evaluated.

The user wishing to calculate material functions with this method should add the get function `MODGetNodeIndexParameter_XX` to the model, XX being the model name.

Description	Function	RF Object
FE kernel needs material function for FE matrix calculation	`GetMatFunction()`	MPC/ENT
Calculation of material function	`CalcMatFunction`	MAT_FP
Specification of model specific parameters	`GetMatFunction=` `GetCalcMatFunctionXX` `↦CalcMatFunction`	MOD

Table 9: Old procedure for material function data access

Description	Function	RF Object
Access to material function in kernel	`rho=MATCalcMatFunction()`	MPC/ENT
Calculation of material function	`MATCalcMatFunction()`	MAT_FP
Overwriting	`MATGetIndexParameter=` `MODGetNodeIndexParameter_XX`	MOD
Definition of model function for access to node index	`MODGetNodeIndexParameter_XX`	MOD

Table 10: New procedure for material function data access

The data input for material properties (fluid properties only to date) has also changed with the introduction of subkeywords. We hope, that this makes the input easier to follow. The first number in the subkeyword is the calculation method that will be used. This is followed for the parameters needed by the particular method. Below, parameter example values are given for each method currently implemented.

```
#FLUID_PROPERTIES_NEW
$DENSITY
0   1000.           ; rho\_0: reference density,
1   1000.  1e-4     ; rho\_0,drho/dp:compressibility
2
3
10 1000.  0.2       ; rho\_0,drho/dC:expansion coeff.
11 1000.  0.2  1e-4 ; rho\_0,drho/dC,drho/dT:therm. expan. coeff.
12 1000.  1e-4      ; rho\_0,drho/dT
13                  ; no parameters needed

$VISCOSITY
 0   1e-3           ; my\_0: reference viscosity

$HEAT_CAPACITY
 0   4800.          ; c\_0: reference heat capacity

$HEAT_CONDUCTIVITY
0   0.6             ; lamda\_0: reference heat conductivity
```

3.2.1 Fluid phase density

Fluid density can be computed in one of the following ways in the Rockflow code :

Case	Function
0	$\rho^\alpha = \rho_0^\alpha$
1	$\rho^\alpha(p) = \rho_0^\alpha + \beta_p^\alpha p^\alpha$
2	$\rho^\alpha(C) = \rho_0^\alpha + max(\rho^\alpha(C), \rho_0^\alpha$
3	$\rho^\alpha(C_i) = \rho_0^\alpha + max(\rho_i^\alpha(C_i), \rho_0^\alpha$
8	Template
9	Template
10	$\rho^\alpha(C) = \rho_0^\alpha + \frac{\partial \rho^\alpha}{\partial C}(C - C_0)$
11	$\rho^\alpha(C,T) = \rho_0^\alpha + max(C,0)\beta_p + max(T,0)\beta_T$
12	$\rho^\alpha(T) = \rho_0^\alpha + \frac{\partial \rho}{\partial T}(T - T_0)$
13	$\rho^\alpha(p^g,T) = \frac{M_a}{RT}p^g + \frac{(M_w - M_a)}{RT}p_{w,sat}^g(T)$

Table 11: Fluid density calculation methods implemented in Rockflow

Data access

The implementation of fluid density functions into the Rockflow code is as follows.

Description	Function	RF Object
Access to fluid density in kernel	rho=MATCalcFluidDensity()	MPC/ENT
Calculation of density	`MATCalcFluidDensity`	MAT
Overwriting	`MATGetNodeIndexTemperature=` `MODGetNodeIndexTemperature_XX`	MOD
Definition of model function for access to node index	`MODGetNodeIndexTemperature_XX`	MOD

Table 12: Fluid density functions in Rockflow

3.2.2 Fluid Viscosity

Fluid viscosity can be computed in one of the ways illustrated in Table 13. To obtain fluid viscosity results, the structure shown in Table 14 is implemented in the program.

Case	Function
0	$\mu^{\alpha}(p) = \mu_0^{\alpha}$
1	$\mu^{\alpha}(p) = GetCurveValue(\text{get\_fp\_curve(fp)}, 0, p_{\text{avg}}, gueltig)$
2	$\mu^{\alpha}(p) = \mu_0^{\alpha} + p_{avg} \cdot \frac{d\mu}{dp}$
8	Template
10	$\mu^{\alpha}(C,T) = \frac{\mu}{f1+f2}\ f1 = f(C), f2 = f(T)$

Table 13: Fluid viscosity calculation methods implemented in Rockflow

Description	Function	RF Object
FE-Kernel needs fluid viscosity for finite element matrix calculation	`GetFluidViscosity`	MPL
Calculation of viscosity using one of the cases as described above	`CalcFluidViscosity`	MAT
Specification of model specific parameters for fluid viscosity calculation	`GetFluidViscosity = THMGetFluidViscosity`	MOD

Table 14: Fluid viscosity functions in Rockflow

3.2.3 Material Properties contained in the input file

The material properties that are used in our application and that are provided by the user in the input file are

- capillary pressure
- permeability
- relative permeability
- specific heat capacity

- thermal conductivity
- diffusion coefficient

The input file contains reference to curves for capillary pressure relationships and for relative permeability relationships. These are summerised in Tables 15 and 16.

	$p_c(S)$ model					
cp[0]		cp[1]	cp[2]	cp[3]	cp[4]	cp[5]
0	No capillary pressure $p_c = 0$					
1	User-defined curve	Curve				
2	Linear function	S_r^w	$S_{\max}^w$	$p_{c\max}$		
3	Parabolic function	S_r^w	$S_{\max}^w$	a	b	
4	van Genuchten (1980)	S_r^w	$S_{\max}^w$	α	m	n
5	Haverkamp et al. (1977)	S_r^w	$S_{\max}^w$	A	b	c
6	Brooks & Corey (1966)	S_r^w	p_b	λ		

Table 15: Rockflow models for capillary pressure

	$k_{rel}(S)$ model						
rp[0]		rp[1]	rp[2]	rp[3]	rp[4]	rp[5]	rp[6]
0	Perfectly mobile phases						
1	User-defined curve	1st	2nd	...			
2	Linear function	S_1^g	S_2^g		S_1^w	S_2^w	
3	Parabolic function	S_1^g	S_2^g	a	S_1^w	S_2^w	b
4	van Genuchten (1980)	S_r^w	$S_{\max}^w$	α	m	n	
5	Haverkamp et al. (1977)	S_r^w	$S_{\max}^w$	α	A	β	
6	Brooks & Corey (1966)	S_r^w	$S_{\max}^w$				

Table 16: Rockflow models for relative premeability

The user has a lot of freedom in the definition of the material properties functions. The text below is a sample extract of an input file. Input files that include material properties have the extension `.rfd`. In general, function 0 denotes a constant value. The keys are in the Rockflow manual.

```
; 7 Materials
------------------------------------------------------------
#REFERENCE_CONDITIONS
 9.810000  0.000000  101325.000000
#FLUID_PROPERTIES ; gas
 0  1.15 ; density function, parameter
 0  1.800000e-005 ; viscosity function, parameter
```

```
 3.000000e+003  1.000000e+000 ; heat capacity, heat conductivity
#FLUID_PROPERTIES ; liquid
 0  1.050000e+003 ; density function, parameter
 0  0.0012 ; viscosity function, parameter
 0.000000 ; real gas factor
 4.000000e+003  2.000000e+000 ; heat capacity, heat conductivity
#SOIL_PROPERTIES ; rock
 2  1.0                       ; dimension, (thickness),
 0                            ; porosity model
 3.79000e-001  1.000000e+000  ; porosity, tortuosity
 0.000000e-006 ; storativity
 0  0  7.68895e-021 ; permeability model, permeability tensor, permeabilities
 4.000000e+000  0.1  1.0  0.37  0.77  4.37  0.000000e+000 ; k-S function
 4.000000e+000  0.1  1.0  0.37  0.77  4.37  0.000000e+000 ; p-S function
 0.000000e+000  0.000000e+000 ; mass dispersion parameters
 3.000000e+000  0.300000e+000 ; heat dispersion parameters
 3.000000e+003  1.000000e+003 ; rock density, heat capacity
 0  3.000000e+000 ; heat conductivity parameters
```

3.3 Finite Element Matrices

The matrices for the water and air component are calculated together in the MPC kernel. This is possible as the matrices are the same for both components. The matrices for the energy equation are calculated separately in the ENT kernel.

The Rockflow function `MPCCalcElementMatrix1D` element matrices of a 1-D linear element of kernel MPC. The Rockflow function `MPCCalcElementMatrix2DTriangle` calculates the finite element matrices of a 2-D linear triangular element of kernel MPC.

The Rockflow function `ENTCalcElementMatrix1D` element matrices of a 1-D linear element of kernel ENT. The Rockflow function `ENTCalculateElementMatrix2DTriangle` calculates the finite element matrices of a 2-D linear triangular element of kernel MPC.

The matrices calculated by the functions are:

- hydraulic conductance matrix
- hydraulic capacitance matrix
- capillary forces
- gravity forces
- vapour diffusion term

The input parameters in hiarchal order are:

- element number
- phase
- component number
- matrix type

The matrices are calculated for a given component first. This means that the component number is set, then the phase number is set and for that component and phase, that matrix type is calculated for all elements. Then the next phase is chosen, and calculation is carried out for all elements, then the component is changed.

3.4 System Matrix and Right Hand Side Vector

The Rockflow kernel, in which the system matrix and RHS vector are calculated is `cgs_mpc.c/h` and `cgs_ent.c/h`. The Rockflow functions `MPCMakeEquationSystem` and `KERMakeEquationSystemENT` calls for calculating element matrices, calculating RHS terms, assembling the system matrix, incorporating boundary conditions and source terms. The Rockflow functions needed for this are:

- `MPCCalculateElementMatrices` / `KERCalculateElementMatricesENT`
- `MPCAssembleSystemMatrix` / `KERAssembleSystemMatrixENT`
- `MPCIncorporateBoundaryConditions` / `KERIncorporateBoundaryConditionsENT`
- `MPCIncorporateSourceTerms` / `KERIncorporateSourceTermsENT`

The function `MPCCalculateElementMatrices` was described in the previous section. The function `MPCAssembleSystemMatrix` assembles the system matrix by calling up the function that makes the element entries. Boundary conditions and source terms are incorporated by `MPCIncorporateBoundaryConditions` and `MPCIncorporateSourceTerms`.

4 Examples

In this section, two examples are presented. The first one shows evaporation from a system. The second one is a two-dimensional example from the DECOVALEX project.

4.1 Evaporation Example

The evaporation example is a test example to check that the model has physical integrity. A one meter long bentonite beam is heated on the left side. The heater has a constant temperature of $100°C$. Figure 11 shows the test setup and the initial conditions. The initial temperature of the bentonite beam is $12°C$, with a gas saturation of 0.5, at a gas pressure of 1 bar.

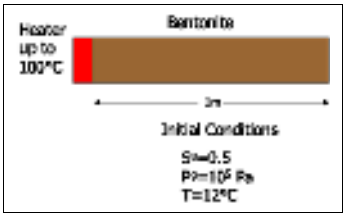

Figure 11: Evaporation example layout

In Figures 12, 13, 14, 15, and the results for the example are shown.

As the bentonite is heated, the temperature distribution across the bentonite slab changes. Figure 12 shows the temperature across the beam. As expected, the temperature at the left side of the beam, where the heater is, increases. From left to right the temperature decreases across the beam.

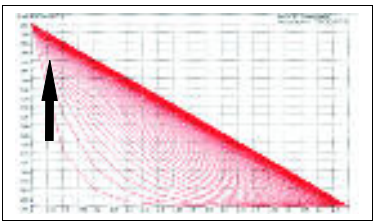

Figure 12: Evaporation example: Temperature

Some of the liquid phase evaporates into the gas phase. The gas pressure has to increase, as we see in Figure 13.

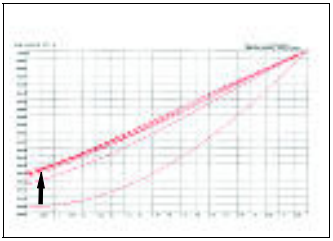

Figure 13: Evaporation example: Gas Pressure

As shown in Figure 14, while gas saturation increases somewhat, liquid saturation has to decrease by the same amount.

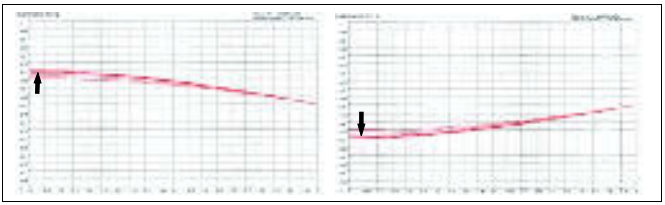

Figure 14: Evaporation example: Gas and Liquid Saturation

The capillary pressure increases, as the temperature rises.

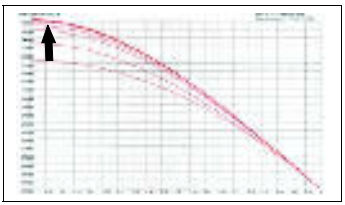

Figure 15: Evaporation example: Capillary Pressure

The mass fraction for vapour increases as expected, whereas the mass fraction for dissolved air decreases.

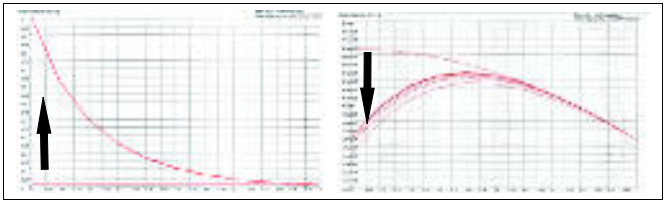

Figure 16: Evaporation example: Mass Fraction Vapour, Mass Fraction Air in Liquid Phase

The results show all expected physical characteristics.

4.2 DECOVALEX Example

This example is taken from task BMT1 of the DECOVALEX project. The DECOVALEX project task BMT1 deals with the modelling of processes in the nearfield of underground nuclear waste storage. The layout is shown in Figure 17. Horizontal tunnels are dug at 1000m depth. At regular intervals, vertical shafts go down from the tunnels. In these shafts, a heating element is stored, surrounded by a bentonite buffer. The tunnel is then backfilled. The heater is set to heat for a predefined amount of time.

In our example, a 2-dimensional vertical cut is made through the setup. The mesh is a coarse triangular element mesh.

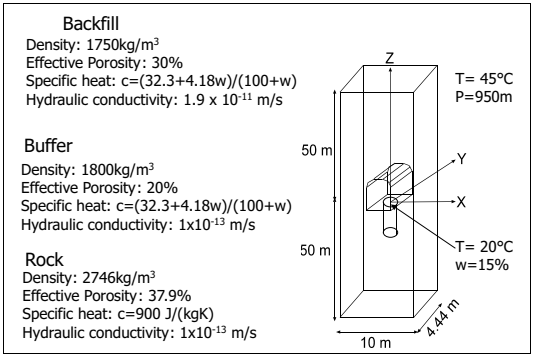

Figure 17: DECOVALEX example layout

In Figure 18 the effects of the heating process of the core can be seen. The gas pressure diminished with a similar pattern with distance from the core, as can be observed in Figure 19.

In Figure 20 the results for saturation are illustrated. On close observation, one can observe that they complement eachother, as they should. Figure 21 illustrates the capillary pressure. Figure 22 illustrates the capillary pressure. These results are conform to expectations

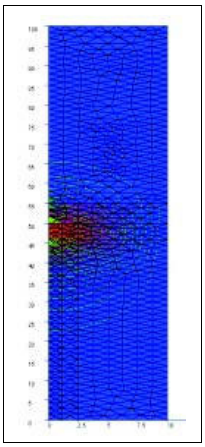

Figure 18: DECOVALEX example: Temperature

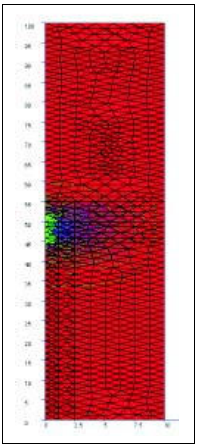

Figure 19: DECOVALEX example: Gas Pressure

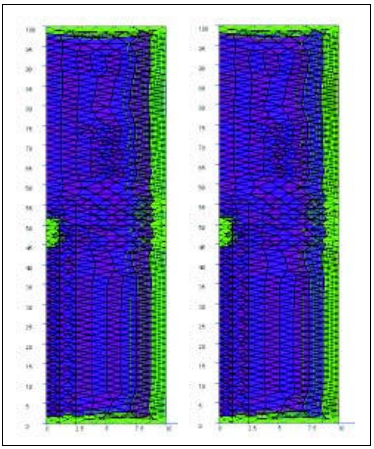

Figure 20: DECOVALEX example:Gas Saturation and Liquid Saturation

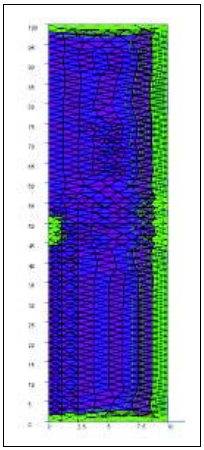

Figure 21: DECOVALEX example: Capillary Pressure

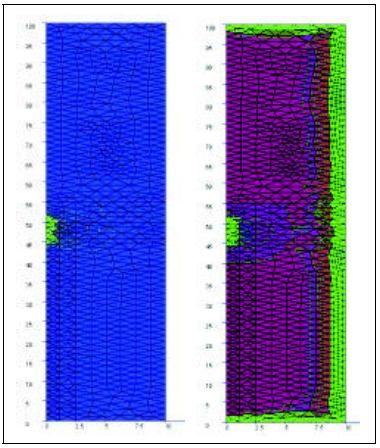

Figure 22: DECOVALEX example: Mass Fraction Vapour, Mass Fraction Air in Liquid Phase

APPENDIX

A Material Functions

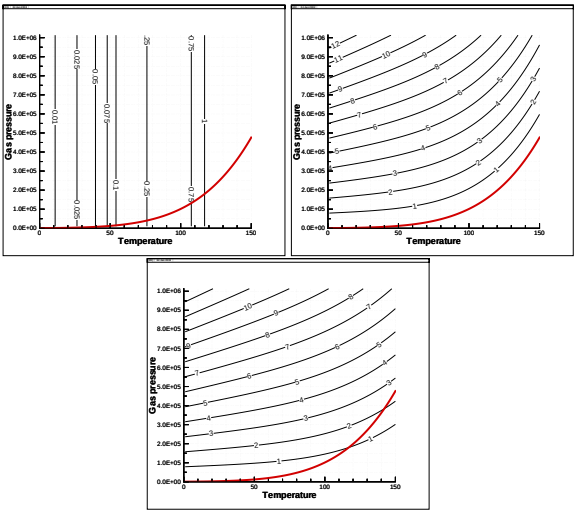

Figure 23: Vapour density (above), gas phase density in the air component (middle), and gas density (below)

State Variable	Water liquid	Component gas	Air liquid	Component gas	Energy	Equation	Data Access
Saturated Water Pressure		$p^g_{w,sat}$					`MATCalcVapourPressure(temperature)`
Capillary Pressure	p_c						user defined
Enthalpy		h^g_w			h^l	h^g	`MATGetEnthalpy(Phase,..)`
Mass Fractions	X^l_w	X^g_w	X^l_a	X^g_a			`MATCalcMassFraction(Phase,..)`
Pressure		p^g_w		p^g_a			by formula
Internal Energy					u^l	u^g	
Material Properties							
Fluid Density	ρ^l_w	ρ^g_w	ρ^l_a	ρ^g_a			`MATCalcDensity(Phase,..)`
Fluid Viscosity	μ^l	μ^g	μ^l	μ^g			`CalcFluidViscosity`
Specific Heat Capacity					c_v		
					c_p		
Thermal Conductivity					λ		by formula
Diffusion Coefficient					D		by formula
Thermal Compressibility	β^l_T						
Permeability							`GetPermeabilityTensor(index)`
Relative Permeability							`CalcAllRelativePermeabilities(...)`

B Algebraic Equations

For $\theta = 1$

Gas Pressure, Air Component

$$\begin{aligned}
\theta(\mathbf{K}_a^{ls} + \mathbf{K}_a^{gs})[\hat{\mathbf{p}}^g]_{\tau+1}^{n+1} &= Q_a \\
&- \frac{1}{\Delta t}\left(\mathbf{C}_a^g - \mathbf{C}_a^l\right)[\hat{S}^g]^{n+1} + \frac{1}{\Delta t}\left(\mathbf{C}_a^g - \mathbf{C}_a^l\right)[\hat{S}^g]^n \\
&+ \mathbf{K}_a^{ls}\frac{\partial p_{\mathsf{c}}}{\partial S}[\hat{S}^g]^{n+1} \\
&+ \mathbf{D}_a^g[\hat{\mathbf{X}}_a^g]^{n+1}
\end{aligned} \tag{84}$$

Saturation, Water Component

$$\begin{aligned}
\left[\frac{1}{\Delta t}\left(\mathbf{C}_w^g - \mathbf{C}_w^l\right) - \mathbf{K}_w^{ls}\frac{\partial p_{\mathsf{c}}}{\partial S}\right][\hat{S}^g]^{n+1} &= Q_w \\
&+ \frac{1}{\Delta t}\left(\mathbf{C}_w^g - \mathbf{C}_w^l\right)[\hat{S}^g]^n \\
&- (\mathbf{K}_w^{ls} + \mathbf{K}_w^{gs})[\hat{\mathbf{p}}^g]^{n+1} \\
&+ \mathbf{D}_w^g[\hat{\mathbf{X}}_w^g]^{n+1}
\end{aligned} \tag{85}$$

B.0.1 Coupling Version 1

Pressure – p^g

$$\begin{aligned}
&+ \nabla\cdot\left(\rho^l X_a^l \frac{k_{\mathsf{rel}}^l \mathbf{k}}{\mu^l}\nabla\hat{p}^g\right) + \nabla\cdot\left(\rho^g X_a^g \frac{k_{\mathsf{rel}}^g \mathbf{k}}{\mu^g}\nabla\hat{p}^g\right) \\
&= Q_a \\
&- \frac{\partial}{\partial t}(n\rho^l X_a^l \hat{S}^l + n\rho^g X_a^g \hat{S}^g) \\
&- \nabla\cdot\left(\rho^l X_a^l \frac{k_{\mathsf{rel}}^l \mathbf{k}}{\mu^l}\nabla\hat{p}_{\mathsf{c}}\right) \\
&+ \nabla\cdot(nS^g\rho^g X_a^g D^g \nabla X_a^g) \\
&- \nabla\cdot\left(\rho^l X_a^l \frac{k_{\mathsf{rel}}^l \mathbf{k}}{\mu^l}\rho^l\mathbf{g}\right) - \nabla\cdot\left(\rho^g X_a^g \frac{k_{\mathsf{rel}}^g \mathbf{k}}{\mu^g}\rho^g\mathbf{g}\right)
\end{aligned} \tag{86}$$

Saturation – S^g

$$
\begin{aligned}
&+ \quad \frac{\partial}{\partial t}(n\rho^l X_w^l \hat{S}^l + n\rho^g X_w^g \hat{S}^g) \\
&+ \quad \nabla \cdot \left(\rho^l X_w^l \frac{k_{\mathsf{rel}}^l \mathbf{k}}{\mu^l} \nabla \hat{p}_{\mathsf{c}} \right) \\
&= \quad Q_w \\
&+ \quad \nabla \cdot \left(\rho^g X_w^g \frac{k_{\mathsf{rel}}^g \mathbf{k}}{\mu^g} \nabla \hat{p}^g \right) + \nabla \cdot \left(\rho^l X_w^l \frac{k_{\mathsf{rel}}^l \mathbf{k}}{\mu^l} \nabla \hat{p}^g \right) \\
&+ \quad \nabla \cdot (n S^g \rho^g D^g \nabla X_w^g) \\
&- \quad \nabla \cdot \left(\rho^l X_w^l \frac{k_{\mathsf{rel}}^l \mathbf{k}}{\mu^l} \rho^l \mathbf{g} \right) - \nabla \cdot \left(\rho^g X_w^g \frac{k_{\mathsf{rel}}^g \mathbf{k}}{\mu^g} \rho^g \mathbf{g} \right)
\end{aligned} \tag{87}
$$

B.0.2 Coupling Version 2

Pressure – p^g

$$
\begin{aligned}
&+ \quad \nabla \cdot \left(\rho^l X_a^l \frac{k_{\mathsf{rel}}^l \mathbf{k}}{\mu^l} \nabla \hat{p}^g \right) + \nabla \cdot \left(\rho^g X_a^g \frac{k_{\mathsf{rel}}^g \mathbf{k}}{\mu^g} \nabla \hat{p}^g \right) \\
&+ \quad \frac{\partial}{\partial t} (n \rho^l X_a^l \hat{S}^l + n \rho^g X_a^g \hat{S}^g) \\
&+ \quad \nabla \cdot \left(\rho^l X_a^l \frac{k_{\mathsf{rel}}^l \mathbf{k}}{\mu^l} \nabla \hat{p}_{\mathsf{c}} \right) \\
&= \quad Q_a \\
&+ \quad \nabla \cdot (n S^g \rho^g X_a^g D^g \nabla X_a^g) \\
&- \quad \nabla \cdot \left(\rho^l X_a^l \frac{k_{\mathsf{rel}}^l \mathbf{k}}{\mu^l} \rho^l \mathbf{g} \right) - \nabla \cdot \left(\rho^g X_a^g \frac{k_{\mathsf{rel}}^g \mathbf{k}}{\mu^g} \rho^g \mathbf{g} \right)
\end{aligned} \tag{88}
$$

Saturation – S^g

$$
\begin{aligned}
&+ \quad \frac{\partial}{\partial t} (n \rho^l X_w^l \hat{S}^l + n \rho^g X_w^g \hat{S}^g) \\
&+ \quad \nabla \cdot \left(\rho^l X_w^l \frac{k_{\mathsf{rel}}^l \mathbf{k}}{\mu^l} \nabla \hat{p}_{\mathsf{c}} \right) \\
&- \quad \nabla \cdot \left(\rho^g X_w^g \frac{k_{\mathsf{rel}}^g \mathbf{k}}{\mu^g} \nabla \hat{p}^g \right) - \nabla \cdot \left(\rho^l X_w^l \frac{k_{\mathsf{rel}}^l \mathbf{k}}{\mu^l} \nabla \hat{p}^g \right) \\
&= \quad Q_w \\
&+ \quad \nabla \cdot (n S^g \rho^g D^g \nabla X_w^g) \\
&- \quad \nabla \cdot \left(\rho^l X_w^l \frac{k_{\mathsf{rel}}^l \mathbf{k}}{\mu^l} \rho^l \mathbf{g} \right) - \nabla \cdot \left(\rho^g X_w^g \frac{k_{\mathsf{rel}}^g \mathbf{k}}{\mu^g} \rho^g \mathbf{g} \right)
\end{aligned} \tag{89}
$$

$$
\begin{aligned}
[\theta(\mathbf{K}_w^{ls} + \mathbf{K}_w^{gs})][\mathbf{p}^g] &= RHS_P \\
\left[\frac{1}{\Delta t} \left(\mathbf{C}_w^g - \mathbf{C}_w^l \right) - \mathbf{K}_w^{ls} \frac{\partial p_{\mathsf{c}}}{\partial S} \right] [\hat{S}^g] &= RHS_S \\
\left(\frac{1}{\Delta t} \mathbf{C}_t^s - \theta \mathbf{K}_t^s \right) [\hat{\mathbf{T}}]_{\tau+1}^{n+1} &= RHS_T
\end{aligned} \tag{90}
$$

$$
\begin{aligned}
\begin{bmatrix} \theta(\mathbf{K}_a^{gs} + \mathbf{K}_a^{ls}) & \frac{1}{\Delta t} \left(\mathbf{C}_a^g - \mathbf{C}_a^l \right) - \mathbf{K}_a^{ls} \frac{\partial p_{\mathsf{c}}}{\partial S} \\ \theta(\mathbf{K}_w^{gs} + \mathbf{K}_w^{ls}) & \frac{1}{\Delta t} \left(\mathbf{C}_w^g - \mathbf{C}_w^l \right) - \mathbf{K}_w^{ls} \frac{\partial p_{\mathsf{c}}}{\partial S} \end{bmatrix} \begin{bmatrix} \mathbf{p}^g \\ \mathbf{S}^g \end{bmatrix} &= RHS \\
\left(\frac{1}{\Delta t} \mathbf{C}_t^s - \theta \mathbf{K}_t^s \right) [\hat{\mathbf{T}}]_{\tau+1}^{n+1} &= RHS_T
\end{aligned} \tag{91}
$$

C Governing Equations

$$
\begin{aligned}
&+ \quad \frac{\partial}{\partial t}(n\rho^{\gamma}X_k^{\gamma}\mathbf{S}^{\gamma}) \\
&- \quad \nabla\cdot\left(\rho^{\gamma}X_k^{\gamma}\frac{k_{\mathsf{rel}}\gamma\mathbf{k}}{\mu^{\gamma}}\nabla\hat{\mathbf{p}}^{\gamma}\right) \\
&- \quad \nabla\cdot(nS^{\gamma}\rho^{\gamma}D^{\gamma}\nabla X_k^{\gamma}) \\
&+ \quad \nabla\cdot\left(\rho^{\gamma}X_k^{\gamma}\frac{k_{\mathsf{rel}}\gamma\mathbf{k}}{\mu^{\gamma}}\rho^{\gamma}\mathbf{g}\right) \\
&= \quad Q_k
\end{aligned}
\tag{92}
$$

D Henry's Law

$$
K^H = (0.8942 + 1.47e^{-0.04394T})10^{-10} \tag{93}
$$

References

K.-J. Bathe. *Finite Element Methoden*. Springer, second edition, 2002.

Jacob Bear. *Dynamics of Fluids in Porous Media*. Dover, 1988.

Jacop Bear and Yehuda Bachmat. *Introduction to Modeling of Transport Phenomena in Porous Media*, volume 4 of *Theory and Applications of Transport in Porous Media*. Kluwer Academic Publishers, Technion, Israel Institute of Technology, Haifa, Israel, 1998.

Martin Emmert. *Numerische Modellierung nichtisothermer Gas-Wasser Systeme in porösen Medien*. PhD thesis, Insitut für Wasserbau, Universität Stuttgart, 1997.

P.A. Forsyth. Simulation of nonaqueous phase groundwater contamination. *Advances in Water Ressources*, 11(2), 1988.

Brian W. Kernighan and Dennis M. Ritchie. *Programmieren in C*. Hanser, second edition, 1990.

O. Kolditz. *Stoff- und Wärmetransport im Kluftgestein*. Habilschrift, Institut für Strömunsmechanik und Elektron. Rechnen im Bauwesen der Universität Hannover, 1996.

O. Kolditz. *Computational Methods in Environmental Fluid Mechanics*. Springer, 2002.

Erwin Kreyszig. *Advanced Engineering Mathematics*. John Wiley & Sons, Inc., seventh edition, 1993.

R. W. Lewis and B. A. Schrefler. *The Finite Element Mehtod in the Static and Dynamic Deformation and Consolidation of Porous Media*. John Wiley & Sons, Inc., second edition.

Pierre Perrot. *A to Z of Thermodynamics*. Oxford University Press.

Bruce E. Poling, John M. Prausnitz, and John P. O'Connell. *The Properties of Gases and Liquids*. Mc Graw Hill, fifth edition, 2001.

Carsten Thorenz. *Model Adaptive Simulation of Multiphase and Density Deiven Flow in Fractured and Porous Media*. PhD thesis, Institut für Strömunsmechanik und Elektron. Rechnen im Bauwesen der Universität Hannover, 2001.

Non-isothermal flow processes in porous media, Part II:

Finite element method - shape functions and element matrices

Technical report, Nr. 2004-1:

Center of Applied Geosciences

University of Tübingen

Center of Applied Geosciences
University of Tübingen

Non-Isothermal Flow Processes in Porous Media

Part II: Finite Element Method - Shape Functions and Element Matrices

Joëlle De Jonge & Wenqing Wang & Olaf Kolditz

ROCKFLOW – Preprint
[2004-1]

Tübingen
February 2004
Version March 3, 2004

Abstract

This report is one in the series describing the finite element simulator GeoSys/RockFlow. The simulator has multiple applications. The application of the work described here are situations where non-isothermal multiphase-multicomponental flow calculations are needed, such as in deep geological nuclear waste storage.

GeoSys/RockFlow is written in an object-oriented way. The process (PCS) kernel described by this work is the multiphase-multicomponental (MPC) kernel of the program. The first section of the report describes general coordinate transformation tools and shape functions used in the finite element method (FEM). Subsequent sections show the development of the element matrix types needed for the kernel. The specific matrices, taking into account all needed material functions are then developed. Finally, a simple example illustrates that the element matrices have been correctly implemented.

List of Symbols

A	Element area $[\mathrm{m}^2]$	n	Porosity $[-]$
$\mathbf{C}$	Mass matrix $[\mathrm{kg}]$	p	Pressure $[\mathrm{Pa}]$
D	Diffusion coefficient $[\frac{\mathrm{m}^2}{\mathrm{s}}]$	S	Saturation $[-]$
e	Element (superscript) $[-]$	V	Element volume $[\mathrm{m}^3]$
$\mathbf{g}$	Gravity vector $[\frac{\mathrm{m}}{\mathrm{s}^2}]$	W	Element thickness $[\mathrm{m}]$
$\mathbf{J}$	Jacobian matrix $[-]$	X	Mass fraction $[-]$
k	Component (subscript) $[-]$		
k	Permeability $[\mathrm{m}^2]$	γ	Fluid phase (superscript) $[-]$
$\mathbf{k}$	Permeability tensor $[\mathrm{m}^2]$	μ	Fluid viscosity $[\mathrm{Pa}\cdot\mathrm{s}]$
k_{rel}	Relative permeability $[-]$	ρ	Density $[\frac{\mathrm{kg}}{\mathrm{m}^3}]$
$\mathbf{K}$	Conductivity matrix $[\frac{\mathrm{W}}{\mathrm{m}\cdot\mathrm{K}}]$	Ω	Domain $[-]$
L	Element length $[\mathrm{m}]$	0	Initial or reference value, subscript $[-]$
N	Interpolation function $[-]$		

Contents

1 Introduction

This report is the second part of the report series on Non-Isothermal Flow Processes in Porous Media. Part I (De Jonge and Kolditz [2002]) dealt with the development of the governing equations from conservation laws and material properties. This part deals more specifically with the development of the element matrices needed for the multiphase-multicomponental formulation.

GeoSys/RockFlow uses the finite element method (FEM). FEM can be defined as the subdivision of complex structures into small substructures assembling the elements (Kolditz [2002]). For the FEM, the domain is discretised into elements. The multiphase-multicomponental formulation supports the following elements: 1-D linear, 2-D triangular, 2-D quadrilateral, 3-D hexagonal. The second step in the FEM consists in writing the the governing equations in integral form. This was the object of report Part I . The last step is the generation of interpolation functions to approximate a solution for the integral equations. This last step will be the object of this report.

In GeoSys/RockFlow, the discretisation is done by the method of weighted residuals, where the unknown function is approximated by a trial solution. Here this is the Bubnov-Galerkin method where the test function is equal to the interpolation function. These functions are usually taken to be polynomials. They are the subject of the first section of this report.

In Part I, the governing and algebraic equations were developed. The matrices used in the derived algebraic equation belong to two types of matrices, denoted C or K types. In subsequent sections, general forms of the two main matrix forms are developed. In the last sections, these matrices are shown especially for the multiphase-multicomponental case for all available element types.

In the appendix the differences between numerical and analytical integration is shown through an example.

Acknowledgement

The work presented in this report was largely funded by the Federal Institute of Geosciences and Natural Resources (BGR). We thank Dr. Liedtke for his support of this research project.

2 Tools for numerical integration

In this section, the interpolation functions and related numerical tools are developed. In RockFlow, the interpolation functions are chosen to be locally defined polynomials, that are null outside the considered element. Interpolation functions for specific element types are called element shape functions. These will be shown in this section. For a more detailed explanation on how these are obtained, the reader should refer to Kolditz [2002].

2.1 1-D linear elements

The shape functions for 1-D elements are as follows in global coordinates.

$$N^T = \left\{ \begin{array}{c} N_1^e(r) \\ N_2^e(r) \end{array} \right\} \tag{1}$$

$$\begin{aligned} N_1^e(r) &= \frac{x_2 - x}{x_2 - x_1} \\ N_2^e(r) &= \frac{x - x_1}{x_2 - x_1} \end{aligned} \tag{2}$$

In local coordinates, the shape functions are expressed by

$$\begin{aligned} N_1^e(r) &= \frac{1 - r}{2} \\ N_2^e(r) &= \frac{r - 1}{2} \end{aligned} \tag{3}$$

Additionally, the determinant of the Jacobian matrix is needed for matrix integration. For the 1-D case this can be written as $\det[J_{1D}] = \frac{L}{2}$.

Matlib functions: No matlib functions are needed, as integration for 1-D elements is done analytically.

2.2 2-D quadrilateral elements

The shape functions for 2-D linear quadrilateral elements are as shown in equation (4). The shape functions N_i are the area coordinates A_i, i.e. we have isoparametric elements.

$$N^T = \left\{ \begin{array}{c} N_1 \\ N_2 \\ N_3 \\ N_4 \end{array} \right\} = \frac{1}{4} \left[\begin{array}{c} (1+r)(1+s) \\ (1-r)(1+s) \\ (1-r)(1-s) \\ (1+r)(1-s) \end{array} \right] \tag{4}$$

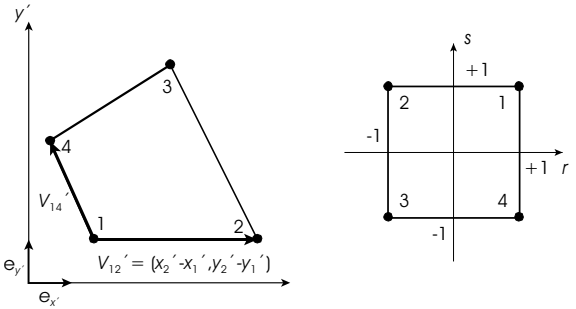

Figure 1: Isoparametric mapping of bilinear quadrilateral elements

Now the derivatives of the shape functions can be written down.

$$\frac{\partial \mathbf{N}}{\partial r} = \left\{ \begin{array}{l} \dfrac{\partial N_1}{\partial r} = \dfrac{1+s}{4} \\ \dfrac{\partial N_2}{\partial r} = -\dfrac{1+s}{4} \\ \dfrac{\partial N_3}{\partial r} = -\dfrac{1-s}{4} \\ \dfrac{\partial N_4}{\partial r} = \dfrac{1-s}{4} \end{array} \right\} \qquad \frac{\partial \mathbf{N}}{\partial s} = \left\{ \begin{array}{l} \dfrac{\partial N_1}{\partial s} = \dfrac{1+r}{4} \\ \dfrac{\partial N_2}{\partial s} = \dfrac{1-r}{4} \\ \dfrac{\partial N_3}{\partial s} = -\dfrac{1-r}{4} \\ \dfrac{\partial N_4}{\partial s} = -\dfrac{1+r}{4} \end{array} \right\} \tag{5}$$

$$\nabla_{xy}\mathbf{N} = \left[\begin{array}{ll} \dfrac{\partial N_1}{\partial x} & \dfrac{\partial N_1}{\partial y} \\ \dfrac{\partial N_2}{\partial x} & \dfrac{\partial N_2}{\partial y} \\ \dfrac{\partial N_3}{\partial x} & \dfrac{\partial N_3}{\partial y} \\ \dfrac{\partial N_4}{\partial x} & \dfrac{\partial N_4}{\partial y} \end{array} \right] \quad , \quad \nabla_{rs}\mathbf{N} = \left[\begin{array}{ll} \dfrac{\partial N_1}{\partial r} & \dfrac{\partial N_1}{\partial s} \\ \dfrac{\partial N_2}{\partial r} & \dfrac{\partial N_2}{\partial s} \\ \dfrac{\partial N_3}{\partial r} & \dfrac{\partial N_3}{\partial s} \\ \dfrac{\partial N_4}{\partial r} & \dfrac{\partial N_4}{\partial s} \end{array} \right] \tag{6}$$

In general we can use the interpolation function to transform coordinates, i.e. $(x, y)real \Longrightarrow (r, s)unit.$

$$x = x(r, s) = \sum_{i=1}^{4} N_i(r, s)\, x_i$$

$$y = y(r,s) = \sum_{i=1}^{4} N_i(r,s)\, y_i \tag{7}$$

Then we speak about an isoparametric coordinate transformation. In this case the two-dimensional Jacobian matrix is given by

$$[J_{2D}] = \begin{bmatrix} \frac{N_i}{\partial r} x_i & \frac{N_i}{\partial r} y_i \\ \frac{N_i}{\partial s} x_i & \frac{N_i}{\partial s} y_i \end{bmatrix} = [\nabla_{rs} \mathbf{N}]\,[A_{2D}] \tag{8}$$

$$\nabla_{xy} \mathbf{N} = [J_{2D}]^{-1} \nabla_{rs} \mathbf{N} \tag{9}$$

with

$$[J_{2D}]^{-1} = \begin{bmatrix} \frac{\partial r}{\partial x} & \frac{\partial s}{\partial x} \\ \frac{\partial r}{\partial y} & \frac{\partial s}{\partial y} \end{bmatrix} \tag{10}$$

Finally we determine $[J_{2D}]^{-1}$ by inversion of the Jacobian. $\det[J_{2D}]$ is $\frac{A}{4}$.

Matlib functions:

- Weighting of gauss points: MXPGaussPkt
- Transposed of the Inverse Jacobi matrix and determinant of that matrix: Calc2DElementJacobiMatrix

2.3 2-D triangular elements

(Kolditz [2002], p146-147)

$$N^T = \begin{Bmatrix} N_1 \\ N_2 \\ N_3 \end{Bmatrix} = \frac{1}{2A} \begin{bmatrix} x_2 y_3 - x_3 y_2 & y_2 - y_3 & x_3 - x_2 \\ x_3 y_1 - x_1 y_3 & y_3 - y_1 & x_1 - x_3 \\ x_1 y_2 - x_2 y_1 & y_1 - y_2 & x_2 - x_1 \end{bmatrix} \begin{Bmatrix} 1 \\ x \\ y \end{Bmatrix} \tag{11}$$

The shape functions N_i are simply the area coordinates L_i, i.e. we have isoparametric elements.

Now the derivatives of the shape functions can be easily written down.

$$\frac{\partial \mathbf{N}}{\partial x} = \begin{Bmatrix} \frac{\partial N_1}{\partial x} = \frac{y_2 - y_3}{2A} \\ \frac{\partial N_2}{\partial x} = \frac{y_3 - y_1}{2A} \\ \frac{\partial N_3}{\partial x} = \frac{y_1 - y_2}{2A} \end{Bmatrix} \qquad \frac{\partial \mathbf{N}}{\partial y} = \begin{Bmatrix} \frac{\partial N_1}{\partial y} = \frac{x_3 - x_2}{2A} \\ \frac{\partial N_2}{\partial y} = \frac{x_1 - x_3}{2A} \\ \frac{\partial N_3}{\partial y} = \frac{x_2 - x_1}{2A} \end{Bmatrix} \tag{12}$$

For 2-D triangular elements the following expression can be used to integrate analytically.

$$\iint_{\Delta} L_1^a L_2^b L_3^c dxdy = 2\Delta \frac{a!b!c!}{(a+b+c+2)!} \tag{13}$$

Because of the analytical integration, no matlib functions for numerical integration are needed.

2.4 3-D hexahedral elements

The shape functions for 3-D hexahedral elements are as shown in equation (14). The shape functions N_i are the area coordinates A_i, i.e. we have isoparametric elements. (Kolditz [2002], pages 154-157.)

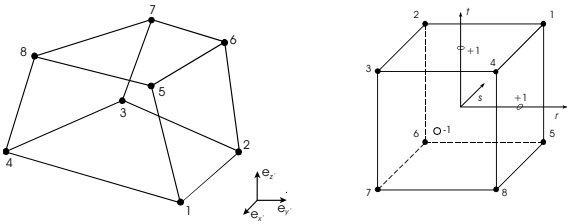

Figure 2: Hexahedron in global and local coordinates

Shape functions in local and global element coordinates. can be defined in following way.

$$N_1 = \frac{1}{8}(1+r)(1+s)(1+t) \quad , \quad N_1 = \frac{x-x_2}{x_1-x_2}\frac{y-y_4}{y_1-y_4}\frac{z-z_5}{z_1-z_5}$$
$$N_2 = \frac{1}{8}(1-r)(1+s)(1+t) \quad , \quad N_2 = \frac{x-x_3}{x_2-x_3}\frac{y-y_1}{y_2-y_1}\frac{z-z_6}{z_2-z_6}$$
$$N_3 = \frac{1}{8}(1-r)(1-s)(1+t) \quad , \quad N_3 = \frac{x-x_4}{x_3-x_4}\frac{y-y_2}{y_3-y_2}\frac{z-z_7}{z_3-z_7}$$
$$N_4 = \frac{1}{8}(1+r)(1-s)(1+t) \quad , \quad N_4 = \frac{x-x_1}{x_4-x_1}\frac{y-y_3}{y_4-y_3}\frac{z-z_8}{z_4-z_8}$$
$$N_5 = \frac{1}{8}(1+r)(1+s)(1-t) \quad , \quad N_5 = \frac{x-x_6}{x_5-x_6}\frac{y-y_8}{y_5-y_8}\frac{z-z_1}{z_5-z_1}$$
$$N_6 = \frac{1}{8}(1-r)(1+s)(1-t) \quad , \quad N_6 = \frac{x-x_7}{x_6-x_7}\frac{y-y_5}{y_6-y_5}\frac{z-z_2}{z_6-z_2}$$
$$N_7 = \frac{1}{8}(1-r)(1-s)(1-t) \quad , \quad N_7 = \frac{x-x_8}{x_7-x_8}\frac{y-y_6}{y_7-y_6}\frac{z-z_3}{z_7-z_3}$$

$$N_8 = \frac{1}{8}(1+r)(1-s)(1-t) \quad , \quad N_8 = \frac{x-x_5}{x_8-x_5}\frac{y-y_7}{y_8-y_7}\frac{z-z_4}{z_8-z_4} \tag{14}$$

$$N = (N_1, N_2, ..., N_8) \tag{15}$$

Implementation: MOmega3D(omega,r,s,t)

The matrix of shape function derivatives is therefore given as follows

$$\nabla_{rst} N = \begin{bmatrix} \frac{\partial N_1}{\partial r} & \frac{\partial N_1}{\partial s} & \frac{\partial N_1}{\partial t} \\ \frac{\partial N_2}{\partial r} & \frac{\partial N_2}{\partial s} & \frac{\partial N_2}{\partial t} \\ \frac{\partial N_3}{\partial r} & \frac{\partial N_3}{\partial s} & \frac{\partial N_3}{\partial t} \\ \frac{\partial N_4}{\partial r} & \frac{\partial N_4}{\partial s} & \frac{\partial N_4}{\partial t} \\ \frac{\partial N_5}{\partial r} & \frac{\partial N_5}{\partial s} & \frac{\partial N_5}{\partial t} \\ \frac{\partial N_6}{\partial r} & \frac{\partial N_6}{\partial s} & \frac{\partial N_6}{\partial t} \\ \frac{\partial N_7}{\partial r} & \frac{\partial N_7}{\partial s} & \frac{\partial N_7}{\partial t} \\ \frac{\partial N_8}{\partial r} & \frac{\partial N_8}{\partial s} & \frac{\partial N_8}{\partial t} \end{bmatrix} \tag{16}$$

$$= \frac{1}{8}\begin{bmatrix} (1+s)(1+t) & (1+r)(1+t) & (1+r)(1+s) \\ -(1+s)(1+t) & (1-r)(1+t) & (1-r)(1+s) \\ -(1-s)(1+t) & -(1-r)(1+t) & (1-r)(1-s) \\ (1-s)(1+t) & -(1+r)(1+t) & (1+r)(1-s) \\ (1+s)(1-t) & (1+r)(1-t) & -(1+r)(1+s) \\ -(1+s)(1-t) & (1-r)(1-t) & -(1-r)(1+s) \\ -(1-s)(1-t) & -(1-r)(1-t) & -(1-r)(1-s) \\ (1-s)(1-t) & -(1+r)(1-t) & -(1+r)(1-s) \end{bmatrix}$$

Implementation: MGradOmega3D(gradient,r,s,t)

Shape function derivatives in global coordinates $(x-y-z)$ can be determined by use of the inverse Jacobian matrix $[J_{3D}]^{-1}$.

$$\nabla_{xyz}\mathbf{N} = [J_{3D}]^{-1}\nabla_{rst}\mathbf{N} \tag{17}$$

The Jacobian matrix in 3-D case is given by

$$[J_{3D}] = \begin{bmatrix} \frac{\partial x}{\partial r} & \frac{\partial y}{\partial r} & \frac{\partial z}{\partial r} \\ \frac{\partial x}{\partial s} & \frac{\partial y}{\partial s} & \frac{\partial z}{\partial s} \\ \frac{\partial x}{\partial t} & \frac{\partial y}{\partial t} & \frac{\partial z}{\partial t} \end{bmatrix} = [\nabla_{rst}\mathbf{N}]\,[A_{3D}] \tag{18}$$

which can be rewritten, if using the isoparametric coordinate transformation equation as

$$[J_{3D}] = \begin{bmatrix} \frac{\partial N_i}{\partial r}x_i & \frac{\partial N_i}{\partial r}y_i & \frac{\partial N_i}{\partial r}z_i \\ \frac{\partial N_i}{\partial s}x_i & \frac{\partial N_i}{\partial s}y_i & \frac{\partial N_i}{\partial s}z_i \\ \frac{\partial N_i}{\partial t}x_i & \frac{\partial N_i}{\partial t}y_i & \frac{\partial N_i}{\partial t}z_i \end{bmatrix} \tag{19}$$

Implementation: Calc3DElementJacobianMatrix(element,r,s,t,invjac,detjac)

The required inverse Jacobian $[J_{3D}]^{-1}$ has to be calculated by formulas for matrix inversion.

Implementation: M3Invertiere(matrix)

$\det[J_{1D}]$ is $\frac{V}{8}$.

2.5 Implementation of Matrix Operations in RockFlow/Geosys

- Matrix multiplication: MMultMatMat
- Matrix multiplication with vector: MMultMatVec
- Vector multiplication with matrix: MMultVecMat
- Matrix transposition: MTranspoMat
- Matrix initialization: MNulleMat
- Vector transposition: MTranspoVec
- Vector initialization: MNulleVec

3 C-Type Matrices

In the algebraic equations for multiphase-multicomponent flow, this type of matrix describes the storage terms of quantities such as pressure. They are present in the equations for both components, air and water and in the energy equation. The matrices below are evaluated for an orthotropic medium. mat denotes the material properties, which are assumed to be element-wise constant. The capacitance matrix is a matrix of the type C-type integral: $\int \mathbf{N}^T f(u_i)\mathbf{N} d\Omega$

3.1 1-D C-Type Matrix

$$
\begin{aligned}
\mathbf{C}_k^\gamma &= \int_{\Omega^e} \mathbf{N}^T (mat)\, \mathbf{N}\, d\Omega^e \\
&= \int_{V^e} \begin{bmatrix} N_1 \\ N_2 \end{bmatrix}^T (mat) \begin{bmatrix} N_1 & N_2 \end{bmatrix} dV^e \\
&= A^e \int_{L^e} \begin{bmatrix} N_1 \\ N_2 \end{bmatrix}^T (mat) \begin{bmatrix} N_1 & N_2 \end{bmatrix} dx' \\
&= A^e \int_{-1}^{+1} \begin{bmatrix} N_1 \\ N_2 \end{bmatrix}^T (mat) \begin{bmatrix} N_1 & N_2 \end{bmatrix} \det[J_{1D}]\, dr \\
&= (mat)^e \frac{A^e L^e}{3 \cdot 2^1} \begin{bmatrix} 2 & 1 \\ 1 & 2 \end{bmatrix} \\
&= (mat)^e \frac{V^e}{6} \begin{bmatrix} 2 & 1 \\ 1 & 2 \end{bmatrix}
\end{aligned} \tag{20}
$$

3.2 2-D C-Type Matrix

$$
\begin{aligned}
\mathbf{C}_k^\gamma &= \int_{\Omega^e} \mathbf{N}^T (mat)\, \mathbf{N}\, d\Omega^e \\
&= W \int_{A^e} \mathbf{N}^T (mat)\, \mathbf{N}\, dA^e \\
&= W (mat) \det \mathbf{J}_{2D} \int_{-1}^{1}\int_{-1}^{1} \mathbf{N}^T \mathbf{N}\, dr ds \\
C &= (mat)^e \frac{V}{9} \begin{bmatrix} 1 & \frac{1}{2} & \frac{1}{4} & \frac{1}{2} \\ & 1 & \frac{1}{2} & \frac{1}{4} \\ & & 1 & \frac{1}{2} \\ & & & 1 \end{bmatrix} \\
C_{11} &= W (mat) \frac{A}{2^2} \int_{-1}^{1}\int_{-1}^{1} \frac{1}{4}(1+r)(1+s) \frac{1}{4}(1+r)(1+s)\, dr ds
\end{aligned}
$$

$$
\begin{aligned}
C_{11} &= W(mat)\frac{A}{4}\frac{1}{16}\int_{-1}^{1}(1+r)(1+r)\int_{-1}^{1}(1+s)(1+s)\,drds \\
C_{11} &= W(mat)\frac{A}{4}\frac{1}{16}\frac{8}{3}\frac{8}{3} \\
C_{11} &= (mat)\frac{V}{9} \\
C_{12} &= W(mat)\frac{A}{2^2}\int_{-1}^{1}\int_{-1}^{1}\frac{1}{4}(1-r)(1+s)\frac{1}{4}(1+r)(1+s)\,drds \\
C_{12} &= W(mat)\frac{A}{4}\frac{1}{16}\int_{-1}^{1}(1-r)(1+r)\int_{-1}^{1}(1+s)(1+s)\,drds \\
C_{12} &= W(mat)\frac{A}{4}\frac{1}{16}\frac{4}{3}\frac{8}{3} \\
C_{12} &= (mat)\frac{V}{18}
\end{aligned}
\tag{21}
$$

3.3 3-D C-Type Matrix

$$
\begin{aligned}
\mathbf{C}_k^{\gamma} &= \int_{\Omega^e}\mathbf{N}^T(mat)\,\mathbf{N}\,d\Omega^e \\
&= \int_{V^e}\mathbf{N}^T(mat)\,\mathbf{N}\,dV^e \\
&= (mat)\det\mathbf{J}_{3D}\int_{-1}^{1}\int_{-1}^{1}\int_{-1}^{1}\mathbf{N}^T\mathbf{N}\,drdsdt \\
C &= (mat)\frac{V}{27}\begin{bmatrix}
1 & \frac{1}{2} & \frac{1}{4} & \frac{1}{2} & \frac{1}{2} & \frac{1}{4} & \frac{1}{8} & \frac{1}{4} \\
 & 1 & \frac{1}{2} & \frac{1}{4} & \frac{1}{4} & \frac{1}{2} & \frac{1}{4} & \frac{1}{8} \\
 & & 1 & \frac{1}{4} & \frac{1}{4} & \frac{1}{2} & \frac{1}{2} & \frac{1}{4} \\
 & & & 1 & \frac{1}{8} & \frac{1}{4} & \frac{1}{2} & \frac{1}{4} \\
 & & & & 1 & \frac{1}{2} & \frac{1}{4} & \frac{1}{2} \\
 & & & & & 1 & \frac{1}{2} & \frac{1}{4} \\
 & & & & & & 1 & \frac{1}{2} \\
 & & & & & & & 1
\end{bmatrix} \\
C_{11} &= (mat)\frac{V}{2^3}\int_{-1}^{1}\int_{-1}^{1}\int_{-1}^{1}\frac{1}{8}(1+r)(1+s)(1+t)\frac{1}{8}(1+r)(1+s)(1+t)\,drdsdt \\
C_{11} &= (mat)\frac{V}{8}\frac{1}{64}\int_{-1}^{1}(1+r)(1+r)dr\int_{-1}^{1}(1+s)(1+s)ds\int_{-1}^{1}(1+t)(1+t)dt \\
C_{11} &= (mat)\frac{V}{8}\frac{1}{64}\frac{8}{3}\frac{8}{3}\frac{8}{3} \\
C_{11} &= (mat)\frac{V}{27}
\end{aligned}
$$

$$
\begin{aligned}
C_{12} &= (mat)\frac{V}{2^3}\int_{-1}^{1}\int_{-1}^{1}\int_{-1}^{1}\frac{1}{8}(1+r)(1+s)(1+t)\frac{1}{8}(1-r)(1+s)(1+t)\,drdsdt \\
C_{12} &= (mat)\frac{V}{8}\frac{1}{64}\int_{-1}^{1}(1+r)(1-r)dr\int_{-1}^{1}(1+s)(1+s)ds\int_{-1}^{1}(1+t)(1+t)dt \\
C_{12} &= (mat)\frac{V}{8}\frac{1}{64}\frac{4}{3}\frac{8}{3}\frac{8}{3} \\
C_{12} &= (mat)\frac{V}{54}
\end{aligned}
\tag{22}
$$

4 K-Type Matrices

K-Type matrices are present in all algebraic equations for the multiphase-multicomponental model. They represent the movement of quantities, such as diffusion. Because of the spatial variation, the derivative of the test function is used. Hence, a matrix of K-type integral has the form: $\int \nabla \mathbf{N}^T f(u_i) \nabla \mathbf{N} d\Omega$.

4.1 1-D K-Type Matrix

$$
\begin{aligned}
\mathbf{K} &= \int_{\Omega^e} \nabla \mathbf{N}^T \, (mat) \, \nabla \mathbf{N} \, d\Omega^e \\
&= \int_{V^e} \begin{bmatrix} \nabla \mathbf{N}_1 \\ \nabla \mathbf{N}_2 \end{bmatrix} (mat^*) \, \mathbf{k} \begin{bmatrix} \nabla \mathbf{N}_1 & \nabla \mathbf{N}_2 \end{bmatrix} dV^e \\
&= A^e \int_{L^e} \begin{bmatrix} \partial \mathbf{N}_1 / \partial x' \\ \partial \mathbf{N}_2 / \partial x' \end{bmatrix} (mat^*) \, \mathbf{k} \begin{bmatrix} \partial \mathbf{N}_1 / \partial x' & \partial \mathbf{N}_2 / \partial x' \end{bmatrix} dx' \\
&= A^e \, (mat^*) \int_{-1}^{+1} \begin{bmatrix} \partial \mathbf{N}_1 / \partial r \\ \partial \mathbf{N}_2 / \partial r \end{bmatrix} [\mathbf{J}_{1D}^{-1}]^T \mathbf{k} [\mathbf{J}_{1D}^{-1}] \times \begin{bmatrix} \partial \mathbf{N}_1 / \partial r & \partial \mathbf{N}_2 / \partial r \end{bmatrix} \det \mathbf{J}_{1D} \, dr \\
&= A^e \, (mat^*) \, [\mathbf{J}_{1D}^{-1}]^T [\mathbf{J}_{1D}^{-1}] \det \mathbf{J}_{1D} \int_{-1}^{+1} \begin{bmatrix} \partial \mathbf{N}_1 / \partial r \\ \partial \mathbf{N}_2 / \partial r \end{bmatrix} \mathbf{k} \times \begin{bmatrix} \partial \mathbf{N}_1 / \partial r & \partial \mathbf{N}_2 / \partial r \end{bmatrix} dr \\
&= (mat^*)^e \, k_x A \frac{\sqrt{2}}{L^e} \frac{\sqrt{2}}{L^e} \frac{L^e}{2} \begin{bmatrix} +1 & -1 \\ -1 & +1 \end{bmatrix} \\
&= (mat^*)^e \, k_x \frac{A^e}{L^e} \begin{bmatrix} +1 & -1 \\ -1 & +1 \end{bmatrix}
\end{aligned} \tag{23}
$$

4.2 2-D K-Type Matrix

As the aim is to evaluate the relationship of K-Type matrices between the dimensions, the Element can be chosen so that the Jacobi matrix is equal to the unity matrix. This avoids having to multiply with the inverse of the Jacobi matrix. Further, only the orthotropic medium is considered, hence the permeability tensor can be extracted and replaced by a scalar.

$$
\begin{aligned}
\mathbf{K}_k^\gamma &= \int_{\Omega^e} \nabla \mathbf{N}^T \, (mat^*) \, \mathbf{k} \nabla \mathbf{N} \, d\Omega^e \\
&= W \int_{A^e} \nabla \mathbf{N}^T \, (mat^*) \, \mathbf{k} \nabla \mathbf{N} \, dA^e \\
&= W (mat^*) \int_{-1}^{1} \int_{-1}^{1} \nabla_{rs} \mathbf{N}^T (\mathbf{J}_{2D}^{-1})^T \mathbf{k} \mathbf{J}_{2D}^{-1} \nabla_{rs} \mathbf{N} \det \mathbf{J}_{2D} \, dr ds \\
&= W (mat^*) \int_{-1}^{1} \int_{-1}^{1} \nabla_{rs} \mathbf{N}^T \mathbf{k} \nabla_{rs} \mathbf{N} \, dr ds
\end{aligned}
$$

(24)

$$
\begin{aligned}
K &= (mat*)^e \frac{2V}{3} \begin{bmatrix} 1 & -\frac{1}{4} & -\frac{1}{2} & -\frac{1}{4} \\ & 1 & -\frac{1}{2} & -\frac{1}{2} \\ & & 1 & -\frac{1}{6} \\ & & & 1 \end{bmatrix} \\
K_{11} &= W(mat)\frac{A}{2^2}\int_{-1}^{1}\int_{-1}^{1}\frac{1}{4}(1+r)(1+s)\frac{1}{4}(1+r)(1+s)\,drds \\
K_{11} &= W(mat)\frac{A}{4}\frac{1}{16}\int_{-1}^{1}(1+r)(1+r)\int_{-1}^{1}(1+s)(1+s)\,drds \\
K_{11} &= W(mat)\frac{A}{4}\frac{1}{16}\frac{8}{3}\frac{8}{3} \\
K_{11} &= (mat)\frac{V}{9} \\
K_{12} &= W(mat)\frac{A}{2^2}\int_{-1}^{1}\int_{-1}^{1}\frac{1}{4}(1-r)(1+s)\frac{1}{4}(1+r)(1+s)\,drds \\
K_{12} &= W(mat)\frac{A}{4}\frac{1}{16}\int_{-1}^{1}(1-r)(1+r)\int_{-1}^{1}(1+s)(1+s)\,drds \\
K_{12} &= W(mat)\frac{A}{4}\frac{1}{16}\frac{4}{3}\frac{8}{3} \\
K_{12} &= (mat)\frac{V}{18}
\end{aligned}
$$

(25)

4.3 3-D K-Type Matrix

The same assumptions as for the evaluation of the 2-D K-Type matrices apply here.

$$
\begin{aligned}
\mathbf{K}_k^{\gamma} &= \int_{\Omega^e} \nabla\mathbf{N}^T\,(mat^*)\,\mathbf{k}\nabla\mathbf{N}\,d\Omega^e \\
&= (mat^*)\int_{-1}^{1}\int_{-1}^{1}\int_{-1}^{1}\nabla_{rst}\mathbf{N}^T(\mathbf{J}_{3D}^{-1})^T\mathbf{k}\mathbf{J}_{3D}^{-1}\nabla_{rst}\mathbf{N}\det\mathbf{J}_{3D}\,drdsdt \\
\mathbf{K} &= \begin{bmatrix}
\frac{2}{3} & 0 & -\frac{1}{6} & 0 & 0 & -\frac{1}{6} & -\frac{1}{6} & -\frac{1}{6} \\
 & \frac{2}{3} & 0 & -\frac{1}{6} & -\frac{1}{6} & 0 & -\frac{1}{6} & -\frac{1}{6} \\
 & & \frac{2}{3} & 0 & -\frac{1}{6} & -\frac{1}{6} & 0 & -\frac{1}{6} \\
 & & & \frac{2}{3} & -\frac{1}{6} & -\frac{1}{6} & -\frac{1}{6} & 0 \\
 & & & & \frac{2}{3} & 0 & -\frac{1}{6} & 0 \\
 & & & & & \frac{2}{3} & 0 & -\frac{1}{6} \\
 & & & & & & \frac{2}{3} & 0 \\
 & & & & & & & \frac{2}{3}
\end{bmatrix}
\end{aligned}
$$

(26)

$$
\begin{aligned}
\mathbf{K}_{11} &= (mat^*)\, k \int_{-1}^{1}\int_{-1}^{1}\int_{-1}^{1} \nabla_{rst}\mathbf{N}^T \nabla_{rst}\mathbf{N} \det \mathbf{J}_{3D}\, drdsdt \\
&= \frac{1}{8^2}\,(mat^*)\, k \int_{-1}^{1}\int_{-1}^{1}\int_{-1}^{1} [(1+s)^2(1+t)^2 + (1+r)^2(1-t)^2 + (1+r)^2(1+s)^2]\, drdsdt \\
&= \frac{1}{8^2} 3 \cdot 2 \cdot \frac{8}{3}\frac{8}{3}\,(mat^*)\, k \\
&= \frac{2}{3}\,(mat^*)\, k \\
\mathbf{K}_{12} &= (mat^*)\, k \int_{-1}^{1}\int_{-1}^{1}\int_{-1}^{1} \nabla_{rst}\mathbf{N}^T \nabla_{rst}\mathbf{N} \det \mathbf{J}_{3D}\, drdsdt \\
&= \frac{1}{8^2}\,(mat^*)\, k \int_{-1}^{1}\int_{-1}^{1}\int_{-1}^{1} [-(1+s)^2(1+t)^2 + (1-r)^2(1+t)^2 + (1-r)^2(1+s)^2]\, drdsdt \\
&= \frac{1}{8^2}\,(mat^*)\, k \cdot 2 \cdot \frac{8}{3}(-\frac{8}{3} + \frac{4}{3} + \frac{4}{3}) \\
&= 0 \\
\mathbf{K}_{13} &= (mat^*)\, k \int_{-1}^{1}\int_{-1}^{1}\int_{-1}^{1} \nabla_{rst}\mathbf{N}^T \nabla_{rst}\mathbf{N} \det \mathbf{J}_{3D}\, drdsdt \\
&= \frac{1}{8^2}\,(mat^*)\, k \int_{-1}^{1}\int_{-1}^{1}\int_{-1}^{1} [-(1-s)^2(1+t)^2 - (1-r)^2(1+t)^2 + (1-r)^2(1-s)^2]\, drdsdt \\
&= \frac{1}{8^2}\,(mat^*)\, k \cdot 2 \cdot \frac{4}{3}(-\frac{8}{3} - \frac{8}{3} + \frac{4}{3}) \\
&= -\frac{1}{6}
\end{aligned}
\tag{27}
$$

5 G-Type Vectors

In this section the derivation of the gravity vector is shown.

Gravity forces can be computed based on the K-Type matrices in the case of the multiphase-multicomponent formulation. This is very efficient and time-saving. The general formula is:

$$\mathbf{g} = \rho g \mathbf{K} \mathbf{z} \tag{28}$$

where $\mathbf{g}$ is the gravity vector, $\mathbf{K}$ is the conductivity matrix $\mathbf{z}$ is the elevation of the element nodes, i.e. the values of the z-coordinates in the global coordinate system (x,y,z).

6 1-D Linear MPC Matrices

Conductivity Matrix/ Capillarity Matrix The conductivity matrix and capillarity matrix are equal. They are matrices of K-type integral: $\int \nabla \mathbf{N}^T f(u_i) \nabla \mathbf{N} d\Omega$.

$$\begin{aligned} \mathbf{K}_k^{\gamma s} &= \int_{\Omega^e} \nabla \mathbf{N}^T \left(\rho^\gamma X_k^\gamma \frac{k_{\mathsf{rel}}^\gamma \mathbf{k}}{\mu^\gamma} \right) \nabla \mathbf{N} \, d\Omega^e \\ &= \left(\rho^\gamma X_k^\gamma \frac{k_{\mathsf{rel}}^\gamma \mathbf{k}}{\mu^\gamma} \right)^e \frac{A^e}{L^e} \begin{bmatrix} 1 & 0 \\ 0 & 1 \end{bmatrix}^T \end{aligned} \tag{29}$$

Capacitance Matrix The capacitance matrix is a matrix of the type C-type integral: $\int \mathbf{N}^T f(u_i) \mathbf{N} d\Omega$

$$\begin{aligned} \mathbf{C}_k^\gamma &= \int_{\Omega^e} \mathbf{N}^T \left(n \rho^\gamma \hat{X}_k^\gamma \right) \mathbf{N} \, d\Omega^e \\ &= \left(n \rho^\gamma \hat{X}_k^\gamma \right)^e \frac{A^e L^e}{6} \begin{bmatrix} 2 & 1 \\ 1 & 2 \end{bmatrix} \end{aligned} \tag{30}$$

Storativity Pressure Matrix The storativity pressure matrix is a matrix of the type C-type integral: $\int \mathbf{N}^T f(u_i) \mathbf{N} d\Omega$

$$\begin{aligned} \mathbf{C}_k^\gamma &= \int_{\Omega^e} \mathbf{N}^T \left(n S_k^\gamma X_k^\gamma (\frac{\partial \rho}{\partial p})^\gamma \right) \mathbf{N} \, d\Omega^e \\ &= \left(n S_k^\gamma X_k^\gamma (\frac{\partial \rho}{\partial p})^\gamma \right)^e \frac{A^e L^e}{6} \begin{bmatrix} 2 & 1 \\ 1 & 2 \end{bmatrix} \end{aligned} \tag{31}$$

Component Diffusion Matrix The component diffusion matrix is a matrix of the type K-type integral: $\int \nabla \mathbf{N}^T f(u_i) \nabla \mathbf{N} d\Omega$

$$\begin{aligned} \mathbf{D}_k^\gamma &= \int_{\Omega^e} \nabla \mathbf{N}^T \left(n S^\gamma \rho^\gamma D^\gamma \right) \nabla \mathbf{N} \, d\Omega^e \\ &= \left(n S^\gamma \rho^\gamma D^\gamma \right) \frac{A^e}{L^e} \begin{bmatrix} +1 & -1 \\ -1 & +1 \end{bmatrix} \end{aligned} \tag{32}$$

Gravity Forces Gravity forces are written as a matrix of g-type integral: $\int \nabla \mathbf{N} f(u_i) d\Omega$

$$
\begin{aligned}
\mathbf{g}_k^{\gamma s} &= \int_{\Omega^e} \nabla \mathbf{N}^T \left(\rho^\gamma X_k^\gamma \frac{k_{\mathsf{rel}}^\gamma \mathbf{k}}{\mu^\gamma} \rho^\gamma \mathbf{g} \right) d\Omega^e \\
&= \left(\rho^\gamma X_k^\gamma \frac{k_{\mathsf{rel}}^\gamma \mathbf{k}}{\mu^\gamma} \rho^\gamma \mathbf{g} \right) \frac{A^e}{L^e} \begin{bmatrix} -1 \\ +1 \end{bmatrix}
\end{aligned} \tag{33}
$$

7 2-D Quadrilateral MPC Matrices

Conductivity Matrix/ Capillarity Matrix The conductivity matrix and capillarity matrix are equal. They are matrices of K-type integral: $\int \nabla \mathbf{N}^T f(u_i) \nabla \mathbf{N} d\Omega$. On the condition that the medium is isothropic, i.e. that $k_{xx} = k_{yy}$, $\mathbf{k}$ can be extracted from the calculation and be treated like a scalar. Further, the way the matrix is computed here is the special case of $\mathbf{J} = 1$

$$\begin{aligned} \mathbf{K}_k^{\gamma s} &= \int_{\Omega^e} \nabla \mathbf{N}^T \left(\rho^\gamma X_k^\gamma \frac{k_{\mathsf{rel}}^\gamma \mathbf{k}}{\mu^\gamma} \right) \nabla \mathbf{N} \, d\Omega^e \\ &= \left(\rho^\gamma X_k^\gamma \frac{k_{\mathsf{rel}}^\gamma \mathbf{k}}{\mu^\gamma} \right)^e \frac{2V}{3} \begin{bmatrix} 1 & -\frac{1}{4} & -\frac{1}{2} & -\frac{1}{4} \\ & 1 & -\frac{1}{4} & -\frac{1}{2} \\ & & 1 & -\frac{1}{6} \\ & & & 1 \end{bmatrix} \end{aligned} \tag{34}$$

Capacitance Matrix The capacitance matrix is a matrix of the type C-type integral: $\int \mathbf{N}^T f(u_i) \mathbf{N} d\Omega$

$$\begin{aligned} \mathbf{C}_k^\gamma &= \int_{\Omega^e} \mathbf{N}^T \left(n \rho^\gamma \hat{X}_k^\gamma \right) \mathbf{N} \, d\Omega^e \\ &= \left(n \rho^\gamma \hat{X}_k^\gamma \right)^e \frac{V}{9} \begin{bmatrix} 1 & \frac{1}{2} & \frac{1}{4} & \frac{1}{2} \\ & 1 & \frac{1}{2} & \frac{1}{4} \\ & & 1 & \frac{1}{2} \\ & & & 1 \end{bmatrix} \end{aligned} \tag{35}$$

Storativity Pressure Matrix The storativity pressure matrix is a matrix of the type C-type integral: $\int \mathbf{N}^T f(u_i) \mathbf{N} d\Omega$

$$\begin{aligned} \mathbf{C}_k^\gamma &= \int_{\Omega^e} \mathbf{N}^T \left(n S_k^\gamma X_k^\gamma (\frac{\partial \rho}{\partial p})^\gamma \right) \mathbf{N} \, d\Omega^e \\ &= \left(n S_k^\gamma X_k^\gamma (\frac{\partial \rho}{\partial p})^\gamma \right)^e \frac{V}{9} \begin{bmatrix} 1 & \frac{1}{2} & \frac{1}{4} & \frac{1}{2} \\ & 1 & \frac{1}{2} & \frac{1}{4} \\ & & 1 & \frac{1}{2} \\ & & & 1 \end{bmatrix} \end{aligned} \tag{36}$$

Component Diffusion Matrix The component diffusion matrix is a matrix of the type K-type integral: $\int \nabla \mathbf{N}^T f(u_i) \nabla \mathbf{N} d\Omega$

$$\begin{aligned}\mathbf{D}_k^\gamma &= \int_{\Omega^e} \nabla \mathbf{N}^T \left(nS^\gamma \rho^\gamma D^\gamma\right) \nabla \mathbf{N} \, d\Omega^e \\ &= \left(nS^\gamma \rho^\gamma D^\gamma\right) \frac{2V}{3} \begin{bmatrix} 1 & -\frac{1}{4} & -\frac{1}{2} & -\frac{1}{4} \\ & 1 & -\frac{1}{2} & -\frac{1}{2} \\ & & 1 & -\frac{1}{6} \\ & & & 1 \end{bmatrix}\end{aligned} \tag{37}$$

Gravity Forces The gravity vector has 4 entries in the 2-D quadrilateral discretization. The conductivity matrix is computed as shown above, and can be used to compute the gravity vector. $\mathbf{z}$ is the vector of the z-values of all element nodes in the global coordinate system. Hence, the gravity vector will be null if the calculation is done in a x-y plane with z coordinates that are 0.

$$\mathbf{g} = \rho g \mathbf{K}_k^{\gamma s} \mathbf{z} \tag{38}$$

8 3-D Hexahedral MPC Matrices

The matrices as shown here are examples that were calculated assuming that $\mathbf{J}$ is equal to the unity matrix, hence also $\det \mathbf{J} = 1$. This development allows an evaluation of the relationship between the matrix entries. In order to see this relationship can only be observed in numerical integrations with at least 2-3 Gauss points. With 1 Gauss point the accuracy of the numerical integration is not good enough. This should also be noted for the execution of calculations.

Conductivity Matrix/ Capillarity Matrix The conductivity matrix and capillarity matrix are equal. They are matrices of K-type integral: $\int \nabla \mathbf{N}^T f(u_i) \nabla \mathbf{N} d\Omega$. On the condition that the medium is isothropic, i.e. that $k_{xx} = k_{yy}$, $\mathbf{k}$ can be extracted from the calculation and be treated like a scalar.

$$\begin{aligned}
\mathbf{K}_k^{\gamma s} &= \int_{\Omega^e} \nabla \mathbf{N}^T \left(\rho^\gamma X_k^\gamma \frac{k_{\mathsf{rel}}^\gamma \mathbf{k}}{\mu^\gamma} \right) \nabla \mathbf{N} \, d\Omega^e \\
&= \left(\rho^\gamma X_k^\gamma \frac{k_{\mathsf{rel}}^\gamma \mathbf{k}}{\mu^\gamma} \right)^e \begin{bmatrix}
\frac{2}{3} & 0 & -\frac{1}{6} & 0 & 0 & -\frac{1}{6} & -\frac{1}{6} & -\frac{1}{6} \\
 & \frac{2}{3} & 0 & -\frac{1}{6} & -\frac{1}{6} & 0 & -\frac{1}{6} & -\frac{1}{6} \\
 & & \frac{2}{3} & 0 & -\frac{1}{6} & -\frac{1}{6} & 0 & -\frac{1}{6} \\
 & & & \frac{2}{3} & -\frac{1}{6} & -\frac{1}{6} & -\frac{1}{6} & 0 \\
 & & & & \frac{2}{3} & 0 & -\frac{1}{6} & 0 \\
 & & & & & \frac{2}{3} & 0 & -\frac{1}{6} \\
 & & & & & & \frac{2}{3} & 0 \\
 & & & & & & & \frac{2}{3}
\end{bmatrix}
\end{aligned} \tag{39}$$

Capacitance Matrix The capacitance matrix is a matrix of the type C-type integral: $\int \mathbf{N}^T f(u_i) \mathbf{N} d\Omega$

$$\begin{aligned}
\mathbf{C}_k^\gamma &= \int_{\Omega^e} \mathbf{N}^T \left(n \rho^\gamma \hat{X}_k^\gamma \right) \mathbf{N} \, d\Omega^e \\
&= \left(n \rho^\gamma \hat{X}_k^\gamma \right)^e \frac{V}{27} \begin{bmatrix}
1 & \frac{1}{2} & \frac{1}{4} & \frac{1}{2} & \frac{1}{2} & \frac{1}{4} & \frac{1}{8} & \frac{1}{4} \\
 & 1 & \frac{1}{2} & \frac{1}{4} & \frac{1}{4} & \frac{1}{2} & \frac{1}{4} & \frac{1}{8} \\
 & & 1 & \frac{1}{2} & \frac{1}{8} & \frac{1}{4} & \frac{1}{2} & \frac{1}{4} \\
 & & & 1 & \frac{1}{4} & \frac{1}{8} & \frac{1}{4} & \frac{1}{2} \\
 & & & & 1 & \frac{1}{2} & \frac{1}{4} & \frac{1}{2} \\
 & & & & & 1 & \frac{1}{2} & \frac{1}{4} \\
 & & & & & & 1 & \frac{1}{2} \\
 & & & & & & & 1
\end{bmatrix}
\end{aligned} \tag{40}$$

Storativity Pressure Matrix The storativity pressure matrix is a matrix of the type C-type integral: $\int \mathbf{N}^T f(u_i) \mathbf{N} d\Omega$

$$
\begin{aligned}
\mathbf{C}_k^\gamma &= \int_{\Omega^e} \mathbf{N}^T \left(n S_k^\gamma X_k^\gamma (\frac{\partial \rho}{\partial p})^\gamma \right) \mathbf{N} \, d\Omega^e \\
&= \left(n S_k^\gamma X_k^\gamma (\frac{\partial \rho}{\partial p})^\gamma \right)^e \frac{V}{27} \begin{bmatrix}
1 & \frac{1}{2} & \frac{1}{4} & \frac{1}{2} & \frac{1}{4} & \frac{1}{8} & \frac{1}{4} & \frac{1}{8} \\
 & 1 & \frac{1}{2} & \frac{1}{4} & \frac{1}{2} & \frac{1}{4} & \frac{1}{8} & \frac{1}{4} \\
 & & 1 & \frac{1}{2} & \frac{1}{4} & \frac{1}{8} & \frac{1}{4} & \frac{1}{8} \\
 & & & 1 & \frac{1}{8} & \frac{1}{4} & \frac{1}{8} & \frac{1}{4} \\
 & & & & 1 & \frac{1}{2} & \frac{1}{4} & \frac{1}{2} \\
 & & & & & 1 & \frac{1}{2} & \frac{1}{4} \\
 & & & & & & 1 & \frac{1}{2} \\
 & & & & & & & 1
\end{bmatrix}
\end{aligned}
\tag{41}
$$

Component Diffusion Matrix The component diffusion matrix is a matrix of the type K-type integral: $\int \nabla \mathbf{N}^T f(u_i) \nabla \mathbf{N} d\Omega$

$$
\begin{aligned}
\mathbf{D}_k^\gamma &= \int_{\Omega^e} \nabla \mathbf{N}^T \left(n S^\gamma \rho^\gamma D^\gamma \right) \nabla \mathbf{N} \, d\Omega^e \\
&= \left(n S^\gamma \rho^\gamma D^\gamma \right) \frac{V}{27} \begin{bmatrix}
\frac{2}{3} & 0 & -\frac{1}{6} & 0 & 0 & -\frac{1}{6} & -\frac{1}{6} & -\frac{1}{6} \\
 & \frac{2}{3} & 0 & -\frac{1}{6} & -\frac{1}{6} & 0 & -\frac{1}{6} & -\frac{1}{6} \\
 & & \frac{2}{3} & 0 & -\frac{1}{6} & -\frac{1}{6} & 0 & -\frac{1}{6} \\
 & & & \frac{2}{3} & -\frac{1}{6} & -\frac{1}{6} & -\frac{1}{6} & 0 \\
 & & & & \frac{2}{3} & 0 & -\frac{1}{6} & 0 \\
 & & & & & \frac{2}{3} & 0 & -\frac{1}{6} \\
 & & & & & & \frac{2}{3} & 0 \\
 & & & & & & & \frac{2}{3}
\end{bmatrix}
\end{aligned}
\tag{42}
$$

Gravity Forces The gravity vector has 8 entries in the 3-D quadrilateral discretization. The conductivity matrix is computed as shown above, and can be used to compute the gravity vector. $\mathbf{z}$ is the vector of the z-values of all element nodes in the global coordinate system.

$$
\mathbf{g} = \rho g \mathbf{K}_k^{\gamma s} \mathbf{z}
\tag{43}
$$

9 Example

A one meter long bentonite beam is heated to $373K$ at the left side. The initial conditions and boundary conditions are shown in Table 9. Material properties are listed in Table 9 and the capillary pressure - saturation relationship is illustrated in Figure 3. Spatial discretization is 0.01m in x,y, and z direction. Calculation time is 1.0e5 seconds.

Initial Conditions	Unit	Value
Gas Pressure	Pa	101325
Liquid Saturation	-	1.0
Temperature	K	285
Boundary Conditions	**Unit**	**Value**
Gas Pressure left	Pa	1.0e6
Gas Pressure right	Pa	101325
Liquid Saturation left	-	0.15
Liquid Saturation right	-	1.0
Temperature left	K	373

Table 1: Initial and Boundary Conditions

Material Property	Unit	Value
Porosity	-	0.407407407
Permeability	m^2	8.22854E-20
Diffusion coefficient	$\frac{m^2}{s}$	2.13e-6
Density	$\frac{kg}{m^3}$	1830
Heat capacity	$\frac{J}{kg \cdot K}$	1605
Heat conductivity	$\frac{J}{K \cdot m \cdot s}$	0.718799939
Börgesson swelling coefficients		
Relative permeability	-	1.0
Void ratio	-	7.0
Eta	-	3293673.0
Swelling pressure	Pa	-0.165
Swelling pressure - saturation curve	-	3.0

Table 2: Material Properties for the benchmark th_partitioned

Figure 4 shows a comparison for 1-D and 3-D results for liquid saturation, gas pressure and temperature at time $t = 1.0e + 5$ seconds. It can be seen that the results are virtually identical.

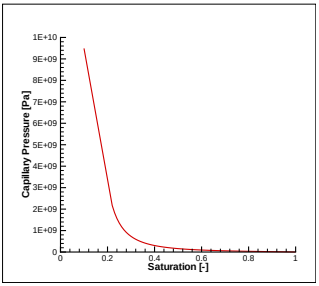

Figure 3: Capillary pressure - saturation relationship for the benchmark th_partitioned

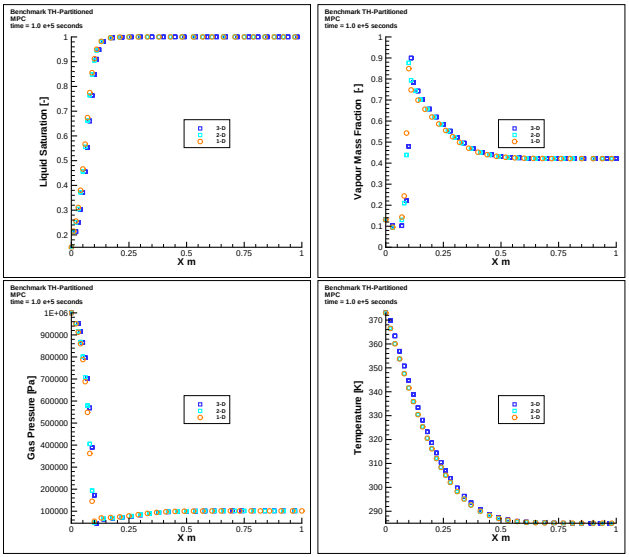

Figure 4: Comparison of 1D, 2D, and 3D results for the benchmark th_partitioned

References

J. De Jonge and O. Kolditz. Non-isothermal flow processes in porous media, part I : Governing equations and finite element implementation. Rockflow-Report 2002-1, Centre of Applied Geosciences, University of Tübingen, 2002.

O. Kolditz. *Computational Methods in Environmental Fluid Mechanics*. Springer, 2002.

Numerical implementation of thermally and hydraulically coupled processes in non-isothermal porous media

To be published as book chapter in:

Coupled Thermo-Hydro-Mechanical processes in geo-systems, ed. O. Stephansson, J. Hudson, L. Jing, Elsevier Science

NUMERICAL IMPLEMENTATION OF THERMALLY AND HYDRAULICALLY COUPLED PROCESSES IN NON-ISOTHERMAL POROUS MEDIA

Joëlle De Jonge, Mingliang Xie, Olaf Kolditz
Centre for Applied Geoscience (ZAG) / Section Geohydrology/Geoinformatics
University of Tübingen, Germany

Abstract: To better understand the coupling of thermal (T), hydraulic (H) and mechanical (M) processes (T-H-M processes) and their influence on the system behaviour, models allowing T-H-M coupling are developed. These models allow simulations in the near-field of the system. Such a model has been developed within the simulator RockFlow/RockMech. This paper concentrates on the thermal and hydraulic processes. For those processes, the material parameters and state variables are highly non-linear and mostly functions of temperature, saturation and pressure. This paper shows how these dependencies are formulated mathematically and are implemented into RockFlow/RockMech. The implementation allows phase changes between the fluid phases (gas and liquid) to occur explicitly. The model allows the simulation of very low permeability clays with high capillary pressures. An example for code validation is shown, where low permeability clay is desaturated, lastly, current work on the calculations performed in the near field study (BMT1) of the DECOVALEX III project is outlined.

1. INTRODUCTION

For deep geological disposal of nuclear waste, engineered barrier systems have to be developed. To develop appropriate barriers, the disposal scenario has to be simulated numerically, as a prediction and engineering tool in the near-field of the disposal site. The numerical model has to be able to reproduce the various processes. Figure 1 shows a plan view of a possible disposal scenario, with nuclear waste packed into the core at the centre, a bentonite buffer surrounding it. Waste canister and buffer are placed into the host rock. The processes arising in this situation are coupled processes, composed of thermal processes (heating, cooling, evaporation, condensation), hydraulic processes (water intrusion, saturation, desaturation), mechanical processes (elastic and plastic deformation), and chemical processes (radiation, reactions). This paper concentrates on the coupling of thermal and hydraulic processes.

The engineered buffer used in deep geological disposal sites is often pure bentonite or a bentonite – sand mixture. Bentonite is a material with very low permeability and swelling properties. The swelling properties are used as a seal against water intrusion.

RockFlow is a simulator that is used to model near-field situation of the type described above (Kolditz et al. (2003)). It is a finite element code, programmed using object-oriented techniques. Object-orientation allows a wide spectrum of applications for the code, and also simultaneous code development (Kolditz (2002)). This paper will concentrate on the model within RockFlow, that is used for simulating the coupling of thermal and hydraulic processes (TH). The governing equations of the model are shown, as well as how these equations are treated numerically. A code application example for the desaturation of bentonite will be presented. The first example is based on an example in Olivella and Gens (2000) and partially serves as model verification. Furthermore, the code development finds application in bench mark test 1 (BMT1) of the DECOVALEX III (International co-operative project for the DEvelopment of COupled models and their VALidation against EXperiments in nuclear waste isolation) project (Jing et al. (1999)). Current work on this project is presented.

Figure 1. THM processes in deep geological disposal sites.

2. GOVERNING EQUATIONS

We use a componental formulation as applied by Emmert (1997) for modelling of steam injection for soil remediation strategies. The TH code in RockFlow has three primary variables, gas phase pressure, liquid phase saturation, and temperature. The set of three governing equations result from two balance equations, the general mass balance equation and the energy balance equation. The general mass balance is shown in equation (1), where n [-] is porosity, S [-] is saturation, ρ [kg/m^3] is density, J [kg/(ms)] is flux, and Q [m^3/s] is a source-sink term. The superscripts l, g, and s denote the liquid phase, gas phase, and solid phase respectively. The subscript k denotes the component, which is air (a) or water (w). The first term of equation (*1*) is a mass storage term, the second term shows mass movement and the right hand side accounts for mass leaving or entering the system.

$$\frac{\partial}{\partial t}\left(n S^{l} \rho_{k}^{l} + n S^{g} \rho_{k}^{g}\right) + \nabla \cdot \left(\mathbf{J}_{k}^{w} + \mathbf{J}_{k}^{gw}\right) + \nabla \cdot \left(\mathbf{J}_{k}^{a} + \mathbf{J}_{k}^{ga}\right) = Q_{k} \tag{1}$$

Equation (2) shows the general energy balance equation, where u [J/kg] is internal energy and J [J/(ms)] is heat flux. The structure of the equation is similar to that of equation (1).

$$\begin{aligned} &\frac{\partial}{\partial t}\left\{(1-n)\rho^{s} u^{s} + n S^{w} \rho^{w} u^{w} + n S^{l} \rho^{l} u^{l}\right\} \\ &+ \left\{\nabla \cdot \mathbf{J}_{h}^{s} + \nabla \cdot \mathbf{J}_{h}^{w} + \nabla \cdot \mathbf{J}_{h}^{a}\right\} = Q_{h} \end{aligned} \tag{2}$$

Equations of state and material laws give the necessary specifications to transform the balance equations into governing equations for the model. The equations of state and material laws used in the TH model are thoroughly described in De Jonge and Kolditz (2002).

In the TH code the governing equations are split according to components, rather than phases. This choice was made in regard to phase changes. Hence, the general mass balance equation results in the component equation for air, and the component equation for water, which are our components in the TH model. Each component equation contains terms for both, the liquid and the gas phase. Equation (3) shows the governing equation for air or water, (k = a, w), where X [-] is the mass fraction, P [Pa] is pressure, k_{rel} [-] is the relative permeability, k [m^2] is the reference permeability, μ [Pas] is viscosity, P_c [Pa] is capillary pressure, g [m/s^2] is the gravity vector, and D [m^2/s] is the diffusion coefficient.

$$\begin{aligned} &n X_{k}^{g}\left(S^{g} \frac{\partial \rho^{g}}{\partial p^{g}} + S^{l} \frac{\partial \rho^{l}}{\partial p^{l}}\right) \frac{\partial p^{g}}{\partial t} \\ &- \nabla \cdot \left(\rho^{g} X_{k}^{g} \frac{k_{rel}^{g} \mathbf{k}}{\mu^{g}} \nabla p^{g}\right) - \nabla \cdot \left(\rho^{l} X_{k}^{l} \frac{k_{rel}^{l} \mathbf{k}}{\mu^{l}} \nabla p^{l}\right) \\ &+ n\left(-\rho^{g} X_{k}^{g} + \rho^{l} X_{k}^{l}\right) \frac{\partial S^{l}}{\partial t} \\ &- Q_{k} \\ &+ \left(n S^{g} X_{k}^{l} \frac{\partial \rho^{l}}{\partial p^{l}} \cdot \frac{\partial p_{c}}{\partial t} - \nabla \cdot \left(\rho^{l} X_{k}^{l} \frac{k_{rel}^{l} \mathbf{k}}{\mu^{l}} \nabla p_{c}\right)\right. \\ &- \nabla \cdot \left(\rho^{g} X_{k}^{g} \frac{k_{rel}^{g} \mathbf{k}}{\mu^{g}} \rho^{g} \mathbf{g}\right) + \nabla \cdot \left(\rho^{l} X_{k}^{l} \frac{k_{rel}^{l} \mathbf{k}}{\mu^{l}} \rho^{l} \mathbf{g}\right) \\ &+ \nabla \cdot \left(n S^{g} \rho^{g} D_{k}^{g} \nabla X_{k}^{g}\right) \end{aligned} \tag{3}$$

Equation (4) shows the governing equation resulting from the energy balance equation, where c [J/(kgK)] is heat capacity, λ [J/(Kms)] is thermal conductivity, and h [J/kg] is enthalpy.

$$\begin{aligned} &\left\{(1-n)\rho^{s} c^{s} + n S^{g} \rho^{g} c^{g} + n S^{l} \rho^{l} c^{l}\right\} \frac{\partial T}{\partial t} \\ &+ \left(\rho^{g} c^{g} \frac{k_{rel}^{g} \mathbf{k}}{\mu^{g}} \left(\nabla p^{g} - \rho^{g} \mathbf{g}\right)\right. \\ &\left. + \rho^{l} c^{l} \frac{k_{rel}^{l} \mathbf{k}}{\mu^{l}} \left(\nabla p^{l} - \rho^{l} \mathbf{g}\right)\right) \nabla T \\ &- \nabla \cdot \left\{\left((1-n)\lambda^{s} + n S^{g} \lambda^{g} + n S^{l} \lambda^{l}\right) \nabla T\right\} \\ &- \nabla \cdot \left\{n S^{g} \rho^{g} D_{h}^{g} h^{g} \nabla X_{h}^{g}\right\} \\ &- \nabla \cdot \left\{n S^{g} \rho^{g} D_{h}^{l} h^{g} \nabla X_{h}^{g}\right\} \\ &- \rho Q_{T} \end{aligned} \tag{4}$$

3. NUMERICAL IMPLEMENTATION

Figure 2 illustrates the numerical implementation used in RockFlow. The method of weighted residuals is applied to the governing equations, resulting the weak formulation of the algebraic equations. The order of spatial derivatives is reduced by using the Gauss-Ostrogradski theorem, thus resulting in the algebraic equation system.

Equation (5) shows the resulting algebraic equation for the water and air components, where (k = a, w) and θ is a value between [0,1]. C_P, C_S, K_P, and K_S are element matrices, that are dependent on element dimension and shape. Development for the case of 1-D elements is shown in Kolditz and De Jonge (2003), and 2-D triangular elements in De Jonge and Kolditz (2002).

Figure 2. Numerical implementation

$$
\begin{aligned}
&\left[\frac{1}{\Delta t}[\mathbf{C}_{vv}^{t+1}-\mathbf{C}_{vv}^{t}]+\delta[\mathbf{K}_{vv}^{t+1}+\mathbf{K}_{vv}^{t}]\right][\mathbf{p}^{g}]^{t+1}\\
&+\left[\frac{1}{\Delta t}[\mathbf{C}_{vs}^{t}-\mathbf{C}_{vs}^{t}]\right][\mathbf{S}^{l}]^{t+1}\\
&-\left[\frac{1}{\Delta t}[\mathbf{C}_{vv}^{t+1}-\mathbf{C}_{vv}^{t}]-[1-\delta][\mathbf{K}_{vv}^{t+1}-\mathbf{K}_{vv}^{t}]\right][\mathbf{p}^{g}]^{t}\\
&+\left[\frac{1}{\Delta t}[\mathbf{C}_{vs}^{t}-\mathbf{C}_{vs}^{t}]\right][\mathbf{S}^{l}]^{t}\\
&+\left[\frac{1}{\Delta t}\mathbf{C}_{vv}^{t}\right][[\mathbf{p}_{c}]^{t+1}-[\mathbf{p}_{c}]^{t}]\\
&+[\mathbf{K}_{v}^{t}][\theta[\mathbf{p}_{c}]^{t+1}+[1-\delta][\mathbf{p}_{c}]^{t}]\\
&-[\mathbf{K}_{v}^{t}][\theta[\mathbf{X}_{v}^{t+1}]+[1-\delta][\mathbf{X}_{v}^{t}]\\
&+[\mathbf{K}_{v}^{t}+\mathbf{K}_{v}^{t}]g
\end{aligned}
\tag{5}
$$

Equation (6) shows the algebraic equation for the energy component in matrix form. As above, the element matrices for the 1-D and 2-D triangular elements can be found in De Jonge and Kolditz (2002).

$$
\begin{aligned}
&\left[\frac{1}{\Delta t}\mathbf{C}_{T}+\delta\mathbf{A}_{T}+\theta\mathbf{K}_{T}\right][\mathbf{T}]^{t+1}\\
&=\theta[\mathbf{f}_{T}]_{T}^{t+1}+[1-\theta][\mathbf{f}_{T}]^{t}\\
&+\left[\frac{1}{\Delta t}\mathbf{C}_{T}-[1-\theta]\mathbf{A}_{T}-[1-\theta]\mathbf{K}_{T}\right][\dot{\mathbf{T}}]^{t}
\end{aligned}
\tag{6}
$$

In the implementation, each algebraic equation is linked to a primary variable. Thus, the algebraic equation for air is linked to gas pressure, the equation for water is linked to liquid phase saturation and the energy equation is linked to temperature. The system of equations can be solved in two ways in the TH model; either they are solved iteratively, gas pressure and liquid saturation are solved simultaneously, followed by temperature, as shown in the system of equations (7).

$$
\begin{aligned}
\left[\frac{1}{\Delta t}\mathbf{C}_{vv}+\mathbf{K}_{vv}\right][\mathbf{p}^{g}]^{t+1}+\left[\frac{1}{\Delta t}\mathbf{C}_{vs}\right][\mathbf{S}^{l}]^{t+1} &= \mathrm{RHS}_{v}\\
\left[\frac{1}{\Delta t}\mathbf{C}_{sv}+\mathbf{K}_{sv}\right][\mathbf{p}^{g}]^{t+1}+\left[\frac{1}{\Delta t}\mathbf{C}_{ss}\right][\mathbf{S}^{l}]^{t+1} &= \mathrm{RHS}_{s}\\
\left[\frac{1}{\Delta t}\mathbf{C}_{T}+\mathbf{K}_{T}+\mathbf{A}_{T}\right][\dot{\mathbf{T}}]^{t+1} &= \mathrm{RHS}_{T}
\end{aligned}
\tag{7}
$$

4. EXAMPLE – DESATURATION

The example presented here is based on the one shown in Olivella and Gens (2000) with slightly modified material properties and temperature boundary condition values. The example portrays the desaturation of bentonite due to heating in a closed system. The set-up is as illustrated in Figure 3. A bentonite block is heated to 100°C on the left side. Dimensions and initial conditions are as shown on Figure 3. The only boundary condition is the temperature boundary condition at the heater.

Figure 3. Desaturation example set-up

The material parameters are as summarised in Table 1. Because the capillary pressures in bentonite are very high (up to 10^{10} Pa, as shown in Figure 5), a large suction pressure is created, that strongly favours saturation of the sample. Vapour movement, and hence desaturation due to sample heating can only be modelled if vapour flow is encouraged. This can be achieved by including a vapour diffusion term into the balance equation or

Table 1. Material parameters for the desaturation example.

Parameter	Value
Porosity [-]	0.44
Tortuosity [-]	0.1
Permeability [m^2]	5×10^{-19}
Relative permeability [-]	Figure 4
Capillary pressure	Figure 5
Density [kg/m^3]	1650
Heat capacity [J/(kg*K)]	1605
Heat conductivity [J/(K*m*s)]	0.5

alternatively, by choosing a dual relative permeability – saturation relationship so that vapour movement is favoured at low liquid phase saturations (when capillary pressure is highest). Olivella and Gens (2000) developed such a model. It is based on experimental observations of bentonite properties. The reasoning behind it is, that in the dry bentonite pore spaces are higher, resulting in a higher permeability. When bentonite is wet however, it swells and pore spaces are accordingly small. Figure 4 shows an example of such a dual relative permeability – saturation model.

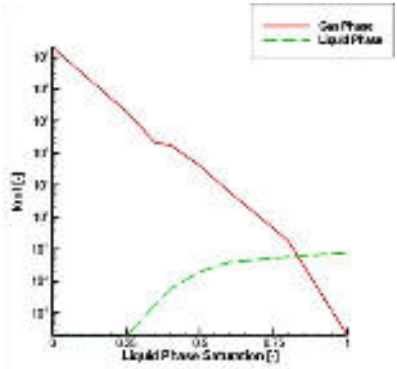

Figure 4. Relative permeability – saturation relationship – dual model

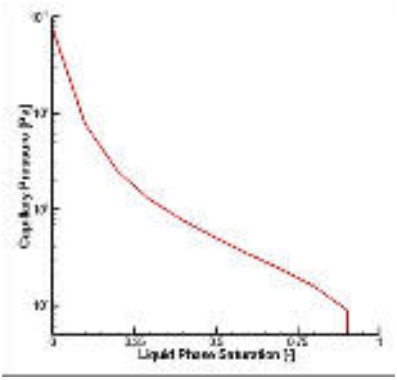

Figure 5. Capillary pressure – saturation relationship.

Because there are no saturation and pressure boundary conditions in the example, saturation is free to fall and rise. This can be observed in the results shown in Figure 7. From the initial liquid phase saturation of 0.4, the value drops progressively next to the heater, as expected. On the right boundary, the effects of capillary pressure can be seen through the higher value of liquid phase saturation. The gas phase pressure shows a small response to the saturation distribution. Where liquid saturation drops, and by reciprocity gas saturation increases, gas pressure also increases. At the right boundary, the decrease in gas pressure corresponds to the increase in liquid saturation. One can see that the stationary temperature is reached in less than ½ day. The vapour mass fraction responds to the temperature distribution immediately.

The results thus show successful modelling of a desaturation process in bentonite, by using the RockFlow TH model.

5. EXAMPLE – BMT1 DECOVALEX III

This section describes the current work on the near-field bench mark test (BMT1) of the DECOVALEX project. The results shown in this section are preliminary and serve to outline the direction of current code development and to further illustrate the working of the RockFlow TH model.

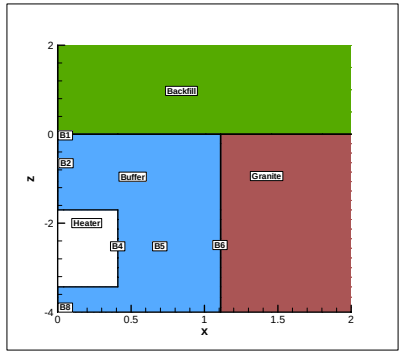

Figure 6. Set-up for BMT1.

In BMT1 a typical deep geological waste repository set-up is studied. Figure 6 shows a detail of the set-up. The waste canister is surrounded by a bentonite buffer material, and the backfill for the tunnel is made of a bentonite-sand mixture. The host rock is granite. Material

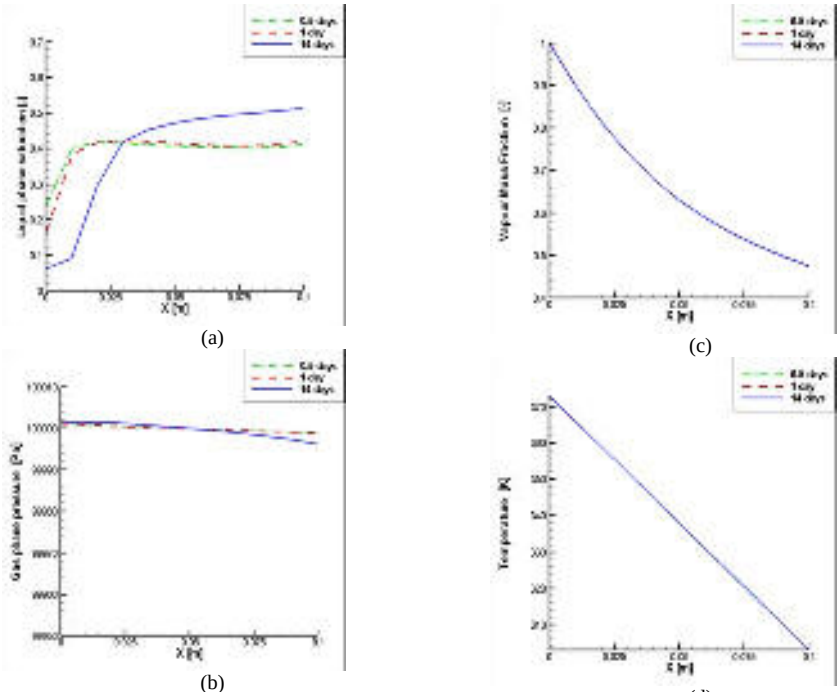

(a) (c)

(b) (d)

Figure 7. Results of desaturation example. (a) liquid phase saturation, (b) gas phase pressure, (c) vapour mass fraction, (d) Temperature.

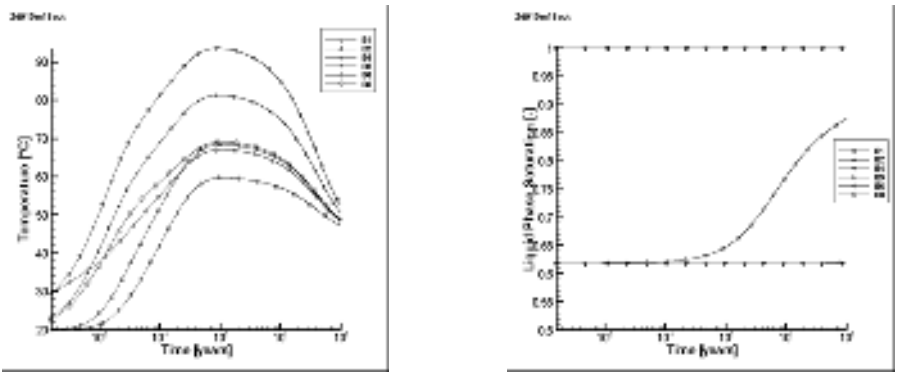

(a) (b)

Figure 8. Preliminary BMT1 Results (a) Temperature evolution , (b) Liquid phase saturation evolution in the observation points.

parameters, initial conditions and boundary conditions are as described in the BMT1 definition.

Table 2. Material properties for BMT1

Property	Buffer	Rock mass	Backfill
Density [kg/m3]	1650	2746	1750
Effective Porosity [%]	20	3	30
Initial Water content [%]	15	100	15
Permeability [m/s]	$1.6\ 10^{-20}$	$1\ 10^{-17}$	$1.9\ 10^{-19}$
Specific heat [J/kg/K]	426	833	826
Thermal conductivity [W/m/K]	1.26	2.71	1.37
Capillary pressure [Pa]	Van Genuchten		
Relative permeability [-]	Van Genuchten		

The liquid saturation rises steadily in observation point B6. At all the other observation points the liquid saturation remains the same over the considered time.

The temperature goes through a maximum after a period of 1.5 years. At observation point B4, the maximum temperature is 78°C. After 100 years, the temperature decreases to a range between 48°C and 52°C for all observation points. The vapour mass fraction follows the temperature pattern, going through the maximum at the same time.

6. CONCLUSIONS

This paper presented the thermo-hydraulic (TH) coupled finite element model that we developed within the object-oriented simulator RockFlow. The governing equations, their numerical implementation, and the algebraic equations, as well as available coupling schemes for the RockFlow TH model were presented.

The model can now be used for the analysis of flow and heat transport processes in the near field of nuclear waste disposal. The model benefits of the componental approach, and is not restrained by the Richards approximation.

The bentonite evaporation example showed that the RockFlow TH model is able to faithfully represent the drying of bentonite near a heat source and a consequent saturation at the far end of the sample within a closed system.

Current work on BMT1 was reported. From the results, one can see that the dual relative permeability – saturation model used in the desaturation example might be useful for larger scale tests, such as the BMT1 application, so that desaturation near the heater can be reproduced correctly by the TH model.

7. ACKNOWLEDGEMENTS

This project is supported by the Federal Institute of Geosciences and Natural Resources (BGR) under grant 2-1003822. We thank Dr. Wallner and Dr. Shao for their support of this research project.

8. REFERENCES

De Jonge, J. and Kolditz, O. (2002): *Non-Isothermal Flow Processes in Porous Media, Part I : Governing Equations and Finite Element Implementation*, Rockflow Preprint [2002-1].

Emmert. M. 1997. *Numerische Modellierung nichtisothermer Gas-Wasser Systeme in porösen Medien.* PhD thesis, Insitut für Wasserbau, Universität Stuttgart.

Jing L. Stephansson O., Börgesson L. Chijimatzu M. Kautsky F. Tsang C-F. 1999. *DECOVALEX II PROJECT Technical Report – Task 2C.* SKI Report 99:23. ISSN 1104-1374

Kolditz. O. 2002. *Computational Methods in Environmental Fluid Mechanics.* Springer.

Kolditz O. and De Jonge J. 2003. *Non-Isothermal Two-Phase Flow in Porous Media.* Submitted to Computational Mechanics.

Kolditz O., Bauer S., Beinhorn M., de Jonge J., Kalbacher T., McDermott C., Wang W., Xie M., Kaiser R., and Kohlmeier M. 2003. ROCKFLOW - Theory and users manual, release 3.9. Groundwater modeling group, Center for Applied Geosciences, University of Tübingen, Institute of Fluid Mechanics, University of Hannover.

Olivella S. and Gens. A. 2000. *Vapour transport in low permeability unsaturated soil with capillary effects.* Transport in Porous Media, 40:219–241.

Benchmarking non-isothermal multi-phase numerical simulations

Technical report, Nr. 2003-12:

Center of Applied Geosciences

University of Tübingen

Benchmarking Non-Isothermal Multi-Phase Numerical Simulations

Joëlle De Jonge[1], Irina Engelhardt[2], Olaf Kolditz[1]

[1]Center for Applied Geoscience Section Geohydrology/Hydroinformatics
University of Tübingen, Germany
[2]Federal Institute for Geosciences and Natural Resources
Hannover, Germany

Abstract

Non-isothermal multi-componental problems describe the interaction of thermal, hydraulic, and mechanical processes (THM Processes). Various computer codes have been developed to simulate that kind of problem. However, few benchmarks have been developed specifically for the coupling of thermal and hydraulic processes (TH Processes). This paper proposes an experiment and its treatment as a benchmark. The experiment is a column setup, where a water saturated bentonite sample is first heated, then nitrogen is injected into sample, thus creating a TH process setup. The experiment was simulated with the code iTOUGH2, an inverse modelling tool, and with RF/RM a forward modelling tool. The simulation approaches of both simulators are described, then the approaches and their implications on the results are compared and discussed.

Introduction

In the last years, a number of codes for solving non-isothermal multi-componental problems have been developed. Non-isothermal multi-componental problems describe the interaction of thermal, hydraulic and mechanical processes (THM). The codes vary in the choice of primary variables, the approach used, the degree of coupling, and the numerical method utilized.

CODE_BRIGHT, RockFlow/RockMech (RF/RM), THAMES, and TOUGH2 are examples of codes that are utilized in the field of multiphase simulations. CODE_BRIGHT is a 3-D THM simulator developed in Barcelona, Spain (Technical University of Catalonia (UPC)). The code is a finite element code, that solves any partial set of the five following equations: stress equilibrium, water mass balance, air mass balance, energy balance, and balance of conservative solute. Its applications lie in the field of nuclear waste disposal and soil remediation (Olivella et al. [1996]). RF/RM is a finite element simulator, developed in Germany (University of Tübingen and University of Hannover). RF/RM is a finite element code, written in C-objective/C++, using object oriented programming techniques. This allows RF/RM to be applied to a variety of THM problem situations (geothermal engineering, soil remediation, and nuclear waste storage), using application specific models and kernels within the simulator. For TH modelling, which is the object of this paper a 1-D and 2-D code has been developed within the RF/RM simulator. The TH code takes phase transitions into account and works with a non-constant gas phase pressure. The code is documented in a variety of publications, for example Kolditz [2002], Kolditz et al. [2003] and Thorenz [2001]. The program THAMES is developed in Japan, originally it was developed by Ohnishi et al. (Ohnisi et al. [1985]). It is a 3-D finite element THM code that has been developed in the context of nuclear waste disposal in the subsurface. The unknown variables are total pressure,

displacement vector and temperature (Chijimatsu et al. [2000]). The program TOUGH2 is developed at the Lawrence Berkeley National Laboratory (LBNL), USA, for geothermal reservoir applications. Time and space are discretized using the finite difference method. The program TOUGH2 is valid for one-, two-, and three-dimensional numerical models to simulate the coupled transport of water, vapor, air, and heat in porous and fractured media (Pruess [1987]). TOUGH2 has further been applied for studies of high-level nuclear waste isolation in partially saturated porous media. The TOUGH2 simulator takes account of fluid flow in the liquid and gas phase under pressure, viscous, and gravity forces according to DARCY' s law with interferences between the phases represented by the relative permeability functions.

Other areas of numerical simulations have classical benchmark problems, such as the Theis or Buckley problems, which can be calculated analytically. This is not the case for THM simulations. There are, however, some benchmarks, that, even if complex help verify and calibrate codes. The DECOVALEX (International co-operative project for the DEvelopment of COupled models and their VALidation against EXperiments in nuclear waste isolation) program and BENCHPAR program include a benchmark test for THM processes in the near-field applied to nuclear waste storage problems. The FEBEX problem is also within the frame of the DECOVALEX and BENCHPAR and deals with a large scale heater test for the same application. Another large scale heater test was performed in Japan, named the BIG-BEN (Big Bentonite facility) test. (Chijimatsu et al. [2000]). However, all these benchmark tests are extremely complex.
We were interested in a direct comparison of how a less complex laboratory experiment was handled by two different codes, RF/RM and iTOUGH2. The aim is to provide an adequate benchmarking example for TH processes and to analyze how two numerically very different codes handle the simulation. The simulation of the experiment also partially serves as a code validation for RF/RM.

1 RF/RM Governing Equations

The formulation adopted is a componental formulation. This means, that rather than expressing the governing equations for the phases, the governing equations are expressed for the components (here these are air and water). Equation (1) shows the mass balance equation for the air and water components ($k = a, w$).

$$\frac{\partial}{\partial t}(nS^l\rho_k^l + nS^g\rho_k^g) + \nabla\cdot(\mathbf{J}_k^{ls} + \mathbf{J}_k^{gs}) + \nabla\cdot(\mathbf{J}_k^g + \mathbf{J}_k^l) = Q_k \tag{1}$$

$n\,[-]$ is porosity, $S\,[-]$ is saturation, $\rho\,[\frac{kg}{m^3}]$ is density, $\mathbf{J}\,[\frac{kg}{m\cdot s}]$ is flux, and $Q\,[\frac{m^3}{s}]$ is a source-sink term. The superscripts l, g, and s denote the liquid phase, gas phase, and solid phase. The subscript k denotes the component, which is air (a) or water (w) in our examples. Taking material parameters and equations of state into account, equation (1) can be rewritten as shown in equation (2).

$$\begin{aligned} & nX_k^g\left(S^g\frac{\partial\rho^g}{\partial p^g} + S^l\frac{\partial\rho^l}{\partial p^l}\right)\frac{\partial p^g}{\partial t} \\ - \quad & \nabla\cdot\left(\rho^g X_k^g\frac{k_{\mathrm{rel}}^g\mathbf{k}}{\mu^g}\nabla p^g\right) - \nabla\cdot\left(\rho^l X_k^l\frac{k_{\mathrm{rel}}^l\mathbf{k}}{\mu^l}\nabla p^g\right) \\ + \quad & n(-\rho^g X_k^g + \rho^l X_k^l)\frac{\partial S^l}{\partial t} \\ = \quad & Q_k \end{aligned}$$

$$
\begin{aligned}
&+ \quad (nS^l X_k^l \frac{\partial \rho^l}{\partial p^l}) \frac{\partial p_c}{\partial t} - \nabla \cdot \left(\rho^l X_k^l \frac{k_{\text{rel}}^l \mathbf{k}}{\mu^l} \nabla p_c \right) \\
&- \quad \nabla \cdot \left(\rho^g X_k^g \frac{k_{\text{rel}}^g \mathbf{k}}{\mu^g} \rho^g \mathbf{g} \right) + \nabla \cdot \left(\rho^l X_k^l \frac{k_{\text{rel}}^l \mathbf{k}}{\mu^l} \rho^l \mathbf{g} \right) \\
&+ \quad \nabla \cdot (nS^g \rho^g D_k^g \nabla X_k^g)
\end{aligned} \tag{2}
$$

X $[-]$ is the mass fraction, p $[Pa]$ is pressure, k_{rel} $[-]$ is the relative permeability, $\mathbf{k}$ $[m^2]$ is the reference permeability, μ $[Pa \cdot s]$ is viscosity, p_c $[Pa]$ is capillary pressure, $\mathbf{g}$ $[\frac{m}{s^2}]$ is the gravity vector, and D $[\frac{m^2}{s}]$ is the diffusion coefficient.

The energy balance equation (equation 3) completes the set of equations.

$$
\begin{aligned}
& \frac{\partial}{\partial t} \left((1-n) \rho^s u^s + nS^g \rho^g u^g + nS^l \rho^l u^l \right) \\
&+ \quad (\nabla \cdot \mathbf{J}_h^s + \nabla \cdot \mathbf{J}_h^g + \nabla \cdot \mathbf{J}_h^l) = Q_h
\end{aligned} \tag{3}
$$

u $[\frac{J}{kg}]$ is the internal energy and $\mathbf{J}_h$ $[\frac{J}{m \cdot s}]$ is heat flux. Equation (4) shows the governing equation for the energy equation.

$$
\begin{aligned}
& \left((1-n) \rho^s c^s + nS^g \rho^g c^g + nS^l \rho^l c^l \right) \frac{\partial T}{\partial t} \\
&+ \quad \Big(\rho^g c^g \frac{k_{\text{rel}}^g \mathbf{k}}{\mu^g} (\nabla p^g - \rho^g \mathbf{g}) \\
& \quad + \rho^l c^l \frac{k_{\text{rel}}^l \mathbf{k}}{\mu^l} (\nabla p^l - \rho^l \mathbf{g}) \Big) \nabla T \\
&- \quad \nabla \cdot \left(\left((1-n) \lambda^s + nS^g \lambda^g + nS^l \lambda^l \right) \nabla T \right) \\
&- \quad \nabla \cdot (nS^g \rho^g D_a^g h^g \nabla X_a^g) \\
&- \quad \nabla \cdot (nS^g \rho^g D_w^g h^g \nabla X_w^g) \\
&= \quad \rho Q_T
\end{aligned} \tag{4}
$$

c $[\frac{J}{kg \cdot K}]$ is heat capacity, λ $[\frac{J}{K \cdot m \cdot s}]$ is thermal conductivity, and h $[\frac{J}{kg}]$ is enthalpy.

2 RF/RM Numerical Methods

RF/RM is a finite element code. To get from the governing equation to the weak formulation of the algebraic equation, the method of weighted residuals is used. The order of spatial derivatives is reduced by the Gauss-Ostrogradsky method. The time derivatives are approximated by the first-order finite difference method. This leads to the algebraic equation (5) for the air and water components and equation (6) for the energy equation.

Fluid component equations ($k = a, w$), where $\theta \in [0, 1]$

$$
\begin{aligned}
& \left[\frac{1}{\Delta t}(\mathbf{C}_{P_k^g} + \mathbf{C}_{P_k^l}) + \theta(\mathbf{K}_{P_k^g} + \mathbf{K}_{P_k^l})\right][\hat{\mathbf{p}}^g]^{n+1} \\
+ & \left[\frac{1}{\Delta t}(\mathbf{C}_{S_k^l} - \mathbf{C}_{S_k^g})\right][\hat{\mathbf{S}}^l]^{n+1} \\
= & \left[\frac{1}{\Delta t}(\mathbf{C}_{P_k^g} + \mathbf{C}_{P_k^l}) - (1-\theta)(\mathbf{K}_{P_k^g} + \mathbf{K}_{P_k^l})\right][\hat{\mathbf{p}}^g]^{n} \\
+ & \left[\frac{1}{\Delta t}(\mathbf{C}_{S_k^l} - \mathbf{C}_{S_k^g})\right][\hat{\mathbf{S}}^l]^{n} \\
+ & \left[\frac{1}{\Delta t}\mathbf{C}_{P_k^l}\right]([\hat{\mathbf{p}}_\mathrm{c}]^{n+1} - [\hat{\mathbf{p}}_\mathrm{c}]^{n}) \\
+ & [\mathbf{K}_k^{ls}]\,(\theta[\hat{\mathbf{p}}_\mathrm{c}]^{n+1} + (1-\theta)[\hat{\mathbf{p}}_\mathrm{c}]^{n}) \\
- & [\mathbf{K}_k^{g}]\,(\theta[\hat{\mathbf{X}}_k^{g}]^{n+1} + (1-\theta)[\hat{\mathbf{X}}_k^{g}]^{n}) \\
+ & (\mathbf{K}_k^{gs} + \mathbf{K}_k^{ls})\mathbf{g}
\end{aligned}
\tag{5}
$$

Heat energy equation

$$
\begin{aligned}
& \left[\frac{1}{\Delta t}\mathbf{C}_T + \theta\mathbf{A}_T + \theta\mathbf{K}_T\right][\hat{\mathbf{T}}]^{n+1} \\
= & \ \theta[Q_T]_\tau^{n+1} + (1-\theta)[Q_T]^n \\
+ & \left[\frac{1}{\Delta t}\mathbf{C}_T - (1-\theta)\mathbf{A}_T - (1-\theta)\mathbf{K}_T\right][\hat{\mathbf{T}}]^{n}
\end{aligned}
\tag{6}
$$

The equations above can be written more compactly as

$$
\begin{aligned}
\left[\frac{1}{\Delta t}\mathbf{C}_{Pa} + \mathbf{K}_{Pa}\right][\hat{\mathbf{p}}^g]^{n+1} + \left[\frac{1}{\Delta t}\mathbf{C}_{Sa}\right][\hat{\mathbf{S}}^l]^{n+1} &= \mathrm{RHS}_a \\
\left[\frac{1}{\Delta t}\mathbf{C}_{Pw} + \mathbf{K}_{Pw}\right][\hat{\mathbf{p}}^g]^{n+1} + \left[\frac{1}{\Delta t}\mathbf{C}_{Sw}\right][\hat{\mathbf{S}}^l]^{n+1} &= \mathrm{RHS}_w \\
\left[\frac{1}{\Delta t}\mathbf{C}_T + \mathbf{K}_T + \mathbf{A}_T\right][\hat{\mathbf{T}}]^{n+1} &= \mathrm{RHS}_T
\end{aligned}
\tag{7}
$$

There are different ways to solve the three equations. So far, two possibilities have been implemented for multiphase, multi-componental problems in RF/RM. The equations can either be solved one after another, iterating between them, or the equations for gas pressure and liquid saturation can be solved simultaneously, then iterating with the temperature equation. Details of the numerical procedure can be found in Kolditz and Jonge [2003].

3 Experimental Data

3.1 Studied Material

Lab experiments were designed to determine material parameters of potential backfill material that is suggested as engineered barrier for a high-level nuclear waste repository at Äspö test site in Sweden. We performed experiments with a specially constructed permeameter to estimate the thermal and unsaturated hydraulic parameters of the backfill under conditions that occur in a deep repository. The analyzed backfill material consists of $30\,\%wgt.$ sodium-bentonite and $70\,\%wgt.$ crushed rock. The sodium-bentonite is used as fine powder, product name SPV Volclay, and contains 75% montmorillonite with 85.5% exchangeable sodium (Müller-Vonmoos and Kahr [1983]). The crushed rock consists of granite with a maximum grain size of $5\,mm$. The used synthetic water has a similar ionic content to the groundwater that prevails at Äspö HRL (Äspö water) (see Table 1).

Table 1: Composition of the synthetic Äspö water

	Parameter						
Äspö Water	Na^+	Mg^{2+}	Ca^{2+}	K^+	S^{2-}	Cl^-	pH
$[mol/L]$	$1.5 \cdot 10^-2$	$2.7 \cdot 10^-3$	$1.8 \cdot 10^-3$	$3.6 \cdot 10^-4$	$5.1 \cdot 10^-4$	$1.9 \cdot 10^-2$	7.4

3.2 Laboratory Equipment

The permeameter we used to study heat and gas flow in the backfill is shown in Figure 1. The permeameter consists of a $30\,cm$-long steel sample column (2) with a diameter of $5\,cm$. Inside the bottom of the sample column a heating element is fixed in a steel chamber. We maintained a constant pressure or a constant pressure gradient along the sample column by use of the water container (1) that can be connected to the bottom and/or to the top of the sample column. The water in the container can be pressurized up to $20\,bar$. A burette (3) is plugged to the top of the sample column. We could connect or disconnect the burette to the sample column. The pressure in the burette can be held at atmospheric pressure or increased up to $10\,bar$.

Inside the sample column of the permeameter, we added backfill to Äspö water, and compacted the mixture with a piston to avoid air entrapment. With this procedure we reached a dry density of $1.6\,g/cm^3$ and a porosity of 48%. At the top and bottom of the sample, we inserted fine sand, geotextile, and a metal filter to assure one-dimensional flow and to prevent the bentonite from being washed out of the sample. The outside of the sample column, we wrapped with insulating wool to minimize heat loss through the boundary.

3.3 Saturated Hydraulic Experiments

We started the experimental procedure with measurements to specify the water saturated hydraulic conductivity. The water flow through the sample due to a pressure gradient of $20\,bar$ was measured in the connected burette. After adjusting a pressure gradient along the sample column, and by measuring the water volume entering the burette, the viscosity, and the density of Äspö water, knowing the cross-sectional area of the sample, we could calculate the hydraulic conductivity up to $90°C$. Results for these calculations are described in Engelhardt et al. [2003].

3.4 Thermal Experiments

Using the water container, the sample was pressurized to $10\,bar$ at the top and bottom so that we maintained a stationary flow field across the sample. During the thermal experiment we disconnected the

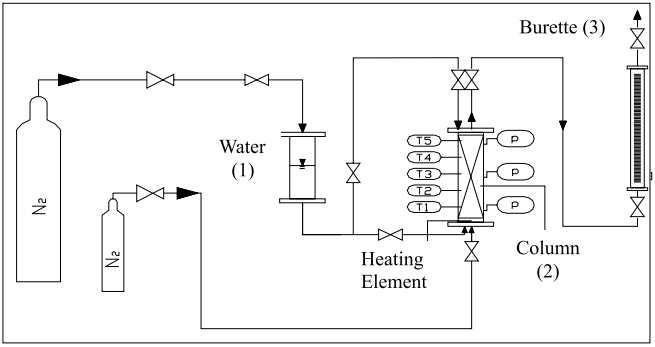

Figure 1: Experimental setup

burette from the column. The heating was submerged in water, and switched on to 90°C. Five temperature sensors recorded the initial temperature increase, and the time-invariant temperature distribution along the axis of the sample during the three week experiment (see Figure 2).

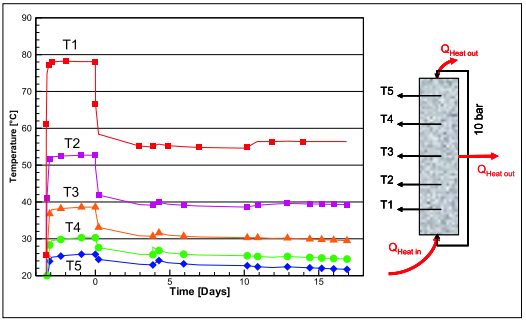

Figure 2: Thermal experiment and measured temperature distribution

3.5 Non-isothermal Drainage Experiment

Four days after starting the thermal experiment we replaced the water surrounding the heating element by air. This replacement from water to air caused the temperature drop as can be seen in Figure 2 at time zero. Then nitrogen was injected from below into the already heated and pressurized sample for 17 $days$. The nitrogen injection pressure was increased stepwise. We started to inject nitrogen with 11.5 bar to remain below the entry pressure of the backfill material. After 4 $days$ we increased the injection pressure to 15 bar, and after 10 $days$ to 20 bar. During the drainage experiment we connected the burette to the sample column, and pressurized it at the beginning to 10 bar. The pressure in the burette increased due to water, and eventually gas entering the burette (see Figure 3). We poured 51 ml Äspö water into the

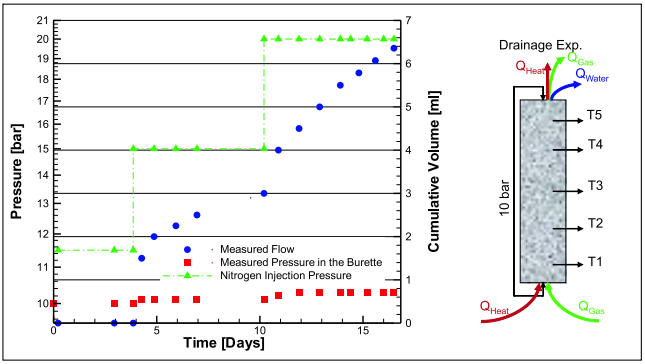

Figure 3: Non-isothermal drainage experiment and measured data

burette, corresponding to 41% of its maximum water capacity. The volume of Äspö water in the burette increased to 57.5 ml after 17 $days$ of drainage. Figure 3 shows the measured drained water volume that entered the burette, the recorded gas pressure increase by the water inflow, and the nitrogen injection pressure at the bottom of the sample.

4 Numerical Analysis

4.1 Parameter Estimation using iTOUGH2

Methodology

We used the measured water discharge rate, gas pressure in the burette, and temperature as calibration data for inverse modeling with the program iTOUGH2 (Finsterle [1999]). By automatically matching the calculated with the measured system behavior we determined the thermal and hydraulic parameters of the backfill material. The inverse modeling procedure used to obtain thermal and unsaturated hydraulic parameters is discussed in detail in Engelhardt et al. [2003].

In the iTOUGH2 simulation a two-dimensional, radial model was developed to capture fluid and heat flow along the axis of the column as well as radial heat losses through the boundary. The column was discretized along the axial direction into 60 $gridblocks$ with a spacing of 0.5 cm. The thermal and gas-injection experiment was simulated in a single model run. The sample column itself was initially fully water saturated with a pressure of 10 bar, and a temperature of 19.4°C. Analyzing the thermal experiment, radial heat loss as well as heat transfer through the top cap of the column was accounted for, by specifying appropriate thermal parameters for the insulation material. We fixed the temperature of the lowest temperature sensor (T1) as a time-dependent temperature boundary condition. The initial and boundary conditions of the simulation with iTOUGH2 are shown in Figure 4.

When simulating the nitrogen injection experiment, the top element was connected to a further element representing the burette. This element had the correct experimental volume and initial gas saturation. This allowed us a correct modeling of the observed increase in pressure due to incoming liquid or nitrogen.

Both, the BROOKS- COREY (Brooks and Corey [1964]) and VAN GENUCHTEN (Van Genuchten [1980]) model, were used to describe the two-phase relative permeability and capillary pressure functions

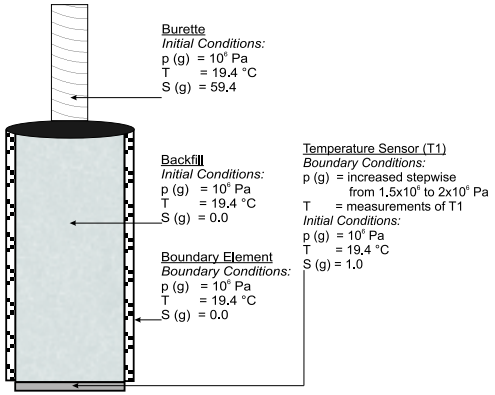

Figure 4: Initial and boundary conditions used for the iTOUGH2 simulation

of the backfill material during the drainage experiment. To avoid overparameterization, the pore size distribution indices λ and n, as well as the residual saturations Swr and Snwr were fixed in the inversion. Only four parameters were estimated by inverse modelling: absolute permeability, gas entry pressure Pd (or capillary strength parameter $1/a$), thermal conductivity, and the specific heat. Since both hydraulic parameters are expected to vary over many orders of magnitude, we estimated their logarithms. The material parameters resulting from the inverse modelling are summarized in Table 2.

Results

Using the program iTOUGH2 the temperatures are well matched throughout the 3-week experiment. The match is independent of the choice between the Brooks- Corey or van Genuchten model. The total heat flow through the column we calculated with the calibrated forward model was about $45.0\,W$, while the heat loss through the boundary was about $2.1\,W$. The calibrated non-isothermal two-phase flow model with the van Genuchten functions provides a reasonably good fit with the measured volume of water collected in the burette during the gas injection experiment, especially of the last $7\,days$. However, during the first part of the gas injection experiment, both the van Genuchten and Brooks-Corey models significantly underestimate the displaced amount of water. The van Genuchten model yields a dispersed gas distribution that reaches the top of the column after $10.8\,days$, with a relatively low maximum gas saturation of 28% near the injection point. The Brooks-Corey model predicts that the nitrogen front penetrates the column to a distance of only $7.5\,cm$, with an almost piston-like displacement resulting in high gas saturations in the injection zone (see Figure 5). The Brooks-Corey model predicts a relatively sharp gas-liquid front within the column, preventing gas breakthrough. However, no gas breakthrough during the three-week experiment was evident from the experimental data. Figure 5 shows a comparison of the predicted gas phase distribution after $16\,days$ for both models calculated with the calibrated model using TOUGH2 (Pruess et al. [1999]).

Table 2: Summary of the inverse modelling results for the backfill

Material Parameter	Model	FixedValue	Best Estimate
Porosity [%]	van Genuchten	48	
	Brooks-Corey	48	
Density $[kgm^{-}3]$	van Genuchten	2700	
	Brooks-Corey	2700	
Pore size Distribution Index			
n [−]	van Genuchten	1.44	
λ [−]	Brooks-Corey	0.4	
Residual Water/Gas Saturation [−]	van Genuchten	0.07/0.01	
	Brooks-Corey	0.07/0.01	
$log(k[m^2])$	van Genuchten		-17.89
	Brooks-Corey		-18.08
$log(1/a[Pa])log(Pd[Pa])$	van Genuchten		5.15
	Brooks-Corey		4.60
$\lambda_T[Wm^{-}1K^{-}1]$	van Genuchten		2.28
	Brooks-Corey		2.35
$c\,[Jkg^{-}1K^{-}1]$	van Genuchten		900
	Brooks-Corey		900

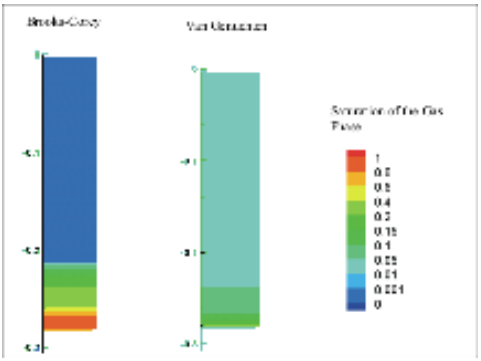

Figure 5: Gas phase distribution calculated with iTOUGH2

4.2 RF/RM Simulation

4.2.1 Thermal Experiment

Methodology
The temperatures recorded in the laboratory experiment described in Section 3 were modelled with RF/RM. The mesh used was a 1-dimensional vertical cut of the laboratory setup. The heating element and the top plate were modelled as separate material groups from the backfill material. The parameters for the model input are summarized in Table 3. The simulation time was 3.3 $days$. This is the time up to the start of the gas injection, equivalent to time 0 in Figure 2. The initial conditions and boundary conditions for the simulation are summarized in Table 4.

Table 3: RF/RM input parameters

Parameter Top plate	Unit	Value	Parameter Backfill	Unit	Value
Cross-sectional area	m^2	0.001964	Cross-sectional area	m^2	0.001964
Porosity	-	0.01	Porosity	-	0.48
Tortuosity	-	1	Tortuosity	-	1
Permeability	m^2	0	Permeability	m^2	$8.6 \cdot 10^{-19}$
Density	$\frac{kg}{m^3}$	7800	Density	$\frac{kg}{m^3}$	2720
Heat capacity	$\frac{J}{kg \cdot K}$	460	Heat capacity	$\frac{J}{kg \cdot K}$	900
Heat conductivity	$\frac{J}{K \cdot m \cdot s}$	14	Heat conductivity	$\frac{J}{K \cdot m \cdot s}$	2.35

Parameter Heating element	Unit	Value
Cross-sectional area	m^2	0.001964
Porosity	-	0.95
Tortuosity	-	1
Permeability	m^2	$1.0 \cdot 10^{-10}$
Density	$\frac{kg}{m^3}$	7800
Heat capacity	$\frac{J}{kg \cdot K}$	460
Heat conductivity	$\frac{J}{K \cdot m \cdot s}$	14

For the thermal experiment, no capillary pressure - saturation or relative permeability - saturation curves were prescribed, as the backfill remains saturated due to the experimental setup. The model only calculated the temperature distribution.

Table 4: Initial and Boundary Conditions for the Thermal Experiment

Condition	Unit	Value
Initial conditions		
Gas Pressure, whole domain	Pa	1013250
Gas Saturation, whole domain, except at top plate	%	0.0
Gas Saturation, top plate	%	0.99
Temperature, whole domain	K	292.65
Boundary conditions		
Pressure at heating element	Pa	1013250
Gas saturation at heating element	%	0.0
Temperature at heating element	K	Figure 1, curve T5

As the model is based on a laboratory test, the backfill steel column has to be taken into consideration. Hence there is a heat flux through the steel column. This is modelled by introducing sinks at nodes (taken to correspond to temperature measurement locations for convenience), as shown in Figure 6. The sinks are highly time dependent. Initially, more heat is lost through the sample enclosing material, than when the temperature is stationary.

Results
Figure 7 shows the simulation results. One can see that there is a good fit with the experimental measurements.

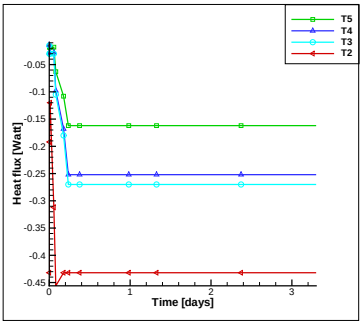

Figure 6: Heat sinks at temperature measurement points

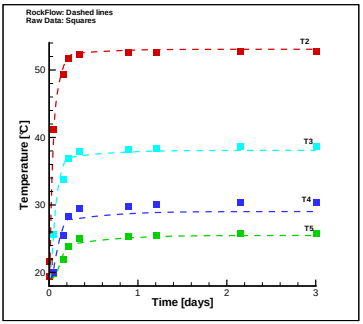

Figure 7: RF/RM simulation results for the thermal experiments

4.2.2 Drainage Experiment

Methodology
The drainage experiment described in Section 3 was also modelled in RF/RM. The aim in modelling the experiment with RF/RM was to simulate the saturation evolution in the sample. For this, a 1-D model was established. The initial and boundary conditions are as illustrated in Figure 8. The injection gas

pressure, the measured pressure in the burette and the flow into the burette were used as time-dependent boundary conditions.

Two constitutive equations describe the material behaviour of partially saturated porous media. The capillary pressure - saturation relationship and the relative permeability - saturation relationship. The choice of model for the capillary pressure - saturation relationship has a particular importance for the measured water flow in the burette. The measured data was represented well in the simulation with iTOUGH2 (Engelhardt et al. [2003]), hence the capillary pressure - saturation curve determined in the iTOUGH simulation using the van Genuchten model was used in the RF/RM simulation.

The measurement of the gas pressure in the burette is closely related to the propagation of the gas phase distribution in the sample. The relative permeability - saturation relationship has a determining effect on those data. Nor the van Genuchten, or the Brooks Corey model take the influence of swelling processes on relative permeability into account. To be able to simulate the propagation of the gas phase distribution in a porous medium capable of swelling, the function after Olivella and Gens [2000] was implemented into RF/RM and used. According to this model, separate permeabilities have to be used for the gas and liquid phases when modelling bentonite. This is because of the swelling effects that occur in bentonite as water imbibes the bentonite. Therefore, in the unsaturated state, permeability is much higher than in the saturated state. Olivella and Gens have determined that the difference between the two permeabilities is of the order of 10^5. The curve for liquid phase and gas phase permeability used in this simulation is shown in Figure 9. The curve is not smooth, as the relative permeability - saturation values determined experimentally by Olivella and Gens have been multiplied with the measured intrinsic permeability for the bentonite sample considered in this experiment. Using such a model makes a great difference to the vapour flow, which gets enhanced.

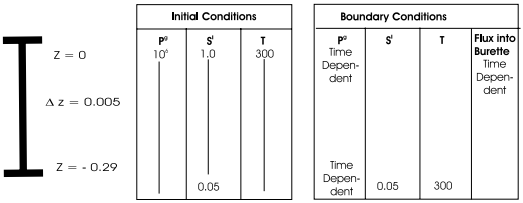

Figure 8: RF/RM simulation setup for the drainage experiment

Results

During the experiment, the nitrogen injection pressure is increased in steps. Numerically these steps present a challenge, as the time stepping scheme has to change. Figure 10 shows the modelling results for the saturation evolution as a profile. Figure 11 shows the time evolution of saturation $3\,cm$ above the nitrogen injection point . Both figures show that the gas travels trough the sample, displacing the liquid, but no gas breakthrough is estimated, as was observed in the experiment.

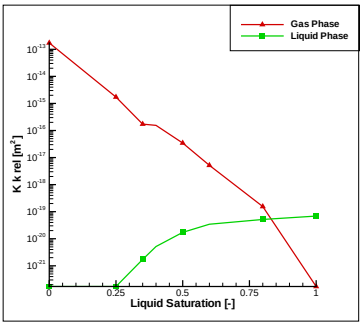

Figure 9: Total Permeability versus Liquid Saturation

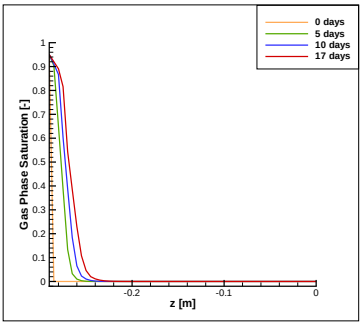

Figure 10: RF/RM simulation results for the drainage experiment - profile

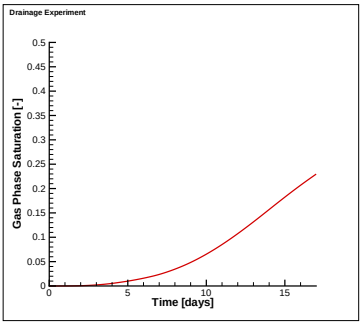

Figure 11: RF/RM simulation results for the drainage experiment - time evolution at 3 cm above the injection point

5 Discussion of Results

Thermal Experiment

Figure 12 shows that both models fitted the temperature evolution well. While separate thermal properties were specified for the insulation material in iTOUGH2 to account for heat loss, sink terms were used in RF/RM.

The influence of different numerical models and methodology (i.e. boundary element versus heat sink terms) can nearly only be seen during the temperature increase. The decisive parameter for the inverse simulation is the thermal conductivity of the sample and of the chosen boundary element. Because of the assumption of a constant thermal conductivity for the boundary element in the iTOUGH2 simulation, the temperature increase at the start is underestimated. From Figure 12 one can extrapolate that for the temperature increase phase the heat loss occurs faster than modelled with iTOUGH2. For the simulation of the heating of the sample a time-dependent thermal conductivity as a function of heat loss would therefore be a better choice for the boundary element. The change of thermal properties of the boundary in dependence of temperature increase was well represented in RF/RM due to the choice in heat sinks.

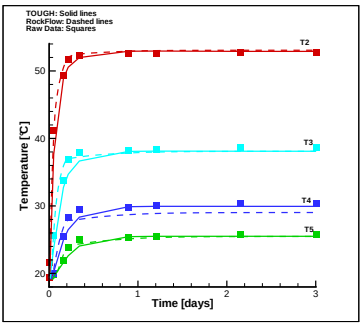

Figure 12: Comparison of results for the thermal experiments

Drainage Experiment

Figure 13 shows the comparison between the simulations made with iTOUGH2 and RF/RM. For simulations made with iTOUGH2, the capillary pressure - saturation relationship and relative permeability - saturation relationship were given according to either the van Genuchten model or the Brooks Corey model. The flow out of the sample into the burette was the calculated parameter. In simulations with RF/RM, only the capillary pressure - saturation relationship was given according to the van Genuchten method. For the relative permeability - saturation relationship a model described in Olivella and Gens [2000] was used. The flow out of the sample into the burette was set as a time dependent boundary condition for the model. Gas phase saturation was the calculated parameter.

One can see in Figure 13 that the calculations of the gas phase distribution made with RF/RM lie in between the calculations performed with iTOUGH2. The relative permeability - saturation relationship used in RF/RM enhances vapour flow. However, as the flow into the burette was used as a boundary condition, the model was prevented from predicting a gas phase breaktrough. The Brooks Corey model

did not predict such a breakthrough either. The van Genuchten model used in iTOUGH2 predicted the breaktrough, which, however was not observed in the experiment.

The gradient of the curve that describes the gas penetration using the the Olivella and Gens [2000] relative permeability - saturation model corresponds somewhat to the gradient of Brooks Corey model curve. The gas penetration using the method by Olivella and Gens [2000] also has a clearly defined plume, but not with the fast increase in gas saturation to 40% predicted by the Books Corey model, but only to 25%.

Using the Olivella and Gens [2000] relative permeability - saturation model results in a gas penetration that lies between the diffusive gas distribution achieved by the van Genuchten model and the piston like displacement resulting from the Brooks Corey model.

Because the water flow into the burette and the pressure in the burette were fixed as time-dependent boundary conditions in the RF/RM simulation, the RF/RM calculated saturation may best represents the measured system behavior.

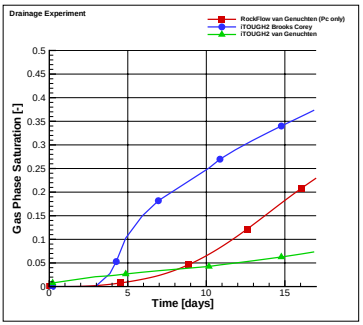

Figure 13: Comparison of results for the drainage experiments

6 Conclusions

To study thermal-hydraulic processes that occur in permanent repositories for the disposal of nuclear waste it is necessary to have numerical codes that are able to calculate the system behavior. The simulated results should be independent of the numerical method used. Therefore, two laboratory experiments were modelled with two different numerical simulation codes, namely iTOUGH2 and RF/RM. While iTOUGH2 is an inverse model, using the finite difference method, RF/RM is a forward model using the finite element method. The approaches to modelling the experiments were thus different. In iTOUGH2, the two experiments were modelled as one, continuous experiment. We could demonstrate that the two codes provided comparable results for the numerical simulation of the laboratory experiment.

For the long term study of disposal sites the simulation of temperature increases is crucial, as a higher temperature influences capillary pressure and the hydraulic properties. For this part of the long term study the choice of heat sinks would be more appropriate than the choice of a boundary element. Both models however concur on the stationary temperature results. The calculation of the extension of the gas phase is important for the simulation of the drainage of a geotechnical barrier in the case of a damage of the radioactive waste container. To model the behavior of clay minerals with swelling properties in the buffer and backfill correctly with respect to gas phase propagation, the assumption of the relative

permeability - saturation after Olivella and Gens (Olivella and Gens [2000]) seems the most appropriate. The choice of the relative permeability-saturation function is more sensitive for predicting the gas phase distribution than the numerical method employed . Measurements within the sample column would have been useful to decide which model estimates the system behavior of swelling clay best.

References

R. N. Brooks and A. T. Corey. Hydraulic properties of porous media. *Hydrology Papers, Colorado State University, Fort Collins*, 3, 1964.

M. Chijimatsu, T. Fujita, A. Kobayashi, and M. Nakano. Experiment and validation of numerical simulation of coupled thermal, hydraulic and mechanical behaviour in the engineered buffer materials. *Int. J. Numer. Anal. Meth. Geomech.*, 24:403–424, 2000.

I. Engelhardt, S. Finsterle, and C. Hofstee. Experimental and numerical investigation of flow phenomena in non-isothermal, variably saturated bentonite/crushed rock mixtures. *Vadose Zone Journal*, 2, 2003. available at http://www.vadosezonejournal.org.

S. Finsterle. iTOUGH2 user's guide. Report LBNL-40040, Lawrence Berkeley National Laboratory, CA, 1999.

O. Kolditz. *Computational Methods in Environmental Fluid Mechanics*. Springer, 2002.

O. Kolditz, S. Bauer, M. Beinhorn, J. de Jonge, T. Kalbacher, C. McDermott, W. Wang, M. Xie, R. Kaiser, and M. Kohlmeier. ROCKFLOW - Theory and users manual, release 3.9. Groundwater modeling group, Center for Applied Geosciences, University of Tuebingen, Institute of Fluid Mechanics, University of Hannover, 2003.

O. Kolditz and J. De Jonge. Non-isothermal two-phase flow in porous media. *Prepared for Computational Mechanics*, 2003.

K. Müller-Vonmoos and G. Kahr. Mineralogische Untersuchungen von Wyoming Bentonit MX80 und Montigel. NTB 83-12, NAGRA, Wettingen, Switzerland, 1983. In German with English Abstract.

Y. Ohnisi, H. Shibata, and A. Kobayasi. Development of finite element code for the analysis of coupled thermo-hydro-mechanical behaviours of saturated - unsaturated medium. Proceedings of the International Symposium on Coupled Processes Affecting the Performance of a Nuclear Waste Repository, 1985. 263-268.

S. Olivella and A. Gens. Vapour transport in low permeability unsaturated soil with capillary effects. *Transport in Porous Media*, 40:219–241, 2000.

S. Olivella, A. Gens, J. Carrera, and E. E. Alonso. Numerical formulation for a simulator (CODE_BRIGHT) for the coupled analysis of saline media. *Engng Comput.*, 13(7):87–112, 1996.

K. Pruess. Tough user's guide. Report LBNL-20700, Lawrence Berkeley National Laboratory, Berkeley, CA, 1987.

K. Pruess, C. Oldenburg, and G. Modidis. Tough2 user's guide, version 2.0. Report LBNL-43134, Lawrence Berkeley National Laboratory, Berkeley, CA, 1999.

C. Thorenz. *Model adaptive simulation of multiphase and density driven flow in fractured and porous media*. PhD thesis, Universität Hannover, 2001.

M. T. Van Genuchten. A closed-form equation for predicting the hydraulic conductivity of unsaturated soils. *Soil Sci. Soc. Am. J.*, 44:892–898, 1980.

Numerical modelling of swelling pressure in unsaturated expansive elasto-plastic porous media.

Manuscript submitted to:

Transport in Porous Media, July 2004

Numerical Modelling of Swelling Pressure in Unsaturated Expansive Elasto-Plastic Porous Media

Mingliang Xie, Wenqing Wang, Joëlle de Jonge and Olaf Kolditz

Center for Applied Geoscience, GeoSystemsResearch
University of Tübingen, Germany

Abstract

The focus of this work is to provide a new concept for accessing the swelling stress in expansive porous media, especially in highly compacted bentonite. The key to the new approach is the simulation with a chemical swelling model of an infinitesimal volume change followed by a back compaction processes. Free swelling is allowed in the first step, to calculate the interlayer porosity change (micro) and the induced volume change (macro).

The object-oriented FEM simulator GeoSys/RockFlow allows the combination of different processes. The hydro-mechanic/chemical (H^2M/C) model takes into consideration two phase flow and deformation, as well as chemical swelling effects. The negative displacements on each boundary after the free swelling simulation are taken as Dirichlet boundary conditions of the back compaction problem. The deformation step is simulated in the context of elasto-plasticity using the modified Cam-Clay model. The stresses obtained by back compaction represent the swelling pressure.

A 2D example of compacted bentonite is analyzed with the new H^2M/C model. The results are in good agreement with existing experimental observations.

Key words: expansive porous media, two phase flow, free swelling, swelling pressure, modified Cam-Clay model, numerical modelling

1 Introduction

Clays rich in bentonite swell and shrink with wetting and drying processes. The magnitude of swelling and shrinking properties of bentonite can be greatly influenced by many factors, which can be divided into two groups - factors that depend on the nature of the soil particles (type and amount of clay minerals) and factors determined by the placement as well as environmental conditions (dry density, initial

water content, compaction method, soil structure, thermal conditions, electrolyte concentration in the pore water) (Norrish (1955), Mielenz and King (1955), Seed et al. (1962), Holtz and Bara (1965), Parcher and Liu (1965), Low (1979), Evans et al. (1985), Low (1987), Kaya et al. (2000), Huyghe and Janssen (1999)). The swelling effect results from additional embedding of water/solution molecules into the soil matrix, especially into the interlayers of expansive minerals. In the case of free swelling, volume changes up to 1400 to 2000 percent for purified dry Na-montmorillonite samples in powder immersed in pure water and changes up to 45 to 145 percent for Ca-montmorillonite are reported (Mielenz and King (1955)). In the case of constrained swelling, however, swelling can result in macro- and mesopore volume reduction and simultaneously in swelling pressure, which can be measured in oedometers or triaxial cells. Effective porosity and consequently, intrinsic permeability decrease (Volkaert et al. (1994), Olivella and Gens (2000)).

Various theoretical approaches have been proposed to relate clay compressibility to basic particle-water-cation interactions. The original Gouy-Chapmann diffuse double layer (DDL) theory (Gouy (1910), Chapman (1913)) is the most widely used one (Bolt (1955); Sridharan and Jayadeva (1982); Mitchell (1993); Quirk (1997); Marcial et al. (2002)). On the basis of this, many other theories were suggested to overcome some of the factors that have not been considered in the original DDL theory (Verwey and Overbeek (1948); Pusch et al. (1990); Low and Margheim (1979); Low (1980); Sridharan and Choudhury (2002); Komine and Ogata (1994); Tripathy and Schanz (2003)). However, these theories can not simulate the saturation process induced swelling pressure.

Classical modelling of the swelling behavior of bentonite was developed in order to obtain the stress-strain behavior of expansive clays on the basis of laboratory oedometer tests and the concept of Terzaghi's effective stresses (Mitchell (1993), Sridharan (1990)). Many numerical models for simulating the complex processes in bentonites as buffer materials have been developed and proved to be important in waste repository design (Börgesson et al. (1995), Murad and Cushman (1997), Olivella and Gens (2000), Bennethum and Cushman (2002a), Bennethum and Cushman (2002b)). A very essential aspect in those hydraulic, thermal, and mechanical operations is the understanding of induced coupled processes. The first model to evaluate those coupled processes was built up by Noorishad et al. (1982). A model developed by Korsawe et al. (2003) is based on the concept of rational mechanics and is using the Raviart-Thomas mixed finite element method, as well as an implicit Euler time discretisation. The model is only developed for the special case of a rigid soil skeleton without taking the chemical influence on swelling into consideration.

In geomechanical models, the stress state and the resulting deformation process is of special interest. As a consequence, the solid phase has to be treated explicitly. The interaction of fluid (phase) flow and solid (phase) deformation in the framework of the porous medium approach can be modelled based on the consolidation theory (Terzaghi (1925), Biot (1941)). Börgesson (1985) and Studer et al. (1984) investigated swelling and shrinking phenomena in bentonites and developed a material model for porosity and permeability changes with moisture transport. Studies of hydro (two phase flow)-mechano-chemical (H^2M/C) processes in partially sat-

urated, thermo-elastic porous media without phase change effects were presented by Geraminegad and Saxena (1986). The model was verified against full scale coupled experimental data. More recently, the Barcelona Expansive Model (BExM) is developed based on the consideration of two levels of structure (Alonso et al. (1999)). It well represents the phenomena of stress-suction path dependency and swelling-shrinkage fatigue. Most of the cited models have found wide application in simulating geotechnical systems (Kolditz (2002)). In most cases, the systems analyzed were restricted to relatively high permeabilities without taking account the influence of porewater chemistry on swelling.

This paper presents a numerical simulation of the swelling pressure by a new back-compaction method using the object-oriented FEM simulator GeoSys/RockFlow H^2M/C - a new chemo-hydro-mechanical model - which has been developed for the purpose of modelling isothermal multiphase flow in bentonite. This model is based on the diffuse double layer theory and connects both, the unique microstructural parameters of bentonite and chemical properties of porewater, with macrostructural swelling effects. In the case of free swelling, the volume change can be calculated according to the interlayer porosity change. This value represents the swelling potential of bentonite, and is assumed to be the strain needed for back compaction. The necessary pressure to achieve the strain thus represents the swelling pressure.

2 Conceptual model

Bentonite is a mixture of clayey minerals, in which smectite plays a central role for swelling. Typical smectite like montmorillonite is composed of two structural units, the silica tetrahedron and the alumina octahedron. These units are interconnected and extend to form thin sheets (each is only about 10 Å in thickness). Several such sheets are stacked one above the other, to form a crystal particle. Owing to the weak connection between the sheets, water easily enters between them with the help of electron repulsion, which results from the net charge of the bentonite particle. Consequently, the particles may be separated into smaller pieces. Katti and Shanmugasundaram (2001) observed the breakdown of the clay agglomerates into small sized particles by increasing saturation through digital analysis of the images obtained by using energy-dispersive X-ray analysis. Herbert and Moog (2002) proved variation of the interlayer distances by changes of pore water chemical compositions.

Swelling/shrinking always results from moisture change within the isothermal multiphase flow in bentonite, which involves several complex interacting phenomena. The main processes involved in swelling/shrinking in bentonite as buffer material are the hydraulic processes (water transport), chemical process (particle-water-cation interaction), mechanical processes (swelling pressure and volume change), and thermal processes (evaporation/condensation). These processes are fully coupled and related to porosity and permeability change (Figure 1). This paper presents numerical modelling of swelling pressure by taking the hydro-mechanical/chemical (H^2M/C) coupled processes in bentonite into consideration.

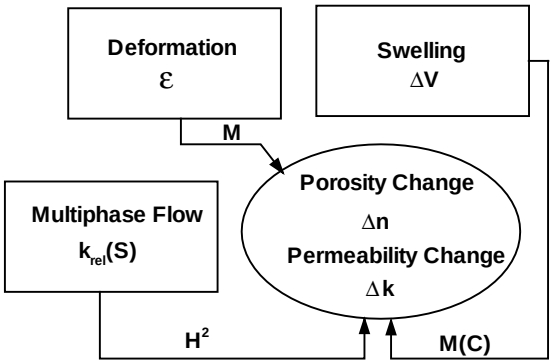

Figure 1: Coupled processes in unsaturated expansive porous media

2.1 Porosity

On the surface of the mineral sheets, nett negative charge exists, which results in the formation of diffuse double layer (DDL) on the surface of sheets (Gouy (1910), Chapman (1913)). The thickness of DDLs depends on the surface charge and effluent, and can be calculated according to the Gouy-Chapman DDL theory developed by Gouy (1910) and Chapman (1913) for single layer, and according to the DLVO theory (named after Derjaguin and Landau (1941) and Verwey and Overbeek (1948)) developed later by Derjaguin and Landau (1941) and Verwey and Overbeek (1948) for adjacent DDLs. Both theories (traditional DDL and DLVO) use the same parameter describing the "thickness" of DDL defined by equation 3 in section 2.1.1. The physical properties of the water within the DDLs, especially water directly in contact with the mineral surfaces, differ from free water owing to electrostatic interaction. Therefore, the mobility of the water molecules in interlayers is largely reduced. Hence, the water entered into interlayer gaps of highly compacted bentonite is practically immovable. Therefore, it is worthwhile to separate the total porosity n of bentonite into interlayer n_{IL} (porosity within the particles) and interparticle porosity n_{IP} (porosity between particles).

$$n = n_{\mathrm{IP}} + n_{\mathrm{IL}} \tag{1}$$

With this definition, n_{IP} reveals the coarse pore and can be assumed as the initial porosity of a dry sample. In the case of constrained swelling, the total porosity remains constant. The interlayer porosity increases with the saturation process. Therefore, interparticle porosity decreases accordingly.

2.1.1 Interlayer porosity (microscopic)

According to the H^2M/C swelling model, volume change resulting from free swelling/shrinking can be obtained by calculating the interlayer porosity change (Xie et al. (2004)).

Around the particles and within the interlayer space, diffuse double layers tend to build up, completely only in the case of free swelling (Figure 2). The maximal interlayer porosity for one particle with m effective layers can be calculated as follows:

$$n_{\mathrm{IL}i} = \frac{2m \cdot A \cdot \delta}{V_0} \tag{2}$$

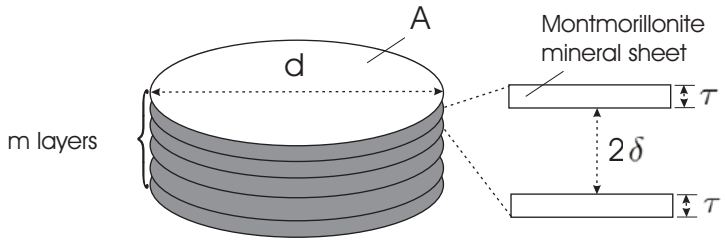

Figure 2: Concept of interlayer porosity within one particle

where A is the particle surface area, V_0 is the specific volume. δ is the effective "thickness" of the DDL:

$$\delta = \left(\frac{\varepsilon\varepsilon_0 RT}{2F^2 I \times 10^3}\right)^{1/2} \tag{3}$$

where R is the universal gas constant [$= 8.3145(J{\cdot}mol^{-1}K^{-1})$], k is the Boltzmann constant ($= 1.38066 \times 10^{-23}$), T is the absolute temperature [K], F is the Faraday constant [$= 96485.309(C \cdot mol^{-1})$], ε is dielectric constant and ε_0 the permittivity of free space [$= 8.854 \times 10^{-12}(CV^{-1}m^{-1})$]. The Debye parameter $1/\kappa$ is inversely proportional to the ionic strength I (see e.g. References Stumm and Morgan (1996), Dzombak and Morel (1990)), where c_i is the ith ion concentration of pore water [M], z_i represents the ion valence of the ith ion.

Assuming that the particle can be represented by a circle with diameter d, then

$$A = \frac{\pi d^2}{4} \tag{4}$$

The number of effective layers m within one particle of expansive minerals in bentonite is a mineral structural parameter, which is defined as the number of layers contributing to the swelling effect. As the montmorillonite particles are very fine in size, the average m value is used and calculated by the ratio of total specific

surface area S_{total} in $m^2\ g^{-1}$ (including the surface between layers, which can separate by swelling) to external specific surface area S_0 in $m^2\ g^{-1}$ (only the surface of particles).

$$m = \frac{S_{total}}{S_0} \tag{5}$$

The value S_{total} is normally determined by the methylene blue and the Keeling hygroscopy methods. The value S_0 is normally measured through BET (Brunnett-Eellete-Deller N2 Adsorption) method (ASTM (2001a), ASTM (2001b), FEBEX Working groups (2000)).

As the bentonite particles are very small, for simplicity, the particle sizes are assumed to be the same. Thus, number of the particles N can be derived from the external specific surface S_0:

$$N = \frac{S_0}{2A + \pi dm\tau} \tag{6}$$

where τ is the mean thickness of the effective sheets (Figure 2).

Hence, the total interlayer porosity n_{IL} of the specimen is defined as:

$$n_{\mathrm{IL}} = \sum_i n_{\mathrm{IL}i} = N n_{\mathrm{IL}i} = \frac{S_0}{2A + \pi dm\tau} \frac{\pi m d^2}{2V_0} \delta \tag{7}$$

After some simplifications, the maximal total interlayer porosity can be computed (Xie et al. (2004)):

$$n_{\mathrm{IL}max} = m S_0 \rho_d \Big(\frac{\varepsilon \varepsilon_0 RT}{2F^2 I \times 10^3} \Big)^{\frac{1}{2}} \tag{8}$$

Taking account of the fact that swelling pressure increases with the saturation process and that the magnitude of swelling potential depends on the expansive fraction, the total interlayer porosity n_{IL} of the specimen can be calculated:

$$n_{\mathrm{IL}} = (S^l)^\eta \cdot \beta \cdot n_{\mathrm{IL}max} \tag{9}$$

in which S^l is degree of liquid saturation, β represents volume fraction of the expansive minerals, η is a dimensionless coefficient.

2.1.2 Effective porosity

Effective porosity is the amount of interconnected pore space in a soil or rock through which fluids can pass, expressed as a percent of bulk volume (US Bureau of Mines (1997)). Owing to electrostatic attraction, interlayer-water in compacted

bentonite is practically immovable. Therefore, the effective porosity n_{eff} of compacted bentonite varies with the saturation and swelling processes. In the case of constrained swelling, the effective porosity decreases with the saturation process. Theoretically, it can be reduced to zero, which means the permeability reaches zero. However, this is not the case in the practice. A fraction of the porosity remains, which is defined here as the minimal porosity. It depends on the swelling pressure and the compressibility of the sample. Therefore, the effective porosity of bentonite in the case of constrained swelling can be derived from the initial porosity n_0, interlayer porosity n_{IL} and minimal porosity n_{min} :

$$n_{\mathrm{eff}} = \begin{cases} n_0 - n_{\mathrm{IL}} & , \quad n_{\mathrm{eff}} \leq n_{\mathrm{min}} \\ n_{\mathrm{min}} & , \quad n_{\mathrm{eff}} > n_{\mathrm{min}} \end{cases} \tag{10}$$

In the case of free swelling, the volume change should be taken into consideration, which means the total porosity n_{tot} changes with swelling/shrinking. The effective porosity is:

$$n_{\mathrm{eff}} = n_{\mathrm{tot}} - n_{\mathrm{IL}} \tag{11}$$

However, if the water content is less than shrinkage limit, free swelling/shrinking is limited. Macroscopically, volume change nearly vanishes. Microscopically, interlayer porosity variation changes the interparticle porosity. In this case, equation (10) can be used for calculating n_{eff}.

2.2 Two phase flow

The saturation process in bentonite significantly contributes to swelling/shrinking of bentonite by changing interlayer structure within the tiny expansive mineral particles through particle-water-cation interactions. This happens also with variations of chemical composition in pore water. As a consequence, the effective porosity and intrinsic permeability of a bentonite specimen change upon saturation/desaturation. Due to the low permeability of bentonite, the compressibility of gas flow has to be taken into account. In the model, functions dealing with concurrent flow of highly compressible (gas phase) and lowly compressible fluids (liquid phase) are considered. The mobility of the fluid phases is characterized by their relative permeabilities and capillary pressure via the degree of saturation, as shown in the van Genuchten's equations (van Genuchten (1980)). For completely dry state, the capillary pressure is limited to $10^9\,Pa$ (Kolditz and de Jonge (2004)).

Capillary Pressure The parameters $p_c(S)$ (capillary pressure) and $k_{\mathrm{rel}}(S)$ (relative permeability) are key factors affecting multiphase flow. Capillary pressure is defined as the difference between partial pressures of non-wetting and wetting phases and

is a function of degree of saturation (Helmig (1997)). The $p_c(S)$ value can be measured for a given soil with respect to various fluids. The measured capillary pressure - water saturation curve is used for the numerical analysis (see Section 5).

Relative permeability - Saturation For porous media containing more than one fluid, relative permeability is a key parameter. It is used to calculate the effective permeability $(k^{\gamma}_{\mathsf{rel}}(S^{\gamma})\mathbf{k})$, which is described in the extended Darcy's law. Different relationships between $k^{\gamma}_{\mathsf{rel}}$ and S^{γ} can be found in literatures, i.g., constant value, linear function, potential function. The van Genuchten model in conjunction with the approach of Mualem is adopted in this study (van Genuchten (1980), Helmig (1997), Lenhard and Parker (1987)):

$$k^{l}_{\mathsf{rel}} = S^{l\frac{1}{2}}_{\mathsf{eff}} \left[1 - (1 - S^{l1/\alpha}_{\mathsf{eff}})^{\alpha}\right]^{2} \tag{12}$$

$$S^{l}_{\mathsf{eff}} = \frac{\theta - \theta_r}{\theta_s - \theta_r} \tag{13}$$

where α is the van Genuchten parameter, s and r indicate saturated and residual values of the water content (θ) respectively.

$$k^{g}_{\mathsf{rel}} = (1 - S^{l}_{\mathsf{eff}})^{\frac{1}{2}} \left[1 - (S^{l1/\alpha}_{\mathsf{eff}})\right]^{2\alpha} \tag{14}$$

where α is the van Genuchten parameter.

Relative Permeability - Swelling Effective porosity of expansive porous media, especially compacted ones, changes with the saturation processes. Consequently, its permeability varies.

A large number of studies were aimed at generating methods to independently predict permeability in sedimentary rocks by bulk porosity (Carman (1937), Berg (1970), Bloch (1991) and Neuzil (1994)). It was found that measured permeabilities of clays and shales varied over the range of $10^{-22}\,m^2$ to $10^{-14}\,m^2$. Oelkers (1996) suggested correlation of intrinsic permeability with effective porosity, which is adopted for highly compacted bentonite. Based on this, the swelling relative permeability $k^{l}_{\mathsf{rel}\,sw}$ for highly compacted bentonite is defined as:

$$k^{l}_{\mathsf{rel}\,sw}\mathbf{k} = 9.87 \times 10^{-12} e^{-10+8n_{\mathrm{eff}}} \tag{15}$$

in which $\mathbf{k}$ in m^2 represents the intrinsic permeability before swelling, and n_{eff} is the effective porosity as in equation (10).

2.3 Elasto-plastic deformation

In the present study we cast the swelling induced inelastic deformation in the framework of elasto-plasticity and employ the modified Cam-Clay model, which has advantages of simplicity and capability to represent the stress strain behaviour of soil realities. The strain rate $\dot{\epsilon}$ is decomposed into two parts taking account of swelling as

$$\dot{\boldsymbol{\epsilon}} = \dot{\boldsymbol{\epsilon}}^e + \dot{\boldsymbol{\epsilon}}^p \tag{16}$$

where $\boldsymbol{\epsilon}^e$ represents the elastic part and $\boldsymbol{\epsilon}^p$ represents the plastic part.

The modified Cam-Clay model is given by

$$\mathcal{F} = \frac{q^2}{M} + p\,(p - p_{crit}) = 0, \tag{17}$$

where $p = -\frac{1}{3}\mathrm{tr}(\boldsymbol{\sigma})$ is volumetric stress, $q = \sqrt{3/2}\|\boldsymbol{\sigma} - \frac{1}{3}\mathrm{tr}(\boldsymbol{\sigma})\mathbf{1}\|$ denotes the deviatoric stress with $\mathbf{1} := \delta_{ij}$, the Kronecker notation, M is the slope of critical state line and p_{crit} is the preconsolidation pressure.

Consider the associative flow rule. The plastic train, $\dot{\boldsymbol{\epsilon}}^p$, can be expressed as

$$\dot{\boldsymbol{\epsilon}}^p = \dot{\lambda}\frac{\partial \mathcal{F}}{\partial \boldsymbol{\sigma}} \tag{18}$$

together with loading-unloading Kuhn-Tucker criterion:

$$\dot{\mathcal{F}} \leq 0, \quad \lambda\,\mathcal{F} = 0\ , \quad \lambda \geq 0 \tag{19}$$

where $\dot{\lambda}$ is the plastic multiplier.

The hardening function in rate form is given by

$$\dot{p}_c = \vartheta p_c \dot{\epsilon}_v^p, \qquad \dot{\epsilon}_v^p = \mathrm{tr}(\boldsymbol{\epsilon}^p), \qquad \vartheta = \frac{1+e}{\lambda - \kappa} \tag{20}$$

where e is the void ratio, λ is the virgin compression index, and κ is the swelling/recompression index.

The relationship of stress and strain is governed by the following constitutive equation as

$$\dot{\boldsymbol{\sigma}} = \boldsymbol{C}^e\dot{\boldsymbol{\epsilon}}^e = \boldsymbol{C}^e(\dot{\boldsymbol{\epsilon}} - \dot{\boldsymbol{\epsilon}}^p) \tag{21}$$

where $\boldsymbol{C}^e$ is a forth order tensor of elasticity.

2.4 Swelling pressure model

The aim of the present study is to model stress induced by swelling effect solely. From the viewpoint of thermodynamics, swelling pressure indicates a type of energy. Kahr et al. (1989) showed with experiments on compacted bentonites that swelling pressure can be calculated from the adsorption isotherms measured by means of the

water vapor adsorption-desorption isotherm and heat immersion with liquid water. This means, drier bentonites swell because of the surface energy. Because of the extremely high value in total specific surface of bentonite and additionally high nett negative charge on the surface of bentonite particles (Grim and Güven (1978)), the surface energy can be very high under dry state (Yan and Luo (1995)). If water enters into the bentonite, this energy can be transformed through wetting into work resulting the volume change in the case of free swelling, or into strain energy resulting swelling pressure in the case of constrained swelling (Figure 3). Therefore, it is reasonable to calculate the swelling pressure from the swelling potential, which is considered to be equal in value to the volume change under free swelling condition.

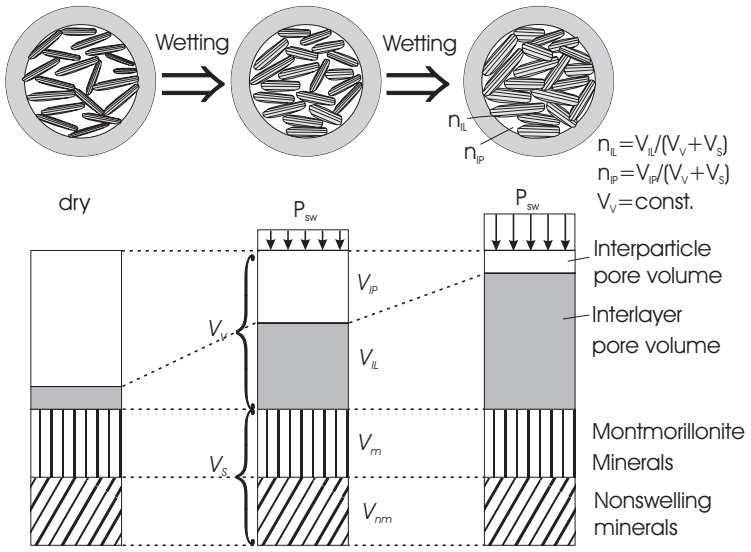

Figure 3: Concept of swelling pressure

The concept to assess the stress induced solely by the swelling effect is illustrated in Figure 4. We consider a bounded domain. The computation of swelling induced stress is performed in two steps: 1. compute the free swelling deformation contributed by volume change (dV) in the domain; 2. press the free swelling strain back and calculate the resulting stress after compaction process. In the second stage, an elasto-plasticity problem is analyzed by taking the negative displacement results on the boundary (after the first computation step) as Dirichlet boundary condition. The stress obtained after the second computation step is the stress induced solely by swelling.

2.4.1 Step 1: free extension

The concept of swelling potential was first used by Seed et al. (1962) to represent the swelling ability of bentonite. In the present paper, swelling potential is defined as

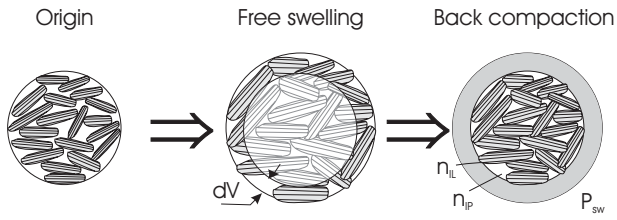

Figure 4: Conceptual model of back compaction

the porosity change potential n_{sw} responsible for swelling pressure (equation (22)). In the case of constrained swelling, interlayer porosity change can not fully be converted into swelling pressure. Part of it is used to compact the large pores (initial interparticle porosity $n_{\mathrm{IP}0}$), especially at the early stage. The looser the sample, the more interlayer porosity change will be converted. Theoretically, the large pores can totally be compacted, but in reality, a certain interparticle porosity always remains. This is defined as the minimal porosity ($n_{\mathrm{IP}min}$). This value is lower, the higher the swelling pressure σ. It depends on the compressibility of the material.

$$n_{\mathrm{sw}} = \triangle n_{\mathrm{IL}} - (n_{\mathrm{IP}0} - n_{\mathrm{IP}min}) \tag{22}$$

$$n_{\mathrm{IP}0} = n_0 - n_{\mathrm{IL}0} \tag{23}$$

$$n_{\mathrm{IP}min} = f(\sigma) \tag{24}$$

where n_0 is the initial porosity, $n_{\mathrm{IL}0}$ is the initial interlayer porosity.

According to this swelling model, the porosity $n_{\mathrm{IP}0}$ in equation (22) can practically be extended to include construction gaps between bentonite blocks plus intergranular porosity within the bentonite blocks, if the gaps disappear through bentonite expansion.

2.4.2 Step 2: back compaction

As described in Section 2.4, the computation of swelling induced stress is carried out in two individual steps.

To compute the free swelling deformation, an admissible strain approach is utilized.

In this approach, it is assumed that the strain $\boldsymbol{\epsilon}$ consists of an elastic part and a swelling induced part as shown in equation (25),

$$\boldsymbol{\epsilon} = \boldsymbol{\epsilon}^e + \boldsymbol{\epsilon}^{sw}, \tag{25}$$

where the swelling induced part $\boldsymbol{\epsilon}^{sw}$ is defined as

$$\begin{aligned} \epsilon_{xx} &= \epsilon_{yy} = n_{sw}/2 \\ \epsilon_{xy} &= 0 \end{aligned} \tag{26}$$

for a plane strain problem. The definition of $\boldsymbol{\epsilon}^{sw}$ implies that the free swelling is an non-linear deformation.

Consider the free swelling phenomena as a coupled hydraulic-mechanical process. The displacement under free swelling conditions can easily be obtained in the framework of the finite element method.

The displacement results obtained by the above approaches are taken into account for the calculation of the domain deformation. Since the deformed domain will be compacted back to its original shape, the swelling induced stress is obtained by solving the compaction process. The swelling behaviour of bentonite in turn causes deformation. This implies that restricted swelling may induce inelastic deformation in bentonite. The analysis of the inelastic deformation during the back compaction process is set in the context of elasto-plasticity using the modified Cam-Clay model described in Section 2.3.

3 Governing equations

In the macroscopic model, two-phase flow is considered. In general, there are two concepts to formulate the balance equations: phase-related and compositional approaches. The compositional approach is advantageous for multiphase-multicomponental processes with phase changes (Gawin et al. (1995), Gens et al. (1998)), and is adopted for the study. The porous medium is considered as a three component system, with the components air, water and soil. Each of these components can be presented in three phases (gas, liquid and solid phase). In the study, air and solid are treated as single pseudo components with averaged properties, even if they consist of several components.

Hydraulic processes resulting from pressure, frictional, and gravitational forces are described by the extension of Darcy's law for multiphase flow. The mobility of the fluid phases is characterized by their relative permeability and capillary pressure via saturation.

The mechanic processes resulting from hydraulic processes and swelling are described in the fully coupled general mass balance equation via deformation:

$$\frac{\partial}{\partial t}(nS^g\rho^g + nS^l\rho^l) + \alpha S^l \frac{\partial}{\partial t}\nabla\cdot\mathbf{u} + \nabla\cdot(\mathbf{J}_k^g + \mathbf{J}_k^l) = Q_k, \tag{27}$$

where n is porosity, S is phase saturation (g, gas; l, liquid), ρ is component mass density, g means gas, l means liquid, subscript k denotes component, a (air) or w

(water), and α is given by Biot's constant as

$$1-\alpha = \frac{K_t}{K_s},$$
$$K_t : \text{bulk modulus of skeleton},$$
$$K_s : \text{bulk modulus of the grain material.}$$

For incompressible porous media, we assume, $\alpha = 1.0$. $\mathbf{J}_k^\gamma$ are fluxes of component k in phase γ (g or l).

The flux terms of the mass of fluid phase as described in the generalized Darcy's law are used to describe the linear momentum balance of multiple fluid phases in a porous medium (see e.g. Bear and Bachmat (1990), Helmig (1997)):

$$\mathbf{J}^{\gamma s} = nS^\gamma \rho^\gamma (\mathbf{v}^\gamma - \mathbf{v}^s) = -\rho^\gamma \frac{k_{\mathsf{rel}}^\gamma \mathbf{k}^\gamma}{\mu^\gamma} (\nabla p^\gamma - \rho^\gamma \mathbf{g}) \tag{28}$$

The flux is a function of pressure gradients and saturation. The decisive material function for the flux term is relative permeability $k_{\mathsf{rel}}^\gamma(S^\gamma)$.

In a partially saturated regime, the momentum balance of porous media is governed by

$$\nabla \left[\boldsymbol{\sigma} - (S^l p^l + S^g p^g)1\right] + \left[(1-n)\rho^s + nS^l\rho^l + nS^g\rho^g\right]\mathbf{g} = 0 \tag{29}$$

4 Numerical approach

Details of the numerical schema for multiphase-multicomponent flow in non-deformable porous media can be found in Kolditz and de Jonge (2004). The extensions for swelling and deformation processes are presented in this paper.

Finite element formulations

The weak forms of the differential field equations for fluid pressure and saturations are formulated using the method of weighted residuals. The unknown functions are approximated by trial solutions based on nodal values and interpolation functions. According to the Darcy's law, fluid fluxes depend on pressure gradients (28). In order to extract the independent field variables, the flux terms are treated in their weak form using the Gauss-Ostrogradskian integral theorem. The weak form is discretized using a mixed "P2/P1" element (quadratic interpolation of displacements and linear interpolation of saturation and pressure).

Denote the shape functions of linear interpolation as $\mathbf{N}_1$ and quadratic interpolation as $\mathbf{N}_2$, respectively. The following equations can be obtained:

$$
\begin{aligned}
& \left[\int_\Omega \mathbf{N}_1^T \left(nS^g X_k^g \frac{\partial \rho^g}{\partial p^g} + nS^l X_k^l \frac{\partial \rho^l}{\partial p^l}\right) \mathbf{N}_1 \,\mathrm{d}\Omega\right] \left[\frac{\mathrm{d}\hat{\mathbf{p}}^g}{\mathrm{d}t}\right] \\
+ & \left[\int_\Omega \nabla \mathbf{N}_1^T \left(\rho^g X_k^g \frac{k_{\mathsf{rel}}^g \mathbf{k}}{\mu^g} + \rho^l X_k^l \frac{k_{\mathsf{rel}}^l \mathbf{k}}{\mu^l}\right) \nabla \mathbf{N}_1 \,\mathrm{d}\Omega\right] [\hat{\mathbf{p}}^g] \\
- & \left[\int_\Omega \mathbf{N}_1^T \left(n\rho^g X_k^g - n\rho^l X_k^l\right) \mathbf{N}_1 \,\mathrm{d}\Omega\right] \left[\frac{\mathrm{d}\hat{\mathbf{S}}^l}{\mathrm{d}t}\right] \\
+ & \left[\int_\Omega \mathbf{N}_1^T \alpha S^l \mathbf{m}\mathbf{B} \,\mathrm{d}\Omega\right] \left[\frac{\mathrm{d}\hat{\mathbf{u}}}{\mathrm{d}t}\right] \\
= & \int_\Omega \mathbf{N}_1^T Q_k \,\mathrm{d}\Omega \\
+ & \left[\int_\Omega \mathbf{N}_1^T \left(nS^l X_k^l \frac{\partial \rho^l}{\partial p^l}\right) \mathbf{N}_1 \,\mathrm{d}\Omega\right] \left[\frac{\mathrm{d}\hat{\mathbf{p}}_{\mathsf{c}}}{\mathrm{d}t}\right] \\
+ & \left[\int_\Omega \nabla \mathbf{N}_1^T \left(\rho^l X_k^l \frac{k_{\mathsf{rel}}^l \mathbf{k}}{\mu^l}\right) \nabla \mathbf{N}_1 \,\mathrm{d}\Omega\right] [\hat{\mathbf{p}}_{\mathsf{c}}] \\
- & \left[\int_\Omega \nabla \mathbf{N}_1^T (nS^g \rho^g X_k^g D_k^g) \nabla \mathbf{N}_1 \,\mathrm{d}\Omega\right] \left[\hat{\mathbf{X}}_k^g\right] \\
- & \int_\Omega \nabla \mathbf{N}_1^T \left(\rho^g X_k^g \frac{k_{\mathsf{rel}}^g \mathbf{k}}{\mu^g} \rho^g \mathbf{g} + \rho^l X_k^l \frac{k_{\mathsf{rel}}^l \mathbf{k}}{\mu^l} \rho^l \mathbf{g}\right) \,\mathrm{d}\Omega
\end{aligned}
\tag{30}
$$

for a mutli-phase flow problem and

$$
\begin{aligned}
\int_\Omega \mathbf{B}^T \boldsymbol{\sigma} \,\mathrm{d}\Omega \;=\; & \int_\Omega \mathbf{B}^T \mathbf{m} \mathbf{N}_1 \,\mathrm{d}\Omega \left[S^l \hat{\mathbf{p}}^l + S^g \hat{\mathbf{p}}^g\right] \\
& - \int_\Omega \mathbf{N}_2 [(1-n)\rho^s + nS^l \rho^l + nS^g \rho^g] g \mathrm{d}\Omega + \int_\Gamma \mathbf{N}_s \mathbf{t} \mathrm{d}\Gamma
\end{aligned}
\tag{31}
$$

for the displacement field, where $\hat{\mathbf{p}}^g$ and $\hat{\mathbf{S}}^l$ and $\hat{\mathbf{u}}$ are nodal variables, $\mathbf{B}$ is the strain displacement matrix, $\mathbf{m}$ is a unit mapping vector, $\mathbf{N}_s$ is the shape function on the face of an element and $\mathbf{t}$ is boundary traction.

Equation (31) is solved by the general Newton-Raphson method with the return mapping of stress. The partitioning iterative scheme is employed to deal with the coupling items in equations (30, 31).

5 Example

5.1 Problem definition

The following example is investigated for swelling pressure calculation by using the back compaction method. The simulation begins with isothermal two phase flow coupled with deformation. Free swelling is allowed at the first stage to calculate the free swelling displacement on the boundary, which is then used as the displacement boundary condition for the back compaction process.

The objectives of this example study are:

- Demonstrating free expansion by the swelling model presented herein
- Calculating swelling pressure by the back-compaction method

The geometric set-up and boundary conditions (BC) are as shown in Figure 5. The sample is a compacted bentonite block, 0.025 m in length and 0.024 m in height. The element discretization is $\triangle x = 0.00125\,m$ and $\triangle y = 0.00124\,m$. The initial conditions (IC) of the isothermal system are: atmospheric gas pressure, liquid saturation $S^l = 0.357$. A water solution (ionic strength $I = 0.316\,M$) enters the sample from the bottom between $x = -0.0075\,m$ and $x = 0.0075\,m$ under a pressure described by the curve in Figure 6. The corresponding part on the boundary is fully saturated. This model set-up is similar to a case of fractured rock/bentonite contact.

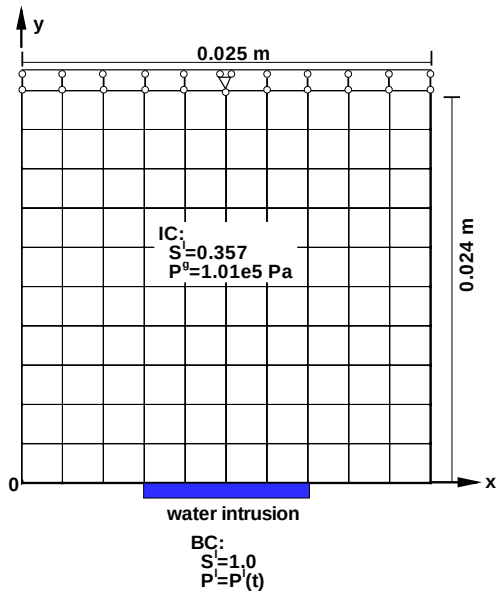

Figure 5: Model set-up of the example

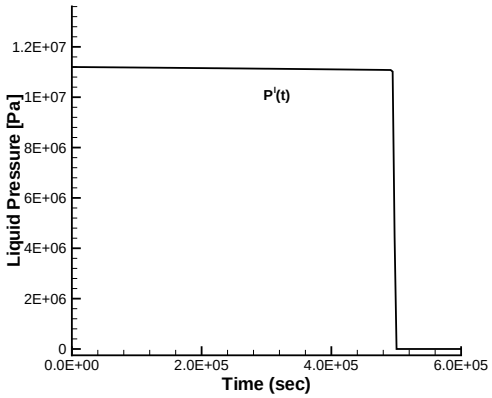

Figure 6: Curve of the liquid pressure on the boundary

The material properties for this example are based on data in the literature (Agus and Schanz (2003), Poling et al. (2001)) and summarized in Table 1 for fluid and in Table 2 for porous medium. The minimum porosity defined in equation (24) is assumed to be constant.

Table 1: Fluid properties

Symbol	Meaning	Value	Unit
ρ^g	initial gas density	1.26	kg/m^3
β_p^g	gas compress. coeff.	6.67×10^{-6}	Pa^{-1}
ρ^l	initial liquid density	1000	kg/m^3
β_p^l	liq. compress. coeff.	4.70×10^{-10}	Pa^{-1}
μ^g	gas viscosity	1.80×10^{-5}	$Pa\ s$
μ^l	liquid viscosity	1.20×10^{-3}	$Pa\ s$
c^g	gas heat capacity	1.01×10^3	$-$
c^l	liquid heat capacity	4.20×10^3	$-$
λ^g	gas heat conductivity	0.026	$W/(m\ K)$
λ^l	liquid heat conductivity	0.60	$W/(m\ K)$

from Poling et al. (2001)

The deformation under free swelling conditions is assumed to be linearly elastic, whereas the deformation during back compaction is elasto-plastic. For the compaction computation, an initial status $\sigma_{xx} = \sigma_{yy} = 1MPa, \quad \sigma_{zz} = 0.7MPa$ is given with $\nu = 0.35$ for the modified Cam-Clay model, which satisfies plane strain conditions. The solid material parameters used in the present computation are given in Table 3.

Table 2: Porous medium properties

Symbol	Meaning	Value/Ref	Unit
ρ	density	1600^*	kg/m^3
n	porosity	0.37^*	$-$
S_0	extern. spec. surface	31.80	m^2/g
β	swelling fraction	0.85	$-$
m	effective layer number	5	$-$
I	ionic strength	0.316	M
$n_{\min}$	min. porosity	0.05	$-$
c	heat capacity	$1.6 \times 10^{3**}$	
λ	heat conductivity	0.718^{**}	$W/(m\ K)$
k	permeability	eqn(15)	
p_c	capillary pressure	Figure 7	Pa
k_{rel}	relative permeability	eqn (12, 14)	

$*$ from Agus and Schanz (2003)

$**$ from Poling et al. (2001)

Table 3: Solid material properties

Symbol	Meaning	Value	Unit
Elasticity	*(free swelling)*		
E	Young's modulus	3.5	MPa
ν	Poisson ratio	0.3	—
Plasticity	*(back compaction)*		
M	Slope of the critical state line	1.4	—
λ	Virgin compression index	0.165^*	—
κ	swelling/recompression index	0.087^*	—
p_c	Initial preconsolidation pressure	4.96^{**}	MPa

$*$ from FEBEX Working groups (2000)

$**$ from Nishimura (2001)

5.2 Results and discussion

The simulation results of the free swelling processes after $5.8 \times 10^5 s$ (6.7 days) are as shown in Figure 9a-d. With the intrusion of water from the bottom, the saturation process starts. This phenomena can clearly be seen from the saturation evolution profile along the vertical symmetric axis (Figure 8). At the early stage, the value of liquid saturation increases quite fast, owing to the high capillary pressure of the specimen and extra liquid pressure (see Figure 6). After $4.9 \times 10^5 s$ (5.7 days), the liquid pressure on the bottom sinks and at $5.0 \times 10^5 s$ (5.8 days) reaches zero. Because of the low permeability of bentonite, the liquid pressure at the center of the

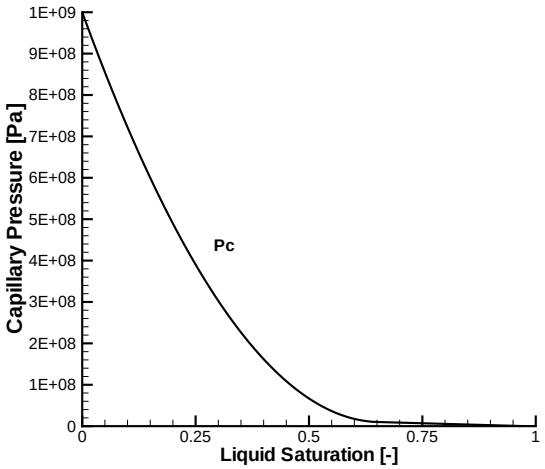

Figure 7: Capillary pressure-saturation curve

specimen sinks slower, which results in the higher pressure region in the specimen after 6.7 days as shown in Figure 9a.

With the intrusion of water, the sample begins to expand. After 6.7 days, the shape of the specimen should be as shown in Figure 9. This is owing to the interlayer porosity increase as shown in the Figure 9d with the increase of the liquid saturation (Figure 9c). The maximal width of the specimen increases about 20% (Figure 9).

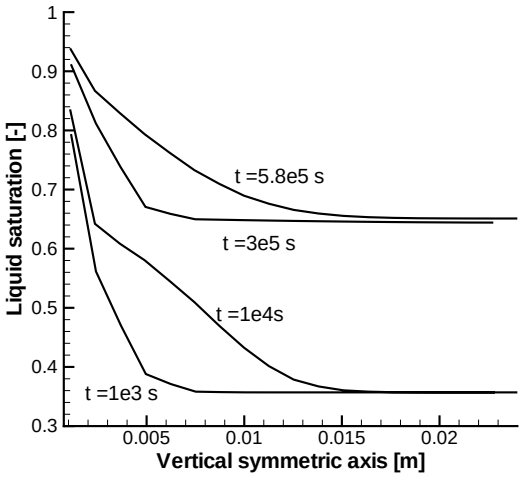

Figure 8: Computed profiles of liquid saturation along the vertical symmetric axis

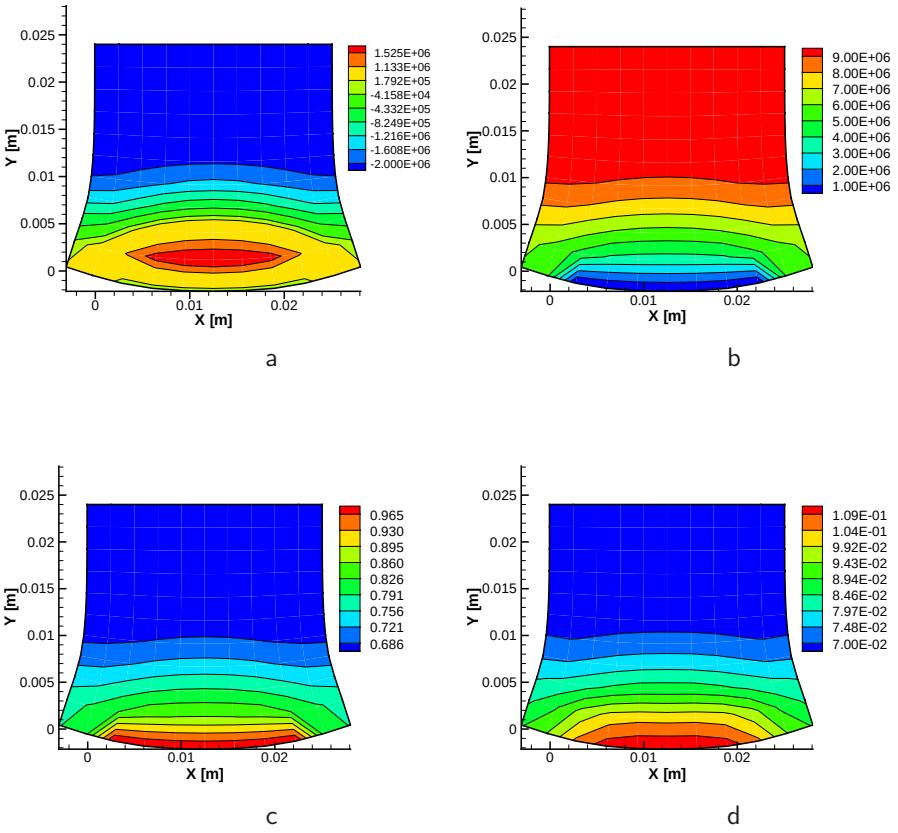

Figure 9: Simulation results of the free swelling process - Distribution of a) liquid pressure, b) capillary pressure, c) liquid saturation, d) interlayer porosity, at $t = 5.8 \times 10^5 s$

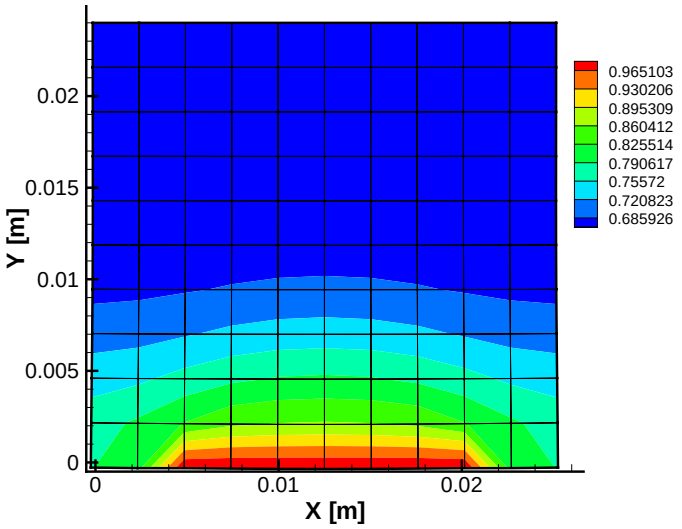

Figure 10: Simulated shape of the sample, and distribution of liquid saturation for non-swelling material at $t = 5.8 \times 10^5 s$

For comparison, the same example is recalculated without the swelling model ($n_{sw} = 0.0$ in equation (26)). In this case, the sample deforms only by the coupling effect of flow and deformation, which appears to be negligibly small as shown in Figure 10. This demonstrates that the swelling effect is significant.

In order to calculate the swelling pressure, the back compaction process is performed using the modified Cam-Clay model. The back compaction of the expanded sample is simulated to the original shape using the computed displacement values on the boundaries at the free swelling stage as displacement boundaries. The distributions of stress (Figure 11a,c) and strain (b,d) are within the expected ranges. The simulated values of stress σ_{yy}, which represent the swelling stress, are between $0.089MPa$ and $0.93MPa$.

The minimum porosity defined in equation (24) is assumed to be constant. This causes negative n_{sw} value at the early saturation stage, which is treated to be zero, owing to the fact that the swelling strain contributes to the compression of large pores. The reactive transport in bentonite, which can cause pore water ionic strength variation, is not taken into account because of the short simulation time.

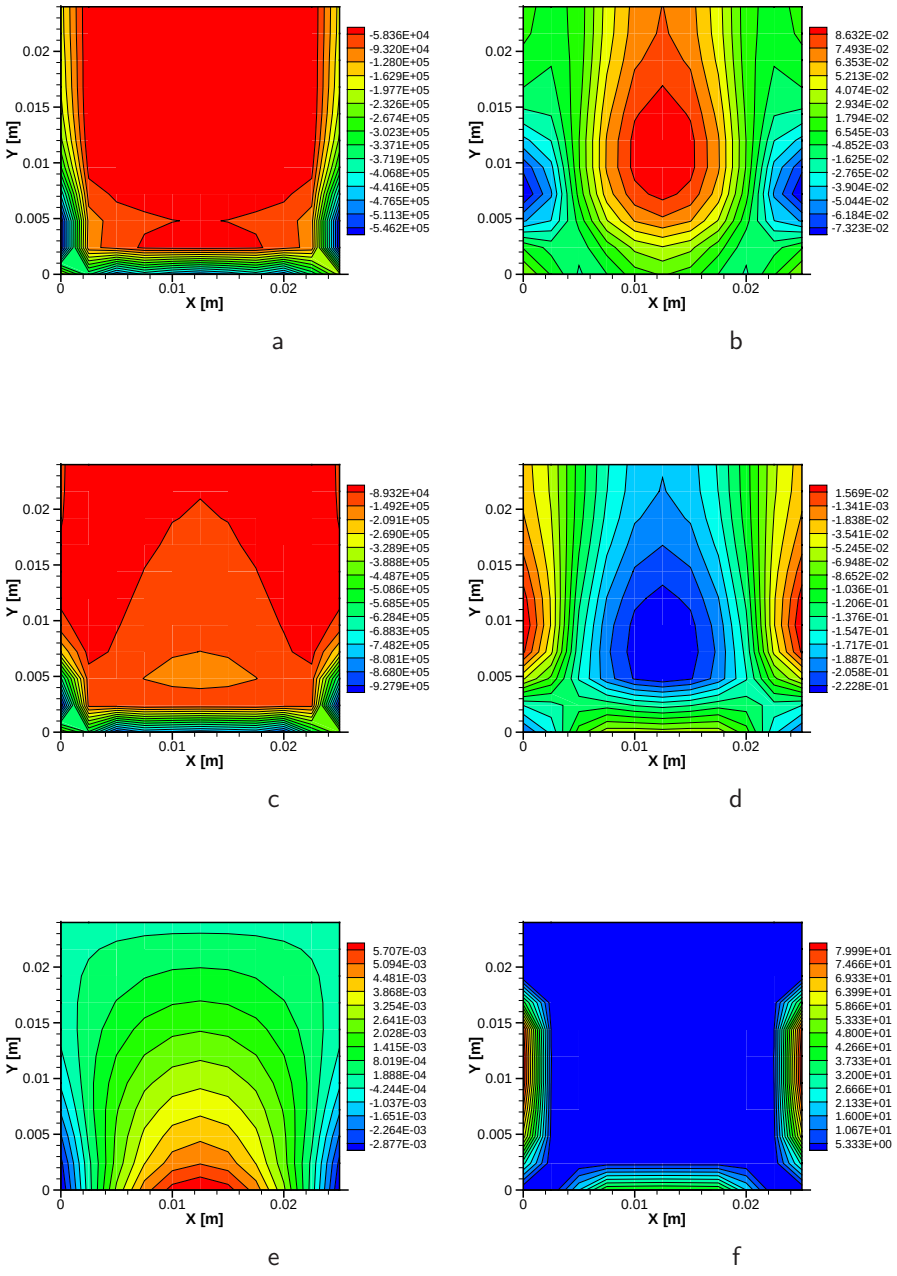

Figure 11: Results of the back compaction process - Distribution of a) stress σ_{xx}, b) strain ϵ_{xx}, c) stress σ_{yy}, d) strain ϵ_{yy}, e) displacement u_y, f) accumulated plastic strain ϵ^p_{yy} at $time = 6.0 \times 10^6 s$

6 Conclusions

This paper presents a new modelling concept of the numerical assessment of swelling pressure, i.e. the stress induced by swelling solely, in expansive porous media. In the presented method, swelling pressure is computed through free swelling followed by a back compaction. The application of this method takes two steps: 1. Free swelling simulation on the basis of the H^2M/C model for accessing displacement on the boundaries. This model is based on the diffuse double layer theory, and connects the microstructural mineral parameters of bentonite and porewater chemistry with macroscopic swelling effects. Variations of effective porosity and consequently, of the permeability of bentonite have been taken into account; 2. Back compaction using the displacement on the boundaries obtained by the first step through the modified Cam-Clay elasto-plastic model. The resulting stress is considered to be the swelling pressure.

The strong non-linearity arising from multiphase flow and elasto-plastic deformation processes are resolved by the Picard and Newton-Raphson methods, respectively. The partitioning iterative scheme is employed to deal with the H^2M/C coupling system equations. The stability of this scheme is observed. A 2D example was computed to demonstrate the capability of the modelling concept for design of swelling pressure experiments.

7 Acknowledgement

The work is supported by German Federal Ministry of Education and Research (BMBF) under grant 02C0881. The authors would like also to acknowledge Hua Shao (BGR Hannover), Tom Schanz (University of Weimar) and Helge Moog (GRS Braunschweig) for providing suggestions and very useful discussions to this research. We thank Dr. Pitterich (FZK) for his support of this research work, and Christopher McDermott (ZAG) for improving the manuscript. Also thanks is extended to Professor Th. van Genuchten (U.S. Salinity Laboratory, USDA, ARS in Riverside) and Dr. Robert J. Lenhard (INEEL, Idaho) for their valuable discussions.

References

Agus, S. and Schanz, T.: 2003, Swelling pressures and soil-water characteristic curves of a highly compacted bentonite-sand mixture, *Proceedings of the international conference from experimental evidence towards numerical modelling of unsaturated soils (in print)* .

Alonso, E., Vaunat, J. and Gens, A.: 1999, Modelling the mechanical behaviour of expansive clays, *Engineering Geology* **54**, 173–183.

ASTM: 2001a, *Standard Test Method for Methylene Blue Index of Clay, C837-99*, chapter In: Book of standards Volume:15.02.

ASTM: 2001b, *Standard Test Method for Precipitated Silica-Surface Area by Single B.E.T. Nitrogen Adsorption, D5604-96*, chapter in: Book of standards Volume:09.01.

Bear, J. and Bachmat, Y.: 1990, *Introduction to modeling of transport phenomena in porous media*, Kluwer Academic Publishers, Dordrecht.

Bennethum, L. and Cushman, J.: 2002a, Multicomponent, multiphase thermodynamics of swelling porous media with electroquasistatics I: Macroscale field equations, *Transport in Porous Media* **47**(3), 309–336.

Bennethum, L. and Cushman, J.: 2002b, Multicomponent, multiphase thermodynamics of swelling porous media with electroquasistatics II: Constitutive theory, *Transport in Porous Media* **47**(3), 337–362.

Berg, R.: 1970, Method of determining permeability from reservior rock properties, *Gulf Coast Assoc Geol Soc Trans* **20**, 303–317.

Biot, M. A.: 1941, General theory of three-dimensional consolidation, *J. Appl. Phys.* **12**, 155–164.

Bloch, S.: 1991, Empirical prediction of porosity and permeability in sandstones, *American Association of Petroleum Geologists Bulletin* **75**(7), 1145–1160.

Bolt, G.: 1955, Analysis of the validity of the Gouy-Chapman theory of the electric double layer, *Journal of Colloidal Science* **10**, 206.

Börgesson, L.: 1985, Water flow and swelling pressure in non-saturated bentonite-based clay barriers, *Engineering Geology* **314**, 229–237.

Börgesson, L., Johannesson, L.-E., Sanden, T. and Herneling, J.: 1995, Modelling of the physical behavior of water saturated clay barriers - Laboratory tests, material models and finite element application, *SKB Technical Report 95-20*.

Carman, P.: 1937, Fluid flow through granular beds, *Tran. Inst. Chem. Eng.* **15**, 150–166.

Chapman, D.: 1913, A contribution to the theory of electrocapillarity, *Philosophical Magazine* **25**, 475.

Derjaguin, B. and Landau, L.: 1941, Theory of the stability of strongly charged lyophobic soils and of the adhension of stronghly charged particles in solutions of electrolytes, *Acta Physiochem. USSR* **14**, 633–662.

Dzombak, D. and Morel, F.: 1990, *Surface Complexation Modelling; Hydrous Ferric Oxide*, Wiley-Interscience, New York.

Evans, J., Fang, H. and Kugelman, I.: 1985, Organic fluid effects on the permeability of soil-bentonite slurry walls, *in* K. M. et. al. (ed.), *Proceedings of the National Conference on Environmental Emergencies*, Cincinnati, OH, The Hazardous Materials Control Research Institute, pp. 267–271.

FEBEX Working groups: 2000, Full-scale engineered barriers experiment for a deep geological repository for high level radioactive waste in crystalline host rock, *Final report*.

Gawin, D., Baggio, P. and Schrefler, B. A.: 1995, Coupled heat, water and gas flow in deformable porous media, *Int. J. Num. Meth. Fluids* **20**, 969–987.

Gens, A., Garcia-Molina, A. J., Oliviella, S., Alonso, E. E. and Huertas, F.: 1998, Analysis of a full scale in situ test simulating repository conditions, *Int. J. Numer. Anal. Meth. Geomech.* **22**, 515–548.

Geraminegad, M. and Saxena, S. K.: 1986, A coupled thermoelastic model for saturated-unsaturated porous media, *Géotechnique* **36**, 539–550.

Gouy, G.: 1910, Sur la constitution de la charge électrique à la surface d´un électrolyte, *Journal de Physique* **9**, 457–468.

Grim, R. E. and Güven, N.: 1978, *Bentonite - Geology, Mineralogy, Properties and Uses*, Elsevier Sci.

Helmig, R.: 1997, *Multiphase flow and transport processes in the subsurface*, Springer, Berlin.

Herbert, H.-J. and Moog, H. C.: 2002, Untersuchungen zur Quellung von Bentoniten in hochsalinaren Lösungen, *Abschlussbericht*, Gesellschaft für Anlagen und Reaktorsicherheit (GRS) mbH.

Holtz, W. G. and Bara, J. P.: 1965, Comparison of expansive clays in the central valley, *Engineering effects of moisture changes in soils: International Research and Engineering Conference on Expansive Clay Soils*, Texas A & M Press, California, pp. 120–151.

Huyghe, J. and Janssen, J.: 1999, Thermo-chemo-electro-mechanical formulation of saturated charged porous solids, *Transport in Porous Media* **34**, 129–141.

Kahr, G., Bucher, F. and Mayor, P.: 1989, Water uptake and swelling pressure in a bentonite-based backfill, *Materials Research Society symposium proceedings, Band:Scientific basis for nuclear waste management, Berlin* **127**.

Katti, D. and Shanmugasundaram, V.: 2001, Influence of swelling on the microstructure of expansive clays, *Canadian Geotechnical Journal* **38(1)**, 175–182.

Kaya, A., Lloyd, T. and Fang, H.-Y.: 2000, Interfacial parameters and work of adhension in soil-liquid systems, *Geotechnical Testing Journal* **23**(4), 464–471.

Kolditz, O.: 2002, *Computational Methods in Environmental Fluid Mechanics*, Springer.

Kolditz, O. and de Jonge, J.: 2004, Non-isothermal two-phase flow in porous media, *Computational Mechanics* **33**(5), 345–364.

Komine, H. and Ogata, N.: 1994, Experimental study on swelling characteristics of compacted bentonite, *Canadian Geotechnical Journal* **33**, 11–22.

Korsawe, J., Perau, E., Potthoff, S. and Starke, G.: 2003, Numerical approximation of water-air two-phase flow by the mixed finite element method, *Computers and Geotechnics* **30**(8), 695–705.

Lenhard, R. J. and Parker, J. C.: 1987, A model for hysteretic constitutive relations governing multiphase flow, 2. permeability-saturation relations, *Water Resources Research* **23**, 2197–2206.

Low, P. F.: 1979, Nature and properties of water in montomorillonite-water systems, *Journal of Soil Science Society of America* **43**, 651–658.

Low, P. F.: 1980, The swelling of clays. II. Montmorillonites, *Journal of Soil Science Society of America* **44**(4), 667–676.

Low, P. F.: 1987, Structural component of the swelling pressure of clays, *Langmuir* **3**, 18–25.

Low, P. F. and Margheim, J.: 1979, The swelling of clays. I. Basic concepts and empirical equations, *Journal of Soil Science Society of America* **43**, 473–481.

Marcial, D., Delage, P. and Cui, Y.: 2002, On the high stress compression of bentonites, *Canadian Geotechnical Journal* **39**, 812–820.

Mielenz, R. C. and King, M. E.: 1955, Physical mechanical properties and engineering performance of clays, *California Division of Mines Bulletin, Clays and clay technology: 1st National Conference on Clays and Clay Technology, Berkeley, California* **169**, 196–254.

Mitchell, J.: 1993, *Fundamentals of soil behaviour*, 2nd edn, John Wiley & Sons.

Murad, M. and Cushman, J.: 1997, A multiscale theory of swelling porous media: II. dual porosity models for consolidation of clays incorporating physical chemical effects., *Transport in Porous Media* **28**(1), 69–108.

Neuzil, C.: 1994, How permeable are clays and shales?, *Water Resources Research* **30**(2), 145–150.

Nishimura, T.: 2001, *Swelling pressure of a compacted bentonite subjected to high suction*, Clay Science for Engineering, Proceedings of the international symposium on suction, swelling, permeability and structure of clays - Is-Shizuoka, Balkema, Rotterdam, pp. 109–114.

Noorishad, J., Ayaollahi, M. S. and Witherspoon, P.: 1982, A finite-element method for coupled stress and fluid flow analysis in fractured rock masses, *Int. J. Rock Mech. Min. Sci.* **19**, 185–193.

Norrish, K.: 1955, Manner of swelling of montmorillonite, *Nature* **4397**, 256–257.

Oelkers, E.: 1996, *Physical and chemical properties of rocks and fluids for chemical mass transport calculations*, Vol. 34, chapter 2 in Reactive Transport in Porous Media, Reviews in Mineralogy (Mineralogy Society of America),P.H.Ribbe (Series Editor), pp. 130–191.

Olivella, S. and Gens, A.: 2000, Vapour transport in low permeability unsaturated soils with capillary effects, *Transport in Porous Media* **40**, 219–241.

Parcher, J. V. and Liu, P.-C.: 1965, Some swelling characteristics of compacted clays, *ASCE, J. Soil Mechanics and Foundations Division* **91**(SM3), 1–17.

Poling, B. E., Prausnitz, J. M. and O'Connell, J. P.: 2001, *The Properties of Gases and Liquids*, fifth edn, Mc Graw Hill.

Pusch, R., Karnland, O. and Hökmark, H.: 1990, GMM-A general microstructural model for qualitative and quantitative studies of smectite clays, *Technical Report 90-43*, SKB, Sweden.

Quirk, J.: 1997, Application of double-layer theories to the extensive crystalline swelling of Li-Montmorillonite, *Langmuir* **13**, 6241–6248.

Seed, H. B., Woodward, R. J. and Lundgren, R.: 1962, Prediction of swelling potential for compacted clays, *J. Soil Mechanics and Foundation Division* **88**(SM 3), 53–87.

Sridharan, A.: 1990, Strength and volume change behaviour of a sand-bentonite mixture, *Canadian Geotechnical Journal* **27**, 404.

Sridharan, A. and Choudhury, D.: 2002, Swelling pressure of sodium montmorillonites, *Géotechnique* **52**(6), 459–462.

Sridharan, A. and Jayadeva, M.: 1982, Double layer theory and compressibility of clays, *Géotechnique* **32**(2), 133–144.

Studer, J., Ammann, W., Meier, P., Müller, C. and Glauser, E.: 1984, Verfüllung und Versiegeln von Stollen, Schächten und Borhlöchern, *Nagra Technischer Bericht 84-33, Baden, Schweiz* **2**.

Stumm, W. and Morgan, J. J.: 1996, *Aquatic Chemistry, third edition*, John Wiley and Sons, New York.

Terzaghi, K.: 1925, *Erdbaumechanik auf bodenphysikalischer Grundlage*, Deuticke, Wien.

Tripathy, S. and Schanz, T.: 2003, Swelling pressure of sodium montmorillonites, *Géotechnique* **53**, No.4, 449.

US Bureau of Mines (ed.): 1997, *Dictionary of Mining, Mineral, and Related Terms*, 2nd edn, American Geological Institute.

van Genuchten, M. T.: 1980, A closed-form equation for predicting the hydraulic conductivity of saturated soils, *J. Soil Science Society of America* **44**, 892–898.

Verwey, E. and Overbeek, J.: 1948, *Theory of the stability of lyophobic colloids*, Elsevier, Amsterdam.

Volkaert, G., Ortiz, L., De Cannière, P., Put, P., Horsman, M., Harrington, S., Fioravante, J. and Impey, M.: 1994, Modelling and experiments on gas migration in repository host rocks, *MEGAS project, Final Report, phase 1*.

Xie, M., Agus, S., Schanz, T. and Kolditz, O.: 2004, An upscaling method and numerical modelling of swelling/shrinking processes in compacted bentonite/sand mixtures, *Submitted to International Journal for Numerical and Analytical Methods in Geomechanics*.

Yan, X. and Luo, M.: 1995, *Physical chemistry*, Wuhan University Press. (in chinese).

A process-oriented approach to compute THM problems in porous media - Part I: Theoretical and informatics background

Book chapter in:

Proceedings of the International Conference "From Experimental Evidence towards Numerical Modeling of Unsaturated Soils, Weimar, Germany, 2003 (Ed. T. Schanz), Springer Proceedings in Physics, Netherlands

A process-oriented approach to compute THM problems in porous media - Part 1: Theoretical and informatics background

Olaf Kolditz, Wenqing Wang, Joëlle de Jonge, Mingliang Xie, and Sebastian Bauer

Center for Applied Geosciences, Geohydrology/HydroInformatics,
University of Tübingen
kolditz@uni-tuebingen.de

Abstract: Object-oriented (OO) methods become more and more important in order to meet scientific computing challenges, such as the treatment of coupled non-linear multi-field problems with extremely high resolutions. This two-part paper introduces an object-oriented concept for numerical modelling multi-process systems in porous media (Part 1). The C++ implementation of the OO design for process objects (PCS) as a class is described and illustrated with several applications. Due to the importance of the encapsulation of processes as individual PCS objects we denote our concept as an process-oriented approach.

The presented examples (Part 2) are dealing with thermal (T), hydraulic (H), mechanical (M) and componental processes (C) in bentonite materials, which are used as buffer material for the isolation of hazardous waste in geologic barriers. In particular, we are interested in coupling phenomena such as thermally induced desaturation, non-isothermal consolidation, swelling/shrinking phenomena as well as in a better understanding of the coupled, non-linear THM system.

1 Introduction

For deep geological disposal of nuclear waste, engineered barrier systems have to be developed. To develop appropriate barriers, the disposal scenario has to be simulated numerically, as a prediction and engineering tool in the near-field of the disposal site. The numerical model has to be able to reproduce the various processes. Figure 1 shows a plan view of a possible disposal scenario, with nuclear waste packed into the core at the centre, a bentonite buffer surrounding it. Core and buffer are placed into the host rock. The processes arising in this situation are coupled processes, composed of thermal processes (heating, cooling, evaporation, condensation), hydraulic processes (water intrusion, saturation, desaturation), mechanical processes (elastic and plastic deformation), and chemical processes (radiation, reactions).

The engineered buffer used in deep geological disposal sites is often pure bentonite or a bentonite - sand mixture. Bentonite is a material with very low permeability and complex swelling properties (Tripathy and Schanz (2002)). The swelling properties are used as a seal against water intrusion.

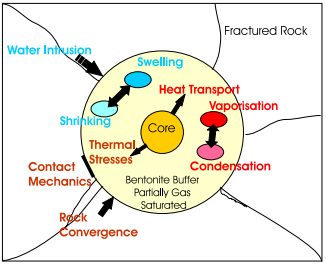

Fig. 1. THM processes in the near field of a disposal site

Natural thermo-hydraulic processes in the surrounding area of geothermal reservoirs have been studied by a large number of authors (e.g. Pruess and Narasimhan (1982), Pruess and Narasimhan (1985)). An excellent review of modelling thermo-hydraulic processes in geothermal systems is presented by Pruess (1990). Bodvarsson and Tsang (1982) investigated the effect of the injection of colder water into a fracture near a geothermal reservoir, and the advance of the thermal front along the fracture was simulated with a numerical model. The role of fracture networks in geothermal reservoirs is discussed and demonstrated in site studies by Kolditz (2001). Long-term fluid and heat extraction from geothermal systems result in significant deformation processes (Lippmann et al. (1976)). Lewis et al. (1989) presented a THM model for geothermal systems, where capillarity effects are neglected.

In geomechanical models the stress state and the resulting deformation process is of special interest. As a consequence the solid phase has to be treated explicitly. The interaction of fluid (phase) flow and solid (phase) deformation in the framework of the porous medium approach can be modeled based on the consolidation theory (Terzaghi (1925), Biot (1941)). Modeling of geotechnical barriers for heat emitting waste often requires a coupled thermo-hydro-mechanical (THM) analysis. First studies of THM processes in that field were presented by Borsetto et al. (1984). However, only one fluid phase was considered. In that case, multiphase effects and phase change processes can not be addressed. Börgesson (1985) and Studer et al. (1984) investigated swelling and shrinking phenomena in bentonites. They developed a material model for porosity and permeability changes with undergoing moisture transport. Studies of THM processes in partially saturated, thermo-elastic porous media without phase change effects were presented by Geraminegad and Saxena (1986). Alonso et al. (1987) discussed the theoretical background of THM modeling including all important effects. Olivella et al. (1994), Gawin et al. (1995) and Gens et al. (1998) introduced the compositional approach for THM modeling of multiphase-multicomponental systems. In their book, Lewis and Schrefler (1998) gave an excellent overview on coupled processes and their modeling in the field of deformation and consolidation theory of

porous media. Kanno et al. (1999) developed and applied a THM model to study the temperature dependency of hydraulic conductivity in saturated porous media and water diffusivity in unsaturated porous media. An excellent overview on existing THM codes is given by Rutqvist et al. (2001). The model was verified against full scale coupled experimental data. Most of the cited models have found wide application in simulating geotechnical systems. In most cases the systems analysed were restricted to relatively large permeabilities.

Thermo-hydraulic processes are important in the field of groundwater remediation techniques as well, i.e. thermally enhanced procedures, such as steam injection, are recognized techniques to treat subsurface contamination by non-aqueous phase liquids (NAPLs). Numerical models for simulation of the related non-isothermal processes were developed by Falta et al. (1992a), Emmert (1997), Helmig (1997), and Class (2000). These codes have found wide application in simulating NAPL remediation but in systems with relatively large permeability.

RockFlow/GeoSys is a simulator that is used to model near-field situation of the type described above (Kolditz et al. (2003)). It is a finite element code, programmed using object-oriented techniques. Object-orientation allows a wide spectrum of applications for the code, and also simultaneous code development. This paper will concentrate on a process-oriented approach, that is used for simulating the coupling of thermal, hydraulic, mechanical and chemical (THMC) processes. The governing equations of the model are shown, as well as how these equations are treated numerically. A code application example for the desaturation of bentonite will be presented. The first example is based on an example in Olivella and Gens (2000) and partially serves as model verification. Furthermore, the code development finds application in bench mark test 1 (BMT1) of the DECOVALEX (International co-operative project for the DEvelopment of COupled models and their VALidation against EXperiments in nuclear waste isolation) project (Jing et al. (1999)). Current work on this project is presented.

2 Model Equations

In multi-field problems we have to deal with several processes, which are described by a corresponding set of partial differential equations (PDEs). We may have different types of processes such as flow (H-Process), heat (T-Process) and component transport (C-Process) as well as deformation (M-Process). Those processes are described by PDEs of different types (compare Table 1), which are derived from the basic conservation principles of mass and energy together with the corresponding material laws (e.g. Kolditz (2002)). Associated with each PDE are the corresponding initial and boundary conditions, as well as the appropriate numerical and solution techniques.

The system of model equations to determine the chosen field variables (fluid gas pressure p^g, fluid liquid saturation S^l and equilibrium temperature T) is based on the balance equations for fluid mass and heat in combination with the flux terms and the equations of state.

Table 1. PDE types of processes

Acronym	Process	PDE type
T	Thermal	mixed parabolic-hyperbolic
H	Hydraulic	parabolic
M	Mechanic	elliptic
C	Componental	mixed parabolic-hyperbolic

2.1 H^2 Processes: Fluid component equations

Here we deal with two-phase flow (H^2) processes (exponent denotes number of fluid phases). Based on the fluid mass balance the following model equation in terms of primary variables: gas pressure, liquid saturation, solid displacement can be derived.

$$
\begin{aligned}
& nX_k^g \left(S^g \frac{\partial \rho^g}{\partial p^g} + S^l \frac{\partial \rho^l}{\partial p^l} \right) \frac{\partial p^g}{\partial t} \\
& - \nabla \cdot \left(\rho^g X_k^g \frac{k_{\mathrm{rel}}^g \mathbf{k}}{\mu^g} \nabla p^g \right) - \nabla \cdot \left(\rho^l X_k^l \frac{k_{\mathrm{rel}}^l \mathbf{k}}{\mu^l} \nabla p^g \right) \\
& + n(-\rho^g X_k^g + \rho^l X_k^l) \frac{\partial S^l}{\partial t} \\
& + \underbrace{(S^g \rho^g + S^l \rho^l) \mathbf{m}^T \mathbf{L} \frac{\partial \mathbf{u}^s}{\partial t}}_{\text{MH coupling term}} \\
& = Q_k \\
& + (nS^l X_k^l \frac{\partial \rho^l}{\partial p^l}) \frac{\partial p_{\mathrm{c}}}{\partial t} - \nabla \cdot \left(\rho^l X_k^l \frac{k_{\mathrm{rel}}^l \mathbf{k}}{\mu^l} \nabla p_{\mathrm{c}} \right) \\
& - \nabla \cdot \left(\rho^g X_k^g \frac{k_{\mathrm{rel}}^g \mathbf{k}}{\mu^g} \rho^g \mathbf{g} \right) + \nabla \cdot \left(\rho^l X_k^l \frac{k_{\mathrm{rel}}^l \mathbf{k}}{\mu^l} \rho^l \mathbf{g} \right) \\
& + \underbrace{\nabla \cdot (nS^g \rho^g D_k^g \nabla X_k^g)}_{\text{TH coupling term}}
\end{aligned}
\tag{1}
$$

where n is porosity, β_p is the fluid compressibility, p is liquid phase pressure, t is time, $\mathbf{k}$ is permeability tensor, μ is liquid viscosity, $\mathbf{g}$ is gravity vector, $\mathbf{u}^s$ is solid phase displacement, $\mathbf{m}^T$ and $\mathcal{L}$ are matrix operators. $\mathcal{L}$ is an operator that gives the relationship between displacement and strain, X is mass fraction, p_{c} is capillary pressure, k_{rel} is relative permeability, ρ is density, and D is componental diffusion coefficient. Index $k = a, w$ denotes air and water components,respectively and exponent $\gamma = g, l, s$ denotes gas, liquid, solid phase, respectively.

The MH and TH coupling terms of deformation and heat transport to the flow processes are highlighted. Coupling is also due to the dependencies of material and state functions such as density, viscosity, capillary pressure,

vapor pressure, mass fractions on the primary variables: gas pressure, liquid saturation, temperature and solid displacement.

2.2 T Process: Thermal energy equation

Based on the heat balance equation for the porous medium consisting of three phases, we obtain the following thermal energy equation.

$$\begin{aligned}
&\left((1-n)\rho^s c^s + nS^g\rho^g c^g + nS^l\rho^l c^l\right)\frac{\partial T}{\partial t}\\
&+\Big(\rho^g c^g \frac{k^g_{\mathrm{rel}}\mathbf{k}}{\mu^g}(\nabla p^g - \rho^g\mathbf{g})\\
&\quad +\rho^l c^l \frac{k^l_{\mathrm{rel}}\mathbf{k}}{\mu^l}(\nabla p^l - \rho^l\mathbf{g})\Big)\nabla T\\
&-\nabla\cdot\left(\left((1-n)\lambda^s + nS^g\lambda^g + nS^l\lambda^l\right)\nabla T\right)\\
&-\nabla\cdot(nS^g\rho^g D^g_a h^g \nabla X^g_a)\\
&-\nabla\cdot(nS^g\rho^g D^g_w h^g \nabla X^g_w)\\
&=\rho Q_T
\end{aligned} \tag{2}$$

where in addition to above equations: c^γ is specific heat capacity of phase γ, T is temperature, λ^γ is thermal conductivity of phase γ, h^γ is enthalpy of fluid phase γ, Q_T is a heat source term.

2.3 M Process: Equilibrium equation

Porous medium momentum conservation in terms of stresses is

$$\nabla\cdot(\boldsymbol{\sigma} - \underbrace{(S^l p^l + S^g p^g)\mathbf{I}}_{\text{HM coupling term}} - \underbrace{\beta_T(T-T_0)\mathbf{I}}_{\text{TM coupling term}}) + \rho\mathbf{g} = 0 \tag{3}$$

where $\boldsymbol{\sigma}$ is the effective stress of the porous medium, $\mathbf{I}$ is the Kronnecker symbol. $\rho = n\rho^l + (1-n)\rho^s$ is the density of porous media. Hereby we assume solid grains itself are incompressible, i.e. $d^s\mathbf{u}/d^s t = 0$

To solve the initial-boundary-value-problem, we have to specify initial and boundary conditions for the field functions and their derivatives (fluxes).

3 Object-oriented design

3.1 Processes of multi-field problems

Processes can have complex relationships and interactions (Fig. 2), e.g. transport processes of chemical species are based on a defined flow field. These chemical species may also react with each other. Those reactions can change the porous material itself. Thermal effects influence flow and deformation processes.

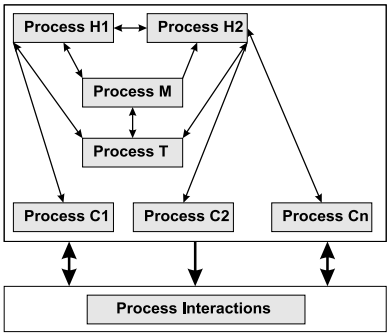

Fig. 2. Dependencies of THMC processes

Traditionally, one computer code was developed to simulate one physical process. The code could therefore deal with one PDE and the associated sets of boundary and initial conditions, and provided a set of numerical techniques to solve the equation system. These codes were then extended to deal with coupled processes or to handle more than one PDE. This was often done without changing the data and programm structure used and thus caused a complicated and inflexible code. Sometimes, as e.g. in the case of the simulation programs MODFLOW and MT3D, two programs have to be run sequentially to simulate both flow (MODFLOW) and transport (MT3D), with intermediate program output and input. Therefore the need for a new design of the multi-process approach is obvious.

The solution of an equation system EQS as the representative of a physical process is a universal procedure which can be applied to each process independently of their specific type. This allows us to generalize the code and to treat processes in an object-oriented way.

The computation scheme must be very flexible concerning the number of fluid phases (number of H processes) and the number of chemical components to be transported (number of C processes). Additionally, there must be a flexible way of specifying the relation between the flow processes as well as very general way to define reactions between the involved chemical species. The new process object therefore corresponds to all numerical and physical properties of a "conventional" program and the multi-process concept presented here can therefore be seen as a merging of many programs, each for a specific physical problem. Data structures as well as the grid and the timestepping are common for all processes, whereas the parameters, boundary conditions and the type of PDE and thus also the solving technique used may vary from process to process.

3.2 PCS object design

Fig. 3 gives a graphical illustration of the process (PCS) relationships to other objects. From these objects information is required to solve a process. Because this information is universal, we build an object for processes, the PCS object, which is implemented as a class.

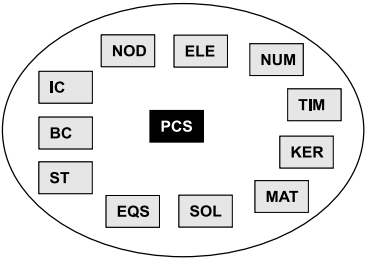

Fig. 3. Relationships of processes

Discrete approximation methods for PDEs result in algebraic equation systems (AES). The general task of a process is, therefore, to build and solve the corresponding equation system (EQS).

- EQS: $\mathbf{Au} = \mathbf{b}$
  Processes must have a related equation system consisting of a system matrix $\mathbf{A}$, a solution vector $\mathbf{u}$, and the right-hand-side (RHS) $\mathbf{b}$. For the solution procedure of an AES we also need parameters to control the equation solver (SOL). During the solution procedure, system matrix, solution vector and RHS vector will be manipulated according to specified initial conditions IC, boundary conditions BC, and source terms ST. All this data is related to nodes of the numerical grid. Having several equation systems to deal with, we must be able to correlate the data with the corresponding equation system. This will be done by names. The EQS name will be selected according to the corresponding field quantity, e.g. `PRESSURE` for fluid flow and `CONCENTRATION` for component transport. In case of multi-phase or multi-component systems, we have to specify these names by adding the related phase or component number, i.e. `PRESSURE1` or `CONCENTRATION1` for the first fluid phase or component, `PRESSURE2` or `CONCENTRATION2` for the second fluid phase or component and so on.
- NUM:
  The numerics object contains parameters of the numerical method, such as time collocation factors, the number of Gaussian points, upwind parameters etc. Again, a NUM object will be related to the PCS by name.
- SOL:
  Solver objects enclose parameters controlling the equation solver algo-

rithm, such as solver method, tolerance criterion, maximum iteration number etc.

– IC:
Initial conditions are necessary for any initial value problem. They prescribe values for a certain time point $\mathbf{u}(t_0)$. Initial conditions are related to PCS by the process name. IC values correspond to grid nodes.
– BC:
Boundary conditions are necessary for any boundary value problem. They can be of different kind, prescribing a value $\mathbf{u}(x_0)$, a flux $\nabla\mathbf{u}(x_0)$ or a combination of both. Boundary conditions are related to PCS by the process name. BC values correspond to grid nodes.
– ST:
Source terms give nodal loads to a system. They can be directly applied to the RHS vector $\mathbf{b}$. Source terms are related to PCS by a name. ST values correspond to grid nodes.
– MAT:
In general, the system matrix is built by material properties MAT, by shape functions N, and their derivatives ∇N. For flow and transport processes in porous media we need fluid , component and medium properties. The number of instances for the fluid, component, and medium properties corresponds to the number of specified fluid phases, chemical components and material groups.
– TIM:
For transient problems we have to apply appropriate time discretization schemes. Time stepping schemes are governed by numerical stability criteria, which depend on the specific type of PDE.
– KER:
As we use the finite element method for the spatial discretization of the multi-field system, we need special data constructs for finite element matrices, which are linked to the element list.

In fact, the size of a multi-field problem in continuum mechanics is defined by the corresponding balance equations to be solved in order to determine the required field quantities. For flow and transport processes in porous media this is equivalent to the number of fluid phases and the number of chemical components involved. Then the set of PDEs consists of fluid and component mass conservation equations. In case of deformable porous medium a stress equilibrium equation has to be solved.

In the framework of discrete approximation methods, such as the finite element method, processes must be able to access node and element data, in order to save the own solution vector $\mathbf{u}_i$ or resultants (e.g. flux vectors). Moreover for coupled multi-field problems, processes must have the right to use solution vectors or resultants of the other processes. This has to be implemented by data access functions to nodes (NOD) and elements (ELE) via the node and element lists.

– NOD:
Each process has to define his related node values (e.g. the field quantity

at the old and new time step, etc.). Nodal values of all field variables will be stored in a vector, which is connected with the node list. This nodal value vector must be flexible in order to account for a variable number of field variables, e.g. as a result of chemical reactions.

– ELE:
Each process has to define his related element values (e.g. element resultants (fluxes, stresses, strains), characteristic numbers, material properties, etc.). Element values of all processes will be stored in a vector, which is connected with the element list. This element value vector must also be flexible in order to account for a variable number of values.

3.3 PCS Methods

After outlining the requirements and the object structure for PCS objects, we turn to the methods associated with them, i.e. the functions of PCS objects. This functionality is determined by the algorithm of the multi-process scheme, which is depicted in Fig. 4.

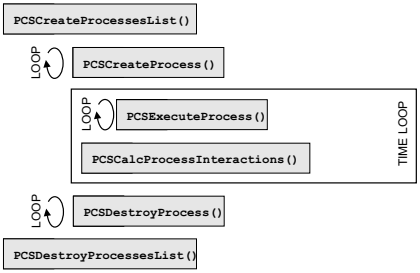

Fig. 4. PCS methods

As is visible in Fig. 4, first the process list is created, which contains all the processes to be handled during a program run. These processes then have to be created and configured and the connections between all objects have to be set. Then the process can be executed within the time loop by solving the corresponding PDE and obtaining the field variables as well as values wanted additionally. Within the time loop interactions of the processes can also be calculated. Functions are thus needed to create the PCS list as well as the PCS instances themselves. In order to destroy the list and its instances, corresponding destroy-functions are required. The symmetry of data construction-destruction is very important for working with dynamic data and is clearly reflected in the structure of Fig. 4. This way the general methods for processes become visible: construction and destruction of the process list and the corresponding list operations, and secondly, process construction and destruction as well as process execution for the individual process.

3.4 PCS Implementation

The PCS object must be able to administrate all required data for the complete solution algorithm of a PDE. PCS objects are implemented as a class:

```
class CRFProcess
{
 ...
 private:
 \\ EQS - equation system for this process
 public:
 \\ Relationships to other objects
 ...
}
```

The PCS has private and public data. The most important private property of a process is the connected equation system EQS, while public data reflect the relationship to other objects (Fig. 2). Typical methods of process instances are PCS creation, configuration, and execution. Instances of the PCS class are organized in a list.

After having created and configured the process object PCS instances, they can be executed to set up and solve the equation system. This is done by

```
void CRFProcess::PCSExecuteProcess(EQUATION_SYSTEM *eqs)
```

The algorithm for process execution consists of the following steps: (1) initialize system matrix $\mathbf{A}$, RHS-vector $\mathbf{b}$, and solution vector $\mathbf{u}$, (2) calculate finite element matrices, (3) assemble equation system, (4) solve equation system, and (5) store time step results.

The source code can be written now in a very compact way.

```
void CRFProcess::PCSExecuteProcess(EQUATION_SYSTEM *eqs) {
  DisplayMsgLn("Process: ", eqs->name);
  // 1 - Initializations ----------------------------
  EQSSetZeroLinearSolver(eqs);
    // system matrix, RHS vector
  nidx = PCSGetNODValueIndex(this->name);
    // get solution vector (initial values)
  NODTransferValues2EQS(nidx,eqs);
  // 2 - Calc element matrices -----------------------
  PCSCalcElementMatrices();
  // 3 - Assemble equation system --------------------
  PCSAssembleSystemMatrix(eqs->b,eqs->x);
  // 4 - Solve EQS -----------------------------------
  EQSExecuteLinearSolver(eqs);
  // 5 - Store solution vector in node values vector -
  EQSTransferNODValues(eqs,nidx);
}
```

The function parameter is the equation system connected to the current process: `pcs->eqs`. Note that the above function sets up and solves a PDE, which can have different types (Table 1). More details of the PCS concept and the implementation can be found in Kolditz and Bauer (2003).

Conclusions

An object-oriented approach is developed to solve coupled, non-linear multi-field problems for porous media. The treatment of processes as objects (PCS) has several advantages

- Standardization of process data,
- Generalization of the solution procedure of PDEs (calculation of element matrices, assembling and solving resulting equation systems),
- Easy to create, configure and execute processes in user-defined loops.

The PCS concept was applied to analyze thermo-hydro-mechanical processes in the near-field of heat emitting container embedded in bentonite material. The variety of phenomena is spreading from TH^2, THM to TH^2M processes.

Acknowledgement

In this paper we assembled results from several research projects. We are very grateful to the Projektträger PtWT+E (Karlsruhe), the Federal Institute for Geoscience and Natural Resources (BGR) and the German Science Foundation (DFG) for the funding to these research works. The authors would like to thank Tom Schanz (Weimar), Horst Pitterich (Karlsruhe), Hua Shao, Manfred Wallner and Gerhard Starke (Hannover) for their scientific, technical and logistic support to our research.

References

E. E. Alonso, A. Gens, and D. W. Hight. Special problem soils: general report. In *Proc. 9th European Conf. on Soil Mechanics and Foundation Engineering*, volume 3, Rotterdam, 1987. Balkema.

M. A. Biot. General theory of three-dimensional consolidation. *J. Appl. Phys.*, 12: 155–164, 1941.

G. S. Bodvarsson and C. F. Tsang. Injection and thermal breakthrough in fractured geothermal reservoirs. *J. Geophys. Res.*, 87(B2):1031–1048, 1982.

L. Börgesson. Water flow and swelling pressure in non-saturated bentonite-based clay barriers. *Engineering Geology*, 314:229–237, 1985.

M. Borsetto, D. Cricci, T. Hueckel, and A. Peano. On numerical models for the analysis of nuclear waste disposal in geologic clay formations. In R. W. Lewis, editor, *Numerical Methods for Transient and Coupled Problems*, Swansea, 1984. Pineridge Press.

H. Class. *Theorie und numerische Modellierung nichtisothermer Mehrphasenprozesse in NAPL-kontaminierten porösen Medien.* Dissertation, TU Braunschweig, 2000.

M. Emmert. *Numerische Modellierung nichtisothermer Gas-Wasser Systeme in porösen Medien.* PhD thesis, Insitut für Wasserbau, Universität Stuttgart, 1997.

R. W. Falta, K. Pruess, I. Javandel, and P. A. Witherspoon. Numerical modeling of steam injection for the removal of nonaqueous phase liquids from the subsurface - 2. code validation and application. *Water Resources Research*, 28(2):451–465, February 1992a.

R. W. Falta, K. Pruess, I. Javandel, and P. A. Witherspoon. Numerical modeling of steam injection for the removal of nonaqueous phase liquids from the subsurface - 1. numerical formulation. *Water Resources Research*, 28(2):433–449, February 1992b.

D. Gawin, P. Baggio, and B. A. Schrefler. Coupled heat, water and gas flow in deformable porous media. *Int. J. Num. Meth. Fluids*, 20:969–987, 1995.

A. Gens, A. J. Garcia-Molina, S. Olivella, E. E. Alonso, and F. Huertas. Analysis of a full scale in-situ test simulating repository conditions. *Int. J. Anal. Num. Meth. Geomech.*, 22:515–548, 1998.

M. Geraminegad and S. K. Saxena. A coupled thermoelastic model for saturated-unsaturated porous media. *Géotechnique*, 36:539–550, 1986.

R. Helmig. *Multiphase Flow and Transport Processes in the Subsurface*. Springer, Berlin, 1997.

L. Jing, O. Stephansson, L. Börgesson, M. Chijimatzu, F. Kautsky, and C.-F. Tsang. Decovalex ii project technical report - task 2c. Ski report 99:23. issn 1104-1374, DECOVALEX team, 1999.

T. Kanno, T. Fujita, H. Ishikawa, K. Hara, and M. Nakano. Coupled thermo-hydro-mechanical modelling of bentonite buffer material. *Int. J. Numer. Anal. Meth. Geomech.*, 23:1281–1307, 1999.

M. Kohlmeier, R. Kaiser, O. Kolditz, and W. Zielke. Finite element simulation of consolidation and bentonite swelling in the framework of unsaturated porous media. *In: Developments in Water Science*, 47:57–64, 2002.

O. Kolditz. Non-linear flow in fractured rock. *Int. J. Numer. Methods for Heat & Fluid Flow*, 11(6):547–575, 2001.

O. Kolditz. *Computational methods in environmental fluid mechanics*. Springer Science Publisher, Berlin - New York - Tokyo, 2002.

O. Kolditz and S. Bauer. A process-oriented approach to compute multi-field problems in porous media. *submitted to Hydroinformatics*, 2003.

O. Kolditz, J. de Jonge, M. Beinhorn, M. Xie, T. Kalbacher, W. Wang, S. Bauer, C. McDermott, R. Kaiser, and M. Kohlmeier. ROCKFLOW - Theory and users manual, release 3.9 (in preparation). Groundwater modeling group, Center for Applied Geosciences, University of Tuebingen, Institute of Fluid Mechanics, University of Hannover, 2003.

R. W. Lewis, P. J. Roberts, and B. A. Schrefler. Finite element modelling of two-phase heat and fluid flow in deforming porous media. *Transport in Porous Media*, 4:319–334, 1989.

R. W. Lewis and B. A. Schrefler. *The finite element method in the static and dynamic deformation and consolidation of porous media*. Wiley, 1998.

M. J. Lippmann, T. N. Narasimham, and P. A. Witherspoon. Numerical simulation of reservoir compaction in liquid-dominated geothermal systems. In *Proc. 2nd Int. Symposium Land Subsidence*, pages 179–189. IAHS, 1976.

S. Olivella, J. Carrera, A. Gens, and E. E. Alonso. Nonisothermal multiphase flow of brine and gas through saline media. *Transport in Porous Media*, 15:271–293, 1994.

S. Olivella and A. Gens. Vapour transport in low permeability unsaturated soil with capillary effects. *Transport in Porous Media*, 40:219–241, 2000.

K. Pruess. Modeling of geothermal reservoirs: Fundamental processes, computer simulations and field applications. *Geothermics*, 19(1):3–15, 1990.

K. Pruess and T.N. Narasimhan. On fluid reserves and the production of superheated steam from fractured, vapor-dominated geothermal reservoirs. *J. Geophys. Res.*, 87(B11):9329–9339, 1982.

K. Pruess and T.N. Narasimhan. A practical method for modeling fluid and heat flow in fractured porous media. *Society of Petroleum Engineers Journal*, 25(1): 14–26, 1985.

J. Rutqvist, L. Börgesson, M. Chijimatsu, A. Kobayashi, L. Jing, T. S. Nguyen, J. Noorishad, and C.-F. Tsang. Thermodynamics of partially saturated geologic media: governing equations and formulation of four finite element models. *International Journal of Rock Mechanics & Mining Sciences*, 38:105–127, 2001.

J. Studer, W. Ammann, P. Meier, Ch Müller, and E. Glauser. Verfüllen und Versiegeln von Stollen, Schächten und Bohrlöchern. Technischer Bericht 84-33, Nagra, Baden, Schweiz, 1984.

K. Terzaghi. *Erdbaumechanik auf bodenphysikalischer Grundlage*. Deuticke, Wien, 1925.

S. Tripathy and T. Schanz. A re-examination of swelling pressure of compacted bentonites from gouy-chapman diffusive double layer theory. In De Gennaro and Delage, editors, *Int Workshop of Young Doctors in Geomechanics - W(H)YDOC 02*, pages 17–19. Ecole Nationale des Ponts et Chaussees, 2002.

A process-oriented approach to compute THM problems in porous media - Part II: Numerical Applications

Book chapter in:

Proceedings of the International Conference "From Experimental Evidence towards Numerical Modeling of Unsaturated Soils, Weimar, Germany, 2003 (Ed. T. Schanz), Springer Proceedings in Physics, Netherlands

A process-oriented approach to compute THM problems in porous media - Part 2: Numerical applications

Olaf Kolditz, Wenqing Wang, Joëlle de Jonge, Mingliang Xie, and Sebastian Bauer

Center for Applied Geosciences, Geohydrology/HydroInformatics,
University of Tübingen
kolditz@uni-tuebingen.de

Abstract: Object-oriented (OO) methods become more and more important in order to meet scientific computing challenges, such as the treatment of coupled non-linear multi-field problems with extremely high resolutions. This two-part paper introduces an object-oriented concept for numerical modelling multi-process systems in porous media (Part 1). The C++ implementation of the OO design for process objects (PCS) as a class is described and illustrated with several applications. Due to the importance of the encapsulation of processes as individual PCS objects we denote our concept as an process-oriented approach.

The presented examples (Part 2) are dealing with thermal (T), hydraulic (H), mechanical (M) and componental processes (C) in bentonite materials, which are used as buffer material for the isolation of hazardous waste in geologic barriers. In particular, we are interested in coupling phenomena such as thermally induced desaturation, non-isothermal consolidation, swelling/shrinking phenomena as well as in a better understanding of the coupled, non-linear THM system.

Part 1 of this paper is about design and implementation of processes in an object-oriented way. Here we give numerical examples to show the variety of problems which can be treated based on the process-oriented approach.

Examples

We consider three classes of THM problems with increasing complexity:

- Non-isothermal single-phase flow in elasto-plastic porous media (THM processes) (section 1)
- Non-isothermal two-phase/two-componental flow in porous media (TH^2/M processes) (section 2)
- Non-isothermal two-phase/two-componental flow in elasto-plastic porous media (TH^2M processes) (section 3)

1 Non-isothermal consolidation of saturated elasto-plastic materials (THM process)

The process features of this problem class and the treatment are given in Table 1.

Table 1. Processes

Acronym	Process	Treatment
T	Heat transport	Heat balance equation
H	Single phase flow	Mass balance equation
M	Inelastic deformation	Momentum balance equation

Example 1: Biaxial test

Example description

The biaxial test with thermal effect is analyzed to demonstrate the efficiency of the process oriented concept. The sample is sand in rectangle shape with size of $0.1\text{m} \times 0.34\text{m}$ under plain strain condition (Mokni and Desrues (1998)). Details of the numerical analysis of the biaxial test can be found in Wang and Kolditz (2003).

The geometry, boundary conditions and mesh are shown in Fig. 1 The initial and boundary conditions are:

- Thermal: The whole sample is under a room temperature of 283K before the boundary condition is applied. Temperature in a range of $x = [0.2, 0.8]$ on the top boundary is kept constant with the value of 383K.
- Hydraulic: The pressure is uniformly distributed in whole sample at the beginning. Boundaries are impervious except for the top boundary, where constant pressure of 3×10^5Pa is imposed.
- Mechanical: The top boundary is imposed a time dependent vertical displacement load at the speed of 0.2mm/s. Both of the lateral boundaries are prescribed with constant pressure, 10^5Pa.

The material parameters are given in Table 2.

Simulation results

The distributions of displacements, stresses and accumulative plastic strain at the time $t = 1980s$ are shown in Fig. 2 and Fig. 3 (a-c), respectively. The impact of temperature increment on the top of boundary to stresses and the accumulative plastic strain can be found in Fig. 4(a-c).

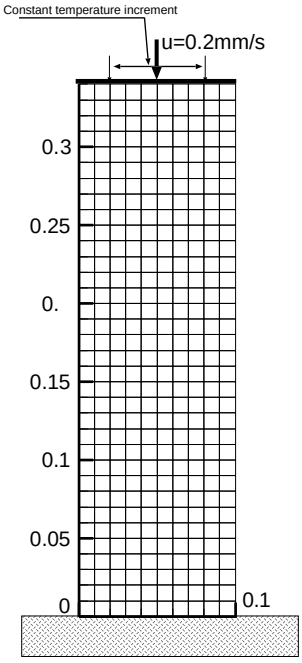

Fig. 1. Set up of biaxial test

Table 2. Material parameters

Parameter	Unit	Value
Young's modulus	MPa	250.0
Poisson ratio		0.328
Initial yield stress	MPa	2.0
Plastic hardenning	MPa	-1.0
Thermal expansion	1/K	5×10^{-5}
Internal friction angle	°	21
Dilatancy angle	°	26
Permeability	m/s	2.55×10^{-12}
Porosity		0.2
Thermal conductivity	W/mK	0.43
Thermal capacity	J/kg	1000.0

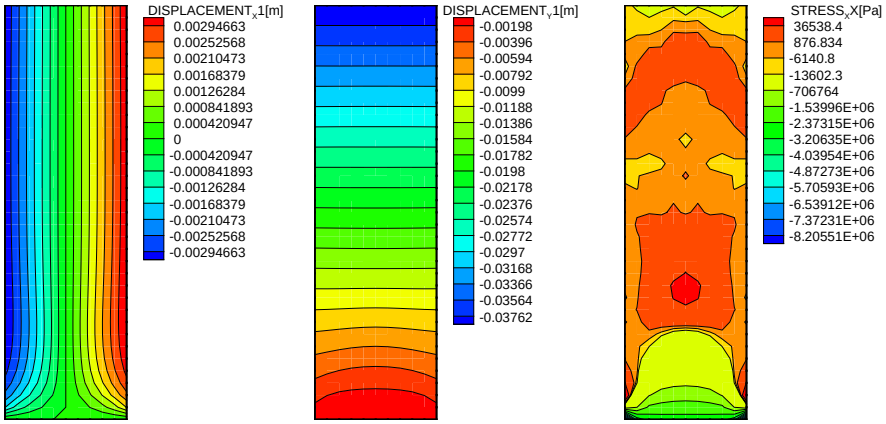

Fig. 2. Distributions of (a) u_x, (b) u_y, (c) σ_{xx}, $t = 1980s$

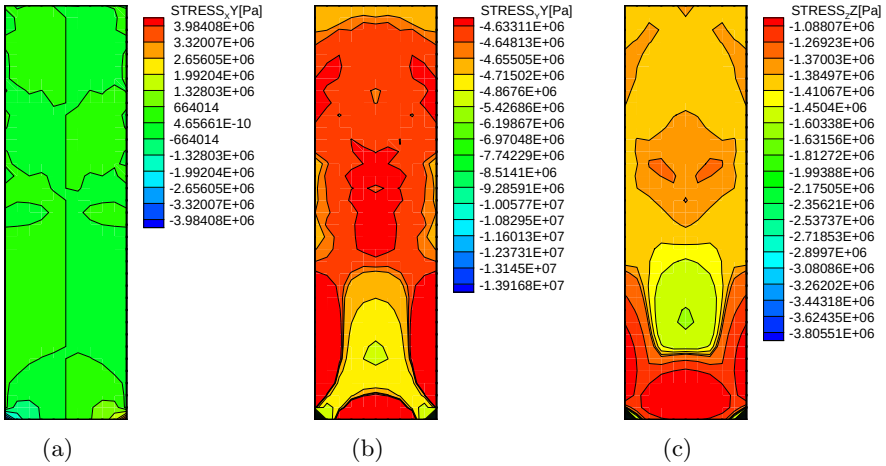

Fig. 3. Distributions of (a) σ_{xy}, (b) σ_{yy}, (c) σ_{zz}, $t = 1980s$

2 Non-isothermal two-phase flow in swelling materials (TH^2/M)

The process features of this problem class and the treatment are given in Table 3.

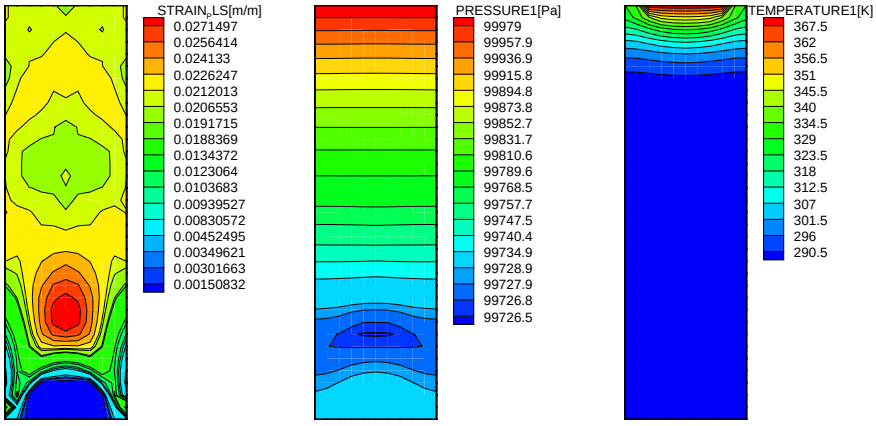

(a) (b) (c)

Fig. 4. Distributions of (a) $\bar{\epsilon}^{pl}$ (b) p^l, (c) T, at $t = 1980s$

Table 3. Processes

Acronym	Process	Treatment
T	Heat transport	Heat balance equation
H^2	Two-phase flow	Mass balance equation
(M)	porosity/permeability change	Material functions

Example 2: Desaturation process in low-permeability media

Example description

This example of the process-oriented approach to multi-field problems is dealing with non-isothermal two-phase flow of water-air through geotechnical buffer materials such as bentonite.

The mathematical formulation of this multi-field problem consists of three partial differential equations derived from the mass balances of fluid components (air, water) and the thermal energy balance. The two-component/two-phase flow equations are highly non-linear and strongly coupled. Details of the continuums-mechanical model and the numerical solution procedure are described in de Jonge et al. (2003) and Kolditz and de Jonge (2003), respectively. The temporal evolutions of the primary variables: gas pressure (p^g), liquid saturation (S^l), and temperature (T) are depicted in Figures 9a,c,d.

This example is to test the effect of the large capillary pressures up to 10^{10} Pa occurring in extremely low-permeable bentonite materials (Fig. 6). Kolditz and de Jonge (2003) also compared the different coupling schemes for solving the set of coupled equations as well as different approaches to multiphase flow (Richards model, two-phase/two-componental systems). For this purpose we start with a simple 1-D case. A one meter long bentonite column is heated on

the left hand side. Element discretization length is $\Delta x = 0.01m$. The initial conditions of the system are: atmospheric gas pressure, full liquid saturation and a temperature of 12^oC. The heater has a constant temperature of 100^oC. Flow boundary conditions on the left side are gas pressure of $10^8 Pa$ and 15% liquid saturation. On the right side we have atmospheric pressure, full liquid saturation and no diffusive heat flux. As a consequence, a typical desaturation process of bentonite is triggered. The complete set of initial and boundary conditions is given in Figure 5. The material properties for this example are summarized in Table 4. Figure 6 shows the capillary pressure - saturation relationship.

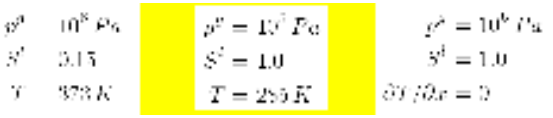

Fig. 5. Example description: initial and boundary conditions

Table 4. Material properties

Symbol	Meaning	Value/Ref	Unit
ρ^g	gas density	$\rho^g(p^g, T)$	kg/m^3
β_p^g	gas compressibility coeff.	6.67×10^{-6}	Pa^{-1}
ρ^l	liquid density	$\rho^l(p^l, T)$	kg/m^3
β_p^l	liquid compressibility coeff.	4.70×10^{-7}	Pa^{-1}
μ^g	gas viscosity	1.8×10^{-5}	$Pa\ s$
μ^l	liquid viscosity	1.2×10^{-3}	$Pa\ s$
c^g	gas heat capacity	1.01×10^3	$J/kg\,K$
c^l	liquid heat capacity	4.2×10^3	$J/kg\,K$
λ^g	gas heat conductivity	0.026	$W/(m\,K)$
λ^l	liquid heat conductivity	0.6	$W/(m\,K)$
ρ	density	1.83×10^3	kg/m^3
n	porosity	0.407	
c	heat capacity	1.6×10^3	$J/kg\,K$
λ	heat conductivity	0.718	$W/(m\ K)$
k	permeability	8.23×10^{-20}	m^2
p_c	capillary pressure	Fig. 6	Pa
k_{rel}	relative permeability	$k_{rel}(S^l, T)$	

Results and discussion

The series of Figures 9 show calculated profiles along the bentonite column at several time stages, $t = 10^3$ to 10^5 seconds for the Richards model, the partitioned and monolithic schemes of the multiphase-multicomponental (MPC) model.

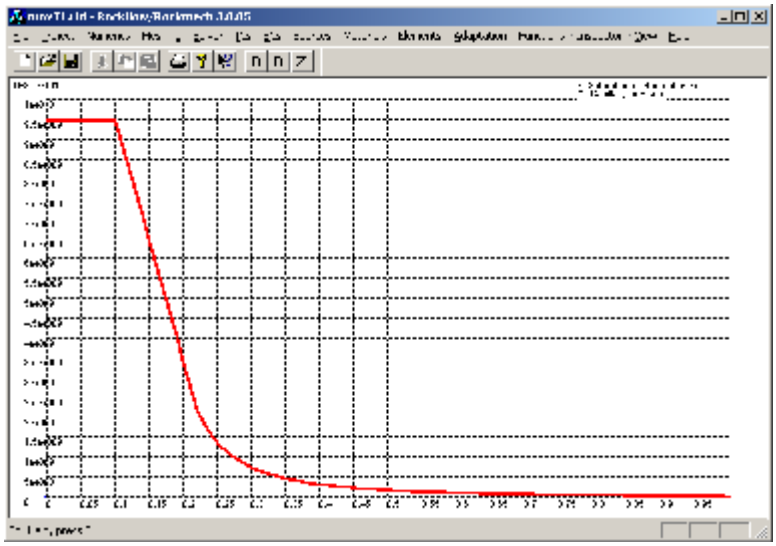

Fig. 6. Capillary pressure as function of liquid saturation $p_C(S^l)$

Flow dynamics - Figs. 9a,b,c:
Pressure and saturation curves illustrate the desaturation process, i.e the advance of the gas phase front from the left to the right side. For the Richards model the liquid pressure is plotted because gas pressure is assumed to be constant. As usual for multiphase systems, there is the typical sharp saturation front in the beginning, which becomes smoother with time. There are differences in the evolution of capillary pressure with time for the Richards model and the MPC models. The differences between the coupling schemes are rather small for the flow process. In the case of the monolithic scheme the saturation and pressure fronts are steeper. The differences of the advance of saturation and capillary pressure fronts indicate additional mechanisms for fluid redistribution. Firstly, the additional fluid transport is a result of componental diffusion effects. Secondly, there are evaporation effects due to the advance of the thermal front.

Heat transport - Figs. 9d:
Fig. 9d show temperature evolution along the bentonite column. The temperature distribution is nearly the same for all models. This is due to heat diffusion being the dominating transport mechanism. Heat advection and dispersion are very small in a low-permeable medium.

Component transport - Figs. 9e,f:
Componental mass fractions depend on both, temperature and gas pressure distributions. Vapour mass in the gas phase X_w^g and dissolved air mass in the liquid phase X_a^l are secondary variables, which are calculated according to ideal gas and Henry equations, respectively. There are clear differences between the Richards model and the multiphase/multi-componental models. In the Richards model the gas pressure is assumed to be constant and equal to atmospheric pressure. As a consequence, the Richards model can account

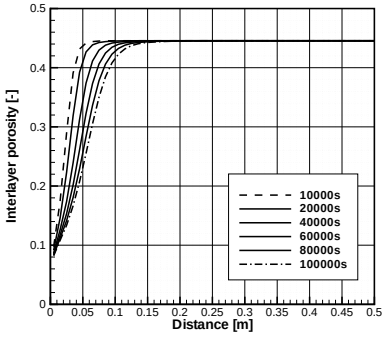

Fig. 7. Evolution of interlayer porosity

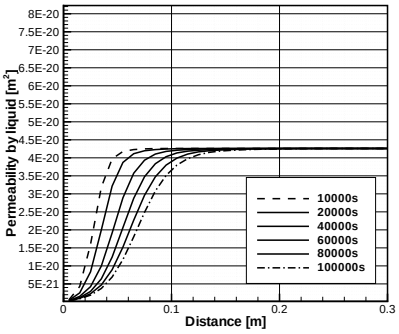

Fig. 8. Evolution of liquid permeability

only for temperature dependencies of the componental mass fractions. At a temperature of $100°C$ and pressure of $101325Pa$ the gas phase is fully saturated with water vapour $X_w^l = 1$. However, at realistic gas pressures of $10^6 Pa$, the water vapour mass fraction at a temperature of $100°C$ is equal to $X_w^l = 0.065$. This emphasises the necessity to take the gas phase dynamics into account. The different advances of the gas pressure and temperature fronts result in peaks of vapour mass fraction at the gas pressure front.

As this example is drying of bentonite material, reduction of liquid saturation will result in decrease of interlayer porosity (Fig. 7) (i.e. increase of effective porosity) and increase of liquid permeability (Fig. 8). Interlayer porosity is defined as $n_{\mathrm{IL}} = e/(1+e)$, where e is void ratio. Details of the chemical swelling model can be found in Xie et al. (2003).

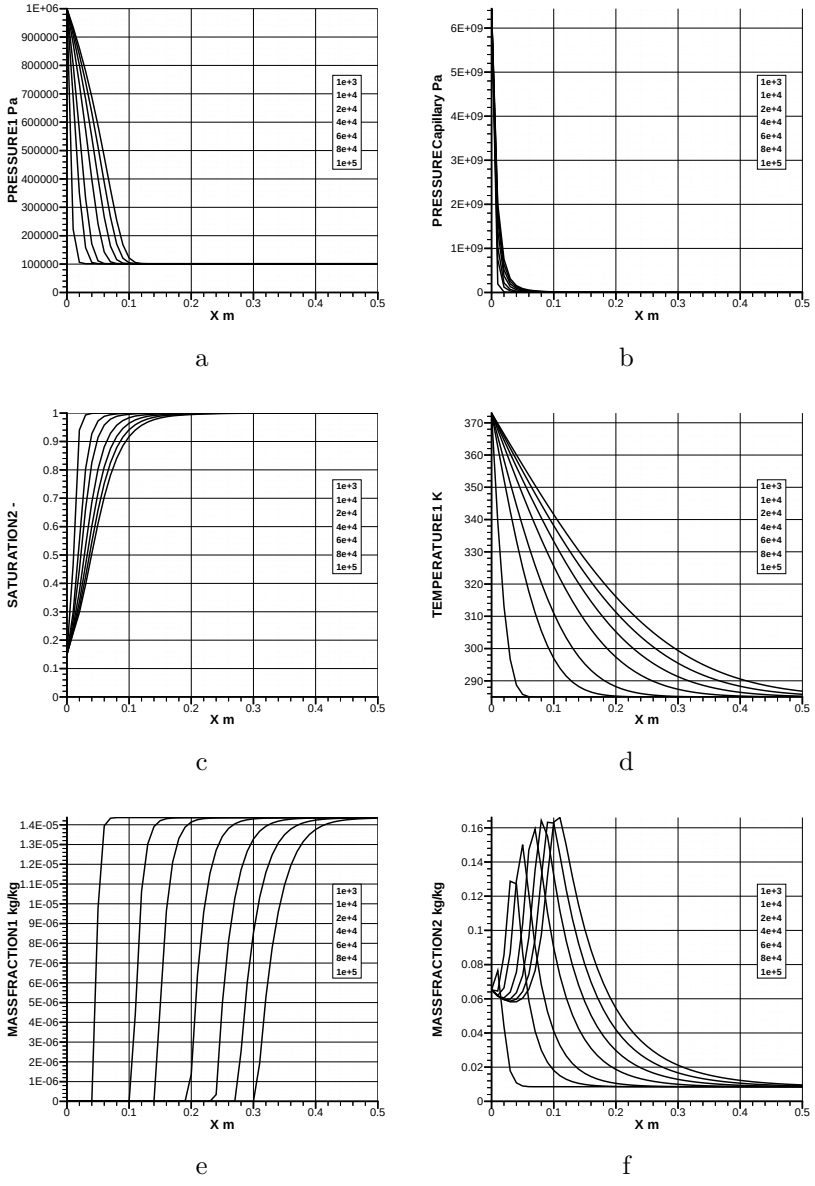

Fig. 9. Multiphase/multi-component model (monolithic coupling scheme): computed profiles a) gas pressure, b) capillary pressure, c) liquid saturation, d) temperature, e) mass fractions of dissolved air, f) mass fraction of water vapour at $t = 10^3, 10^4, 2 \times 10^4, 4 \times 10^4, 6 \times 10^4, 8 \times 10^4, 10^5 s$

Example 3: Desaturation by evaporation

Example set-up

This test case is based on an example proposed by Olivella and Gens (2000). This example portrays the desaturation of a bentonite sample due to heating in a closed system. The set-up is as illustrated in Fig. 10.

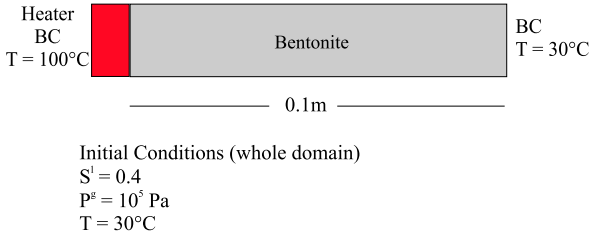

Fig. 10. Definition of the test case

The corresponding material parameters are as summarized in Table 5.

Table 5. Material properties

Parameter	Unit	Value
Porosity	$[m^3/m^3]$	0.44
Tortuosity	$[m^3/m^3]$	0.1
Permeability	$[m^2]$	5×10^{-19}
Relative permeability	[-]	Figure 11
Capillary pressure	[-]	Figure 11
Bentonite density	$[kg/m^3]$	1650
Bentonite heat capacity	$[J/kgK]$	1605
Bentonite heat conductivity	$[J/Kms]$	0.5

Because the capillary pressures in bentonite are very high (up tp $10^4 MPa$, as shown in Fig. 11), a large suction pressure is initiated, that strongly favors saturation of the sample from the open side (at the right). Vapor movement, and hence desaturation due to sample heating can only be modelled if vapor flow is encouraged. This due to the vapour diffusion term of the balance equation for fluid masses (air and water components).

Olivella and Gens (2000) were introducing a dual relative permeability model, i.e. different relative permeabilities for gases and liquids, so that vapor movement is favored at low liquid phase saturations (S^l), when capillary pressure is highest. This dual permeability model is based on experimental evidence for bentonite. The reason behind it is, that in the dry bentonite accessible pore spaces are larger resulting in higher permeability. When bentonite is wet however, it swells and pore spaces are reduced accordingly. Fig.

11(right) shows an example of such a dual relative permeability model for bentonite used in this study.

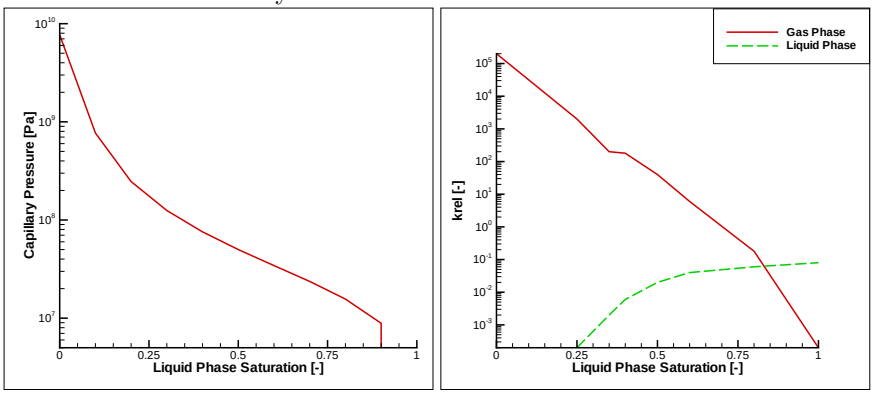

Fig. 11. Capillary pressure - saturation relationship (left), Dual relative permeability - saturation relationships (right)

Simulation results

Because there are no saturation and pressure boundary conditions in the example, saturation is free to fall and rise. This can be observed in the results shown in Fig. 12b. From the initial liquid phase saturation of 0.4, the value drops progressively next to the heater, as expected. On the right boundary, the effects of capillary pressure can be seen through the higher value of liquid phase saturation. The gas phase pressure shows a small response to the saturation distribution. Where liquid saturation drops, and by reciprocity gas saturation increases, gas pressure also increases. At the right boundary, the decrease in gas pressure corresponds to the increase in liquid saturation (Fig. 12a). One can see that the stationary temperature is reached in less than 0.5 day (Fig. 12c). The vapor mass fraction responds to the temperature distribution immediately.

The results thus show successful modelling of a desaturation process in bentonite due to evaporation, by using the TH^2 model. We obtained very similar results as Olivella and Gens (2000) did. Additionally, we used this benchmark to check different element types for TH^2 processes. We obtain identical results for different element types (bar, triangular, quadrilateral elements) which serves as verification tests for the element implementations.

Example 4: Desaturation / saturation of bentonite sample

Example description

This example is proposed to study two processes in the near field of heat emitting containments: First, desaturation due to evaporation at heating elements and second, saturation due to a high-permeable fracture supplying

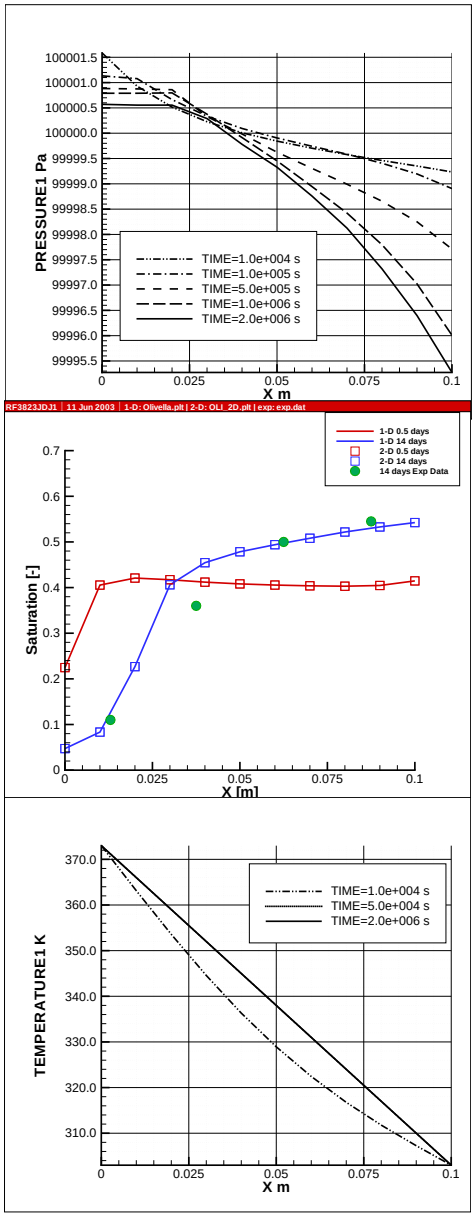

Fig. 12. Profiles of primary variables along the buffer material: gas pressure, liquid saturation, temperature (from top to bottom) for time points: $10^3, 10^4, 2 \times 10^4, 4 \times 10^4, 6 \times 10^4, 8 \times 10^4, 10^5$ seconds (curves from left to right)

water to the heated area. Set-up of this example is shown in Fig. 13 as well as boundary conditions for temperature and liquid saturation.

The material parameters used for example are the same as for example 2 (Table 5).

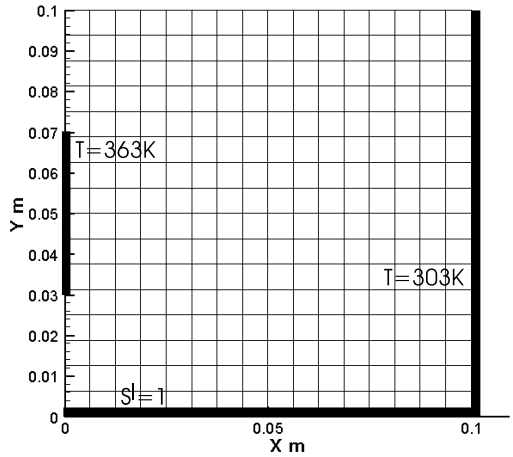

Fig. 13. Boundary conditions of example 4

Simulation results

Fig. 14 show the temporal evolution of the redistribution of the liquid saturation as well as temperature and gas pressure pattern. There are two interesting regions. First, near the heater there is a desaturation due to evaporation and vapor diffusion. Second, the fracture supplies liquid water into the system which is transported to the heater due to capillary forces. The desaturation near the heater results in increased suction. After 5×10^5 the heater area is almost flooded by liquid water delivered from the fracture.

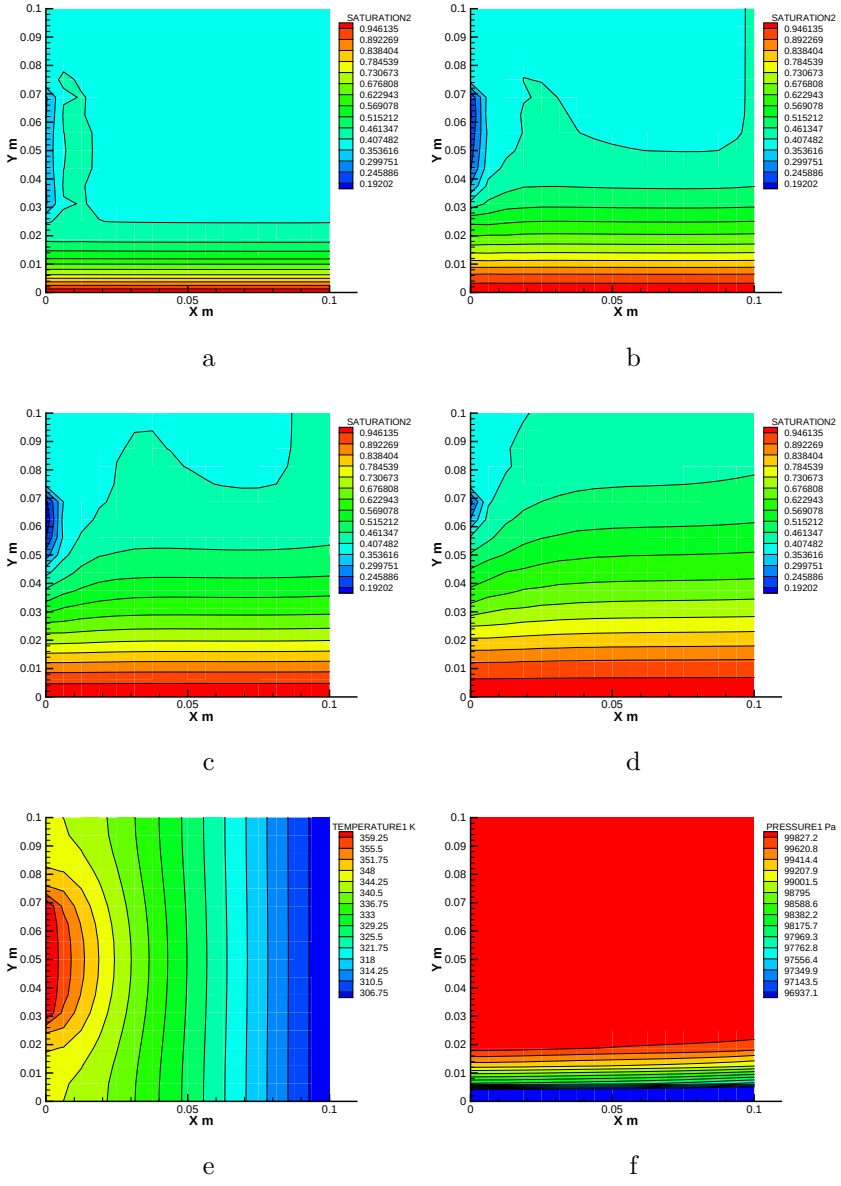

Fig. 14. TH^2 processes in bentonite: computed distributions of primary variables: a),b),c),d) liquid saturation at $t = 10^4, 5 \times 10^4, 10^5, 5 \times 10^5 s$, e) temperature, f) gas pressure at $5 \times 10^5 s$

We will return to this example in section 3, when discussing TH^{2}M processes.

Example 5: BMT1B test case of the DECOVALEX project

This section describes the current work on the near-field bench mark test (BMT1) of the DECOVALEX project (see introduction of part 1). The results shown in this section are preliminary and serve to outline the direction of current code development and to further illustrate the working of the RockFlow TH^2 processes.

Example description

In BMT1 a typical deep geological waste repository set-up is studied. Figure 15 shows a detail of the set-up. The waste canister is surrounded by a bentonite buffer material, and the backfill for the tunnel is made of a bentonite-sand mixture. The host rock is granite. Material parameters, initial conditions and boundary conditions are as described in the BMT1 definition.

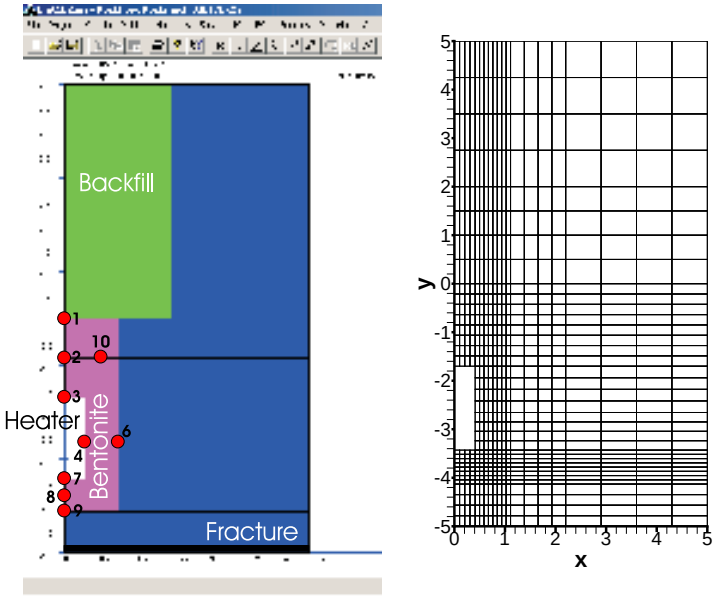

Fig. 15. Definition of the BMT1b test case: distribution of materials (heater, bentonite, backfill, granite and fracture) and observation points (left); computation mesh (right)

Results

The evolution of liquid saturations shows a complex picture of the desaturation / saturation process due to evaporation near the heater element and liquid water supply by the fracture. The liquid saturation rises steadily in observation points B8, B9 nearest to the fracture. Observation points at the heater B3, B7 exhibit first a drying and then resaturation from the fracture water (Fig. 16, left). The corresponding capillary pressure are given in Fig.

17 (left). The development of vapor mass fractions (Fig. 16, right) is mainly controlled by the temperature evolution (Fig. 17, right).

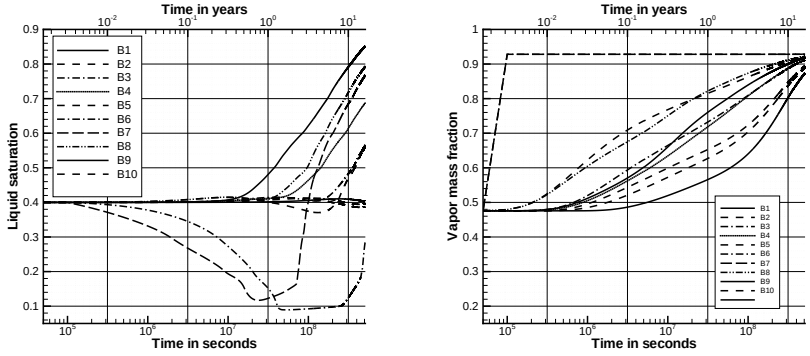

Fig. 16. Evolution of liquid saturations (left) and vapor mass fractions (right) at observation points

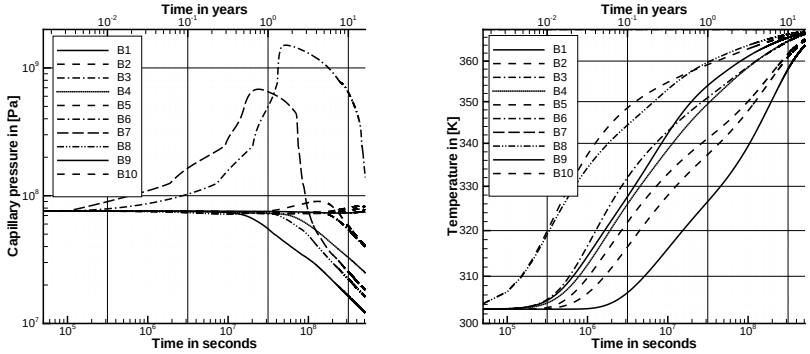

Fig. 17. Evolution of capillary pressures (left) and temperature (right) at observation points

3 Non-isothermal consolidation of unsaturated elasto-plastic materials (TH^2M process)

The process features of this problem class and the treatment are given in Table 6.

Table 6. Processes

Acronym	Process	Treatment
T	Heat transport	Heat balance equation
H^2	Two-phase flow	Mass balance equation
M	Inelastic deformation	Momentum balance equation

Example 6: Non-isothermal desaturation/saturation of elasto-plastic sample

Example description

We return to example 4 (section 2). In this section we considered non-isothermal two-phase/two-componental flow in static porous media. Now we include deformation processes ruled by elasto-plasticity according to Drucker-Pragers constitutive relationship (see Wang and Kolditz (2003)).

Simulation results

The developed object-oriented approach is working for very different processes as well as for different finite element types. We showed examples using line, triangular, quadrilateral elements as well as combinations of them.

The mechanical load are uniformly distributed pressures on top boundary of 10^6Pa and on the left side of 3.5×10^6Pa. The mechanical properties of the material are given in Table 7.

Table 7. The mechanical material parameters

Parameter	Unit	Value
Young's modulus	MPa	20.0
Poisson ratio		0.4
Initial yield stress	MPa	0.5
Plastic hardenning	MPa	-1.0
Thermal expansion	1/K	10^{-5}
Internal friction angle	°	20.0
Dilatancy angle	°	10.0

The distribution of stresses and displacements are illustrated in Figs. 18, respectively. Gas phase pressures, liquid phase saturation and temperature are depicted in Fig. 19 (a-c). In the computation, the stresses decrease along with the time elapses. The resulting accumulated plastic strain at the time of 5×10^5s is shown in Fig. 19(d).

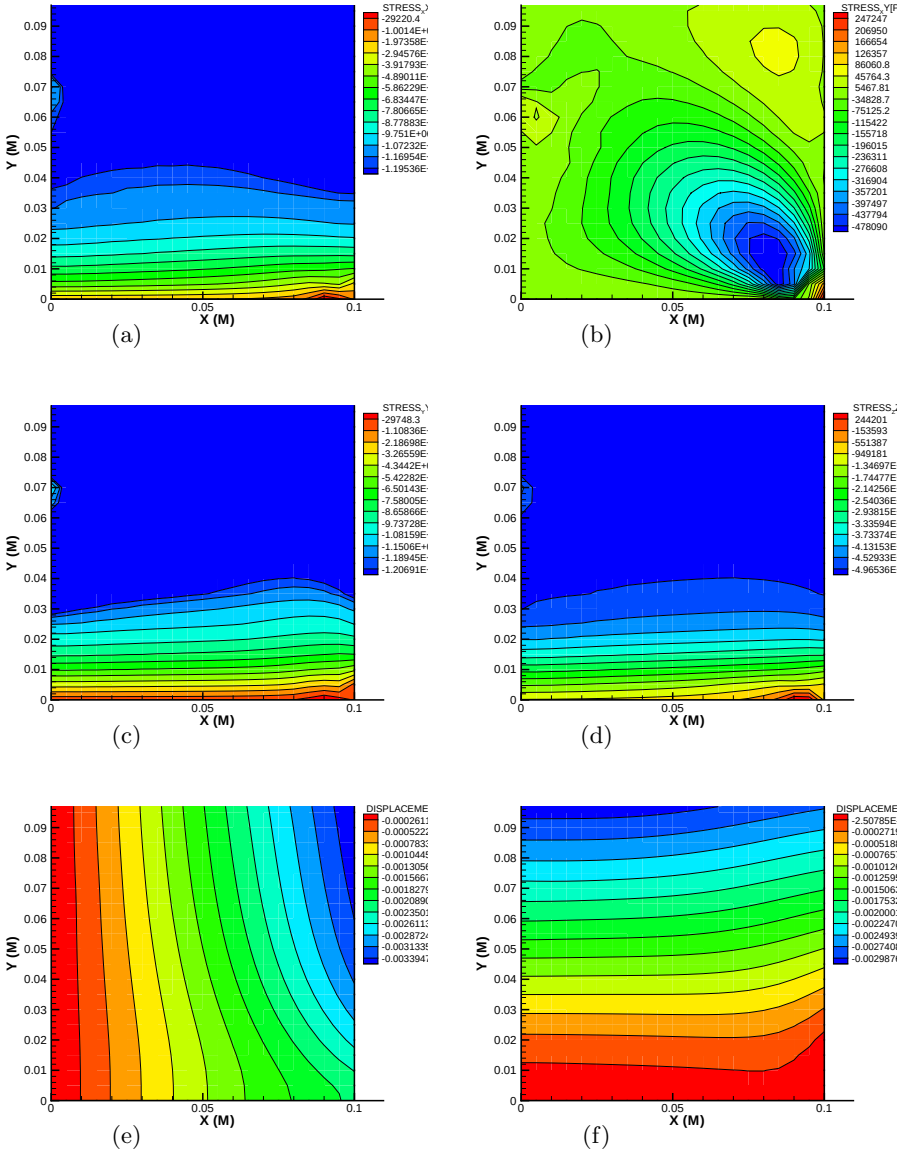

Fig. 18. $\boldsymbol{\sigma}_{xx}(a), \boldsymbol{\sigma}_{yy}(b), \boldsymbol{\sigma}_{xy}(c), \boldsymbol{\sigma}_{zz}(d), \mathbf{u}_x(e), \mathbf{u}_y(f)$ at $t = 5 \times 10^5 s$

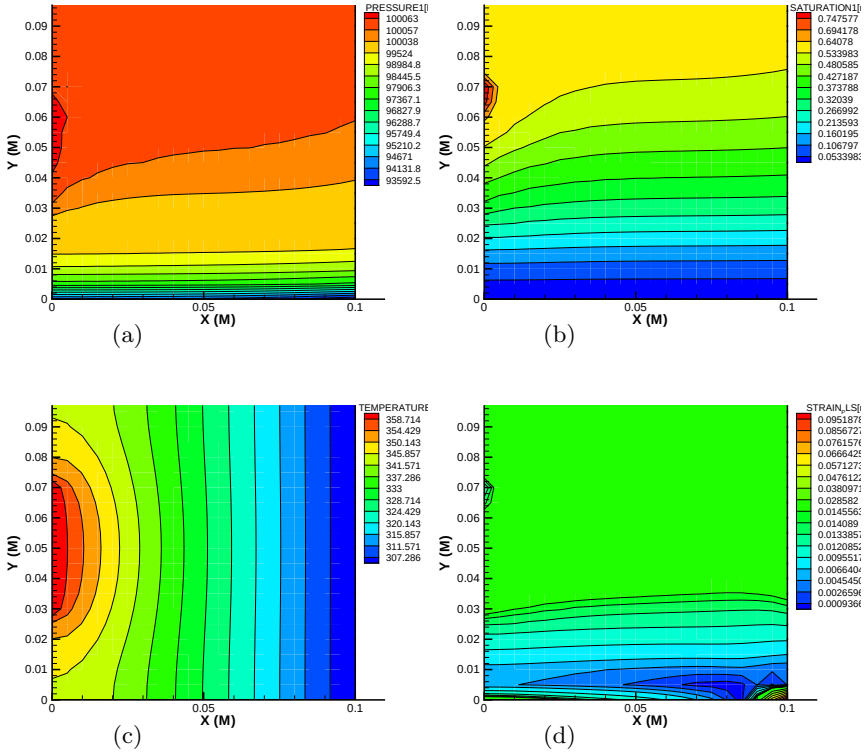

Fig. 19. p^g (a) , S^l (b) , T (c) and accumulated plastic strain (d) at $t = 5 \times 10^5 s$

Conclusions

An object-oriented approach is developed and implemented (paper part 1) to solve coupled, non-linear multi-field problems for porous media. The treatment of processes as objects (PCS) has several advantages

- Standardization of process data,
- Generalization of the solution procedure of PDEs (calculation of element matrices, assembling and solving resulting equation systems),
- Easy to create, configure and execute processes in user-defined loops.

The PCS concept was applied to analyze thermo-hydro-mechanical processes in the near-field of heat emitting containers embedded in bentonite material (paper part 2). The variety of phenomena is spreading from TH^2, THM to TH^2M processes.

Acknowledgement

In this paper we assembled results from several research projects. We are very grateful to the Projektträger PtWT+E (Karlsruhe), the Federal Institute for

Geoscience and Natural Resources (BGR) and the German Science Foundation (DFG) for the funding to these research works. The authors would like to thank Tom Schanz (Weimar), Horst Pitterich (Karlsruhe), Hua Shao, Manfred Wallner and Gerhard Starke (Hannover) for their scientific, technical and logistic support to our research.

References

J. de Jonge, M. Xie, and O. Kolditz. Numerical implementation of thermally and hydraulically coupled processes in non-isothermal porous media. In Stephanson et al., editor, *GeoProc 2003*. accepted paper, 2003.

M. Kohlmeier, R. Kaiser, O. Kolditz, and W. Zielke. Finite element simulation of consolidation and bentonite swelling in the framework of unsaturated porous media. *In: Developments in Water Science*, 47:57–64, 2002.

O. Kolditz and J. de Jonge. Non-isothermal two-phase flow in low-permeable porous media. *submitted to Computational Mechanics*, 2003.

M. Mokni and J. Desrues. Strain localization measurements in undrained plane-strain biaxial tests on Hostun RF sand. *Mech. Cohes.-Frict. Mater.*, 4:419–441, 1998.

S. Olivella and A. Gens. Vapour transport in low permeability unsaturated soil with capillary effects. *Transport in Porous Media*, 40:219–241, 2000.

W. Wang and O. Kolditz. Numerical analysis of elasto-plastic consolidation in porous media. Rockflow-Report 2003-1, www.rockflow.net, submitted to Computational Mechanics, Centre for Applied Geosciences, University of Tübingen, March 2003.

M. Xie, O. Kolditz, S. Tripathy, and T. Schanz. Numerical modeling of swelling processses in porous compacted bentonite. Rockflow-Report 2003-4, www.rockflow.net, Centre for Applied Geosciences, University of Tübingen, Soil Mechanics Lab, University of Weimar, March 2003.

Education record

Education record

Joëlle DE JONGE

18. March 1974

1992	European Baccalaureate, European School Brussels I, Belgium
1992-1994	Chemistry, Université Libre de Bruxelles, Brussels, Belgium
1994-1998	Master of Engineering, Environmental Engineering, University of Southampton, United Kingdom 1997 – 1998: ERASMUS exchange to the Technical University Darmstadt, Germany
2/1999 – 9/2001	Associate Engineer, Brown and Caldwell, Walnut Creek, California, USA
10/2001 – 10/2004	Doctorate Degree in Applied Geology, University of Tübingen, Germany Title: Contributions to computational geotechnics – Non-isothermal flow in low-permeable porous media

ACADEMIC TEACHERS

- Olaf Kolditz
- Rainer Helmig
- Stefan Finsterle